Universidad de Huelva

Departamento de Ingeniería Electrónica, de Sistemas Informáticos y Automática

Desarrollos experimentales de sistemas basados en hidrógeno. Integración en plataformas móviles terrestres y aéreas

Memoria para optar al grado de doctor
presentada por:

Fernando Isorna Llerena

Fecha de lectura: 23 de septiembre de 2021

Bajo la dirección de los doctores:

José Manuel Andújar Márquez

Francisca Segura Manzano

Huelva, 2021

UNIVERSIDAD DE HUELVA

Programa de Doctorado de Ciencia y Tecnología Industrial y Ambiental

Línea de Investigación

Ingeniería Eléctrica, Electrónica, de Control y Robótica

DESARROLLOS EXPERIMENTALES DE SISTEMAS BASADOS EN HIDRÓGENO. INTEGRACIÓN EN PLATAFORMAS MÓVILES TERRESTRES Y AÉREAS

Tesis Doctoral

FERNANDO ISORNA LLERENA

2021

Directores:

Dr. José Manuel Andújar Márquez

Dra. Francisca Segura Manzano

D. José Manuel Andújar Márquez, Catedrático de Universidad de la Escuela Técnica Superior de Ingeniería de la Universidad de Huelva,

Dña. Francisca Segura Manzano, Profesora Titular de Universidad de la Escuela Técnica Superior de Ingeniería de la Universidad de Huelva,

CERTIFICAN:

Que D. Fernando Isorna Llerena, Químico Industrial por la Universidad de Sevilla, ha realizado bajo nuestra dirección y dentro del programa de doctorado de Ciencia y Tecnología Industrial y ambiental (CyTIA) y en la línea de investigación de Ingeniería Eléctrica, Electrónica, de Control y Robótica el trabajo correspondiente a su Tesis Doctoral titulada:

Desarrollos experimentales de sistemas basados en hidrógeno. Integración en plataformas móviles terrestres y aéreas

Revisado el presente trabajo, estimamos que puede ser presentado al Tribunal que ha de juzgarlo.

Y para que así conste a efectos de lo establecido Real Decreto 99/2011 y por la normativa Reguladora del título de Doctor de la Universidad de Huelva, autorizamos la presentación de este trabajo en la Universidad de Huelva.

Huelva, a 7 de Junio de 2021

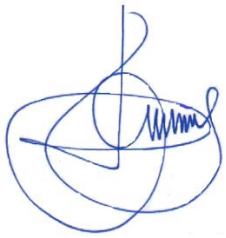

Director: Dr. José Manuel Andújar Márquez

Doctorando: D. Fernando Isorna Llerena

Directora: Dra. Francisca Segura Manzano

Reconocimientos

En primer lugar, quisiera agradecer a mis directores de tesis, el Dr. José Manuel Andújar y la Dra. Francisca Segura, porque sin su infinita paciencia, pasión, confianza y dedicación nunca habría sido posible la finalización de esta tesis doctoral.

A todos mis compañeros del INTA, en el Laboratorio de Sistemas de Energía (LSE-CEDEA), a quienes sabéis que os guardo un gran cariño. Gracias Eduardo López por tus consejos, ánimos y ayuda.

Y, finalmente, quiero agradecer a mi familia, en concreto a mis padres Nani y Manolo, por haberme dado la gran oportunidad de la educación recibida y porque sé la ilusión que les hace tener un hijo doctor. Y por supuesto a mi mujer, Marta, y a mis hijos, Fernando, Javier e Ignacio, por haberles privado de muchos momentos dedicados a elaborar esta tesis. Sin su apoyo nunca podría haber finalizado este trabajo.

"En ciencia, si sabes lo que estás haciendo, no deberías estar haciéndolo."

Richard Wesley Hamming.

Contenidos

Capítulo 1. Enfoque general de la Tesis **12**
1.1. Resumen de la Tesis **14**
1.2. Innovaciones aportadas por la tesis. **15**
1.3. Contribución científica de la tesis **16**
1.3.1. Proyectos científicos que han financiado la tesis **16**
1.3.2. Producción científica (publicaciones en revistas y congresos) **17**
1.3.3. Otras contribuciones científicas (publicaciones en revistas y congresos) **20**
Capítulo 2. Objetivos y Metodología **29**
2.1 Objetivos **29**
2.2 Metodología **29**
Capítulo 3. Materiales **37**
3.1. Banco de ensayos de pilas de combustible **37**
3.1.1. MEAs **38**
3.1.2. Placas bipolares para ensayos de MEAs **39**
3.2. Pila de combustible **40**
3.3. Banco de ensayos de baterías **41**
3.2.1. Canales de alto voltaje **42**
3.2.2. Canales de bajo voltaje **43**
3.2.3. Cámara climática **44**
Las características técnicas de la cámara climática se muestran a continuación: **44**
3.3. Baterías usadas en el vehículo aéreo no tripulado **47**
3.4. Baterías usadas en la plataforma terrestre (vehículo unipersonal) **48**
3.4. Plataforma aérea **50**
3.5. Plataforma terrestre **52**
Capítulo 4. Resultados **57**
4.1. Artículo 1 ..... **57**
4.2. Artículo 2 ..... **71**
4.3. Artículo 3 ..... **107**
4.4. Congreso 1 ..... **127**
4.5. Congreso 2 ..... **133**
4.6. Congreso 3 ..... **137**
4.7. Congreso 4 ..... **143**
4.8. Congreso 5 ..... **149**
Capítulo 5. Conclusiones Generales **156**
Capítulo 6. Otras contribuciones científicas **160**

6.1. Contribución 1 ..... **160**
6.2. Contribución 2 ..... **184**
6.3. Contribución 3 ..... **197**
6.4. Contribución 4 ..... **215**
6.5. Contribución 5 ..... **221**
6.6. Contribución 6 ..... **235**
6.7. Contribución 7 ..... **247**
6.8. Contribución 8 ..... **257**
6.9. Contribución 9 ..... **263**
6.10. Contribución 10 ..... **267**
6.11. Contribución 11 ..... **269**
6.12. Contribución 12 ..... **273**
6.13. Contribución 13 ..... **277**
6.14. Contribución 14 ..... **287**
6.15. Contribución 15 ..... **290**
6.16. Contribución 16 ..... **292**
6.17. Contribución 17 ..... **303**
6.18. Contribución 18 ..... **311**
6.19. Contribución 19 ..... **323**
Lista de Tablas **329**
Lista de Figuras **331**
Lista de Acrónimos **333**

Capítulo 1

Enfoque general de la tesis

Capítulo 1. Enfoque general de la Tesis

Esta Tesis no se concibe como un trabajo aislado, sino dentro de la producción científica y tecnológica que el Laboratorio de Energía del CEDEA viene realizando desde hace años en el campo de la tecnología del hidrógeno y las pilas de combustible.

Se cumplen este año los 30 años de la construcción de la primera planta en España de producción de hidrógeno verde por electrolisis de agua a partir de fuentes renovables, en las instalaciones del INTA en Mazagón, Huelva.

Entre las principales tareas desarrolladas por este Laboratorio destacan la investigación, desarrollo, demostración y transferencia de tecnología de sistemas alternativos de energía, entre los que se integran las tecnologías del hidrógeno y baterías como sistemas de almacenamiento de energía.

Dentro de las tareas del Laboratorio mencionadas anteriormente, esta tesis tiene como objetivo dar soluciones energéticas basadas en sistemas de hidrógeno e implementar las mismas a bordo de diferentes plataformas, ya sean terrestres o aéreas.

Estas soluciones pasan por el uso de pilas de combustible, principalmente de tecnología de polímero sólido, de baja o de alta temperatura. A pesar de ser una tecnología suficientemente robusta y eficiente, este tipo de pilas de combustibles son muy sensibles a la presencia de ciertos contaminantes en el hidrógeno de alimentación.

Por otra parte, esta Tesis se enmarca plenamente en la recientemente publicada *Hoja de Ruta del Hidrógeno* por el Gobierno de España que sigue las directrices europeas en este sentido. El hidrógeno renovable es una solución sostenible clave para la descarbonización de la economía. El hidrógeno renovable es parte de la solución para lograr la neutralidad climática en 2050 y desarrollar cadenas de valor industriales innovadoras en España y en la UE, así como una economía verde de alto valor añadido.

El hidrógeno renovable está llamado a ser un valioso vector energético para usos finales donde sea la solución más eficiente en el proceso de su descarbonización, como la industria intensiva en hidrógeno y procesos de alta temperatura, transporte pesado de larga distancia, transporte marítimo, transporte ferroviario o aviación. Además, la cualidad de vector energético le otorga un gran potencial como instrumento para el almacenamiento energético y la integración sectorial.

En este contexto, el artículo 1 se estudia el efecto de un contaminante muy poco estudiado en pilas de combustible de polímero sólido de baja temperatura y sin casos encontrados en la literatura para alta temperatura. Este contaminante es el NH_3. El reformado de gas natural (metano) y metanol obtenido a partir de biomasa son los métodos predominantes para producir

hidrógeno. En el proceso de reformado para la producción de hidrógeno, es inevitable la aparición de impurezas. El resultado es un gas rico en hidrógeno llamado "gas reformado" que normalmente contiene, además de hidrógeno, óxido y dióxido de carbono, pequeñas cantidades de gases inertes (vapor de agua y nitrógeno) e impurezas de azufre. Se puede formar amoníaco durante el proceso de reformado a niveles de hasta 375 ppm en H_2 puro o incluso más si hay transitorios en los reformadores.

A continuación, para demostrar la aplicación y ventajas del hidrógeno en sistemas de propulsión eléctricos, los artículos 2 y 3 presentan el diseño, desarrollo e implementación de diferentes plataformas móviles aéreas y terrestres.

Así, el artículo 2 muestra la conversión de un RPAS (Remoted Piloted Aircraft System) con un motor de combustión interna (ICE) de ala fija, que se utilizó hace veinte años como objetivo para aplicaciones militares, en un RPAS eléctrico impulsado por batería LiPo para agricultura de precisión en aplicaciones de cultivos de gran tamaño. El motivo por el que se desarrolló este trabajo surgió dentro del proyecto Tecnolivo en el que se ha participado junto con otros socios en España y Portugal en los últimos tres años. Los RPAS utilizados en el proyecto agotaban las baterías en muy corto periodo de tiempo, y no pudieron cubrir grandes superficies. Por esa razón, se pensó en usar un dron de ala fija movido con un motor eléctrico.

Pero también se puso de manifiesto que este RPAS podría utilizarse en entornos naturales protegidos para el seguimiento y vigilancia de determinadas especies aprovechando las principales ventajas de este RPAS: su bajo nivel sonoro y su gran autonomía.

Por último, centrados en las aplicaciones terrestres, el artículo 3 tiene como objetivo demostrar una solución sostenible para la movilidad urbana basada en un vehículo eléctrico unipersonal propulsado por hidrógeno, que aporta grandes ventajas sobre el vehículo eléctrico unipersonal convencional alimentado por batería. Para demostrarlo, se han desarrollado ambos vehículos en versiones comparables, utilizando la misma plataforma, buscando que el peso total del vehículo eléctrico unipersonal sea el mismo en ambos casos. Han sido sometidos a pruebas experimentales que respaldan las características de la configuración basada en hidrógeno frente a la basada en batería, como mayor energía específica, más autonomía y menor tiempo de recarga de la primera.

Los autores consideran que el contenido de este artículo es significativo en estos tiempos en los que las personas reciben instrucción diaria para evitar la interacción social (miedo a compartir con otra persona) mientras que la humanidad debe seguir preservando la sostenibilidad y el respeto al medio ambiente. En este sentido, los vehículos unipersonales que funcionan con baterías presentan algunos desafíos aún no resueltos: las baterías son pesadas y tienen grandes proporciones, en términos de potencia específica limitada.

1.1. Resumen de la Tesis

Esta Tesis está organizada en seis Capítulos según el siguiente orden:

El Capítulo 1 trata del *Enfoque General de la Tesis*, en el que se describe la estructura de la Tesis y un breve resumen de cada uno de los Capítulos que la integran, centrándose en las principales aportaciones. Además, se realiza un análisis del aporte científico que se ha producido con la realización de esta Tesis.

Capítulo 2, *Objetivos y Metodología*, se presentan los objetivos individuales necesarios para lograr el objetivo principal de la tesis, presentar los desarrollos experimentales de sistemas basados en hidrógeno y ejemplos de integración en plataformas móviles terrestres y aéreas. Según la estructura de la tesis, cada una de las aportaciones científicas incluidas en el Capítulo 4, tiene como finalidad dar respuesta a cada uno de los objetivos planteados.

Finalmente, se presenta la metodología de trabajo utilizada para lograr todos y cada uno de los objetivos propuestos.

En el Capítulo 3, *Materiales*, se detallan los sistemas más importantes utilizados para el desarrollo del presente trabajo.

Aparte de la descripción detallada de los bancos de ensayos comerciales que se han usado para la caracterización tanto de baterías como de pilas de combustible, cabría destacar el diseño y construcción de la plataforma terrestre de ensayos y la total transformación de la plataforma aérea donde se han integrado los sistemas eléctricos.

En el Capítulo 4, *Resultados & Métodos*, se presenta el conjunto de contribuciones científicas que sustentan esta tesis. En este sentido, se presentan tres artículos científicos publicados como primer autor en revistas de alto índice de impacto JCR, así como diferentes contribuciones a congresos internacionales, referentes del sector de las energías renovables y el hidrógeno.

En el Capítulo 5, *Conclusiones Generales*, se discuten las conclusiones más relevantes obtenidas de esta Tesis, y se enmarcan las líneas de investigación que han sido abiertas por el trabajo desarrollado, además de proponer estrategias y acciones en este sentido.

Finalmente, en el Capítulo 6, *Otras contribuciones científicas*, se presenta un conjunto de aportaciones científicas en las que el doctorando ha participado activamente como coautor durante la realización de la tesis doctoral. Este compendio de trabajos incluye una serie de artículos de investigación publicados en revistas de índice de alto impacto JCR, así como contribuciones a los principales congresos nacionales e internacionales del sector de las energías renovables y el

hidrógeno. Estas aportaciones complementan la actividad investigadora del doctorando, por lo que se incluyen en el conjunto de aportaciones que sustentan esta tesis.

1.2. Innovaciones aportadas por la tesis.

En esta sección se revisan las principales novedades que y contribuciones derivadas del desarrollo de la tesis, respecto a la revisión del estado del arte llevado a cabo.

En primer lugar, el artículo 1 presenta una extensa revisión sobre aquellos contaminantes que afectan al rendimiento de las pilas de combustible. A pesar de que existen numerosos trabajos científicos sobre cómo influyen negativamente en el rendimiento de las pilas de combustibles ciertos contaminantes como CO_2, CO, H_2S, etc. se han encontrado muy pocos trabajos sobre el NH_3 en pilas de baja temperatura y hay una carencia total de trabajos en la afección de este contaminante en pilas de alta temperatura. Con base en la literatura científica, la novedad de este trabajo radica en la comparativa de pruebas experimentales realizadas sobre PEFC (Polymer Electrolyte Fuel Cell) de alta y baja temperatura. Se muestra cómo, aunque la presencia de trazas de amoníaco en la corriente de alimentación del ánodo, provoca una disminución en la corriente de la celda, y las PEFC de baja temperatura recuperan casi por completo el rendimiento con hidrógeno puro después de exposiciones breves, las PEFC de alta temperatura, incluso con un tiempo de exposición corto, dan como resultado un daño grave e irreversible. Adicionalmente, el trabajo incluye esquemas para describir los mecanismos por los cuales el amoníaco afecta el desempeño de la celda tanto en el lado del ánodo y cátodo, como en la membrana.

En el segundo artículo se presenta un caso real y práctico de transformación de un sistema aéreo no tripulado de ala fija, utilizado como objetivo aéreo y propulsado por un motor de combustión interna, en un RPAS eléctrico para su uso en el cultivo de olivos y otras especies que ocupan grandes extensiones de tierra. Asimismo, y aprovechando una de las principales características de estos sistemas eléctricos, como es su bajo nivel sonoro, esta aeronave eléctrica podría ser utilizada en entornos protegidos, como parques naturales, para la vigilancia y supervisión de diferentes especies animales.

El principal motivo para llevar a cabo esta transformación es aumentar la autonomía de vuelo del RPAS para poder tomar medidas de los diferentes parámetros que afectan a este cultivo a gran escala. Este propósito se ha logrado aumentando la autonomía en casi un 50%.

Por otro lado, este presente trabajo es un paso intermedio para completar un RPAS propulsado con hidrógeno.

Los trabajos futuros, que ya se están llevando a cabo, en esta plataforma aérea consistirán

en la sustitución de parte de las baterías a bordo por un sistema a base de hidrógeno y pilas de combustible. De esta manera, se pretende aumentar aún más la autonomía del UAV.

Finalmente, el tercer artículo presenta la construcción de una plataforma de pruebas para establecer una comparación entre un vehículo eléctrico unipersonal alimentado únicamente por baterías, y el mismo alimentado por un sistema híbrido basado en hidrógeno y baterías. Una de las innovaciones de este artículo es hacer posible la comparación entre ambas tecnologías, ajustando el peso para que el de ambos sistemas sea similar. De esta forma, ha sido posible confrontar ambas tecnologías, sus ventajas y desventajas, en una misma plataforma. La autonomía del sistema híbrido a base de hidrógeno fue de 290 km, siendo mucho mayor que la del sistema a batería que alcanzó aproximadamente los 15 km. Las conclusiones preliminares permiten reconocer que la hibridación energética aporta grandes ventajas específicas a las aplicaciones de movilidad urbana. Los resultados muestran que el vehículo eléctrico unipersonal equipado con un sistema de propulsión a base de hidrógeno proporciona no solo una mayor autonomía, sino que también tiene tiempos de recarga más cortos.

Las capacidades obtenidas en términos de autonomía, tiempo de recarga y, sobre todo, ventajas medioambientales en cuanto a la reducción de contaminantes, hacen de esta una propuesta prometedora y escalable para su uso en ciudades sostenibles.

1.3. Contribución científica de la tesis

Esta sección está dedicada a destacar el entorno científico en el que se ha desarrollado la Tesis y los resultados de cada experimento realizado. Para ello se detallarán las publicaciones relevantes en revistas internacionales indexadas, así como los congresos nacionales e internacionales en los que se han difundido los trabajos desarrollados. En definitiva, el principal objetivo de este apartado es mostrar que la memoria que se presenta constituye el resumen ordenado de la producción científica realizada durante los últimos 7 años.

1.3.1. Proyectos científicos que han financiado la tesis

Este trabajo de investigación ha sido parcialmente financiado por el proyecto TECNOLIVO. Con 2,5 millones de euros de presupuesto, cofinanciado con Fondos FEDER y presentado a la primera convocatoria del Programa INTERREG VA España-Portugal (POCTEP 2014-2020. 0115_TECNOLIVO_6_E), el proyecto ha tenido como objetivo principal el desarrollo de una solución tecnológica comercializable (TecnOlivo) para ser fácilmente utilizado por los agricultores de modo que permita la gestión integral, ecológica y optimizada del olivar

mediante el seguimiento de parámetros agronómicos no invasivos de interés para los olivicultores socios.

1.3.2. Producción científica (publicaciones en revistas y congresos)

Artículo 1. *Effects of Ammonia Impurities on the Hydrogen Flow in High and Low Temperature Polymer Electrolyte Fuel Cells*

Título: Effects of Ammonia Impurities on the Hydrogen Flow in High and Low Temperature Polymer Electrolyte Fuel Cells

Autores: F. Isorna, A. De las Heras, E. López, F. Segura, J.M. Andújar

Revista: Fuel Cells

Referencia: FUEL CELLS 19, 2019, No. 6, 651–662

Año: 2019

Índice de Calidad: 2019 Journal Citation Reports (Clarivate Analytics): 20/27 (Electrochemistry)81/112 (Energy & Fuels), IF (2019): 1.876

Número de citas: 7

En este artículo se estudian los efectos que producen las diferentes concentraciones de NH_3, que pueden estar presentes en el flujo de hidrógeno debido a la producción de reformado a partir de combustibles, como el gas natural, sobre el rendimiento de diferentes tipos de pilas de combustible (de polímeros de alta y baja temperatura), diferenciando entre daños irreversibles y recuperables.

El efecto de la contaminación por NH_3 se analiza y cuantifica comparando las curvas de polarización. Después de la etapa de contaminación, las celdas de combustible se someten a un proceso de regeneración (alimentando la celda de combustible con H_2 puro) con el objetivo de conocer la capacidad de recuperación de la membrana.

El artículo se redactó en base a una revisión bibliográfica exhaustiva con más de 150 referencias consultadas, de las cuales se incluyeron 40 como bibliografía.

Con relación a este Artículo 1, se han presentado también las siguientes contribuciones en congresos:

Contribución a congreso 1.1: Comparison of the influence of ammonia as a contaminant in high and low temperature proton exchange membrane fuel cell performance

Autores: Isorna Llerena, Fernando, López González, Eduardo, De las Heras Jiménez, Ainhoa, Saenz Cuesta, Jaime, Andújar, J.M. and Bolívar Raya, Juan Pedro

Eventoo: V Iberian Symposium on Hydrogen, Fuel Cells and Advanced Batteries

Publicación: Actas del V Iberian Symposium on Hydrogen, Fuel Cells and Advanced Batteries. (Hyceltec 2015)

ISSN: 978-84-606-8621-7

Fecha: Julio 5-8, 2015. Tenerife, España

Contribución a congreso 1.2: Influence of ammonia as contaminant on high temperature proton exchange membrane fuel cell performance

Autores: Fernando Isorna Llerena, Eduardo López González, Jaime Luis Sáenz Cuesta, Felipe Rosa Iglesias, Juan Pedro Bolívar Raya

Evento: European Hydrogen Energy Conference 2014. EHEC 2014

Publicación: Libro de Actas del EHEC 2014

Fecha: 12-14 de marzo de 2014. Sevilla, España

Artículo 2. *Converting a Fixed-Wing Internal Combustion Engine RPAS into an Electric Lithium-Ion Battery-Driven RPAS*

Título: Converting a Fixed-Wing Internal Combustion Engine RPAS into an Electric Lithium-Ion Battery-Driven RPAS

Autores: F. Isorna, A. Fernández, J. A. Bogeat, F. Segura, J.M. Andújar

Revista: Applied Sciences

Referencia: Appl. Sci. 2020, 10, 1573; doi:10.3390/app10051573

Año: 2020

Índice de Calidad: 2020 JCR - Q2 (Engineering, Multidisciplinary) / CiteScore - Q2 (General Engineering), Factor de Impacto (2020): 2.217

Número de citas: 8

Este trabajo ha consistido en la transformación de una aeronave pilotada de forma remota (RPAS) propulsada con un motor de combustión interna en un RPAS eléctrico.

La aeronave resultante incorpora un sistema de baterías de ion polímero (LiPo) y ha sido utilizada en agricultura de precisión en aplicaciones de cultivos de gran tamaño (olivos) en el seno del proyecto TECNOLIVO.

La metodología aplicada ha consistido en el diseño de un nuevo sistema de propulsión, basado en un motor eléctrico y baterías, manteniendo las principales características de aeronavegabilidad de la aeronave.

Posteriormente se modificará esta misma aeronave eléctrica para incorporar un sistema de propulsión basado en hidrógeno y pilas de combustible.

Con relación a este artículo 2, se ha presentado también la siguiente contribución en

congresos:

Contribución a congreso 2.1: Converting a fixed wing ICE RPA into an electric LiPo battery driven RPA for Precision Agricultural Purposes.

Autores: F. Isorna Llerena, A. Fernández Barranco, J.A. Bogeat, J.M. Andújar, F. Segura
Evento: VII Symposium on Hydrogen, Fuel Cells and Advanced Batteries
Publicación: Proceeding's book. Vol. 1, pp. 41-43. (Keynote 4)
Fecha: 1-3 de Julio de 2019. Barcelona (España).

Article 3. *Hydrogen vs battery-based propulsion systems in unipersonal vehicles. Developing solutions to improve the sustainability of urban mobility*

Este trabajo tiene como objetivo demostrar una solución sostenible para la movilidad urbana basada en un vehículo eléctrico unipersonal propulsado por hidrógeno, que, como se muestra, aporta grandes ventajas sobre el vehículo eléctrico unipersonal convencional alimentado por batería. Para demostrarlo, los autores han desarrollado ambos vehículos en versiones comparables, utilizando la misma plataforma, buscando que el peso total del vehículo eléctrico unipersonal sea el mismo en ambos casos. Han sido sometidos a pruebas experimentales en test de laboratorio y ensayos en carretera, que respaldan las características de la configuración basada en hidrógeno frente a la basada en batería, como mayor energía específica, más autonomía y menor tiempo de recarga.

Title: Hydrogen vs battery-based propulsion systems in unipersonal vehicles. Developing solutions to improve the sustainability of urban mobility

Autores: F. Isorna Llerena, E. López González, J.J. Caparrós, F. Segura, J.M. Andújar
Revista: Sustainability (ISSN: 2071-1050)
Referencia: Sustainability 2021, 13, 5721; doi: 2071-1050/13/10/5721
Año: 2021
Índice de Calidad: JCR category rank: 120/265 (Q2) in 'Environmental Sciences' (SCIE); 26/41 (Q3) in 'Green & Sustainable Science & Technology', Factor de Impacto (2020): 2.576

Con relación a este artículo 3, se han presentado también las siguientes contribuciones en congresos:

Contribución a congreso 3.1: Fuel cell-battery hybrid powered electric tricycle as a testing platform

Autores: F. Isorna Llerena, A. Fernández Barranco, J.A. Bogeat1, J. Sáenz Cuesta1, J.M. Andújar, F. Segura
Evento: VII Symposium on Hydrogen, Fuel Cells and Advanced Batteries

Publicación: Proceeding's book. Vol. 1, pp. 110-112.
Fecha: 1-3 de Julio de 2019. Barcelona (España).

Contribución a congreso 3.2: Use of unmanned fuel cell ground vehicles (UGVs) for precision agriculture (TecnOlivo Project).

Autores: F. Isorna Llerena, A. Fernández Barranco, J.A. Bogeat, E. López González, J.M. Andújar, F. Segura
Evento: VII Symposium on Hydrogen, Fuel Cells and Advanced Batteries
Publicación: Proceeding's book. Vol. 1, pp. 235-237.
Fecha: 1-3 de Julio de 2019. Barcelona (España).

1.3.3. Otras contribuciones científicas (publicaciones en revistas y congresos)

Además de las contribuciones científicas detalladas anteriormente, el estudiante de doctorado ha sido coautor de las siguientes contribuciones.

Publicaciones en Revistas Científicas

1. Título: Multi-Objective Fuzzy Logic-Based Energy Management System for Microgrids with Battery and Hydrogen Energy Storage System
   Autores: Francisco José Vivas, Francisca Segura, José Manuel Andújar, Adriana Palacio, Jaime Luis Sáenz, Fernando Isorna y Eduardo López
   Revista: Electronics
   Referencia: Electronics 2020, 9, 1074; doi:10.3390/electronics9071074
   Año: 2020
   Índice de calidad: Indexada en JCR ranking: 125/266 (Q2) in "Engineering, Electrical & Electronic", Factor de Impacto (2020): 2.412

2. Título: Experimental evaluation of a passive fuel cell/battery hybrid power system for an unmanned ground vehicle
   Autores: Eduardo López González; Jaime Sáenz Cuesta; Francisco José Vivas Fernández; Fernando Isorna Llerena; Miguel A. Ridao Carlini; Carlos Bordons Alba; Emili Hernández; Alberto Efes
   Revista: International Journal of Hydrogen Energy
   Referencia: Volume 44, Issue 25, 17 May 2019, Pages 12772-12782 https://doi.org/10.1016/j.ijhydene.2018.10.107

Year: 2019

Índice de Calidad: Cited Score: 8.0; SCImago Journal Rank (SJR): 1.141, Factor de Impacto (2019): 4.939

3. Título: Comprehensive diagnosis methodology for faults detection and identification, and performance improvement of Air-Cooled Polymer Electrolyte Fuel Cells
   Autores: J.M.Andújar, F.Segura, F.Isorna, A.J.Calderón
   Revista: Renewable and Sustainable Energy Reviews
   Referencia: Volume 88, May 2018, Pages 193-207 https://doi.org/10.1016/j.rser.2018.02.038
   Year: 2018
   Índice de Calidad: Cited Score: 25.5; SCImago Journal Rank (SJR): 3.632, Factor de Impacto (2019): 12.110

4. Título: Incremento de la autonomía en vehículos no tripulados mediante el uso de sistemas híbridos de potencia con pila de combustible: Proyecto IUFCV
   Autores: Eduardo López, Fernando Isorna, M. Ángel Ridao, Carlos Bordons, Alberto Elfes, Emili Hernández
   Revista: Boletín de Observación Tecnológica en Defensa
   Referencia: Vol. 53 Paginas 15–19, Primer Trimestre 2017
   Año: 2017
   Índice de calidad: Indexada en JCR ranquing: 125/266 (Q2) in 'Engineering, Electrical & Electronic', Factor de Impacto (2020): 2.412

5. Título: Optimization of a PEM fuel cell operating conditions: Obtaining the maximum performance polarization curve
   Autores: J. Antonio Salva, Alfredo Iranzo, Felipe Rosa, Elvira Tapia, Eduardo Lopez, Fernando Isorna
   Revista: International Journal of Hydrogen Energy
   Referencia: Volume 41, Issue 43, 16 November 2016, Pages 19713-19723 https://doi.org/10.1016/j.ijhydene.2016.03.136
   Year: 2016
   Índice de Calidad: Cited Score: 8.0; SCImago Journal Rank (SJR): 1.141, Factor de Impacto (2019): 4.939

6. Título: Effect of carbon dioxide on the contamination of low temperature and high temperature PEM (polymer electrolyte membrane) fuel cells. Influence of temperature, relative humidity and analysis of regeneration processes
   Autores: Manuel Antonio Díaz, Alfredo Iranzo, Felipe Rosa, Fernando Isorna, Eduardo López, Juan Pedro Bolivar
   Revista: Energy
   Referencia: Volume 90, Part 1, October 2015, Pages 299-309 https://doi.org/10.1016/j.energy.2015.06.097
   Year: 2015
   Índice de Calidad: Cited Score: 9.9; SCImago Journal Rank (SJR): 2.166, Factor de Impacto (2019): 6.082

7. Título: Energy evaluation of a solar hydrogen storage facility: Comparison with other electrical energy storage technologies
   Autores: Eduardo Lopez Gonzalez, Fernando Isorna Llerena, Manuel Silva Perez, Felipe Rosa Iglesias, Jose Guerra Macho
   Revista: International Journal of Hydrogen Energy
   Referencia: Volume 40, Issue 15, 27 April 2015, Pages 5518-5525 https://doi.org/10.1016/j.ijhydene.2015.01.181
   Year: 2015
   Índice de Calidad: Cited Score: 8.0; SCImago Journal Rank (SJR): 1.141, Factor de Impacto (2019): 4.939

Contribuciones a Congresos Nacionales e Internacionales

8. Título: Development, integration and evaluation of hybrid fuel cell power systems for unmanned ground vehicles.
   Autores: E. López González, J. Sáenz Cuesta, F. Isorna Llerena, M.A. Ridao, C. Bordons, E. Hernandez, J. Brett
   Evento: VII Symposium on Hydrogen, Fuel Cells and Advanced Batteries (HYCELTEC 2019)
   Publicación: Libro de actas del Congreso Vol. 1, pp. 106-109.
   Fecha: 1-3 de julio de 2019. Barcelona, (España)

9. Título: Energy Management System for a Microgrid with hydrogen storage and two batteries using Model Predictive Control
   Autores: Miguel A. Ridao, P. Fernández, C. Bordons, E. López, F. Isorna

Evento: VII Symposium on Hydrogen, Fuel Cells and Advanced Batteries (HYCELTEC 2019)
Publicación: Libro de actas del Congreso Vol. 1, pp. 73-75.
Fecha: 1-3 de julio de 2019. Barcelona, (España).

10. Título: Evaluación de un vehículo terrestre no tripulado (UGV) con pila de combustible
Autores: Eduardo López González, Jaime Sáenz Cuesta, Fernando Isorna Llerena, M.A. Ridao, E. Hernández
Evento: VII Congreso Nacional de i+d en Defensa y Seguridad 2019
Publicación: Proceeding's book. Vol. 1, DESEID-2019-96, pág. 91
NIPO: 083-19-215-9
Fecha: 19-21 de noviembre de 2019. San Fernando, Cádiz (España).

11. Título: Green hydrogen production methods. A review of solar-driven water splitting techniques.
Autores: Isorna Llerena, F; Segura Manzano , F; Andújar Márquez, J
Evento: European Hydrogen Energy Conference 2018 (EHEC 2018)
Publicación: Proceedings book. Vol. 1, pp. 160-161.
Fecha: 14-16 marzo, 2018. Málaga (España).

12. Título: Evaluation of fuel cell/battery passive hybrid power system for unmanned vehicles.
Autores: Alberto Efes; Eduardo López González; Jaime Sáenz Cuesta; Francisco José Vivas Fernández; Fernando Isorna Llerena; Miguel A. Ridao Carlini; Carlos Bordons Alba; Emili Hernández
Evento: European Hydrogen Energy Conference 2018 (EHEC 2018)
Publicación: Proceedings book. Vol. 1, pp. 176-177.
Fecha: 14-16 marzo, 2018. Málaga (España).

13. Título: Diseño y desarrollo de una microrred para la gestión y el almacenamiento de energía eléctrica de origen renovable.
Autores: Fernando Isorna; Eduardo López González; Jaime Sáenz Cuesta
Evento: VI Congreso Nacional de i+d en Defensa y Seguridad (DESEi+d)
Publicación: Libro de Actas del Congreso. Vol. 1, pp. 451-459.
Fecha: 14-16 marzo, 2018. Valladolid (España).

14. Título: Increasing energy efficiency and autonomy in unmanned vehicles using hybrid fuel cell power systems.
    Autores: E. López González, F. Isorna Llerena, M.A. Ridao Carlini, C. Bordons Alba, A. Elfes, E. Hernandez.
    Evento: VI Symposium on Hydrogen, Fuel Cells and Advanced Batteries (HYCELTEC 2017)
    Publicación: Libro de actas del Congreso. Vol. 1, pp. 176-177.
    ISBN 978-972-752-233-0
    Fecha: 19-23 junio, 2017. Oporto (Portugal).

15. Título: Cómo incrementar la duración de las misiones en vehículos submarinos no tripulados (y otras plataformas robóticas) ProyectoIUFCV
    Autores: E. López González, F. Isorna Llerena, M.A. Ridao Carlini, C. Bordons Alba, A. Elfes, E. Hernandez.
    Evento: Feria de la Ciencia 2017
    Publicación: Libro de actas del Evento.
    Fecha: 11-13 mayo, 2017. Sevilla (España).

16. Título: Incremento de la eficiencia energética y autonomía en vehículos no tripulados mediante el uso de sistemas de energía híbridos con pila de combustible.
    Autores: López González, Eduardo, Isorna Llerena, Fernando, Ridao Carlini, Miguel Ángel, Bordons Alba, Carlos, Elfes, Alberto, Hernández, Emili.
    Evento: IV Congreso Nacional de I+D en Defensa y Seguridad, 2016
    Publicación: Libro de actas del Congreso.
    ISBN: 978-84-946021-3-9
    Fecha: 16-18 noviembre, 2016. San Javier, Murcia (España).

17. Título: Analysis of high-pressure hydrogen and natural gas cylinders explosions through TNT equivalent method.
    Autores: E. López, R. Rengel, G. W. Mair, F. Isorna.
    Evento: V Iberian Symposium on Hydrogen, Fuel Cells and Advanced Batteries.
    Publicación: Actas del V Iberian Symposium on Hydrogen, Fuel Cells and Advanced Batteries. (Hyceltec 2015)
    ISSN: 978-84-606-8621-7
    Fecha: Julio 5-8, 2015. Tenerife, España

18. Título: Aplicación en vehículos no tripulados de sistemas híbridos de potencia basados en pilas de combustible
    Autores: López González, Eduardo, Isorna Llerena, Fernando, Argumosa Martínez, Mª Pilar, Maellas Benito, Jesús, Ridao Carlini, Miguel Ángel, Bordons Alba, Carlos
    Evento: II Congreso Nacional de I+D en Defensa y Seguridad, 2014
    Publicación: Libro de Actas del Congreso. Vol 1 pp 305-315.
    ISBN: 978-84-940583-2-5
    Fecha: 6 y 7 de noviembre de 2014. Zaragoza (España).

19. Título: Energy evaluation of a solar hydrogen storage facility
    Autores: Eduardo López González, Fernando Isorna Llerena, Manuel Silva Pérez, Felipe Rosa Iglesias
    Evento: European Hydrogen Energy Conference 2014
    Publicación: Libro de Actas del Congreso. Volumen 1, pp. 226-227.
    Fecha: 12-14 de marzo de 2014. Sevilla (España).

Capítulo 2

Objetivos y Metodología

Capítulo 2. Objetivos y Metodología

2.1 Objetivos

El principal objetivo de esta Tesis es demostrar diferentes desarrollos experimentales basados en hidrógeno de manera que puedan dar soluciones para su posterior integración en plataformas móviles, ya sean terrestres, aéreas o acuáticas.

Para alcanzar el objetivo principal de la Tesis se han definido una serie de objetivos específicos, que se describen a continuación:

- **Objetivo I: Análisis de los efectos de diferentes contaminantes en el rendimiento de las pilas de combustible de polímero sólido.**

Al objetivo de determinar el efecto sobre el rendimiento de las pilas de combustible de ciertos contaminantes, se le une el de conocer los posibles mecanismos por los que el NH_3, y otros contaminantes, afectan al rendimiento de las celdas de combustible. Del mismo modo se tratará de determinar procedimientos para recuperar el rendimiento una vez contaminadas.

- **Objetivo II: Diseño de una plataforma tipo RPAS eléctrico, impulsado por baterías de iones de litio para fines agrícolas de precisión a partir de uno de motor de combustión interna.**

El objetivo específico es poder disponer de una plataforma de ensayos operativa donde ensayar los diferentes sistemas de propulsión basados en tecnología del hidrógeno y pilas de combustible. La primera será la construcción de la aeronave totalmente eléctrica (baterías) y posteriormente su implementación a pilas de combustible.

- **Objetivo III: Diseño de una plataforma terrestre para movilidad urbana, donde poder establecer comparaciones entre sistemas de propulsión basados en hidrógeno frente a baterías en vehículos unipersonales.**

El objetivo es desarrollar ambos vehículos en versiones comparables, utilizando la misma plataforma, buscando que el peso total del vehículo eléctrico unipersonal sea el mismo en ambos casos.

2.2 Metodología

Para lograr los objetivos específicos definidos en el apartado anterior, se define una metodología de trabajo, que se fundamenta y se implementa posteriormente en las diferentes Contribuciones científicas presentadas en el Capítulo 4.

La metodología propuesta se establece de acuerdo con los objetivos específicos de la Tesis definidos en el apartado anterior.

- **Objetivo I: Análisis de los efectos de diferentes contaminantes en el rendimiento de las pilas de combustible de polímero sólido**

Para conseguir este objetivo, la metodología empleada ha consistido en que los ensayos experimentales se realizaron tanto en modo galvanostático como potenciostático, y con modo de funcionamiento de flujo continuo, aunque también se realizaron en modo de funcionamiento sin salida (dead.end). Los parámetros de funcionamiento que se han controlado son: (1) flujo de combustible, (2) flujo de oxidante, (3) temperatura de reactivos, (4) humedad relativa de los reactivos, (5) presión del ánodo, (6) presión del cátodo y (7) temperatura de la celda.

Para las pruebas de alta temperatura, se utilizaron dos calentadores integrados para el control de la temperatura. Estos consistían en calentadores de cartucho ubicados dentro de las placas finales. Aparte de esto, la celda se aisló para reducir los gradientes de temperatura y fue necesario un ventilador para eliminar el exceso de calor producido por la celda.

Para los experimentos de baja temperatura, el banco de pruebas FuelCon está equipado con un sistema de calefacción/enfriamiento de calentador externo controlado por un controlador proporcional-integral-derivado (PID) que está integrado en el banco de pruebas y se utiliza para el control de la temperatura. Este calentador externo constaba de una resistencia flexible que rodeaba la celda. Aparte de esto, la celda se aisló de la misma manera que en las pruebas de alta temperatura.

Para ambas pruebas experimentales (alta y baja temperatura), se utilizó un termopar (Rössel MesstechnikTM) ubicado dentro de una de las placas bipolares para medir la temperatura de la celda.

Con el fin de caracterizar la influencia del amoniaco en las PEFC de alta y baja temperatura, se han diseñado dos experimentos para PEFC formadas a partir de una sola celda. Esto se ha hecho de esta forma porque los resultados esperados de los stacks implementados a partir de varias celdas deberían ser similares.

- **Objetivo II: Diseño de una plataforma tipo RPAS eléctrico, impulsado por baterías de iones de litio para fines agrícolas de precisión a partir de uno de motor de combustión interna**

La plataforma RPAS seleccionada para este trabajo fue elegida del Proyecto ALO (Avión Ligero de Observación) que es un RPAS desarrollado por INTA, que puede proporcionan información de reconocimiento, vigilancia y adquisición de objetivos en tiempo real mediante

cámaras de TV y FLIR (sensor de infrarrojos orientables) intercambiables y orientables. Las imágenes se pueden enviar en tiempo real a la estación de control terrestre (GCS) donde se proporcionan capacidades de procesamiento de imágenes.

En una misión típica realizada por ALO, el RPAS se transporta al sitio de lanzamiento en el vehículo de transporte que también desempeña el papel de estación de control terrestre. Todo el RPAS se transporta en un solo vehículo (tamaño Unimog), lo que proporciona una gran capacidad de movilidad y transporte, lo que permite misiones desde ubicaciones no preparadas. El montaje y la instalación del RPAS se pueden realizar en menos de 30 minutos sin el uso de herramientas especiales.

Después de cargar los puntos de referencia en la computadora de a bordo, el RPAS se lanza desde un lanzador hidráulico o neumático. El RPAS volará la misión programada sobre el área de vigilancia transmitiendo, en tiempo real, las imágenes captadas por la cámara y datos de telemetría relevantes, como, posición del RPAS, velocidad, consumo de combustible, revoluciones por minuto (rpm) del Motor RPA o altitud. En caso de detectar cualquier posible objetivo, actividad o área de interés, el piloto ubicado en la estación de control terrestres (Ground Control Station, GCS), puede tomar el control manual del RPAS volando alrededor del punto seleccionado.

Cuando finalice la misión, o cuando así lo decida el piloto, el RPAS podrá regresar de forma autónoma al lugar de lanzamiento y la recuperación se realizará mediante un paracaídas. Además, para la evaluación de la misión, toda la misión se graba y se puede reproducir en un monitor de video donde se muestran todos los parámetros de vuelo principales.

La metodología utilizada para la consecución de este objetivo ha sido el mantener las principales características de aeronavegabilidad del RPAS mientras que se cambiaban aquellos sistemas propios de la aeronave con motor de combustión interna para su transformación aérea. Ha habido que realizar así mismo numerosas pruebas de empuje del motor eléctrico sobre la nueva hélice de la aeronave eléctrica.

- **Objetivo III: Diseño de una plataforma terrestre para movilidad urbana, donde poder establecer comparaciones entre sistemas de propulsión basados en hidrógeno frente a baterías en vehículos unipersonales**

Para demostrar las capacidades de la hibridación de hidrógeno en el transporte urbano eléctrico frente a la tecnología basada en baterías, se diseñan dos vehículos unipersonales: el primero es un vehículo eléctrico unipersonal alimentado por batería, mientras que el segundo es un vehículo eléctrico unipersonal basado en hidrógeno. El objetivo es montar los sistemas de propulsión basados batería y en hidrógeno en plataformas similares, buscando que el peso total del vehículo eléctrico unipersonal sea el mismo en ambos casos. Cabe destacar que el hidrógeno

utilizado en las instalaciones del Laboratorio de Energía de CEDEA, tipo hidrógeno verde, producido a partir de fuentes renovables.

La metodología desarrollada para obtener los resultados de los datos experimentales, se ha fundamentado en realizar pruebas dinámicas de laboratorio y en carretera con las dos configuraciones: vehículo eléctrico unipersonal basado en batería y basado en hidrógeno.

Para comprobar la plataforma del vehículo unipersonal a batería, esta se somete en primer lugar a un perfil de conducción dinámico de laboratorio. Se aplican diferentes etapas de aceleración, provocando fricciones o frenadas manuales.

Para la prueba dinámica en carretera, se aplica una prueba de conducción real sobre el vehículo eléctrico unipersonal en movimiento.

La prueba de autonomía en carretera ha recorrido un total de 48 kms a una velocidad media de 12 km/h. El vehículo eléctrico unipersonal se ha operado primero con propulsión eléctrica mediante batería y después con propulsión eléctrica a partir de hidrógeno, por carril bici, desde las instalaciones del INTA hasta la localidad de Mazagón.

Capítulo 3

Materiales

Capítulo 3. Materiales

3.1. Banco de ensayos de pilas de combustible

Para la caracterización de los sistemas basados en pilas de combustibles, así como para toda la investigación realizada sobre el comportamiento de las MEAs (Membrane Electrode Assembly) frente a la contaminación del hidrógeno de alimentación, se ha utilizado un banco de ensayos de monoceldas y stacks de pilas de combustible de FuelCon© modelo CT-1000. El mismo cuenta con una serie de especificaciones técnicas idóneas para el desarrollo de los ensayos necesarios. Éstas se resumen en la Tabla 1.

Parámetro	Valor
Caudal ánodo (Nl/min)	0.2 a 10
Caudal cátodo (Nl/min)	0.4 a 20
Humidificación	Ánodo y Cátodo
Medidas de tensión	Celda individual
Máxima potencia (W)	600
Máxima intensidad (A)	100
Modos de operación	*Dead-End* y continuo

Tabla 1: Especificaciones del banco de ensayos de pilas de combustible

Este banco tiene además la posibilidad de programar los ensayos y cuenta con un analizador de impedancia. La Figura 1 muestra una imagen del banco de ensayos.

Figura 1: Banco de ensayos de pilas de combustible

3.1.1. MEAs

Para la experimentación llevada a cabo con objeto de caracterizar la influencia del amoniaco, tanto en pilas de combustible de polímero sólido de alta y baja temperatura, se han utilizado membranas (Membrane Electrode Assembly, MEAs) consistentes en un conjunto de dos electrodos y una membrana. Los resultados obtenidos son extrapolables a un stack de pila de combustible que conste de varias celdas.

Con los ensayos de alta temperatura se han utilizado MEAs de Danish Power Systems™ hechas de polibencimidazol (PBI) con cinco capas y una carga de catalizador de 1,5 mg/cm^2, tanto en el lado del ánodo como en el del cátodo. El espesor de la membrana es de 40 mm, el área del electrodo de 72 x 72 mm^2 y el área de la celda activa 68 x 68 mm^2. Podemos Se puede ver una imagen de la misma en la Figura 2.

Por el contrario, para los ensayos de baja temperatura, las MEAs empleadas han sido de Paxitech©, elaboradas con Nafion©. Son conjuntos de 7 capas y una carga de catalizador de 0.5 mg/cm^2 tanto en el lado del ánodo como en el del cátodo, con un espesor de membrana de 50 mm y un área de celda activa de 68 x 68 mm^2 (Figura 3).

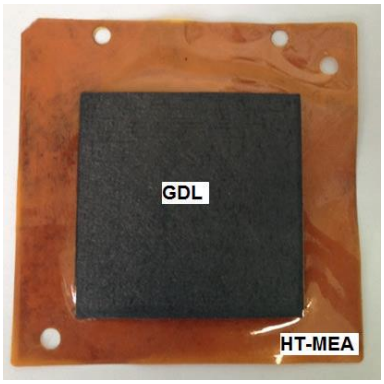

Figura 2: Membrane Electrode Assembly de alta temperatura

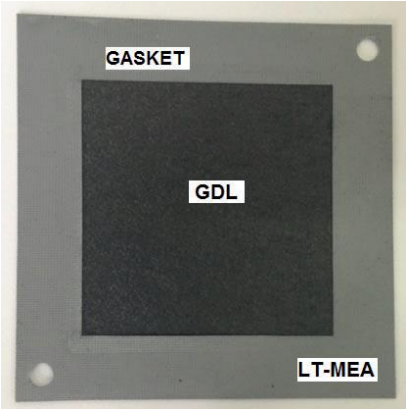

Figura 3: Membrane Electrode Assembly de baja temperatura

3.1.2. Placas bipolares para ensayos de MEAs

Las MEAs se han ensayado en un dispositivo compuesto por dos placas terminales, con sus respectivos conductos de alimentación de hidrógeno y aire, que alojan en su interior las MEAs. Este dispositivo cuenta además con resistencias calefactoras para ensayos con membranas de alta temperatura. Tiene un área activa de 50 cm^2 con tres canales de flujo en serpentín paralelos (canales de 0,76 mm de ancho y profundidad). El diseño de la placa bipolar de grafito es de flujo cruzado con canales horizontales tanto en el ánodo como en el cátodo. Es de la empresa Teledyne Energy Systems©.

Unas imágenes de este dispositivo se reproducen en las Figura 4 y Figura 5.

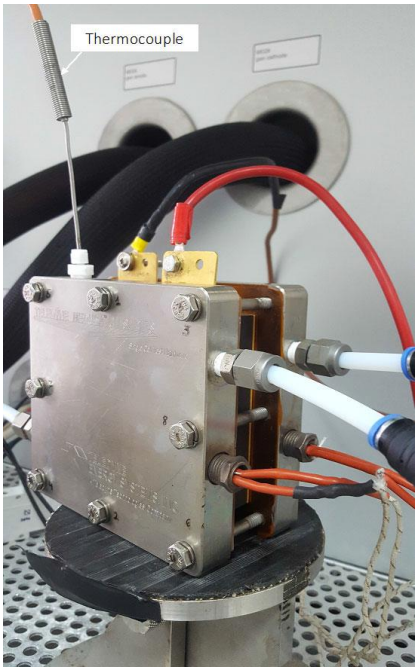

Figura 4: Placas bipolares para ensayos

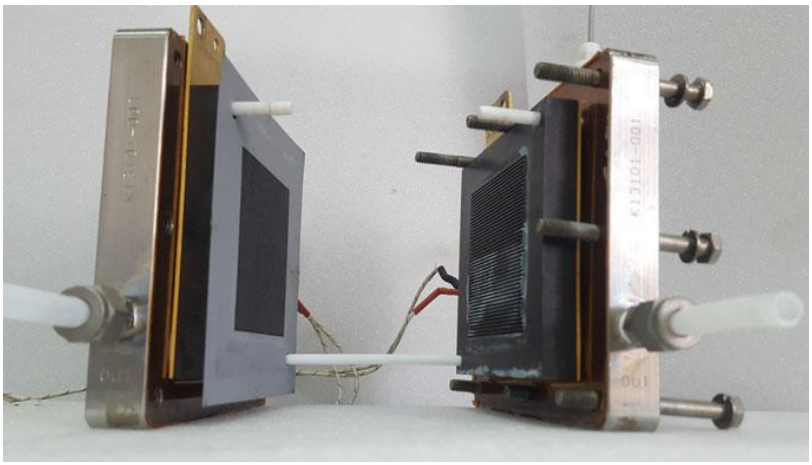

Figura 5: Imágenes de placas bipolares de grafito y una MEA

3.2. Pila de combustible

La pila de combustible utilizada en la plataforma eléctrica ha sido un stack de polímero sólido de la empresa rusa BMPower©. Se trata de una pila de combustible de 500 W de potencia nominal. Las principales características se muestran en la Tabla 2.

Parámetro	Valor
Modelo	BMPower© 500
Voltaje nominal (V)	50
Potencia nominal (W)	500
Dimensiones con el controlador (mm)	225 x 145 x 124
Peso (incluye controlador y ventilador) (Kg)	1.1
Nº de celdas	48

Tabla 2: Características técnicas de la pila de combustible

En las Figura 6 y Figura 7 se muestran imágenes de la pila de combustible empleada.

Figura 6: Pila de combustible utilizada BMPowwer© 500

Figura 7: Pila de combustible instalada en la plataforma

Los parámetros de la pila de combustible se monitorizan a través de una conexión Wi-Fi y son registrados durante las pruebas experimentales del sistema. La herramienta de software BMPower® está diseñada para monitorear y controlar el funcionamiento del sistema de propulsión. La Figura 2 representa una captura de pantalla de dicho software.

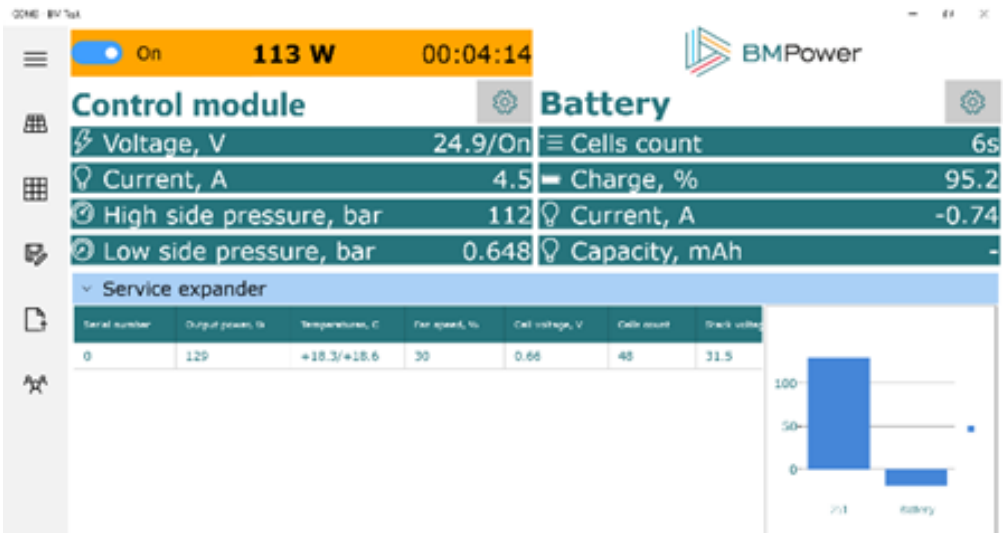

Figura 8: Software de control de la pila de combustible

3.3. Banco de ensayos de baterías

Para la caracterización de los sistemas basados en baterías utilizados en las diferentes plataformas, se ha contado con un banco de ensayos de baterías y supercondensadores de Arbin Instruments©. El mismo cuenta con 4 canales para alto voltaje y 4 para bajo voltaje. Además, existe la posibilidad de operar conjuntamente con una cámara climática de Dycometal©. De esta manera se pueden realizar los ensayos de las diferentes baterías en condiciones controladas de temperatura y humedad.

Algunas características comunes a todos los canales son:

- Precision: ±0.05% FSR (Full Scale Range)
- Modos de Operación:
    - Voltaje constante (CV)
    - Corriente constante (CC)
    - Potencial constante (CP)
    - Resistencia constante (CR)

- Rampas de voltaje (Ramp)
- Rampa de Corriente (Ramp)
- Barrido en escalón de Corriente y Tensión
- CC-CV sistema de seguridad y suavizado para pulsos de corriente constante o tensión constante.
- Medida de Resistencia Interna DC para todos los canales

3.2.1. Canales de alto voltaje

Las características principales se muestran a continuación:

- Número de Canales: 4 canales
- Posibilidades de conexión: los canales permiten conectarse en paralelo sumando la corriente de cada canal, permitiendo una intensidad máxima de 400A. Los canales deberán estar firmemente sujetos al dispositivo a probar. Está posibilidad es válida tan solo para trabajar a corriente constante, voltaje y control de potencia.
- Rango de Voltaje (mín. / máx.): 0 a 60V
- Exactitud de control y medida de Voltaje (±0.05% FSR): ± 60mV
- Voltaje mínimo a la máxima corriente (100A): 0V
- Impedancia de entrada: ~10GΩ
- Máxima Corriente (carga / descarga): 100ª
- Resolución de corriente y voltaje: 16 bits
- Rangos de corriente (± 0.05% FSR): Alto: 100A ± 100mA
  Medio: 10A ± 10mA
  Bajo: 1A ± 1mA
- Tiempo de subida de corriente: 3mS. Dado que este es un circuito bipolar, el tiempo de conmutación entre la carga y descarga es NULO.
- Tipo de circuito: Bipolar lineal
- Potencia Continua Máxima por canal: 6000W

La Figura 9 muestra una imagen de estos módulos.

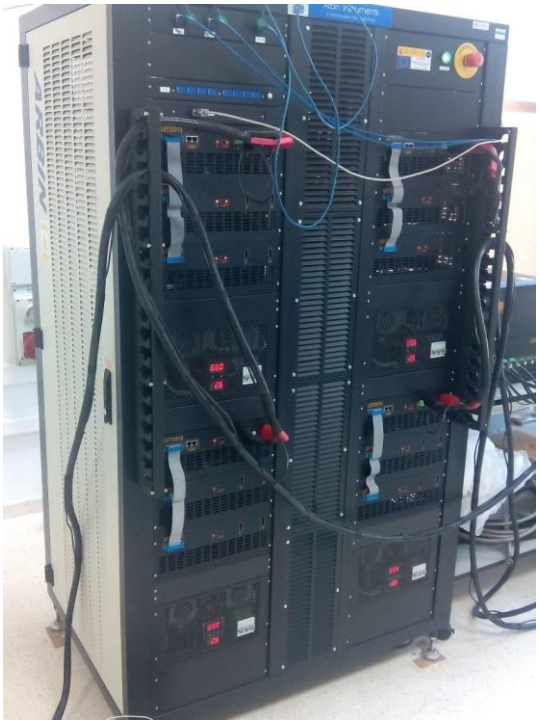

Figura 9: Módulos de alto voltaje

3.2.2. Canales de bajo voltaje

Las características principales se muestran a continuación:

- Número de Canales: 4 canales.
- Posibilidades de conexión: los canales permiten conectarse en paralelo sumando la corriente de cada canal, consiguiendo una intensidad máxima de 40A. Los canales deberán estar firmemente sujetos al dispositivo a probar. Está posibilidad es válida tan solo para trabajar a corriente constante, voltaje y control de potencia.
- Rango de Voltaje (mín. / máx.): 0 a 5V
- Exactitud de control y medida de Voltaje (±0.05% FSR): ± 2mV
- Voltaje mínimo a la máxima corriente (10A): 0V
- Impedancia de entrada: ~10GΩ
- Máxima Corriente (carga / descarga): 10A
- Resolución de corriente y voltaje: 14 bits
- Permite pulsos con anchura menor a 5 milisegundos
- Rangos de corriente (± 0.05% FSR): Alto: 10A ± 4mA

- Medio: 100mA ± 40µA
- Bajo: 1mA ± 400nA
- Tiempo Subida de Corriente: 50-100µs. Dado que este es un circuito bipolar, el tiempo de conmutación entre carga y descarga es NULO.
- Tipo de circuito: Bipolar lineal
- Potencia Continua Máxima por canal: 50W

La Figura 10 muestra el módulo de canales de bajo voltaje.

Figura 10: Módulos de bajo voltaje

3.2.3. Cámara climática

Las características técnicas de la cámara climática se muestran a continuación:

- Volumen cámara: 300 litros
- Medidas interiores: 700 x 700 x 625mm (Al x An x Fo)
- Medidas exteriores: 1950 x 1000 x 1220 (Al x An x Fo)
- Interior fabricado totalmente en acero inoxidable de calidad AISI 316 pulido, satinado, antimagnético, totalmente estanco y sin soldaduras interiores. Revestido en su parte exterior con placas Newtherm, especialmente diseñadas para soportar sin deterioro el funcionamiento de la cámara a la máxima temperatura de trabajo.

- Exterior en acero galvanizado lacado.
- Aislamiento compuesto por poliuretano sin CFC y paneles de lana de roca mineral. Impermeabilidad total y resistencia al ataque corrosivo de ácidos y álcalis.
- Control de temperatura y humedad.
- Temperatura mínima de ensayo de menos cuarenta grados centígrados (-40ºC)
- Temperatura máxima de ensayo de ciento cincuenta grados centígrados (150ºC)
- Estabilidad de la temperatura: ±0.1ºC a ±0.3ºC (en vacío)
- Precisión de la temperatura: ±0.1ºC
- Rango de humedad de 10 al 98% HR
- Estabilidad de la humedad: ±1% HR a ±3%HR
- Precisión de la humedad: ±0.1%HR
- Control mediante controlador Eurotherm 2604
- Puerta de apertura frontal con mirilla de observación ubicada y centrada en la puerta y de dimensiones de 400 x 350 mm en multicristal atemperado compuesto por 7 lunas en vidrio securit selladas al vacío. Resistencias en marco de puerta y ventana (antivaho): 2 x ±92 W. Junta de silicona flexible de alta y baja temperatura en todo el burlete para facilitar la hermeticidad del cierre de la puerta. Bisagras cromadas y cierre de ajuste.
- Puntos de acceso (portholes) para monitorización de los ensayos mediante el ECCM. Fabricado en silicona de 80 mm de diámetro con tapón estanco para la introducción de cableado eléctrico, termosondas o termómetros, situado ambos en lateral izquierdo de la cámara climática.
- Base equipada con 4 ruedas multidireccionales.
- Sistema de calefacción compuesto por elementos calefactores blindados y aleteados, fabricados totalmente en acero inoxidable. Su baja resistencia térmica facilita una rápida respuesta en la transferencia de energía eléctrica a térmica. Una protección especial entra en funcionamiento ante la ausencia del movimiento del aire. La ubicación de dichos elementos es de fácil acceso para su mantenimiento. El control electrónico de potencia se lleva a cabo mediante triacs (relés estáticos), con circuito de disparo por paso de cero, evitando así la generación de ruido eléctrico tan indeseable en todo laboratorio.
- Potencia calefactora instalada: 3 kW
- Sistema de humidificación basado en la utilización de un baño de agua controlado electrónicamente con resistencias eléctricas perfectamente aisladas del agua, para evitar así derivaciones eléctricas. El hecho de producir vapor con una sobrepresión facilita la entrada y posterior mezcla en los conductos generales del aire. Absolutamente todos los elementos que componen este circuito son de acero inoxidable. Este sistema se aloja en el exterior de la cámara aislado y protegido de los otros elementos.

La Figura 11 muestra una imagen de la cámara climática, mientras que en la Figura 12 se observa el conjunto integrado del banco de ensayos de baterías.

Figura 11: Cámara climática

Figura 12: Conjunto de cámara climática y bancos de ensayos de baterías

3.3. Baterías usadas en el vehículo aéreo no tripulado

Entre los diferentes tipos de baterías comerciales disponibles (plomo ácido, NiMH, NiCd, LiPo y $LiFePO_4$), con el estado actual de la tecnología y los precios del mercado, se concluyó que la mejor batería para ser utilizada en el vehículo aéreo no tripulado fuera la batería de polímero de litio (LiPo). Es la que tiene mayor energía específica, a pesar de ser la más frágil. Sus principales ventajas y características se reflejan a continuación:

- Alto voltaje por celda. En este caso, el voltaje nominal de cada celda es de 3,7 V y puede alcanzar un valor máximo de 4,2 V.
- Energía específica alta, alrededor de 200 Wh / kg.
- Poco peso.
- Alta densidad de potencia.
- Carga rápida.
- Larga vida, que se traduce en ahorro económico.
- Fenómeno de pasivación: consiste en la formación de una película de cloruro de litio que se forma en la superficie del ánodo e impide su autodescarga. Esto es beneficioso si la batería no se usa durante un período de tiempo prolongado, ya que evita que se descargue.

Por el contrario, algunas desventajas son:

- Degradación a temperaturas superiores a 60 °C.
- Degradación si se descarga por debajo de su voltaje mínimo, 3 V.

El paquete de baterías final que se usó en el UAV estuvo compuesto por 28 celdas comerciales de polímero de litio 15 C 3,7V de 16.000 mAh con configuración 14 en serie y 2 en paralelo (14s2p), logrando un paquete final con 32.000 mAh de capacidad teórica y 58,8 V.

Las celdas se empaquetaron en un habitáculo realizado con una impresora 3D (Figura 13 y Figura 14) con todos los acoplamientos y anclajes asegurados en la bahía principal del UAV. También tenía aberturas verticales para una mejor gestión de la temperatura.

Figura 13: Habitáculo de las baterías con los 3 bloques debidamente soldados

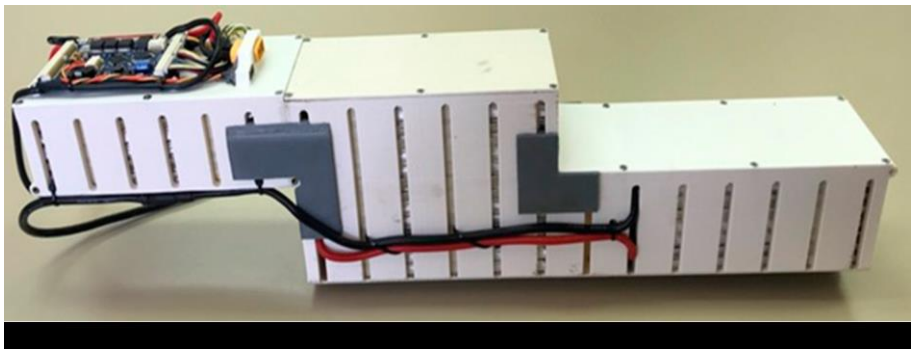

Figura 14: Baterías conectadas dentro del habitáculo

3.4. Baterías usadas en la plataforma terrestre (vehículo unipersonal)

Utilizando esta plataforma se han realizado dos tipos de ensayos, uno de ellos con un sistema de propulsión basado solo en baterías y otro con sistema de propulsión híbrido (hidrógeno, pila de combustible y una batería de apoyo).

En la Tabla 3 se recogen las principales características de las baterías del sistema de propulsión de la plataforma a baterías.

Parámetro	Valor
Modelo	Herewin MG-12000P
Voltaje nominal (V)	24
Energía nominal (Wh)	266
Capacidad (Ah)	12
Weight (Kg)	3.6
Tecnología	LiPo

Tabla 3: Características técnicas de las baterías empleadas en la plataforma terrestre

La Figura 15 muestra las baterías empleadas en la plataforma terrestre.

Figura 15: Imágenes de las baterías usadas en el sistema de propulsión de la plataforma aérea

Por otro lado, en el sistema basado en pila de combustible, se ha utilizado una batería a modo de *buffer*.

Las características de esta batería se muestran en la Tabla 4 y se puede ver una imagen de la misma en la Figura 16.

Figura 16: Batería buffer

Parámetro	Valor
Voltaje nominal (V)	22.2
Energía nominal (Wh)	73
Capacidad (Ah)	3.3
Peso (Kg)	0.5
Tecnología	LiPo

Tabla 4: Características técnicas de la batería buffer

3.4. Plataforma aérea

Para el desarrollo experimental del sistema de potencia, se ha utilizado un RPAS (Remoted Piloted Aircraft System) de ala fija con un motor original de combustión interna, utilizado como objetivo para aplicaciones militares. El mismo ha sido profundamente modificado para transformarlo en un RPAS eléctrico, equipado con un paquete de baterías LiPo con el sistema de gestión de baterías (BMS) y un motor eléctrico con su respectivo controlador. También se cambió la hélice, pero se mantuvieron las principales características de aeronavegabilidad de la plataforma aérea. Dicha plataforma aérea se ha sometido a todas las pruebas pertinentes de ensayos en vuelo y está lista para poder modificar el nuevo sistema de propulsión eléctrico basado en baterías por uno híbrido con H_2 y pilas de combustible. Las características principales de la aeronave original se resumen en la Tabla 5.

Parámetro	Valor
Envergadura (m)	3.03
Longitud (m)	1.8
MOTW (Peso máximo al despegue, Kg)	25
Superficie alar (m^2)	0.85
Carga de pago máxima (Kg)	7.5
Autonomía (h)	1
Velocidad (Km/h)	50-225
ROC (tasa de ascenso, m/s)	6
Alcance (Km)	50

Tabla 5: Características principales de la aeronave original

Una imagen de la plataforma aérea se muestra en la Figura 17.

Figura 17: Imagen de la plataforma aérea eléctrica

En la Tabla 6 se resumen las principales diferencias de las dos plataformas aéreas, la eléctrica y la de motor de combustión interna.

	RPAS combustión interna	RPAS eléctrico
Fuselaje	3,5 Kg	3,5 Kg
Motor	3,5 Kg	1,9 Kg
Hélice	0,35 Kg	0,4 Kg
FCS (sistema de control de vuelo)	0,85 Kg	0,31 Kg
Módulo de telemetría	0,70 Kg	0,20 Kg
Tanques de combustible + Combustible	6,35 Kg	-
Sistema suministro de combustible	0,27 Kg	-
Batería principal	-	2,39 Kg
Caja de batería + BMS	-	0,95 Kg
Batería auxiliar FCS	1,76 Kg	1,37 Kg
Peso sin carga útil	17,43 Kg	19,84 Kg
Max. Carga útil	7,57 Kg	5,16 Kg
Autonomía	60 min	90 min
Emisiones	CO_2 + CO + NO_x	Cero

Tabla 6: Principales diferencias de las dos plataformas aéreas

3.5. Plataforma terrestre

Para demostrar las capacidades de la hibridación de hidrógeno en el transporte urbano eléctrico frente a la tecnología basada en baterías, se han diseñado dos vehículos unipersonales: un vehículo eléctrico unipersonal alimentado por batería y un vehículo eléctrico unipersonal a base de hidrógeno.

El objetivo era montar los sistemas de propulsión a base de batería y a base de hidrógeno en plataformas similares y garantizar que el peso total del vehículo eléctrico unipersonal fuera el mismo en ambos casos. La Figura 18 muestra la plataforma construida con un chasis de hierro que incluye todos los componentes del sistema de propulsión; (a) diseño conceptual, (b) implementación física.

La plataforma integra un motor eléctrico de 24 V y 250W de la empresa Golden Motor®, modelo MP3-20F Magic Pie® 3, acoplado a la rueda delantera de 20 pulgadas. Se ha dimensionado en este rango para cumplir con los requisitos de energía típicos en baterías comerciales y celdas de combustible, promoviendo la escalabilidad del diseño. El sistema ha sido regulado a través de un controlador programable, modelo Magic® MX25 BAC-281P de Golden Motor®. Las especificaciones del sistema se resumen en la Tabla 7.

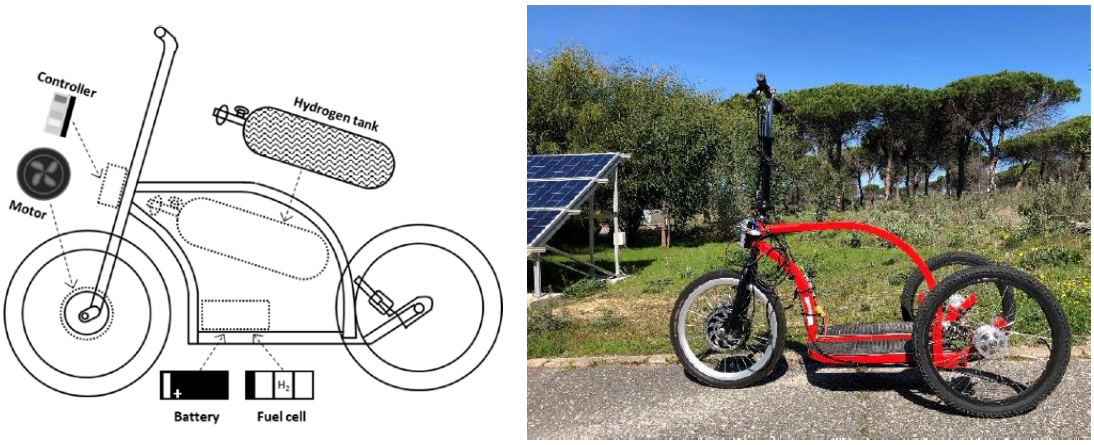

Figura 18: Plataforma de vehículo eléctrico unipersonal: (a) diseño conceptual; (b) implementación física

Dispositivo	Parámetro	Valor
Motor	Voltaje (V)	24
	Potencia (W)	250
	Peso incluyendo la rueda (Kg)	7.5
Rueda	Diámetro (cm)	50,8
Controlador del motor sin escobillas	Rangos de voltaje (V)	24, 36, 48
	Máxima potencia (W)	1000

Tabla 7: Características del sistema

Capítulo 4

Resultados

CAPÍTULO 4: RESULTADOS y CAPÍTULO 6: OTRAS CONTRIBUCIONES CIENTÍFIAS

Algunos trabajos publicados, debido a restricciones relativas a derechos de autor, han sido retirados de la tesis. En sustitución de los documentos ofrecemos la siguiente información: referencia bibliográfica, y en el caso de artículos, además, enlace al texto completo y resumen

- Isorna Llerena, F. López González, E., Heras Jiménez, A., Saenz Cuesta, J., Andújar, J.M. and Bolívar Raya, J.P. "Comparison of the influence of ammonia as a contaminant in high and low temperature proton exchange membrane fuel cell performance". En: V Iberian Symposium on Hydrogen, Fuel Cells and Advanced Batteries (Tenerife, del 5 al 8 de julio de 2015).

- Isorna Llerena, F., López González, E., Luis Sáenz Cuesta, J., Rosa Iglesias, F., Bolívar Raya, J.P.: "Influence of ammonia as contaminant on high temperature proton exchange membrane fuel cell performance". En: European Hydrogen Energy Conference (EHEC 2014) (Sevilla, del 12 al 14 de marzo de 2014).

- Isorna Llerena, F., Fernández Barranco, A., Bogeat, J.A., Andújar, J.M., Segura, F.: "Converting a fixed wing ICE RPA into an electric LiPo battery driven RPA for Precision Agricultural Purposes". En: VII Symposium on Hydrogen, Fuel Cells and Advanced Batteries, HYCELTEC 2019 (Barcelona, del 1 al 3 de julio de 2019). ISSN: 0360-3199.

- Isorna Llerena, F., Fernández Barranco, A., Bogeat, J.A., Sáenz Cuesta, J., Andújar, J.M., Segura, F.: "Fuel cell-battery hybrid powered electric tricycle as a testing platform". En: VII Symposium on Hydrogen, Fuel Cells and Advanced Batteries, HYCELTEC 2019 (Barcelona, del 1 al 3 de julio de 2019). ISSN: 0360-3199.

- Isorna Llerena, F., Fernández Barranco, A., Bogeat, J.A., López González, E., Andújar, J.M., Segura, F.: "Use of unmanned fuel cell ground vehicles (UGVs) for precision agriculture (TecnOlivo Project)". En: VII Symposium on Hydrogen, Fuel Cells and Advanced Batteries, HYCELTEC 2019 (Barcelona, del 1 al 7 de julio de 2019). ISSN 0360-3199

- López González, E., Sáenz Cuesta, J., Vivas Fernandez, F. J., Isorna Llerena, F., Ridao Carlini, M. A., Bordons, C., Hernandez, E., & Elfes, A. (2019). Experimental evaluation of a passive fuel cell/battery hybrid power system for an unmanned ground vehicle. In International Journal of Hydrogen Energy (Vol. 44, Issue 25, pp. 12772–12782). Elsevier BV. https://doi.org/10.1016/j.ijhydene.2018.10.107

Enlace al texto completo: https://doi.org/10.1016/j.ijhydene.2018.10.107

RESUMEN:

Unmanned vehicles are increasing the performance of monitoring and surveillance in several applications. Endurance is a key issue in these systems, in particular in electric vehicles, powered at present mainly by batteries. Hybrid power systems based on batteries and fuel cells have the potential to achieve high energy density and specific energy, increasing also the life time and safe operating conditions of the power system. The objective of this research is to analyze the performance of a passive hybrid power system, designed and developed to be integrated into an existing Unmanned Ground Vehicle (UGV). The proposed solution is based on six LiPo cells, connected in series, and a 200 W PEM fuel cell stack, directly connected in parallel to the battery without any limitation to its charge. The paper presents the characterization of the system behavior, and shows the main results in terms of performance and energy management.

- Andújar, J. M., Segura, F., Isorna, F., & Calderón, A. J. (2018). Comprehensive diagnosis methodology for faults detection and identification, and performance improvement of Air-Cooled Polymer Electrolyte Fuel Cells. In Renewable and Sustainable Energy Reviews (Vol. 88, pp. 193–207). Elsevier BV. https://doi.org/10.1016/j.rser.2018.02.038

Enlace al texto completo: https://doi.org/10.1016/j.rser.2018.02.038

RESUMEN:

This paper presents a comprehensive practical diagnosis methodology for the detection and identification of faults in Air-Cooled Polymer Electrolyte Fuel Cells (AC-PEFCs). The proper operation of an AC-PEFC depends on many factors to ensure the electrochemical process in the stack and the electricity generation from hydrogen and air. However, the stack performance depends on several factors like state of its cells, stack cooling state, stack operating and non-operating time, hydrogen and air supply pressure, hydrogen and airflow rates, and load demand. So, the diagnosis methodologies development is very helpful as part of the AC-PEFCs advanced monitoring and control systems, and of course for predictive maintenance. The developed diagnosis methodology in this paper can be understood like a *diagnosis tree*, in the sense that it implies an structured framework tests over the AC-PEFC: hydrogen line, air/cooling subsystem, electrical circuit and even in the stack itself. The developed diagnosis methodology allows to analysis and improving the performance of an AC-PEFC, and consequently its durability, helping to achieve this challenge, perhaps the main, to bring the fuel cells into the market.

- López, E., Isorna, F., Ridao, M.A., Bordons, C., Elfes, A., Hernández, E.: "Proyecto IUFCV: Incremento de la autonomía en vehículos no tripulados mediante el uso de sistemas híbridos de potencia con pila de combustible". Boletín de Observación Tecnológica en Defensa. N.º 53. Primer trimestre 2017. ISSN: 2444-4839; NIPO: 083-15-183-4.

- Díaz, M. A., Iranzo, A., Rosa, F., Isorna, F., López, E., & Bolivar, J. P. (2015). Effect of carbon dioxide on the contamination of low temperature and high temperature PEM (polymer electrolyte membrane) fuel cells. Influence of temperature, relative humidity and analysis of regeneration processes. In Energy (Vol. 90, pp. 299–309). Elsevier BV. https://doi.org/10.1016/j.energy.2015.06.097

Enlace al texto completo: https://doi.org/10.1016/j.energy.2015.06.097

RESUMEN:

An experimental investigation of the performance and contamination of low and high temperature PEMFCs (polymer electrolyte membrane fuel cells) operating with different concentrations of CO2 at the anode inlet is presented. 50 cm2 MEAs are used in the investigation: Nafion membranes with catalyst Pt loading 0.5 mg cm−2 for both anode and cathode for the low temperature cell, and Celtec P1000 PBI MEAs with catalyst loading 0.75 mg cm−2 in anode and 1 mg cm−2 in cathode for the high temperature cell. An analysis of the relative humidity influence in the contamination process for low temperature polymer electrolyte membrane fuel cells and the temperature effect for both low and high temperature operation range are also investigated in this work. The results show that the performance loss is larger than expected if only a dilution effect were considered, so that a real contamination process occurs in the cell when CO2 is fed to the anode, due to the RWGS (reverse water gas shift) reaction. This contamination effect is analysed and quantified by comparing the polarization curves of the contaminated cell with the ones corresponding to the cell operating with pure hydrogen, following the method described in section 2. The overpotentials for different current densities, CO2 concentrations, relative humidity, and cell temperatures are presented and discussed for both types of fuel cells. Two different regeneration processes (anode feeding with pure H2 and with air) are also presented and discussed. The analysis of the effectiveness of each regeneration strategy also supports that CO produced via the RWGS reaction is adsorbed onto the catalyst.

- López González, E., Isorna Llerena, F., Silva Pérez, M., Rosa Iglesias, F., & Guerra Macho, J. (2015). Energy evaluation of a solar hydrogen storage facility: Comparison with other electrical energy storage technologies. In International Journal of Hydrogen Energy (Vol. 40, Issue 15, pp. 5518–5525). Elsevier BV. https://doi.org/10.1016/j.ijhydene.2015.01.181

Enlace al texto completo: https://doi.org/10.1016/j.ijhydene.2015.01.181

RESUMEN:

Storage of electricity from renewable energy sources is one of the main challenges to be overcome to ensure a proper integration of renewable technologies into the power grid, paving the way for their gradual introduction into future energy scenarios.
The use of hydrogen as an energy carrier is a potential and promising option among the different technologies that can be used to store electrical energy from renewable sources on a large scale. Typical hydrogen facilities used to store renewable electricity are currently based on electrolysis systems connected to the power source, mainly wind or photovoltaic. Hydrogen is stored in accordance with the facility requirements for its use in stationary fuel cells for electric power production.
This article presents the evaluation, in terms of energy-related parameters, of a hydrogen storage system, connected to a renewable energies power plant. The system is located at INTA R&D facilities in Huelva, SW of Spain. These parameters will be representative of the real performance of the system, and can be used as indicators to compare different electrical energy storage systems based on hydrogen and other technologies.

- López González, E., Sáenz Cuesta, J., Isorna Llerena, F., Ridao, M.A., Bordons, C., Hernandez, E., Brett, J.: “Development, integration and evaluation of hybrid fuel cell power systems for unmanned ground vehicles”. En: VII Symposium on Hydrogen, Fuel Cells and Advanced Batteries, HYCELTEC 2019 (Barcelona, del 1 al3 de julio de 2019)- ISSN: 0360-3199.

- Ridao, M.A., Fernández, P., Bordons, C., López, E., Isorna, F.. “Energy Management System for a Microgrid with hydrogen storage and two batteries using Model Predictive Control”. En: VII Symposium on Hydrogen, Fuel Cells and Advanced Batteries, HYCELTEC 2019 (Barcelona, del 1 al 3 de julio de 2019). ISSN: 0360-3199.

- Isorna Llerena, F., Segura Manzano, F., Andújar Márquez, J.M.: “Green hydrogen production methods. A review of solar-driven water splitting techniques”. En: : European Hydrogen Energy Conference 2018 (EHEC 2018) (Málaga, del 14 al 16 de marzo de 2018).

- López, E., Sáenz, J., Vivas, F.J., Isorna, F., Ridao, M.A., Bordons, C., Hernández, E., Efes, A. “Evaluation of fuel cell/battery passive hybrid power systems for unmanned vehicles”. En: European Hydrogen Energy Conference (Málaga, del 14 al 16 de marzo de 2018).

- Isorna Llerena, F., López González, E., Sáenz Cuesta, J.L.: “Diseño y desarrollo de una microrred para la gestión y el almacenamiento de energía eléctrica de origen renovable”. En: VI Congreso Nacional de i+d en Defensa (DESi+d 2018) (Valladolid, del 20 al 22 de noviembre de 2018).

- López, E., Isorna, F., Ridao, M.A., Bordons, C., Elfes, A., Hernández, E.: “Increasing energy efficiency and autonomy in unmanned vehicles using hybrid fuel cell power systems”. En; VI Symposium on Hydrogen, Fuel Cells and Advanced Batteries, HYCELTEC 2017 (Oporto, del 19 al 23 de junio de 2017). ISBN 978-972-752-233-0

- López, E., Isorna, F., Ridao, M.A., Bordons, C., Elfes, A., Hernández, E. “Cómo incrementar la duración de las misiones en vehículos submarinos no tripulados (y otras plataformas robóticas) Proyecto IUFCV”. En: 15ª Feria de las Ciencias (Sevilla, del 11 al 13 de mayo de 2017)

- López González, E., Isorna Llerena, F., Ridao Carlini, M.A., Bordons Alba, C., Elfes, A., Hernández, E.: “Incremento de la eficiencia energética y autonomía en vehículos no tripulados mediante el uso de sistemas de energía híbridos con pila de combustible”. En: IV Congreso Nacional de I+D en Defensa y Seguridad (Murcia, del 6 al 18 de noviembre de 2016). ISBN: 978-84-946021-3-9

- López, E., Rengel, R., Mair, G.W., Isorna, F: “Analysis of high-pressure hydrogen and natural gas cylinders explosions through TNT equivalent method”. En: V Iberian Symposium on Hydrogen, Fuel Cells and Advanced Batteries (Tenerife, del 5 al 8 de julio de 2015). ISBN: 978-84-606-8621-7

- López González, E., Isorna Llerena, F., Argumosa Martínez, M.P., Maellas Benito, J., Ridao Carlini, M.A., Bordons Alba, C.: “Aplicación en vehículos no tripulados de sistemas híbridos de potencia basados en pilas de combustible”. En: II Congreso Nacional de I+D en Defensa y Seguridad (Zaragoza, del 6 al 7 de noviembre de 2014). ISBN: 978-84-940583-2-5

- López González, E., Isorna Llerena, F., Silva Pérez, M., Rosa Iglesias, F.: “Energy evaluation of a solar hydrogen storage facility”. En: European Hydrogen Energy Conference (Sevilla, del 12 al 14 de marzo de 2014)

Capítulo 4. Resultados

4.1. Artículo 1

Effects of Ammonia Impurities on the Hydrogen Flow in High and Low Temperature Polymer Electrolyte Fuel Cells

F. Isorna Llerena, A. de las Heras Jiménez, E. López González, F. Segura Manzano, J. M. Andújar Márquez

Publicado en:

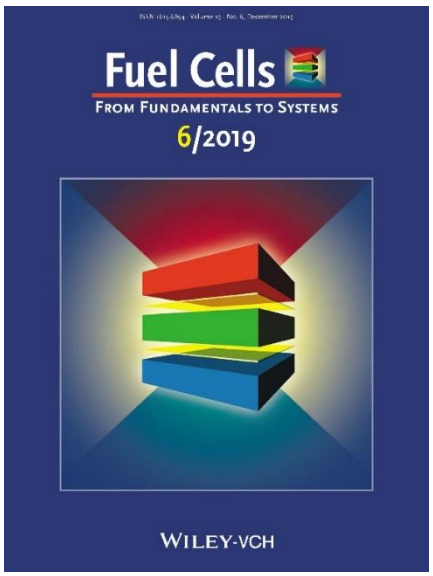

Revista: Fuel Cells
Editorial: WILEY
Editor: Ulrich Stimming
Referencia: FUEL CELLS 19, 2019, No. 6, 651–662
Año: 2019
ISSN: 1615-6846
DOI 10.1002/fuce.201900031

Categoría	Rango revista / Total revista	Cuartil
Electrochemistry	20/27	Q3
Energy & Fuels	81/112	Q3
Factor de impacto JCR (2019)	1,876	
Citas	3	

DOI: 10.1002/fuce.201900031

Fuel Cells

ORIGINAL RESEARCH PAPER

Effects of Ammonia Impurities on the Hydrogen Flow in High and Low Temperature Polymer Electrolyte Fuel Cells

F. Isorna Llerena[1], A. de las Heras Jiménez[2], E. López González[1], F. Segura Manzano[2]*, J. M. Andújar Márquez[2]

[1] Instituto Nacional de Técnica Aeroespacial (INTA), Ctra. S. Juan-Matalascañas, km. 34, 21130, Mazagón (Huelva), Spain
[2] Universidad de Huelva, Departamento de Ingeniería Electrónica, de Sistemas Informáticos y Automática, Carretera Huelva – Palos de la Frontera, 21819, La Rábida – Palos de la Frontera (Huelva), Spain

Received March 14, 2019; accepted November 04, 2019; published online November 25, 2019

Abstract

Fuel cells are a promising technology to use as a source of electricity and heat for buildings, and as an electrical power source for electric motors propelling vehicles. They consume hydrogen as fuel and oxygen to produce electricity, heat and water. Conventional fuels, such as natural gas, methanol, or even gasoline are reformed to produce the hydrogen required by the fuel cells. During the reforming process, impurities are inevitably obtained in the hydrogen flow. One of them is ammonia (NH_3) that can result in serious damage to the fuel cell operation. In this paper, the effects produced by different concentrations of NH_3 present in the hydrogen flow on the membrane electrode assembly (MEA) performance are studied, differentiating between irreversible and recoverable damages. Strictly experimental, the study includes both low and high temperature polymer electrolyte fuel cells (PEFC). The NH_3 poisoning effect is analyzed and quantified by comparing the polarization curves. After the poisoning stage, the cells are subjected to a regeneration process (feeding the cell with neat H_2) with the aim of knowing the membrane's recovery capacity. The experimental results demonstrate that in low temperature (LT)-PEFCs, the cell recovers its performance almost completely with a new exposure to neat H_2, in spite of the damage previously caused by the presence of traces of NH_3 in the anode feed stream. In contrast, in high temperature (HT)-PEFCs, the cell suffers irreversible damage, even with short time exposure to NH_3. The paper concludes with discussing the possible chemical interactions by which NH_3 affects the cell performance.

Keywords: Ammonia Poisoning, Diagnostic, Experimental Test, HT-PEFC, LT-PEFC

1 Introduction

Polymer electrolyte fuel cells (PEFC) are a promising technology of producing electricity from hydrogen, for both portable and stationary applications [1, 2]. The integration of a PEFC in a power generation system requires an thorough design in the balance of plant [3, 4] and a detailed power conditioning stage [5] to guarantee the best performance of the fuel cell. However, even if the balance of plant is optimized, the quality of the fuel supply (hydrogen purity) affects severely the fuel cell's performance due to the presence of contaminants [6]. Through there is some example where ammonia is used as fuel in fuel cells (fuel cells type SOFC) [7], hydrogen continues to be the most widespread fuel and impurities in the flow feed are a barrier to the hydrogen oxidation reaction (ORR) [8–10].

Recently, high temperature polymer electrolyte fuel cells (HT-PEFC) are drawing attention owing to [11–13]: the rates of electrochemical kinetics are enhanced; the water management and cooling subsystem are simplified; the useful waste heat

[*] *Corresponding author, francisca.segura@diesia.uhu.es*

This is an open access article under the terms of the Creative Commons Attribution License, which permits use, distribution and reproduction in any medium, provided the original work is properly cited.

can be recovered; and, particularly, lower quality reformed hydrogen may be used as fuel. It is broadly known that HT-PEFC membranes tolerate higher CO concentrations than low temperature polymer electrolyte fuel cells (LT-PEFC). Therefore, they are more suitable for using with reforming gas; however, there is hardly any information about the influence of other pollutants, such as NH_3, with which the response may not be as suitable as previously assumed [14, 15].

On the other hand, ammonia can be considered not as a contaminant but as a fuel carrier [16], and even there are studies focused on the clean ammonia production [17] in the last stage of the hydrogen supply chain there is needed both ammonia separation and hydrogen purification process [18].

At present, several alternatives can be selected to produce the hydrogen according the raw material used in the conversion [19], see Figure 1. Globally, 48% of the hydrogen produced is derived from the reforming of natural gas. Other reforming processes followed by conventional fossil fuels such as oil (contributing 30% to global hydrogen production), coal (with 16%), and the last place are the hydrogen production from water splitting, mainly by electrolysis (with 6%).

Additionally, the hydrogen used to feed fuel cells comes from commercial containers, the main option, or it is produced *in situ*. In the latter, production *in situ*, electrolysis [20], natural gas reformatted (methane) and methanol obtained from biomass are the most common methods for producing hydrogen.

In the reforming process to produce hydrogen, it is unavoidable that impurities appear [9, 18]. The result is a hydrogen-rich gas called "reformate gas", which typically consists of 40–70% H_2, 15–25% CO_2, 1–2% CO, small amounts of inert gases (water vapour and nitrogen) and sulfur impurities [22]. However, ammonia can be also formed during the reforming process at levels up to 375 ppm in "neat" H_2, or even more if there are transients in the reformers [14]. Traces of NH_3 in the anode feed stream cause a decrease in cell performance. The severity of the effects depends on NH_3 concentration and time of exposure of the anode to the contaminant. High concentrations and a long exposure time can result in irreversible damage [13, 18]. Indeed, impurity substances can affect the water and/or gas transport behavior of the gas diffusion layer, resulting in mass transport decrease and fuel cell performance loss [24]. In this sense, impurities such as ammonia can react with hydrogen protons to form ammonium protons according to reaction Eq. (1):

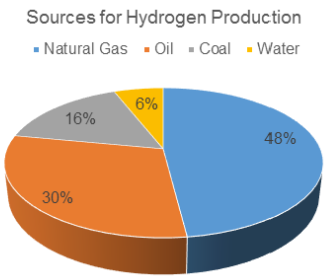

Fig. 1 Hydrogen production classified by raw material.

$$NH_3 + H^+ \rightarrow NH_4^+ \quad (1)$$

The result is a decrease in gas transport and, therefore, a decrease in fuel cell performance.

In scientific papers, the effects of potential contaminants such as CO, CO_2 and H_2S have been well-studied [12, 15, 19–23]; however, only a few have been found that focus on the effect of NH_3 particles on LT-PEFC performance [14, 24–26]. The lack of research is even greater regarding the NH_3 effects on HT-PEFC [18, 27]. In terms of LT-PEFC, Soto et al. analyze in [14] the effects of high NH_3 concentrations on the MEA (membrane electrode assembly) performance (from 200 ppm to 1,000 ppm). In contrast, Zhang et al. [30] studied the effects of ammonia at fixed concentration (25 ppm) with long term exposure (> 6h), varying the relative humidity, but without the cell functioning, or operating. Additionally, very low concentrations (1–2 ppm) effects are studied in [31]; however, in this case, the NH_3 input is in the cathode side. A detailed study on the conductivity of Nafion® membranes *via* electrochemical impedance spectroscopy was explored by Hongsirikarn et al. in [32]; though, the authors did not analyze the performance of the entire cell. Regarding HT-PEFC, Sun et al. presented in [33] the polarization curves and AC impedances of the cell after NH_3 poisoning. Moreover, the catalyst layer was scanned with the electron microscope.

In this paper, the effects of NH_3 particles in the hydrogen flow inlet (anode side) of both LT-PEFC and HT-PEFC are analyzed to determine the severity of potential damages, reversible or not, in the fuel cell's performance. To highlight the novelty of the work, the study includes the NH_3 concentration ranges that previous research do not cover: from 25 ppm (for LT-PEFC) and 50 ppm (for HT-PEFC) to 250 ppm (for LT-PEFC) and 500 ppm (for HT-PEFC). These concentrations were selected according to the typical levels of impurities in reformed hydrogen, which can be up to 375 ppm [16, 28]. The reason why NH_3 concentrations values over LT-PEFC are half of those of HT-PEFC is explained in Section 2.3.

The need to research the effect of hydrogen pollutants in the performance of fuel cells is one of the requirements set by the European companies of the sector (grouped in the FCH JU, Fuel Cells and Hydrogen Joint Undertaking). The reason for this is to develop products that are reliable and competitive in economic terms to facilitate their introduction into the market and widespread implementation. Besides, the need for purification entails a high additional cost to the use of fuel cells (see Topic SP-JTI-FCH.2013.3.1) [35].

The applicability of the research work developed in this paper goes in line with two key aspects above commented: (i) the main hydrogen source is ammonia and (ii) HT-PEFC face to LT-PEFC are catching especial attention because they are more suitable for using with reforming gas. Then, regarding the first issue, almost the half of the global hydrogen production today comes from natural gas, NH_3, (Figure 1) and according to the second issue, one of the emerging technologies (high temperature) related with the most extended fuel cells (PEFC) allow to be fed with hydrogen produced *in situ*

 © 2019 The Authors. Published by WILEY-VCH Verlag GmbH & Co. KGaA, Weinheim

from natural gas reforming. Then, there will be useful to have proven results that show the importance of the presence of NH_3 pollutant particles in the hydrogen supply and it influence of the fuel cell performance.

The study carried out is presented as follows: Section 2 explains materials and methods; results and discussion are presented in Section 3. Finally, Section 4 gathers the conclusions and future studies are pointed out.

2 Experimental

Attending to poisoning mechanisms and mitigation strategies studied in scientific literature [36] in relation to the impurities effects on PEFC performance, in this section there will be explained the procedure and used material to carried out the experimental test. Then, firstly there will be explained the test bench used, next a detail of the high and low temperature membrane used during experimentation and the last parts of the section describe the gas supply facility and the procedure to make the experiments.

2.1 Test Bench and Fuel Cell

The experiments were carried out with a CT-1000 test station from FuelCon™ (Figure 2) located in the fuel cell laboratory belonging to the Spanish National Institute for Aerospace Technology (INTA, *Instituto Nacional de Técnica Aeroespacial*). The test station was able to operate cells up to 600 W and a maximum current of 100 A.

The tests were conducted with both galvanostatic and potentiostatic modes, and with flow-through operation mode; although, it was also possible to carry them out with dead-end operation mode. The operating parameters which were controlled were: (i) fuel flow (0.2–10 NL min^{-1} in the anode); (ii) oxidant flow (0.4–20 NL min^{-1} in the cathode); (iii) temperature of reactants; (iv) relative moisture of the reactants; (v) anode pressure; (vi) cathode pressure; and (vii) cell temperature. All bench piping and cell may be purged with N_2.

To characterize the influence of ammonia in the PEFC from high and low temperature, two experiments for PEFC whose stacks were made up by a single cell were designed. This was done so, knowing that the expected results from multi-cell stacks were to be similar.

The PEFC used for the experiments (Figure 3) has been a 50 cm^2 active area cell from Teledyne™ with three-channel parallel serpentine flow fields (channels of 0.76 mm wide and deep). The graphite bipolar plate's layout is cross-flow with horizontal channels in both anode and cathode (Figure 4).

For the high temperature tests, two integrated heaters were used for temperature control. These consisted of cartridge hea-

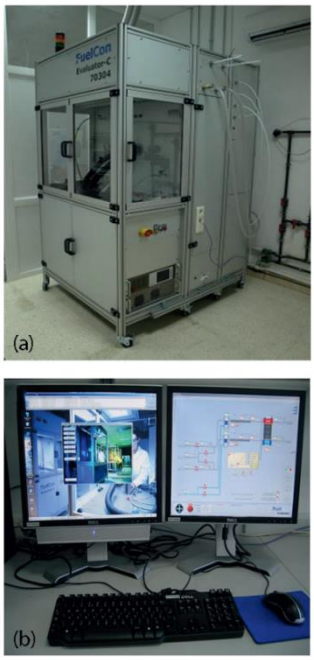

Fig. 2 Images of the test bench used during the experiments.

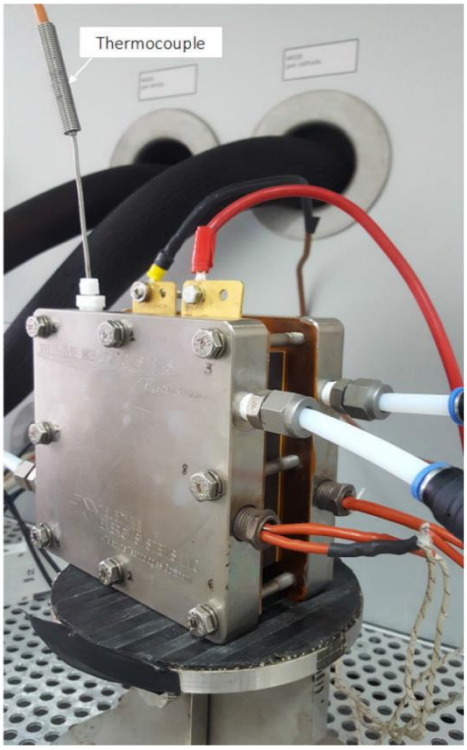

Fig. 3 Image of the single polymer electrolyte fuel cell (PEFC) used during the experiments.

 © 2019 The Authors. Published by WILEY-VCH Verlag GmbH & Co. KGaA, Weinheim

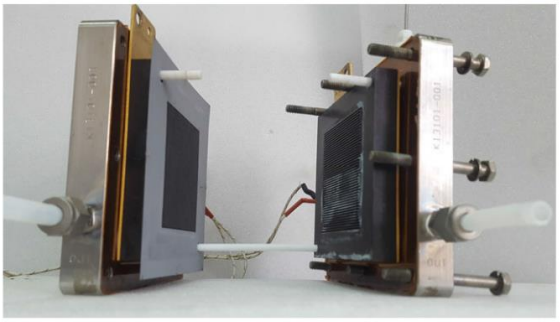

Fig. 4 Images of graphite bipolar plates and membrane electrode assembly (MEA).

ters located inside the final plates. Apart from this, the cell was insulated to reduce temperature gradients and a fan was necessary to remove the excess heat produced by the cell.

For the low temperature experiments, the test-bench FuelCon is equipped with a heating/cooling system controlled by a proportional-integral-derivative (PID) controller that is embedded into the test-bench and used for temperature control. This external heater consisted of a flexible resistance surrounding the cell. Apart from this, the cell was insulated in the same way as in the high temperature tests.

For both experimental tests (high and low temperature), a thermocouple (Rössel Messtechnik™) located inside of one of the bipolar plates was used to measure the cell temperature.

2.2 Membranes

Membrane electrode assembly (MEA) from Danish Power Systems™ (Figure 5a), made from polybenzimidazole (PBI), were used for high temperature tests. The MEA had five layers and catalyst loading of 1.5 mg cm^{-2} in both anode and cathode side. Membrane thickness was 40 µm with Kapton edge reinforcement. The electrode area was 72×72 mm^2 and the active cell area 68×68 mm^2.

In contrast, a MEA from Paxitech™ (Figure 5b), made with Nafion™, were used in the low temperature experiments. The MEA had seven layers and catalyst loading of 0.5 mg cm^{-2} in both anode and cathode side. Membrane thickness was 50 µm. The active cell area was 68×68 mm^2. The MEA consist of a polymer electrolyte membrane (perfluorinated cation exchange membrane). Both sides were coated with a catalyst ink and combined with a GDL (gas diffusion layer). Apart from this, a 15 µm sub-gasket material and silicon gaskets around the active layers from GDL edge to outer edge of the polymer electrolyte were included. GDLs were pressed onto the catalyst active area and they were made of a carbonized non-woven material with a polytetrafluoroethylene (Teflon, PTFE) surface treatment. The sub-gasket material protected the active layer/GDL contact area and the polymer electrolyte membrane border.

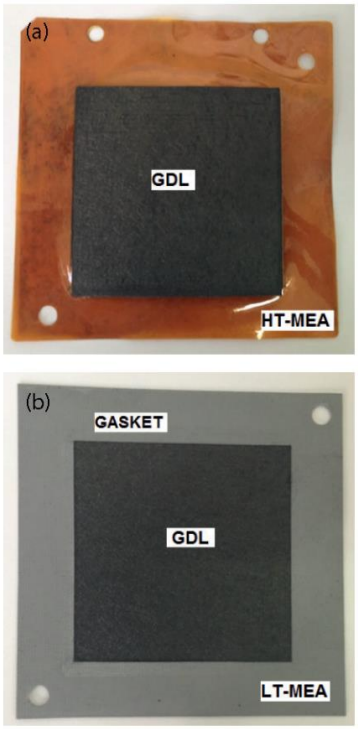

Fig. 5 Images of the high (a) and low (b) temperature membrane electrode assemblies.

2.3 Gases

To carry out the tests, ultra-high pure (99.999%) hydrogen and nitrogen pre-mixed at different concentrations mixtures, were provided by Praxair™. Bellows et al. [26] show that reformate mixtures contain around 40% of H_2. This means that ammonia can be formed during the processes at levels up to 150 ppm. Therefore, this may correlate up to 375 ppm in neat H_2 or even higher concentrations because of the transients in the reformers.

For high temperature experiments, the impurity (NH_3) concentrations for the anode were obtained from pre-mixed 50, 150, 300, and 500 ppm NH_3/H_2 concentration cylinders. These concentrations have been selected according to typical levels of impurities in reformed hydrogen up to 375 ppm [13].

Conversely, for low temperature tests, the NH_3/H_2 stream had to be humidified because it was necessary to avoid membrane dehydration. However, it was not suitable to humidify directly the NH_3/H_2 stream because of the ammonia absorption in the de-ionized (DI) water, and there was a risk that the ammonia would stay in the humidifier instead of the NH_3/H_2 stream. To resolve this, the neat hydrogen stream was humidified to keep the membrane hydration and the NH_3/H_2 stream was not humidified to keep the ammonia in the NH_3/H_2 stream; and, after that, these two streams were mixed.

 © 2019 The Authors. Published by WILEY-VCH Verlag GmbH & Co. KGaA, Weinheim

Therefore, the impurities of NH_3 concentrations for the anode were obtained by diluting the NH_3/H_2 stream with the humidified hydrogen stream. The flow rate of NH_3/H_2 concentration was controlled by a mass flow controller (MFC, Bronkhorst™) for the inlet impurity (25, 75, 150, and 250 ppm). With this method (Figure 6), authors ensured that only neat hydrogen flows through the humidifiers. Hence, potential contamination of the humidifier by absorption of ammonia into the DI water was suppressed. This is why level of impurities were just 50% of those used in high temperature experimental tests. The humidifier temperature was controlled for the desired final (NH_3/H_2) concentration moisture.

2.4 Experimental Test Description

For each test, the amount of ammonia in the fuel and operating parameters values are shown in Table 1 (high temperature PEFC) and Table 2 (low temperature PEFC).

Polarization curves for different conditions were obtained following the FCTESTnet procedure for single cells and the technical specification IEC/TS 62282-7-1 of the IEC (International Electrochemical Commission) [30,31].

All of the experiments included an activation stage which was used to reach the operating conditions and stabilization for the measurement phase where the change in the single cell voltage, generated by variation of the current density, was quantified.

For high temperature experiments, the manufacturer recommends to carry out a conditioning stage by fixing the current density at 200 mA cm^{-2} for at least 50 h. The system keeps working to ensure stability in the measured voltage.

Following Table 1, a stoichiometric factor of 1.5 was fixed for the anode (λ_a) and 2.5 for the cathode (λ_c). The pressure and temperature were fixed in 1 bar and 160 °C, respectively. The only parameter which varied was the fuel composition.

For low temperature experiments, the conditioning stage consists of increasing the current density up to 200 mA cm^{-2}. The system kept working up to 40 °C. Following, the cell current was decreased up to OCV (open circuit voltage) and the humidification was then activated. Afterwards, the current density was increased up to 200 mA cm^{-2} again and the system kept working up to a temperature of 60 °C for 5 h [39]; the humidification was 100% in both anode and cathode. The system kept working to ensure stability in the measured voltage.

Table 1 Conditions for HT experiments (oxidant is dry air from compressor).

High Temperature Tests								
Test	Conditions							
	P / bar	T / °C	RH_a / %	RH_c / %	λ_a	λ_c	Fuel	Oxidant
1	1	160	–	–	1.5	2.5	Neat H_2 + 50 ppm	Air
2	1	160	–	–	1.5	2.5	Neat H_2 + 150 ppm	Air
3	1	160	–	–	1.5	2.5	Neat H_2 + 300 ppm	Air
4	1	160	–	–	1.5	2.5	Neat H_2 + 500 ppm	Air

Table 2 Conditions for LT experiments.

Low Temperature Tests								
Test	Conditions							
	P / bar	T / °C	RH_a / %	RH_c / %	λ_a	λ_c	Fuel	Oxidant
5	1	60	50	100	1.5	3.5	Neat H_2 + 25 ppm	Air
6	1	60	50	100	1.5	3.5	Neat H_2 + 75 ppm	Air
7	1	60	50	100	1.5	3.5	Neat H_2 + 150 ppm	Air
8	1	60	50	100	1.5	3.5	Neat H_2 + 250 ppm	Air

As for Table 2 conditions, a stoichiometric factor of 1.5 was fixed for the anode and 3.5 for the cathode. The pressure and temperature were fixed in 1 bar and 60 °C, respectively. The only parameter which varied was the fuel composition.

It is important to point out that each experiment has been repeated at least three times to ensure the reproducibility of the results.

Figures 7 and 8 show the stage sequences carried out for high and low temperature tests. In both cases, the first stage was to characterize the PEFC using neat H_2 as fuel. This experiment consisted of an activation stage which was used to reach the operating conditions. This activation stage was carried out with neat H_2 as fuel. After the activation stage, the following phase consisted of obtaining the polarization curves for a period of 2.5 h to know the initial behavior of the membrane without poisoning. When the activation and characterization were finished, a poisoning phase for 2 h using a H_2/NH_3 concentration was staged. After that, the polarization curves were obtained to compare the results with the initial ones. The final step was an attempt to regenerate the membrane. For this purpose, the presence of NH_3 was eliminated by using neat H_2 for 2 h, and carrying out a new characterization stage with neat H_2 (following the same testing procedure as used to develop the characterization of the PEFC [40]).

The described procedure was carried out to compare the results of the different characterization

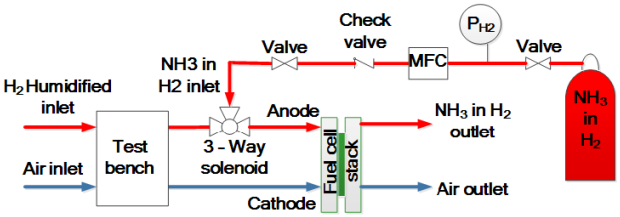

Fig. 6 Scheme of the ammonia mixing system for tests in LT-PEFC.

 © 2019 The Authors. Published by WILEY-VCH Verlag GmbH & Co. KGaA, Weinheim

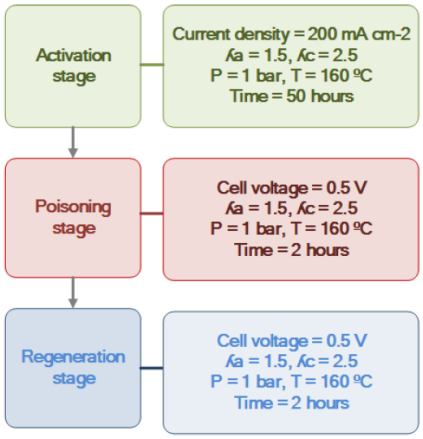

Fig. 7 Diagram of the different stages carried out for the high temperature tests.

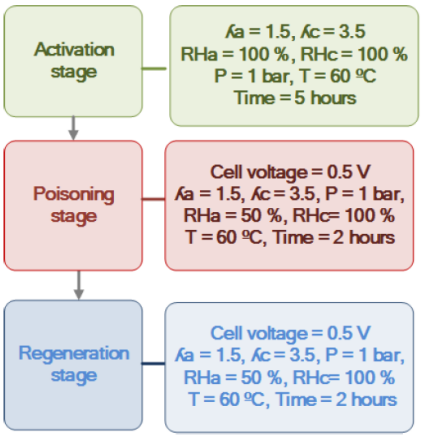

Fig. 8 Diagram of the different stages carried out for the low temperature experiments.

stages to study the poisoning and the effectiveness of the regeneration under the same conditions. Additionally, one new identical MEA for each test is used because after poisoning, the MEA is completely damaged.

The methodology followed to study the effect of the presence of NH_3 in the fuel flow consisted of comparing the polarization curves obtained with neat H_2 and those acquired with the different H_2/NH_3 concentrations. The experiments to find the polarization curves were always carried out according to the properly defined procedure in [40] with fixed operating times for all the stages of the experiments.

3 Results and Discussion

In the following subsections, the cell performance working under different H_2/NH_3 concentrations are shown. The influence of the different H_2/NH_3 concentrations were studied for polymer electrolyte membranes under 2 h of high and low temperature exposure. Once the contamination process was finished, neat H_2 was fed as fuel to investigate the recovery of the cell performance in an attempt to achieve the same performance that was obtained before introducing NH_3. Thus, the attempt to regenerate the polymer electrolyte membrane was carried out with neat H_2 for 2 h.

3.1 HT-PEFC Experimental Tests

Firstly, the poisoning produced due to the presence of NH_3 in the anode fuel has been analyzed. To do this, the measured polarization curves at 160 °C (baselines, neat H_2 curves) have been used. The poisoning was acquired using different H_2/NH_3 concentrations (50, 150, 300 and 500 ppm) to compare them with the polarization curves obtained with neat H_2 as fuel.

Figures 9–12 show the differences between the polarization curves obtained using neat H_2, the different H_2/NH_3 concen-

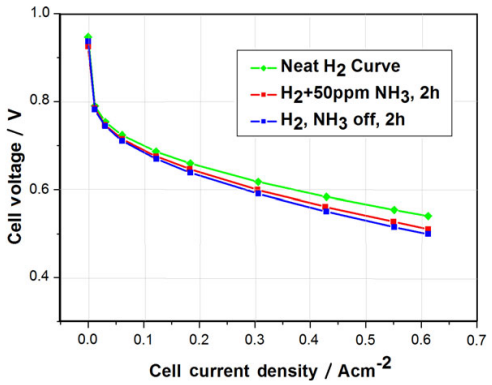

Fig. 9 HT-PEFC Test 1: Comparison between baseline (neat H_2) and polarization curves after 50 ppm-concentration exposure.

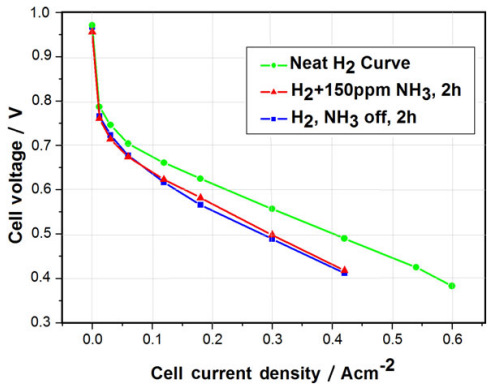

Fig. 10 HT-PEFC Test 2: Comparison between baseline (neat H_2) and polarization curves after 150 ppm-concentration exposure.

 © 2019 The Authors. Published by WILEY-VCH Verlag GmbH & Co. KGaA, Weinheim

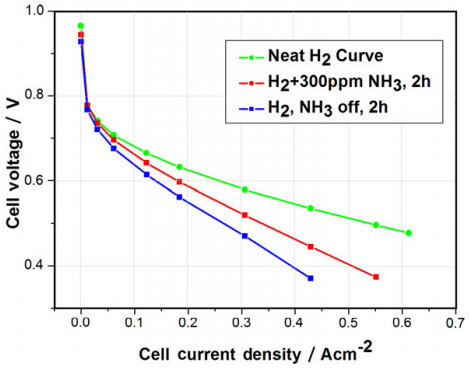

Fig. 11 HT-PEFC Test 3: Comparison between baseline (neat H_2) and polarization curves after 300 ppm-concentration exposure.

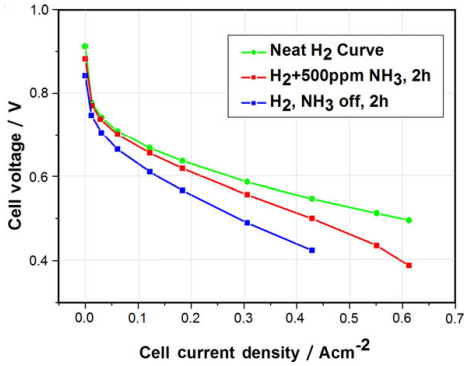

Fig. 12 HT-PEFC Test 4: Comparison between baseline (neat H_2) and polarization curves after 500 ppm-concentration exposure.

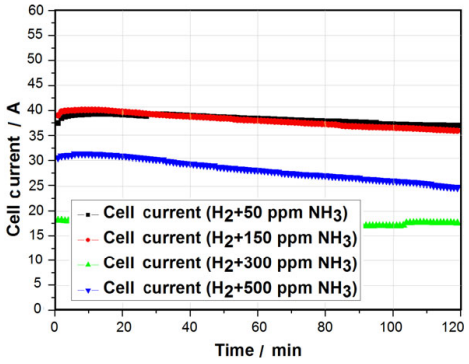

Fig. 13 HT-PEFC experimental tests: Nominal cell current comparative (at 0.5 V) after poisoning stage.

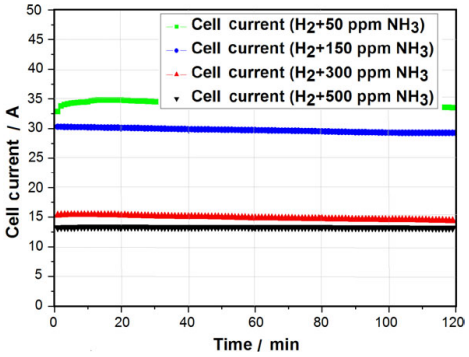

Fig. 14 HT-PEFC experimental tests: Nominal cell current comparative (at 0.5 V) after regeneration stage.

trations as fuel and thereafter the regeneration stage with every H_2/NH_3 concentration. It is notable that for each test a baseline curve was found. This is due to the use of one new MEA for each test knowing that after poisoning, the MEA is completely damaged. Each MEA shows a slightly different behavior because it is handmade, and is not industrial. Therefore, each MEA has its own baseline so each poisoning can only be compared to its own MEA baseline.

Additionally, Figure 13 shows the nominal cell current (at 0.5 V) provided by the cell after poisoning stage with the different H_2/NH_3 concentrations, and Figure 14 shows the nominal cell current (at 0,5 V) after the regeneration stage with neat H_2.

Table 3, based on Figures 13 and 14, shows how for the different H_2/NH_3 concentrations (50, 150, 300, and 500 ppm), after the 2 h of poisoning stage, the performance of the polymer electrolyte membrane decreases 1.29%, 7.91%, 17.18%, and 19.34%, respectively. These values are acquired with respect to the first and the last value obtained from the cell nominal current in the poisoning stage (Figure 13). In contrast, after the regeneration stage, the cell performance continues to decrease even more, 2.06%, 3.38%, 6.06%, and 6.02%, respectively, according to the first value and the last value obtained from the cell nominal current in the 2 hours regeneration stage (Figure 14). That is, in high temperature experiments, the cell does not regenerate; but rather H_2 regeneration after contamination produces an even worse performance as if the contamination further continued.

Table 3 HT-PEFC experimental tests: Performance losses after poisoning and regeneration stage.

Concentration / ppm NH_3	HT-PEFC Tests: Polymer Electrolite Membrane Performance Degradation	
	Long Term Exposure / %	Regeneration / %
Test 1: 50	–1.29	–2.06
Test 2: 150	–7.91	–3.38
Test 3: 300	–17.18	–6.06
Test 4: 500	–19.34	–6.02

 © 2019 The Authors. Published by WILEY-VCH Verlag GmbH & Co. KGaA, Weinheim

3.2 LT-PEFC Experimental Tests

Like the HT-PEFC experiments, the authors analyzed the poisoning produced due to the presence of NH_3 in the anode fuel in a LT-PEFC. In order to do this, the measurement of the polarization curves at 60 °C (baselines, neat H_2 curves) were used. After that, the poisoning was determined using different H_2/NH_3 concentrations (25 ppm, 75 ppm, 150 ppm, and 250 ppm) and analysing the difference obtained with the experiment using neat H_2 as fuel.

Figures 15–18 show the differences between the polarization curves obtained using neat H_2, different H_2/NH_3 concentrations as fuel and after the regeneration stage with each H_2/NH_3 concentration. Figure 19 shows the nominal cell current (at 0.5 V) available by the cell after exposure to NH_3 contaminants, and Figure 20 shows the nominal cell current (at 0.5 V) after the regeneration stage with neat H_2.

Table 4 shows how for the different H_2/NH_3 concentrations (25, 75, 150, and 250 ppm), after 2 h of poisoning stage, the performance of the PE cell decreases 27.01%, 34.40%, 46.13%, and 71.18%, respectively. As it has been commented before, these values are obtained with respect to the first and the last value acquired from the cell nominal current in the poisoning stage (Figure 19). Conversely, after the regeneration stage, the performance of the polymer electrolyte membrane improves 2.84%, 10.22%, 21.30%, and 64.09%, respectively, according to the first value and the last value obtained from the cell nominal current in the 2 hours-regeneration stage (Figure 20).

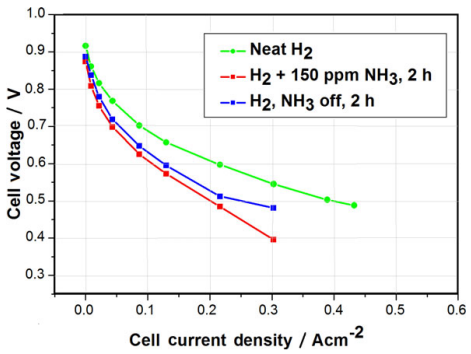

Fig. 17 LT-PEFC Test 7: Comparison between baseline (neat H_2) and polarization curves after 150 ppm-concentration exposure.

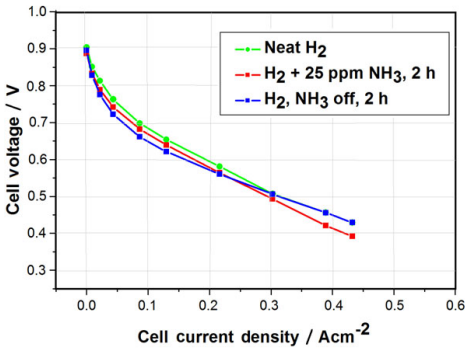

Fig. 15 LT-PEFC Test 5: Comparison between baseline (neat H_2) and polarization curves after 25 ppm-concentration exposure.

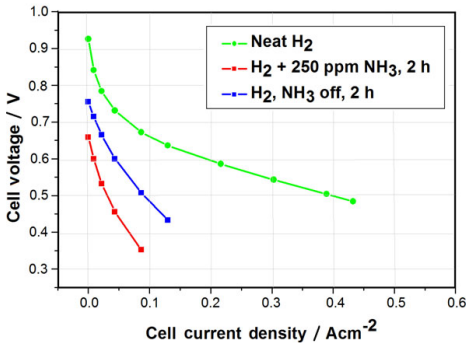

Fig. 18 LT-PEFC Test 8 test: Comparison between baseline (neat H_2) and polarization curves after 250 ppm-concentration exposure.

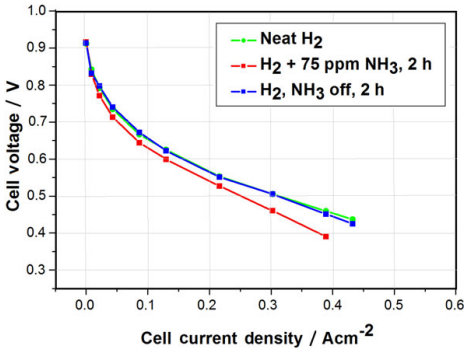

Fig. 16 LT-PEFC Test 6: Comparison between baseline (neat H_2) and polarization curves after 75 ppm-concentration exposure.

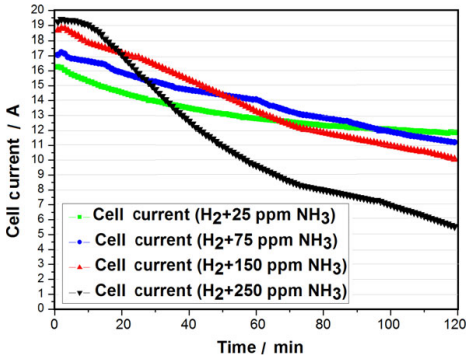

Fig. 19 LT-PEFC experimental test: Nominal cell current comparative (at 0.5 V) after poisoning stage.

 © 2019 The Authors. Published by WILEY-VCH Verlag GmbH & Co. KGaA, Weinheim

Table 4 LT-PEFC experimental test: Performance losses after poisoning and regeneration stage.

Concentration / ppm NH_3	LT-PEFC Experiments: Polymer Electrolyte Membrane Performance Degradation	
	Long Term Exposure / %	Regeneration / %
Test 5: 25	–27.01	+2.84
Test 6: 75	–34.40	+10.22
Test 7: 150	–46.13	+21.30
Test 8: 250	–71.18	+64.09

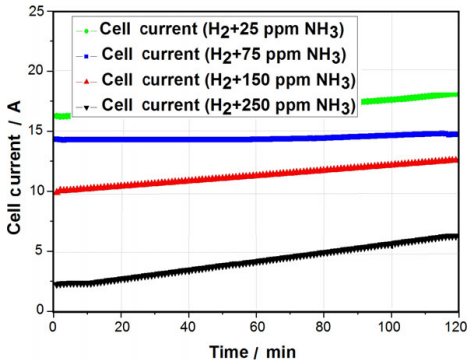

Fig. 20 LT-PEFC experimental test: Nominal cell current comparative (at 0.5 V) after regeneration stage.

However, the baseline is not achieved in none of the experiments after the regeneration stage.

Once the experimental results have been presented, we are going to comment some issues related with them. Regarding HT-PEFC, it is necessary to point out that even for low concentrations of NH_3 in the fuel, noticeable losses are observed on the polarization curves. The results obtained (Figures 9–12) show that an increase of NH_3 concentrations results in higher losses. When the poisoning stage is completed, neat H_2 is fed as fuel so as to analyze the cell performance recovery, trying to achieve the baseline acquired before the poisoning stage. If only a dilution effect exists, once the H_2/NH_3 concentration is changed by neat H_2, the cell performance would be completely recovered. Nevertheless, this is not the case, and the polarization curve obtained after the regeneration stage shows worse cell performance than after the exposure to NH_3 contaminants. Indeed, even after operating the cell for hours using neat H_2 for the regeneration stage, the baseline is not achieved in none of the experiments. Because of this, such behavior suggests the presence of a compound adsorbed on the platinum surface which cannot be completely eliminated by just using neat H_2.

The results shown in Figures 9 and 10 point out that after the regeneration stage for low NH_3 concentrations, the performance is similar to the polarization curve obtained after the poisoning stage. Additionally, for high NH_3 concentrations, the cell performance results to be even worse than the polarization curve obtained after the poisoning stage, Figures 11 and 12. Thus, we can conclude that for HT-PEFC as the poisoning increases, the cell's performance after the regeneration stage worsens even more than the original.

In relation to the cell nominal current, from Figure 13 we can observe how the membrane resistance increases during the 2 hours-poisoning stage and this is due to the poisoning of the membrane because of the ammonia. Moreover, Figure 14 shows that the membrane resistance keeps stable during the 2 hours-regeneration stage. Additionally, we can foretell that even after 2 h of regeneration stage, there is no recovery of the membrane.

Concluding with HT-PEFC, Table 3 shows that during the poisoning stage, the cell performance decreases. The decrease depends on the H_2/NH_3 concentration of every experimental test, namely the greater the poisoning, the larger the decrease. Thus, we can assume that after 2 hours-poisoning stage, the polymer electrolyte membrane performance decreases 1.29%, 7.91%, 17.18%, and 19.37%, respectively. After 2 hours-regeneration stage, the performance continues to decrease 2.06%, 3.38%, 6.06%, and 6.02%, respectively (between 300 and 500 ppm it stabilizes). Therefore, the baseline is not achieved in none of the experimental tests after the regeneration stage.

The behavior for the low current densities can be justified by the activation losses and, because of that, the membrane conductivity does not have much influence. Otherwise, when the current density increases, the system is affected by ohmic losses and it is influenced by the state and the conductivity of the membrane. This can be explained due to the fact that the MEA used in the experiments was built from an acid doped polybenzimidazole (PBI) membrane containing phosphoric acid in HT-PEFC: the most likely mechanism by which performance drops is the formation of some type of ammonium phosphate which decreases the protonic activity (Figure 21a). The negative effect gradually starts at the anode catalyst layer, the first region exposed, and continues into the membrane as the ammonia diffuses up to reach the cathode [13]. Figure 21b shows the result obtained from microscopy, where effectively the formation of ammonium phosphate in the membrane-cathode surface can be observed.

Then again, from LT-PEFC tests, polarization losses are also observed, even for low concentrations of NH_3 in the fuel, which agrees with the previous work developed to study the NH_3 poisoning in LT-PEFC. Experimental results (Figures 15–18) show that, as in the case of HT-PEFC, higher performance losses are due to an increase in NH_3 concentrations. When the poisoning stage is finished, neat H_2 is fed as fuel in the regeneration stage to analyze the cell's performance recovery. The purpose of doing this is the same for that of the HT-PEFC tests. However, for LT-PEFC, the polarization curve obtained after the regeneration stage should be nearly to that of the neat H_2 polarization curve. The baseline is almost achieved for the tests of 25 and 75 ppm of NH_3. However, the baseline is not achieved for higher NH_3 concentrations (150 and 250 ppm of NH_3) even after operating the cell for 2 h of regeneration stage using neat H_2.

 © 2019 The Authors. Published by WILEY-VCH Verlag GmbH & Co. KGaA, Weinheim

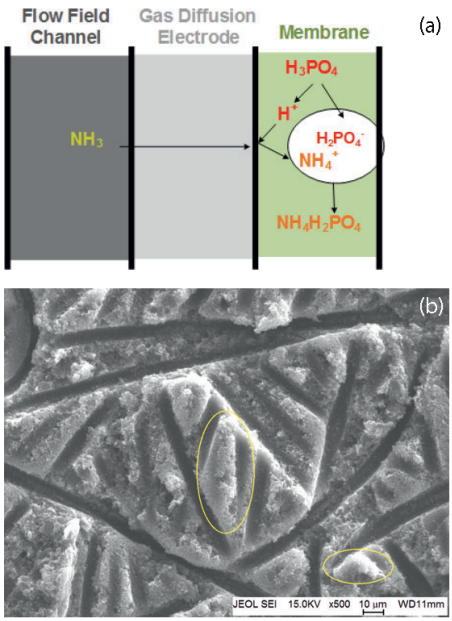

Fig. 21 a) HT-PEFC: Formation of some type of ammonium phosphate due to NH_3 poisoning; b) HT-PEFC: Microscopy image of the membrane with the formation of ammonium phosphate (highlighted in yellow) in the membrane-cathode surface (scale bar referring to 10 µm).

Additionally, Figure 19 shows that the membrane resistance increases during the 2 hours-poisoning stage and this is due to the poisoning of the membrane by the ammonia. In contrast, Figure 20 shows that the membrane resistance decreases during 2 hours-regeneration stage. This is due to the recovery of the membrane by way of the neat hydrogen.

Regarding the recovery stage, as shown in Table 4 (made from Figures 19 and 20), for the different H_2/NH_3 concentrations, after 2 hours-poisoning stage, the performance of the polymer electrolyte membrane decreases 27.01%, 34.40%, 46.13%, and 71.18%, respectively. After the 2 hours-regeneration stage, the recovery of the performance is 2.84%, 10.22%, 21.30%, and 64.09%, respectively. This is a huge difference from the HT-PEFC test; because in that case, after the regeneration stage, the cell performance is not recovered but worsens.

Then, accordingly, data point to the presence of a compound adsorbed on the platinum surface which can be partially eliminated by just using neat H_2.

There are several possible mechanisms by which NH_3 affects the PE fuel cell performance in LT-PEFC. The membrane conductivity decreases by the ammonia reacting with the protons of the protonic membrane forming NH_4^+ (Figure 22).

The same effect could be possible within the catalyst layer, which contains recast ionomer in protonic form (Figure 23). NH_3 crosses over to the cathode inhibiting the O_2 reduction reaction (ORR) [13], [23]. Similarly, the anode catalyst could inhibit hydrogen oxidation because of NH_3 adsorption onto Pt.

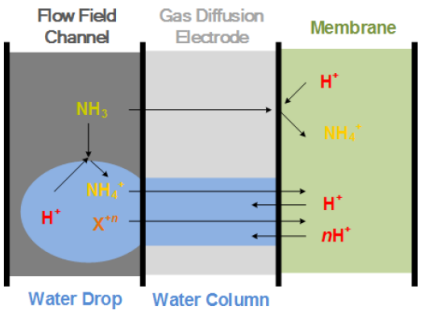

Fig. 22 LT-PEFC: Formation of ammonium ions due to reaction of ammonia with the hydrogen protons.

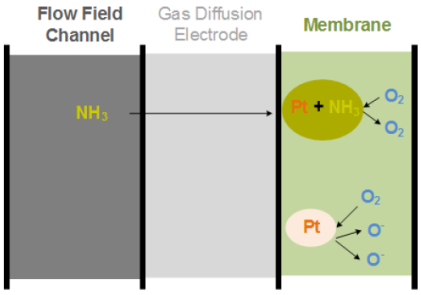

Fig. 23 LT-PEFC: Inhibition of oxygen reduction because of NH_3 adsorption onto Pt.

Finally, it is worth noticing that Borup et al. [23] and Uribe et al. [13] showed how cyclic voltammetry (CV) of the anode, after exposure, does not indicate any noticeable NH_3 adsorption onto the catalyst layer; however, the degradation mechanism seems to be a protonic conductivity loss. After the study carried out in this work, it can be assumed that NH_3 reacts with ionomeric H^+ producing NH^{4+}, which results in an increased of the protonic activity.

4 Conclusions

This paper contributes to the few studies that cover the effects of NH_3 on high and low temperature PE fuel cells showing the mechanisms by which the membrane performance decreases after a poisoning stage.

The need to have research works related with this subject can be justified because on the one side, the main hydrogen source today in the world is ammonia and on another side, there is arising a fuel cell technology, HT-PEFC, which can operate with lower quality hydrogen produced by reforming process. But, it is unavoidable the presence of impurities in the hydrogen gas produced and although the influence in the fuel cell performance of some pollutant particles, such as CO, CO_2 and H_2S have been widely studied, traces of NH_3 have been scarily addressed in scientific literature.

 © 2019 The Authors. Published by WILEY-VCH Verlag GmbH & Co. KGaA, Weinheim

Additionally, the need to research the effect of hydrogen pollutants in the performance of fuel cells is one of the requirements set by the FCH JU.

Based on above, the results presented in this paper contribute to meet with these global objectives.

Regarding the tests carried out (low and high temperature), the results clearly show that the presence of traces of NH_3 in the anode feed stream poisons the membrane electrode assembly resulting in downstream cell performance. The poisoning depends on the amount of NH_3 in the anode feed stream.

As for the experiments with LT-PEFC, the performance shows a recovering during the 2 hours-regeneration stage. The recovery mechanism possibly involves proton generation by anodic hydrogen oxidation current. Conversely, for tests with HT-PEFC, the performance decreases even during the 2 hours-regeneration stage.

On the basis of the results obtained, it was confirmed that longer exposure time in HT-PEFC, decreases the cell performance to unusable levels and the cell never recovers to original conditions. In contrast, with LT-PEFC, despite severe poisoning with ammonia, the performance degradation is in most cases reversible, but only after operating with neat hydrogen for long periods of time.

Finally, based on achieved results (analysis of the electrical behavior) authors are working on studying the effect of pollutants in high and low MEAs regarding physical properties like temperature, relative humidity and analysis of regeneration processes.

Acknowledgements

This work is a contribution of the DPI2017-85540-R Project supported by the Spanish Ministry of Economy and Competitiveness and by the European Union Regional Development Fund.

List of Symbols

A	Amp
A cm^{-2}	Amperes per square centimeter
CO	Carbon monoxide
CO_2	Carbon dioxide
CV	Cyclic voltammetry
DI	De-ionized
EIS	Electrochemical impedance spectroscopy
HT-PEFC	High temperature polymer electrolyte fuel cell
GDL	Gas diffusion layer
H_2	Hydrogen
H^+	Hydrogen cation
H_2S	Hydrogen sulfide
HFR	High frequency resistance
INTA	Spanish national institute for aerospace technology
IEC	International electrochemical commission
LT-PEFC	Low temperature polymer electrolyte fuel cell
λ_a	Anode stoichiometric
λ_c	Cathode stoichiometric
MEA	Membrane electrode assembly
MFC	Mass flow controller
NH_3	Ammonia
NH^{4+}	Ammonium ion
NL	Normal litres
N_2	Nitrogen
OCV	Open circuit voltage
O_2	Oxygen
PBI	Polybenzimidazole
PEFC	Polymer electrolyte fuel cells
PTFE	Polytetrafluoroethylene
PID	Proportional-integral-derivative
Pt	Platinum
ppm	parts per million
RHa	Relative humidity of anode
RHc	Relative humidity of cathode
V	Volt
X^{+n}	Cations contaminants

References

[1] S. Mukhopadhyay, S. Fernandes, M. Shihab, D. Waleed, *Appl. Sci.* **2018**, *8*, 942.
[2] H.-W. Wu, *Appl. Energy* **2016**, *165*, 81.
[3] A. de las Heras, F. J. Vivas, F. Segura, J. M. Andújar, *Int. J. Hydrogen Energy* **2017**, *42*, 12841.
[4] A. de las Heras, F. J. Vivas, F. Segura, M. J. Redondo, J. M. Andújar, *Renew. Energy* **2018**, *125*, 1.
[5] M. Derbeli, O. Barambones, L. Sbita, M. Derbeli, O. Barambones, L. Sbita, *Appl. Sci.* **2018**, *8*, 2449.
[6] U. Misz, A. Talke, A. Heinzel, G. Konrad, *Fuel Cells* **2016**, *16*, 444.
[7] G. Cinti, U. Desideri, D. Penchini, G. Discepoli, *Fuel Cells* **2014**, *14*, 221.
[8] M. A. Díaz, A. Iranzo, F. Rosa, F. Isorna, E. López, J. P. Bolivar, *Energy* **2015**, *90*, 299.
[9] S. M. M. Ehteshami, A. Taheri, S. H. Chan, *J. Ind. Eng. Chem.* **2016**, *34*, 1.
[10] X. Wang, P. Baker, X. Zhang, H. F. Garcese, L. J. Bonvilleb, U. Pasaogullari, T. M. Molterabc, *Int. J. Hydrogen Energy* **2014**, *39*, 19701.
[11] Q. Li, R. He, J. O. Jensen, N. J. Bjerrum, *Chem. Mater.* **2003**, *15*, 4896.
[12] X. Cheng, Z. Shi, N. Glass, L. Zhang, J. Zhang, D. Song, Z-S. Liu, H. Wang, J. Shen, *J. Power Sources* **2007**, *165*, 739.
[13] F. A. Uribe, S. Gottesfeld, T. A. Zawodzinski, *J. Electrochem. Soc.* **2002**, *149*, A293.
[14] H. J. Soto, W.-K. Lee, J. W. Van Zee, M. Murthy, *Electrochem. Solid-State Lett.* **2003**, *6*, A133.
[15] N. Zamel, X. Li, *Prog. Energy Combust. Sci.* **2011**, *37*, 292.

 © 2019 The Authors. Published by WILEY-VCH Verlag GmbH & Co. KGaA, Weinheim

[16] A. Valera-Medina, H. Xiao, M. Owen-Jones, W. I. F. David, P. J. Bowen, *Prog. Energy Combust. Sci.* **2018**, *69*, 63.
[17] A. Yapicioglu, I. Dincer, *Renew. Sustain. Energy Rev.* **2019**, *103*, 96.
[18] K. E. Lamb, M. D. Dolan, D. F. Kennedy, *Int. J. Hydrogen Energy* **2018**, *44*, 3580.
[19] T. L. Levalley, A. R. Richard, M. Fan, *Int. J. Hydrogen Energy* **2014**, *39*, 16983.
[20] E. López, F. Isorna, M. Silva, F. Rosa, J. Guerra, *Hydrog. Energy* **2015**, *40*, 5518.
[21] A. L. Dicks, *J. Power Sources* **1996**, *61*, 113.
[22] *Fuel Cells: Technologies for Fuel Processing*, (Eds. D. Shekhawat, J. J. Spivey, D. Berry), Elsevier Science, Oxford, United Kingdom, **2011**.
[23] R. Borup, J. Meyers, B. Pivovar, Y. S. Kim, R. Mukundan, N. Garland, D. Myers, M. Wilson, F. Garzon, D. Wood, P. Zelenay, K. More, K. Stroh, T. Zawodzinski, X. J. Boncella, J. E. Mcgrath, O. M. Inaba, K. Miyatake, M. Hori, K. Ota, Z. Ogumi, S. Miyata, A. Nishikata, Z. Siroma, Y. Uchimoto, K. Yasuda, K. Kimijima, N. Iwashita, *Chem. Rev.* **2007**, *17*, 3904.
[24] Y. Acevedo Gomez, A. Oyarce, C. Lagergren, *J. Electrochem. Soc.* **2018**, *165*, 189.
[25] S. L. Holleck, G. L. Pasquariello, D. M. Clauson, *Proc. 2nd International Symposium on Proton Conducting Membrane Fuel Cells II*, (Eds. S. Gottesfeld, T. F. Fuller), Boston, Massachusetts, **1999**, p. 150.
[26] R. J. Bellows, E. P. Marucchi-Soos, D. T. Buckley, *Ind. Eng. Chem. Res.* **1996**, *35*, 1235.
[27] S. K. Das, A. Reis, K. J. Berry, *J. Power Sources* **2009**, *193*, 691.
[28] C. G. Farrell, C. L. Gardner, M. Ternan, *J. Power Sources* **2007**, *171*, 282.
[29] H. Yoshiyuki, M. Yoshiyuki, I. Daichi, A. Motoaki, *J. Nucl. Cardiol.* **2004**, *11*, S43.
[30] X. Zhang, U. Pasaogullari, T. Molter, *Int. J. Hydrogen Energy* **2009**, *34*, 9188.
[31] X.-Z. Yuan, H. Li, Y. Yu, M. Jiang, W. Qian, S. Zhang, H. Wang, S. Wessel, T. H. Cheng, *Int. J. Hydrogen Energy* **2012**, *37*, 12464.
[32] K. Hongsirikarn, J. G. Goodwin, S. Greenway, S. Creager, *J. Power Sources* **2010**, *195*, 30.
[33] L. L. Sun, Hong, M. Yu, F. Zhang, *J. Shenyang Jianzhu Univ.* **2005**, *31*, 543.
[34] V. M. Schmidt, P. Bröckerhoff, B. Höhlein, R. Menzer, U. Stimming, *J. Power Sources* **1994**, *49*, 299.
[35] Fuel Cell and Hydrogen Joint Undertaking Annual Report, can be found under https://www.fch.europa.eu/page/publications, **2012**.
[36] B. Shabani, M. Hafttananian, S. Khamani, A. Ramiar, A. A. Ranjbar, *J. Power Sources* **2019**, *427*, 21.
[37] IEC TS 62282-7-1:2017 Single cell test methods for polymer electrolyte fuel cell (PEFC), can be found under https://webstore.iec.ch/publication/31478, **2010**.
[38] Test Module PEFC SC 5-2, FCTESTNET, can be found under https://ec.europa.eu/jrc/en, **2010**.
[39] M. V. Williams, H. R. Kunz, J. M. Fenton, *J. Power Sources* **2004**, *135*, 122.
[40] PEFC power stack performance testing procedure I, FCTESTNET, can be found under https://ec.europa.eu/jrc/en, **2009**.

 © 2019 The Authors. Published by WILEY-VCH Verlag GmbH & Co. KGaA, Weinheim

4.2. Artículo 2

Converting a Fixed-Wing Internal Combustion Engine RPAS into an Electric Lithium-Ion Battery-Driven RPAS

F. Isorna Llerena, Álvaro Fernández Barranco, José Antonio Bogeat, F. Segura Manzano, J. M. Andújar Márquez

Publicado en:

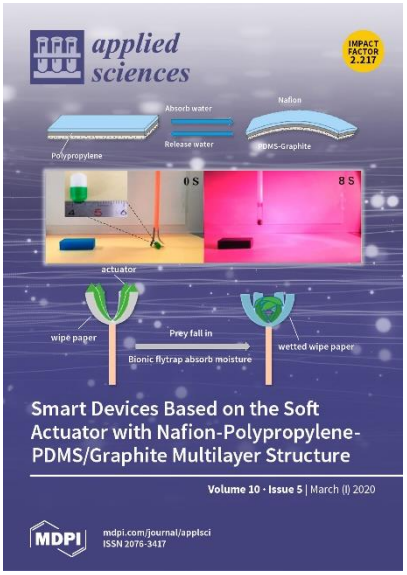

Revista: Applied Sciences
Editorial: MDPI
Editor ejecutivo: Prof. Dr. Takayoshi Kobayashi
Referencias: Vol. 10, Issue 5, pp. 1573: (1-33)
Año: 2020
ISSN: 2076-3417
DOI 10.3390/app10051573

Categoría	Rango revista / Total revista	Cuartil
Chemistry, Multidisciplinary	88 / 177	Q2
Physics, Applied	62 / 154	Q2
Engineering, Multidisciplinary	32 / 91	Q2
Impact Factor (2019)	2,474	
Citations	1	

applied sciences

MDPI

Article

Converting a Fixed-Wing Internal Combustion Engine RPAS into an Electric Lithium-Ion Battery-Driven RPAS

Fernando Isorna Llerena [1,*], Álvaro Fernández Barranco [1], José Antonio Bogeat [1], Francisca Segura [2] and José Manuel Andújar [2]

[1] Instituto Nacional de Técnica Aeroespacial (INTA), Área de Energía. Ctra, Huelva-Matalascañas, km. 34, 21130 Mazagón, Huelva, Spain; alvar0.gate@gmail.com (Á.F.B.); bogeatspja@inta.es (J.A.B.)

[2] Departamento de Ingeniería Electrónica, Universidad de Huelva, de Sistemas Informáticos y Automática, 21007 Huelva, Spain; francisca.segura@diesia.uhu.es (F.S.); andujar@diesia.uhu.es (J.M.A.)

* Correspondence: isornaf@inta.es; Tel.: +34-959208847

Received: 8 January 2020; Accepted: 20 February 2020; Published: 25 February 2020

check for updates

Featured Application: The main application was to give a second life to an obsolete and declassified type of RPAS (remotely piloted aircraft system) for use in monitoring key parameters, in the cultivation of the olive tree and in other types of cultivation that occupy large areas of land. Similarly, it can be used to track and monitor endangered animal species. INTA (National Institute for Aerospace Applications) is located on the grounds of the Doñana National Park, where the Iberian lynx lives, one of the most threatened felines in the world, taking advantage of some of the main advantages of this RPA (remotely piloted aircraft) like autonomy, efficiency, low-noise level, and non-polluting.

Abstract: It is well proved that remotely piloted aircraft systems (RPASs) are very useful systems for remote sensing in precision agricultural labors. INTA (National Institute for Aerospace Applications) and the University of Huelva are involved in Tecnolivo Project that proposes the development of a marketable and easy-to-use technological solution that allows integrated, ecological, and optimized management of the olive grove through non-invasive monitoring of key agronomic parameters using RPASs. The information collected by the RPAS in regards to the state of the vegetation, such as hydric stress levels, plague detection, or maturation of the fruit, are very interesting for farmers when it comes to make decisions about their crops. Current RPAS applications for precision agriculture are mainly developed for small- to medium-sized crops using rotary-wing RPASs with small range and endurance operation, leaving aside large-sized crops. This work shows the conversion of a fully declassified and obsolete fixed-wing internal combustion engine (ICE) remotely piloted aircraft (RPA), used as aerial target for military applications and in reconnaissance and surveillance missions at low cost, into an electric lithium polymer (LiPo) battery-driven RPA that will be used for precision agriculture in large-sized crop applications, as well as other applications for tracking and monitoring of endangered animal species in national parks. This RPA, being over twenty years old, has undergone a deep change. The applied methodology consisted of the design of a new propulsion system, based on an electric motor and batteries, maintaining the main airworthiness characteristics of the aircraft. Some other novelties achieved in this study were: (1) Change to a more efficient engine, less heavy and bulky, with a greater ratio of torque vs. size. Modernization of the fly control system and geolocation system. (2) Modification of the type and material of the propeller, reaching a higher performance. (3) Replacement of a polluting fuel, such as gasoline, with electricity from renewable sources. (4) Development of a new control software, etc. Preliminary results indicate that the endurance achieved with the new energy and propulsion systems and the payload weight available in the RPA meet the expectations of the use of this type of RPAS in the study of large areas of crops and surveillance.

Keywords: remotely piloted aircraft (RPA); remotely piloted aircraft system (RPAS); unmanned aerial system (UAS); unmanned aerial vehicle (UAV); battery; precision agriculture; crops; remote sensing

1. Introduction

An unmanned aerial system (UAS) or unmanned aerial vehicle (UAV) is defined as a powered aerial vehicle that does not carry a human operator, uses aerodynamic forces to provide vehicle lift, and can fly autonomously or be remotely piloted aircrafts. In this last case, they are also called a remotely piloted aerial system (RPAS) (i.e., aerial platform (RPA) plus control station for pilot and operator (if applicable) actions [1–3]). UASs and RPASs (usually the same denomination is employed, even in the everyday jargon they are called drones) are mostly associated with military, industry, and other specialized operations, but with recent developments in the area of sensors and information technology in the last two decades, the scope of drones has been widened to other areas like agriculture [4].

The technology of RPASs for areas such as precision agriculture is drawing increasing attention from different sectors interested in seeking real-time, high-quality, high-volume crop data to accelerate crop improvement through breeding and to optimize agronomic practices [5–19].

Traditional imagery, provided, for example, by RGB (read green blue) and/or NIR (near infared) sensors, has proven to be useful in many agroforestry applications. However, it lacks the spectral range and precision to profile materials and organisms that only hyperspectral sensors can provide. This kind of high-resolution spectroscopy was firstly used in satellites and later in manned aircraft, which are significantly expensive platforms and extremely restrictive due to availability limitations and/or complex logistics. More recently, UASs have emerged as a very popular and cost-effective remote sensing technology, composed of aerial platforms capable of carrying small-sized and lightweight sensors. Meanwhile, hyperspectral technology developments have been consistently resulting in smaller and lighter sensors that can currently be integrated in UASs for either scientific or commercial purposes. The hyperspectral sensors' ability for measuring hundreds of bands raises complexity when considering the sheer quantity of acquired data, whose usefulness depends on both calibration and corrective tasks occurring in pre- and post-flight stages [15].

Independent of the aerial platform, sensors play an important role in data acquisition. According to [20], in which an extensive work addressing hyperspectral technology can be found, there are four main techniques for acquiring measurable data from a given target: By hyperspectral imaging, multispectral imaging, spectroscopy, and RGB imagery. The most significant differences are synthetized in Table 1, which considers not only the comparison carried out by [20] but also the vision of Sellar and Boreman [21], who stated that imaging sensors for remote sensing can be divided into the method by which they achieve (1) spatial discrimination and (2) spectral discrimination.

Table 1. Differences between hyperspectral and multispectral imaging, spectroscopy, and RGB (read green blue) imagery. A classification based on a bullet rate (1–3) was used to quantify both the spectral and spatial information associated to each acquisition technique, in relative terms.

	Spectral Information	Spatial Information
Hyperspectral Imaging	•••	•••
Multispectral Imaging	••	•••
Spectroscopy	•••	•
RGB Imagery	•	•••

Regarding the aerial platform, different types of RPAS models which have been used in the last two decades are shown in Table 2 [22].

Table 2. Different types of RPAS (remotely piloted aircraft system) models developed in past studies for precision agriculture.

Type	Reference
Fixed-wing	[23–26]
Single-rotor helicopter	[27–31]
Quad copter	[32–36]
Hexa copter	[30,37–40]
Octo copter	[41–45]

Fixed-wing (Figure 1a) RPASs are entirely different in their design compared to multi rotors, and aerodynamic shape of two wings provides an easy glide for RPAs. The single-rotor helicopter (Figure 1b) is a model with just one big-sized rotor on top and one small-sized rotor on the tail of the RPA. Quad copter (Figure 1c), hexa copter (Figure 1d), and octo copters (Figure 1e) are multi-rotors which are lifted and propelled by four, six, and eight rotors, respectively.

(**a**) (**b**) (**c**) (**d**) (**e**)

Figure 1. RPAS (remotely piloted aircraft system) types: Fixed-wing (**a**). Single-rotor (**b**). Quad Copter (**c**). Hexa Copter (**d**). Octo Copter (**e**).

Current RPAs applications for precision agriculture are mainly developed for small- to medium-sized crops, using rotary-wing RPASs with small range and endurance operation, leaving aside large-sized crops, but farmers with a lot of hectares of land find it difficult to reach each corner of field for inspection each time. The fixed-wing RPAS does this task without any hiccup, as farmers can do regular air monitoring of fields to know the status of their crops at regular intervals of time. Table 3 compares the main features of fixed-wing vs. rotary-wing UAVs.

Table 3. Advantages and disadvantages of fixed- and rotary-wing aircraft.

Fixed-Wing		Rotary-Wing	
Advantages	**Disadvantages**	**Advantages**	**Disadvantages**
Autonomy Range Altitude Speed Consumption	Non-stationary flight Difficult maneuverability Non-modifiable designs	Stationary flight Stability Control Maneuverability Size	Autonomy Consumption

In Table 4, an evaluation was done to compare electric vs. internal combustion engine (ICE) engines in both fixed-wing and rotary-wing UAVs regarding some technical characteristics, like payload, wind resistance, autonomy, and landing distance. It can be seen that fixed-wing electric UAVs are those that present more equitable flying parameters.

Table 4. Evaluation of some UAV (unmanned aerial vehicle) platforms, according to the literature [46–48] and the authors' experience. The evaluation is from 1 (low) to 5 (high).

	Fixed-wing		Rotary-wing	
	Electric	**ICE (Internal Combustion Engine) Engine**	**Electric**	**ICE Engine**
Payload	3	4	2	4
Wind resistance	2	3	2	4
Minimum speed	2	2	4	4
Flying autonomy	3	5	2	4
Portability	2	2	3	3
Landing distance	3	2	4	4

Concerning the power supply system of UAVs, electric UAVs are characterized by great advantages such as reliability, efficiency, low-noise, reduction of heat losses, as well as getting an energy supply free of polluting emissions [49]. However, the energy management of these UAVs requires more advanced control, which also takes into account many storage and power supply options [50].

Although it is usual to find that electric UAVs make use of batteries, among which many types have to be differentiated, these have, in general, low-energy density and very large charging times. However, batteries provide great autonomy and reliability of a technology with much development today. Within the different types of batteries, it is not only necessary to assess their electrical characteristics, but also their weight, since this critically influences the energy consumption of the UAV, and; therefore, its autonomy. Looking at the Table 5 [51], the energy comparison of the four main types of batteries used in electric UAVs today can be seen. It is found that lithium polymer (LiPo) batteries have a very large specific power, which is the reason why they are used in 90% of UAVs of micro-aerial vehicles. LiPo batteries also have a good relationship of specific energy and energy density, although it can be found in higher values in Li-S (lithium–sulfur) batteries, at the expense of an obvious lower specific power.

Table 5. Batteries electric characteristics comparison.

	Ni-Cd (Nickel-Cadmium)	**Ni-Mh (Nickel Metal Hydride)**	**LiPo (Lithium Polymer)**	**Li-S (Lithium-Sulphur)**
Specific energy (Wh/kg)	40	80	180	350
Energy density (Wh/L)	100	300	300	350
Specific power (W/kg)	300	900	2800	600

In addition to different types of batteries, alternatives for recharging can also be considered. Swapping involves exchanging a battery for another already charged, which avoids great complexity in energy management but reduces the necessary size of the batteries [52]. With the laser-beam charging base, an optimal receiver transforms the received light into electricity, thereby avoiding the risks associated with landings, at the cost of reducing the useful height where it can be operated, as well as the search for a location without obstructions for an effective recharge [53]. Tethered UAVs are the safest form of energy transfer, when performed directly, although they reduce the area of operation in a limited way [54].

When a more balanced operation is wanted, supercapacitors can be used. These allow a very high-energy density with a rapid response dynamic, which facilitates the start-up of the equipment, as well as maneuvers that require a greater instantaneous energy supply. It is also possible to make use of fuel cells, where hydrogen as an energy vector provides electricity [55], with great advantages in terms of weight and equipment maintenance, although with a slow dynamic. Additionally, fixed-wing UAVs have the possibility to carry solar cells and use solar energy, so fuel consumption can be reduced [56,57].

In Figure 2, it can be seen how each technology has very differentiating characteristics in terms of its energy supply capacity. That is why more and more electric UAVs makes use of hybridization

among the different technologies [58], taking the benefits of the advantages of each one of them, and adapting to the application for which the electric UAV is designed for [59].

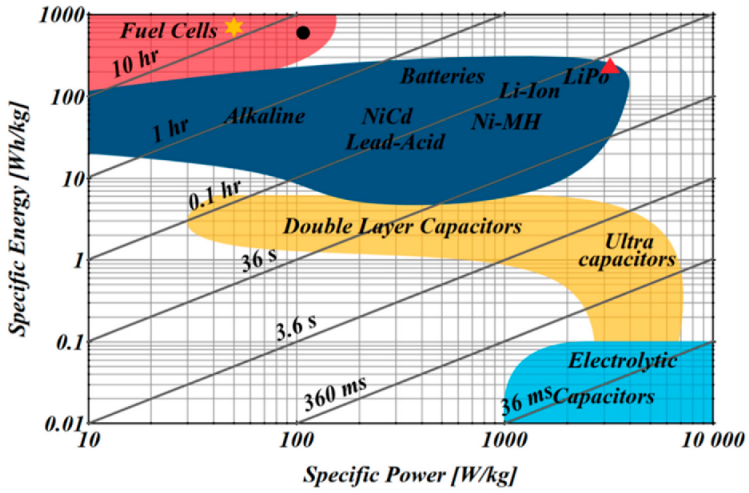

Figure 2. Specific energy/power comparison among different energy sources.

The hybrid combination of different types of energy storage also requires the implementation of larger control systems [60], so that they must reach a balance between energy management alternatives and the size required for computer control equipment, together with the different sensors and actuators that make up the plant balance [61].

After this review of the state-of-the-art of electric UAVs, it is realized that one of the solutions, that the literature shows as the most promising in terms of flight autonomy, is the use of hydrogen and fuel cells in electric RPASs [62–65]. As a first step for this ambitious ultimate goal, a fixed-wing electric RPA was developed.

This work shows how a fixed-wing RPA with an internal combustion engine, used as a target for military applications, was deeply modified in order to transform it into an electric RPA, equipped with a pack of LiPo batteries with the proper battery management system (BMS) and an electric engine with suitable controller. A propeller was also changed, but the main airworthiness characteristics of the RPA were maintained.

Among the main advantages of electric engine is that they are of universal use, widely understood, simple in concept and operation, large efficiency, low cost due to economies of scale, and very low-noise level [66].

TecnOlivo Project

TecnOlivo pursues modernizing a traditional agricultural sector such as olive cultivation, by creating a pioneering technological device that opens up new business opportunities, and places the olive production industry of Huelva and that of the southeast of Portugal at the forefront of international innovation and, by extension, the rest of Andalusia, Spain, and Portugal.

With 2.5 million euros of budget, co-financed with FEDER Funds and submitted to the first call of the INTERREG V-A Spain-Portugal Programme (POCTEP 2014–2020), the project targeted the development of a marketable technological solution (TecnOlivo) to be easily-used by farmers, and which allows the integral, ecological, and optimized management of the olive grove by monitoring non-invasive agronomic parameters of interest to partner olive growers. With TecnOlivo, partners sought to improve the sustainability of olive cultivation, by favoring an optimal use of resources.

TecnOlivo represented a holistic solution to traditional olive farming in which an unmanned aerial vehicle captured georeferenced crop information through cameras or other sensors, and integrated the data collection, transmission, analysis, processing, visualization, action guidelines, and "learning processes," in an easy and ergonomic way for the farmer. It was supported by a network of low-cost ground sensors, which will constitute a relevant intelligent tool for olive farmers, such as those ancient farming tools and farm tractors were in their days. Thus, TecnOlivo will allowed olive growers to know, in real-time and on-the-spot, information on key parameters such as the hydric status and nutrients of the groves, what extent treatments were needed, and in what areas of the orchards.

During the development of the project Tecnolivo [67–70], different types of rotary-wing RPASs were used, but when the extensions of the study area were very large, an RPA with greater autonomy was missing.

The TecnOlivo project proposed a methodology for plant detection, geolocation, and counting in olive orchards, based on aerial imagery and image processing and analysis. To that end, an RPAS equipped with a multispectral camera was used to carry out image acquisition. The captured multispectral images were processed in order to yield a DSM (digital surface model). This data structure was subsequently transformed by means of mathematical morphology, aiming to individually segment the olive trees appearing in the images from the ground.

Aerial imaging was conducted using a DJITM Matrice 100 RPAS (SZ DJITM Technology Co., Ltd., Shenzhen, Guangdong, China). This aircraft is propelled by four rotors (quadcopter), enabling its vertical take-off and landing.

Images were taken with the multispectral camera MicaSense RedEdge-MTM (MicaSense, Inc., distributed by ACRE surveying solutions, Spain), installed on the RPAS. This sensing device was capable of capturing information in five different spectral bands within the visible and the infrared spectrum.

The main problem was that the quadcopter batteries had to be changed every 15 or 20 min, making the data collection missions very short. For this reason, the goal of this paper is to propose a methodology to transform an ICE RPA into an electric RPA with the aim that the developed aerial platform takes advantages from both ICE and electric technology.

Preliminary results indicate that the endurance achieved with the new energy and propulsion systems and the payload weight available in the RPA meet the expectations of the use of this type of aerial platform in the study of large areas of crops. The autonomy achieved by the electric RPA is almost 50% more than the same model with internal combustion engine. If it is compared with the commercial UAV (multicopters) models currently used in the TecnOlivo project, the advantage in terms of flight autonomy and surface to be treated is enormous.

Because of this transformation, additional novelties were achieved: (1) A more efficient engine, less heavy and bulky; (2) a greater ratio of torque vs. size; (3) the development of a dedicated software in order to monitor and control the parameters related to the new power system; (4) the design of a new and less-consuming telemetry module able to establish communication between the ground control station (GCS) and the RPA BMS and motor controller; and (5) the design and 3D printing of parts such as battery case, telemetry module chassis, propeller cone, and motor controller housing.

This work is divided into the following sections. After this introduction, Section 2 describes in detail the materials and method used. Afterwards, the tests performed are presented in Section 3, including the results obtained with the modified electric RPA. Lastly, discussion and conclusions are explained and future works are depicted in Sections 4 and 5, respectively.

2. Materials and Methods

2.1. Description of Original RPA. ALO project

The selected RPA for this work was chosen from the Project ALO (in Spanish, Avión Ligero de Observación—lightweight reconnaissance plane) that is an RPA developed by INTA (in Spanish, Instituto Nacional de Técnica Aeroespacial—National Institute of Aerospace Technology) which

can provide real-time reconnaissance, surveillance, and target acquisition information by means of interchangeable, steerable TV and FLIR (forward-looking infrared sensor) cameras. The images can be sent in real-time to the ground control station (GCS) where image processing capabilities are provided.

In a typical mission performed by ALO, the RPA is transported to the launching site in the transportation vehicle that also plays the role of ground control station, Figure 3. The whole RPAS is transported on a single vehicle (Unimog size), which provides great mobility and transport capabilities, allowing missions from non-prepared locations. Assembly and installation of the RPA can be accomplished in less than 30 min without the use of special tooling.

Figure 3. Completed ALO (Avión Ligero Observación) system: Control ground station, rubber bungee launcher, and aerial aircraft.

After loading the waypoints on the on-board computer, the UAV is launched from a hydraulic or pneumatic launcher. The RPA will fly the programmed mission over the surveillance area transmitting, in real-time, the images captured by the camera and relevant telemetry data, such as, position of the RPA, speed, fuel consumption, revolutions per minute (rpm) of the RPA engine, or altitude. In case of detecting any possible target, activity, or area of interest, the pilot located at the GCS can take manual control of the RPA flying around the selected point.

When the mission finishes, or whenever decided by the pilot, the RPA can return autonomously to the launching site and the recovery will be performed by means of a parachute. Furthermore, for mission evaluation, the whole mission is recorded and can be replayed on a video monitor where the all the main flight parameters are displayed.

ALO RPAS Description

The ALO RPA could perform reconnaissance, surveillance, and target acquisition missions at a distance of up to 50 km from the GCS for a maximum of 60 min. Nominal observation speed of the RPA is 70 km/h.

To carry out an operation, the RPAS was divided in the Air Segment (RPA + payload + spare parts) and the Ground Segment (GCS + transportation vehicle + launcher + tools and spare parts). Specifically:

(a) Air Segment:

- RPA
- Steerable TV and FLIR cameras
- Spare parts to guarantee 1 week of deployment with 3 missions per day

(b) Ground Segment:

- Transportation vehicle
- GCS

- Hydraulic or pneumatic launcher
- Maintenance tools
- Spare parts

The specific design features of the engine and aerial platform provides the RPA with very high climbing rates and a wide range of flight speeds: The UAV can reach the area of interest at a high speed and then decrease the speed down to facilitate recognition and identification of targets. Figure 4 shows an ALO RPA in the launching pad and Table 6 states the main features of the RPA regarding dimensions, weights, and performance values.

a) **b)**

Figure 4. (**a**) ALO Avión Ligero Observación) RPA in the launching pad (**b**) ALO taking off.

Table 6. ALO RPA technical characteristics.

Characteristics	Value
Wingspan	3.03 m
Length	1.8 m
MTOW (Max. Take-Off Weight)	25 kg
Wing Area	0.85 m^2
Max. Payload	7.5 kg
Endurance	1 h
Speeds	50–225 km/h
ROC (Rate of Climb)	6 m/s
Range	50 km

To understand the RPA architecture, the main parts are:

(1) **Airframe:** The RPA is a conventional V tail fixed-wing aircraft made of reinforced fiber glass. The airframe can be easily disassembled in parts: fuselage, tail cone, and wing. The tips of the wing can also be disassembled. This modularity improves maintainability and allows and easy transportation of the RPA.
The main components of the airframe are:

- Fuselage: Made of epoxy resin and fiberglass layers. The fuselage is a non-divided compartment without bulkheads or internal structural elements. This feature gives ALO the possibility to accommodate a wide variety of payloads and avionics equipment.
- Tail cone: Fiberglass layers enclosing a core of Rohacell©. Very simple union with the fuselage.
- Wing: The wing is a sandwich structure made of fiberglass layers and Nomex©. As in the fuselage, no internal ribs or structural elements are provided. The volume enclosed by the fuselage is in contact with the volume enclosed by the wing, significantly increasing

the available volume for payload of fuel. The wing tips can be disassembled in order to facilitate the transport.
- Control surfaces: Fiberglass layers enclosing a core of Rohacell©. The control surfaces are deflected by commercial "off-the-shelf" brushless servo motors.

(2) **Propulsion system:** The power plant consists of a two-cylinder two stroke reciprocating engine providing 6.8 HP (horse power). The engine drives a fixed-pitch two-blade propeller. The propulsion system is located at the front of the RPA and is joined to the bulkhead by means of four silent blocks. The fuel tank is located in the wing. The carburetor has an integrated fuel pump. The fuel used is an oil: gasoline mixture 1:50 [71].

(3) **Electric Power System:** The main electric power source are packs of Ni-Cd batteries that provide the required power for a period of 60 min, just for auxiliary electrical loads.

(4) **Navigation Guidance and Flight Control Systems (NGFCSs):** The NGFCS is an extensively-proven "off-the-shelf" package including a GPS receiver that allows autonomous flights, an autopilot for stabilization, and an azimuth control unit to fly the RPA following the different commanded azimuth directions. The NGFCS allows different flight modes:

- Autonomous: Follow the waypoints loaded in the mission planning.
- Semi-automatic: The RPA is controlled by the pilot but without direct control on all control surfaces.
- Manual: The pilot has full control of the RPA.
- Failsafe: In case of loss of up-link the RPA will enter in Failsafe mode. In this mode the RPA adopts a predefined configuration which was selected by the pilot/operator during the pre-flight phase.

2.2. *Modifications Performed to Original ALO RPA*

An ALO block diagram of the internal combustion engine version can be seen in Scheme 1.

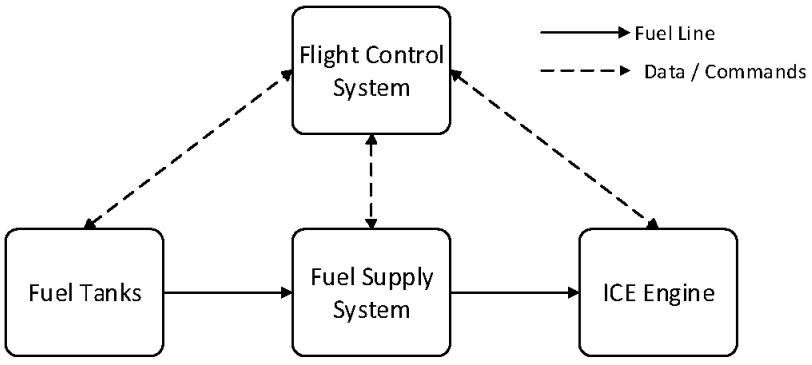

Scheme 1. ICE ALO Block Diagram. Where ICE is internal combustion engine.

With the aim to achieve a 100% electric RPA, the first task performed in ALO RPA was to remove all the components related to the ICE propulsion system, Scheme 2:

- ICE engine.
- Harnesses.
- Fuel tanks (in wing).
- Fuel supply system.

And the new power plant of the ALO consists of four fundamental elements:

- Electric engine.
- Electronic Speed Controller (ESC).
- Battery and BMS (Battery management system).
- Propeller.
- Telemetry module.

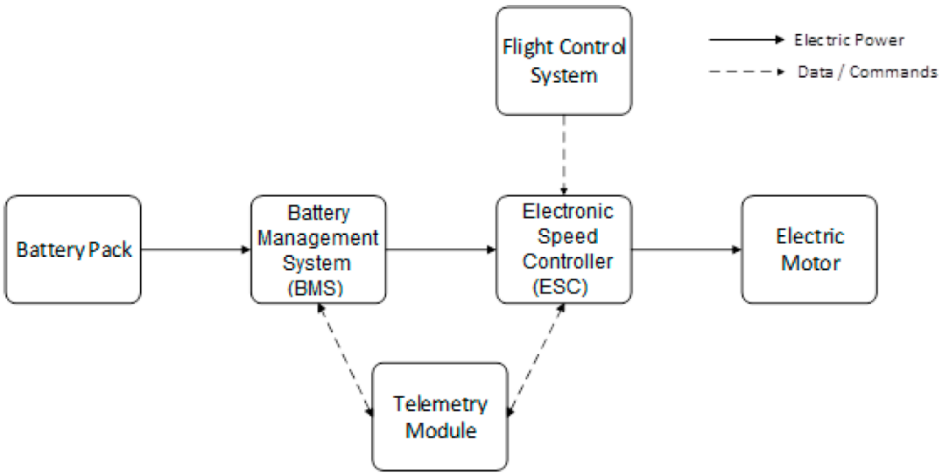

Scheme 2. Electric ALO Block Diagram. Where BMS is battery management system) and ESC is Electronic Speed Controller.

2.2.1. Electric Engine

ALO RPA originally had a two-cylinder two-stroke reciprocating engine (see Figure 5). The new configuration, with an electric engine, needs to achieve at least the same power. The chosen electric engine for the retrofitting platform is the DC electric engine Plettenberg© Predator 37-6 brushless (BLDC) outrunner type, manufactured by Plettenberg© Elektromotoren GmbH and Co., Baunatal, Germany. It weighs only 1.9 kg, has a maximum power of 12 kW, allows a maximum current intensity of 308 A, and can work with 12–14-cell (3 V each) battery packs. The manufacturer also declares an efficiency of 87%. The main characteristics of the electric engine are shown in Table 7.

Figure 5. Original ALO internal combustion engine with a two-blade wooden propeller.

Table 7. Electric engine characteristics.

Voltage (V)	14 × 3.0 V	42 V
Maximum current (I)		308 A
Motor Efficiency (η)		87%
Maximum power:	$P = V \times I \times \eta$	11.25 kW

As shown, the engine has more than enough power to propel the RPA, even if it finally had an increase in total weight [72].

The main feature of BLDC engines is the absence of brushes on switching for the transfer of power, since brushes produce friction, decrease performance, generate heat, are noisy, require periodic replacement, and; therefore, require greater maintenance [73]. Some of the advantages of the BLDC motors in regards to conventional DC motors are:

- Best relationship speed torque engine.
- Greater dynamic response.
- Greater efficiency.
- Greater life time.
- Lower noise.
- Greater range of speed.

In addition, the torque: size ratio is much greater, thus are very useful in work environments with reduced space. These motors develop their maximum torque from 0 rpm, so reduction gear is usually not needed, and it can be attached directly to a propeller. It has permanent magnets installed in the outer shell of the engine and the winding is attached to the shaft. These motors require ESC, which transform DC battery power into a three-phase alternating current and feed it to the windings in a certain sequence depending on the position of the rotor.

2.2.2. Electronic Speed Controller

The used ESC for this motor is the HBC series V7 25063-3 by MGM-ComPro©. It is a controller for low-power programmable brushless electric motors.

This motor speed controller provides high-quality and smooth motor control for the RPA and gives the possibility for safe disconnection of the battery when running the motor (emergency STOP).

ESC uses the best available power MOSFETs (metal oxide semiconductor field effect transistor) or IGBT (Insulated gate bipolar transistor) modules for higher voltage and synchronous pulse-width modulation (PWM) and very powerful 32-bit ARM© microcontrollers to achieve very high efficiency. Software and firmware updates can be carried out by connecting to the internet at any time. Thanks to this, ESC is easily accessible and customer-specific modifications and adjustments can be performed. Its basic features are:

- Working range: from low voltage up to 63 V, up to 250 A continuous power.
- Small dimension and weight.
- Very clear and easy parameter settings by PC.
- Data transfer to PC (or other equipment) and displaying in real-time (monitoring).
- Synchronous rectification, very high efficiency 98%–99%.
- Motor PWM in range 8–32 kHz.
- Suitable for motors without pole limiting.
- Sensor motors as well as sensorless motors are supported.
- Support regenerative braking and battery charging under braking.
- Support many working modes (PWM, constant rpm, constant torque/car mode, boat mode, plain mode).

- Electronic reversing.
- Support measuring (monitoring) of each battery cell.
- Support any type of battery: NiCd, NiMH, Lipo, Li-Ion, LiFePo4, Pb, etc.
- Monitors controller temperature, motor temperature, and battery temperature.

With respect to the possibility of parameters setting, it is necessary to have a PC running the Microsoft operating system and a USB cable. The PC must have the "Controller 2" software installed, see Figure 6.

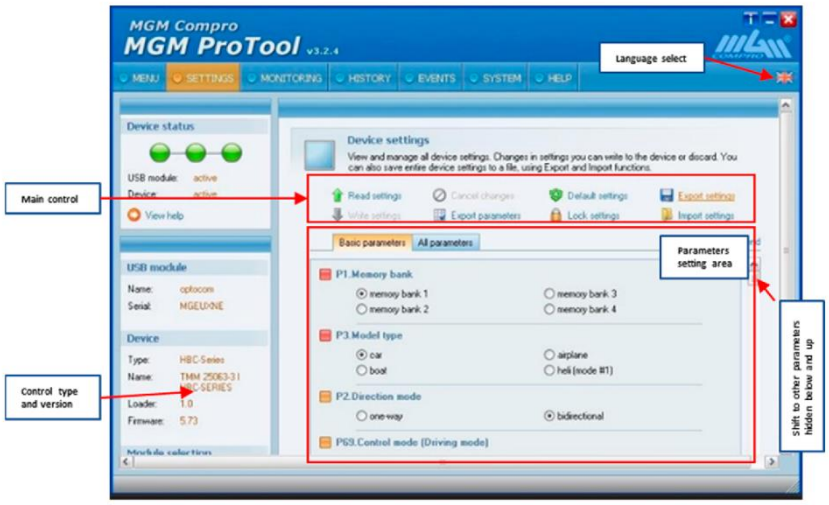

Figure 6. Controller 2 software screen with description and the possible values for all the parameters.

By default, settings of parameters in "Controller 2" software represents only average values. These values are usable as "starting values" for starting the system testing. In this case, it was necessary to adapt many parameters for the best behavior of the ESC with the available hardware. The description and the possible values for all the parameters are available in the operating manual of the controller [74].

2.2.3. New Electronic Power System

Battery and BMS

Taking into account a typical mission power needs, and the expressions for energetic content and capacity of a battery [75], the final battery pack was composed by 28 commercial 16,000 mAh 15 C 3.7 V Lithium Polymer battery cells [76] with 14-series and 2-parallel configuration (14s2p), achieving a final pack with 32,000 mAh theoretical capacity and 58.8 V [77,78].

For the selected electric motor, the different types of commercial batteries available were taken into account: Acid lead, NiMH, NiCd, LiPo, and LiFePO4, although new materials for batteries in aerospace and aeronautical applications will be available in the coming years [79–81]. However, with the actual state of technology and market prices, it was concluded that the best battery to be used in the electric ALO is the lithium polymer (LiPo) battery. It is the one with the highest specific energy, despite being the most fragile. Its main advantages are reflected below:

(a) High voltage per cell. In this case, the nominal voltage of each cell is 3.7 V, and can reach a maximum value of 4.2 V.
(b) High specific energy, around 200 Wh/kg.
(c) Low weight.

(d) High power density.
(e) Fast charge.
(f) Long life, which translates into economic savings.
(g) Passivation phenomenon: it consists in the formation of a lithium chloride film that forms on the surface of the anode and prevents its self-discharge. This is beneficial if the battery is not used for a long period of time, as it prevents it from discharging.

In contrast, some disadvantages are:

(a) Degradation at temperatures higher than 60 °C.
(b) Degradation if discharged below its minimum voltage, 3 V.
(c) Because of the two previous limitations, it is essential to use a BMS (battery management system), which controls the operating range of the batteries, and is able to disconnect them if their operation exceeds the permitted thresholds.

The amount of energy, E, stored in the battery is expressed in watt.hours (Wh) and is represented by Equation (1):

$$E = \int_0^t U(t) * I(t)dt \quad (1)$$

Usually when calculating this value, a constant current discharge mode can be used in such a way that the only variable in the equation is the voltage. The specific energy is measured in watt-hours per kg (Wh/kg) and it should be as high as possible since in mobile applications the weight is a key factor. This parameter will then be decisive when deciding what type of battery will be used in the ALO, which will be introduced later.

The battery capacity, C_{Ah}, is defined internationally as the electric charge, in amp hour (Ah) units, which can be extracted from a battery. When a battery is discharged at a non-constant current, the capacity is given by Equation (2):

$$C_{Ah} = \int_0^t I(t)dt \quad (2)$$

The capacity depends on discharge parameters, as well as: (1) The discharge current, (2) limits imposed by the voltage (cut-off voltage, final discharge voltage, initial voltage, state of charge, etc.), and (3) operating temperature.

When reaching the necessary voltage or achieving the desired capacity, the cells must be connected in series, parallel, or a combination of both. The serial connection consists of connecting the positive and negative terminals of two cells in such a way that the voltage increases, although the capacity remains the same. The parallel connection consists of connecting the terminals of the same sign (positive with positive and negative with negative) in such a way that the total voltage remains the same, but the capacity doubles. When selecting the configuration to be used in the application, it is necessary to take into account the voltage first and finally the capacity. In this case, the named 14-series and 2-parallel (14s2p).

The cells were packed in a custom 3D printed case (Figure 7) with all the couplings and fasteners secured in the main bay of the RPA. It also had vertical openings for better temperature management.

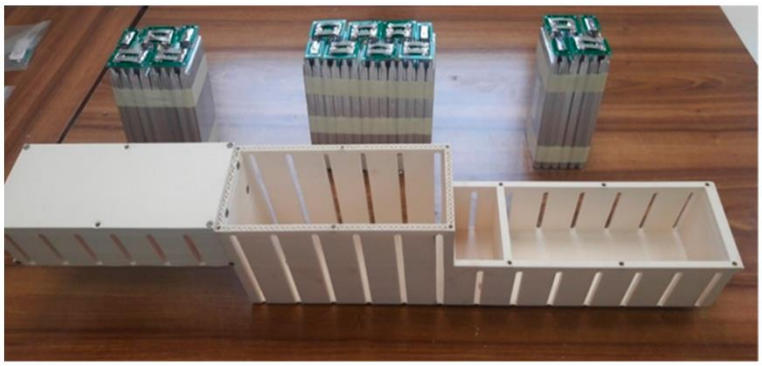

a)

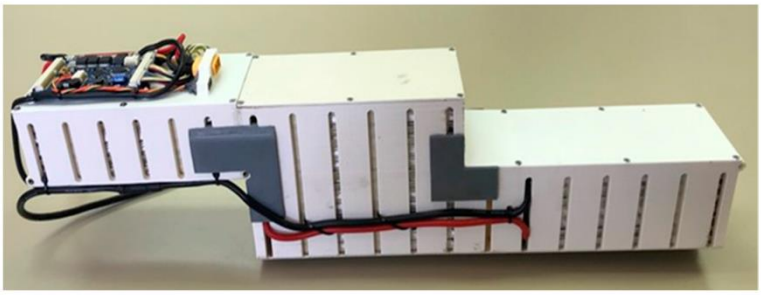

b)

Figure 7. (**a**) 3D printed batteries case with 3 blocks duly welded together (**b**) batteries connected inside the case.

The BMS is the Tiny BMS s516 150 A model from the company Energus Power Solutions©, Vilnius, Lithuania. It is widely used in the battery pack charging process, allowing the balance of the different cells. Cell balancing starts when the difference between any of the 14 series cells is bigger than 30 mV. BMS also monitors voltage cell levels and two temperature sensors distributed in the battery pack.

The BMS can be configured using the Battery Insider Windows application and a USB cable connected to the BMS communication interface connector. Alternatively, all the BMS configuration can be done using UART (Universal asynchronous receiver-transmitter), MODBUS or CAN (controller area network) communication commands [82].

BMS Cell Settings

The correct order of setting the battery and cells parameters would be to first adjust the settings under balancing and state of charge (SOC) group boxes in the cell settings tab of the battery insider, Annex 1.

Then, on the safety tab, adjust the cells critical parameters over-voltage cutoff and under-voltage cutoff. Upload the settings again to the device.

Only then go back to the cell settings tab and adjust fully charged voltage and fully discharged voltage parameters accordingly. These settings have a relationship under-voltage cutoff < fully discharged voltage < fully charged voltage < over-voltage cutoff, and the Battery Insider will not allow the user to set these values in any other way which would contradict the parameters relationship.

BMS Temperature Sensor Configuration

NTC (negative temperature coefficient) thermistors 10 K at 25 °C are used in the battery pack, the temperature sensor type parameter should be configured to Dual 10K NTC Sensor, Annex 1.

Once the previous parameters are correctly configured, it is in position to go into the battery insider live data tab (1) where the following parameters are shown, Figure 8:

- Cells voltage graph (2)
- Charging/discharging current status bar (3)
- BMS current operation state (4)
- BMS last recorded event (5)
- BMS estimated SOC value (6)
- Battery pack voltage calculated as the sum of all individual cells voltage connected in series (7)
- Battery pack current (8)
- Minimal battery pack cell voltage (9)
- Maximal battery pack cell voltage (10)
- BMS on board NTC temperature sensor value (11)
- External NTC temperature sensor #1 value (12)
- External NTC temperature sensor #2 value (13)

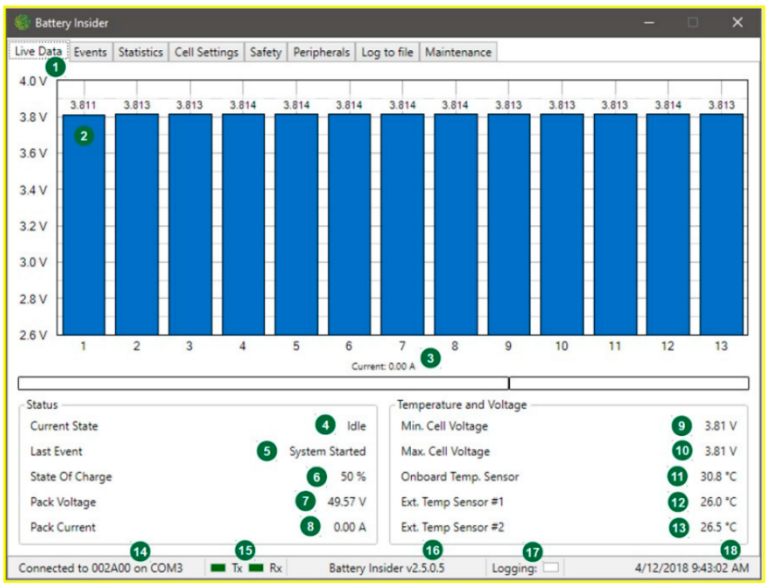

Figure 8. Live data tab parameters.

2.2.4. Propeller

As mentioned in the introduction of the present paper, one of the changes in the elements introduced in this new version of the ALO is the replacement of the two-bladed propeller with a carbon fiber three-bladed propeller with similar thrust. The mounted propeller is the model 28 × 12 3-Blatt. Table 8 shows its detailed dimensions and characteristics of the propeller mounted on the RPA.

Table 8. ALO propeller main characteristics.

Type	Three-Bladed
Diameter	28″
Pitch	12″
Weight	364 g
Max. rpm	8000
shaft diameter	10 mm

Made of carbon fiber, its main characteristic is lightness, as well as its specific rigidity, with a low-noise emission level for high rpm. In addition, the central mount has a wood reinforcement. The profile used is Clark Y, widely used in the aeronautical industry for general uses. It has a relative thickness of 11.7%, with a maximum thickness of 30% of the rope.

2.2.5. Telemetry Module

Emitter

The emitter is installed in the ALO and does not interfere with any other elements of the RPA, making the telemetry module completely autonomous and not dependent on the ALO battery pack. The emitter consists of the following elements (Figure 9): Microcontroller Arduino NANO, Real-time clock (RTC), SD card slot, and a 2.4 GHz Xbee module. To power all these elements, two 3.6 Ah LiPo batteries were installed in the back of the emitter module.

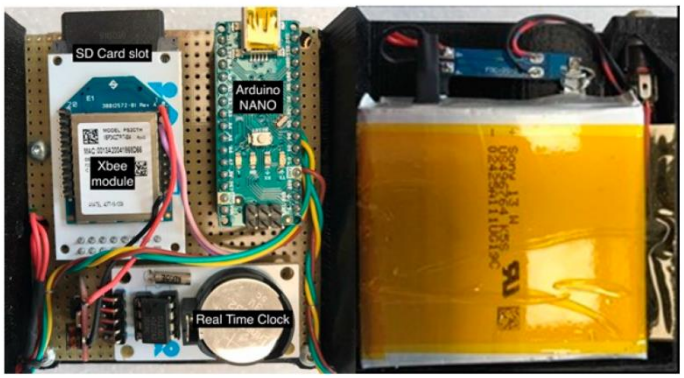

Figure 9. Emitter module front and rear view.

The emitter is able to communicate with the main battery pack BMS and the motor controller. This way it is possible to check all the parameters during tests and during take-off phase.

In the event of loss of communication, the emitter module is equipped with an SD memory card that saves all the data, acting as an onboard black box. Once on the ground, it is possible to collect the SD card and analyze all the flight data.

Receiver

The receiver module (Figure 10) is plugged in a PC USB port and consists of a 2.4 GHz Xbee module and an antenna.

Figure 10. Receiver: Xbee card with antenna and USB cable.

The receiver receives data from the emitter and, through the USB port, communicates with a custom software developed under Labview© environment, by National Instruments©, that allows the operator to check live parameters, Figure 11.

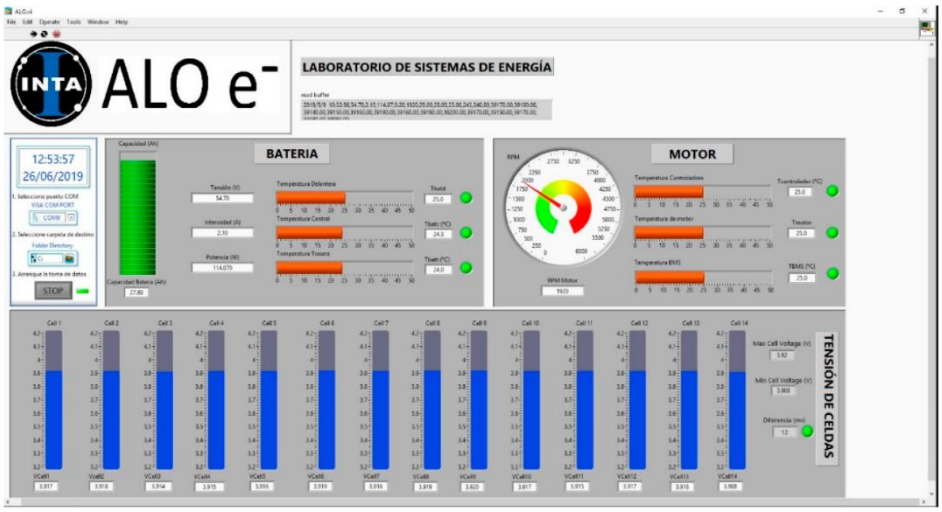

Figure 11. Developed SCADA software for electric ALO platform.

The software uses serial 8N1 communication protocol at 9600 bauds. 8N1 is a common abbreviation for the configuration of the serial port in asynchronous mode where there are eight (8) data bits, no (N) parity bit, and one (1) stop bit. With this configuration, only 80% of the data transmit information, since every 10 bits one is used for the start and end of each piece of information: The byte. 8N1 is the most common configuration for serial port communications at the INTA Energy Systems Laboratory. The transmission rate is usually in bits per second (bauds), such as 9600. The software is configured to ask the transmitter once per second for the incoming data (data string), which will be no longer than 300 characters. This transmission frequency, 1 Hz, is more than enough for live plotting and for post-flight data analysis.

The data string contains checksum detection. This checksum is a redundancy function whose main purpose is to detect accidental changes in the sequence of data to protect their integrity and to verify that there are no discrepancies between the controlled values when making an initial and final check after the transmission. The idea is that the data is transmitted along with its checksum value so the software calculate that value and compare it with the checksum value received. If there is a discrepancy, the software is able to reject the data or request a retransmission. Normally, increasing the ability to detect errors in the transmission increases the complexity of the algorithm, and with it, the required process needs, which in the present work is not a problem since the processor is a dedicated

laptop. However, it provides means for reliably detecting errors in the transmission. This software shows the main parameters related to the new power supply system of the electric ALO such as: remaining battery capacity, instant battery current and voltage, battery pack temperature sensors values, battery pack individual cell voltage and main motor parameters, such as, motor temperature and motor rpm. There are four different charts in the software main window. The small white chart shows communication parameters in the computer and in the path to the saving file. The next chart is for the main information of the battery pack, like temperature, voltage, current, and remaining capacity. The chart on the right side shows motor parameters as rpm and different elements temperatures. In the bottom chart there are information about individual battery cells in order to check the behavior of each cell in each situation. All these charts show the information using graphics, displays, and error lights to easily understand the operation of the system and to make decisions if there is any problem. All these values are also saved in a file for later analysis.

2.3. *Auxiliary Testing Platforms*

In order to test the RPA in safety environments and check the performance of the modified elements, the following auxiliary testing platforms are needed:

2.3.1. Arbin Battery Test Bench

In order to carry out the different tests to the battery individual cells and the battery pack the Arbin MT-ML-40V-20-2Chanels [83,84] battery testing system was used (Figure 12). This battery testing system provides:

- Fully independent high-precision test channels with full potentiostatic, galvanostatic control.
- True bipolar linear circuitry providing cross-zero linearity and zero switching time between charge and discharge.
- Each channel provides 3 or 4 current ranges with 16-bit resolution.
- Powerful embedded controllers provide fast data logging (2000 points per second, per system) and control flexibility for the most advanced test requirements.
- Any number of channels can be operated in parallel for increased current-handling capacity.
- Communicate with internal BMS via CANBus or SMBus protocols.
- Systems are air-cooled so no additional facility infrastructure or regular maintenance is needed.
- Software provides easy data analysis and plotting based in Data Watcher and Microsoft Excel.
- A wide array of auxiliary inputs/outputs are available for additional data collection or control such as temperature monitoring, additional reference electrodes, and more. Table 9 summarizes the main characteristics and Figure 12 shows a detail of the battery test bench.

Table 9. Arbin© battery test bench characteristics.

Number of Channels	**4**
Voltage range	0 to 60 V
Control and voltage measurement accuracy	(± 0.05% FSR (full scale range)) ± 60 mV
Min voltage to max current	0 V
Input impedance	~10 GΩ
Max current (charge/discharge)	100 A
Current and voltage resolution	16 bits
Current ranges (±0.05% FSR (full scale range))	
(a) High	100 A ± 100 mA
(b) Medium	10 A ± 10 mA
(c) Low	1 A ± 1 mA
Current rise time	3 ms

Figure 12. Arbin© battery test bench.

2.3.2. Thrust Test Bench

Due to the nature of all the modifications performed in the original ALO, a thrust test with the original ICE configuration and with the final configuration of the electric ALO was driven, in order to ensure the global behavior of the complete system and to be able to compare the on ground thrust for both the original and the final electric configurations. For that reason, a test bench was specifically designed to measure the real thrust of the system considering the new electric power plant, the motor controller, the electric motor, and the new 3-blade propeller (Figure 13).

a) **b)**

Figure 13. Modified electric ALO in thrust test bench. (**a**) lateral view, (**b**) stern view.

This test bench is based on a trolley securely attached to the ground by means of slings and carabiners. On top of this trolley the ALO is installed on a wheeled cradle attached to the main trolley with a dynamometer. These wheels allow the cradle to freely move forward/backwards and pull the dynamometer axle.

For safety reasons, the test bench was installed in an appropriate hangar for motor/turbine test equipped with a security glass window.

2.3.3. Launcher

To launch these types of RPAS, they need an initial boost. The most widespread way to give this momentum is by using a launching ramp. The ramp used in these tests was a Kinetic Energy Catapult Launcher manufactured by QuinetiQ© Target Systems. This launching system is elastic based and the amount of energy transmitted to the plane depends on how many dual elastic bands are used (Figure 14).

Figure 14. Detail of the QinetiQ© Energy Catapult launcher with a dummy on the ramp.

The catapult launcher was designed to launch targets at an angle of 20° and speeds in excess of 30 m/s. This may be up to 35 m/s when fitted with 10 "Y"-shaped dual powerbands and a lightweight ALO RPA. ALO launch speed is indicated by a launch speed indicator supplied with the launcher.

3. Experimental Results

The objective of this section is to check the proper operation of the adapted electric ALO. In previous works (see Annexes 2, 3, and 4), the different flight modes for this UAV were determined, as well as the energy needed for them. Table 10 shows a summary of the energy needs of each of the phases of the main flight plan that will have a cruising speed and altitude of 32 m/s and 720 m, respectively.

Table 10. Energy requirements for each phase of the main flight plan.

	V_0 (m/s)	V_f (m/s)	γ (°)	t (min)	Max Power (kW)	E (*J*)
Phase 1 of ascent	15	32	10	0,6	3.910	1047×10^5
Phase 2 of ascent	32	32	10	1.78	2.706	4843×10^5
Cruise	32	32	0	90	0.544	2927×10^6
Descent phase	32	28.5	2.54	6.75	0	0
TOTAL	-	-	-	98.89	-	3516×10^6

Phase 1 of ascent: The first phase is immediate to the launching of the aircraft from the ramp and will consist of a rectilinear ascent with constant acceleration, until reaching 32 m/s, with an angle of ascent of 10°. The height reached is around 120 m.

Phase 2 of ascent: Once reached the previous level of 120 m and the speed of 32 m/s, the ascent continues. Due to the need to stay close to the coast, it is necessary to carry out the ascent to the height of 720 m cruise flight in a small space. Therefore, an ascent will be made following a helical path.

Cruise: The phase of flight corresponding to cruise will take place at an altitude of 720 m, and at a speed of 32 m/s. With the aim of causing turns in the aircraft, both right and left, the layout of an eight-shaped circuit was chosen.

Descent phase: This last phase of the flight will consist of a gliding flight from an altitude of 720 m and a speed of 32 m/s, to a height of 200 m and an approximate speed of 25 m/s, at which time the parachute will be deployed prior to recovery.

Regarding the different phases of the flight plan described above, the experimental tests must be focused on (1) testing the capacity of the electric power supply system (battery test), (2) checking the dynamometer value and power consumption with different throttle demands (thrust test), and (3) determining the number of dual elastic bands needed to appropriately launch the RPA (launching dummy tests). Next, the experimental results obtained from each category test are presented.

3.1. Battery Tests

Extensive tests were performed to the individual battery cells and the battery pack in order to ensure its performance during a typical flight.

3.1.1. Battery Individual Cell Tests

As per the battery product specification datasheet [76], standard charge and discharge procedure were carried out to the battery individual cells to check their condition one month after delivery and to confirm the capacity stated by the manufacturer.

The battery individual cells were charged to 4.2 V with 8 A (C0.5), from constant current to constant voltage, Figures 15 and 16, interval 0 < time < 1700 s. When the SOC achieves 95%, the charge is stopped. Then they were discharged at 8 A (C0.5) until the voltage decreased up to 3.0 V. After 10 min rest, the individual cells were charged again following the standard charging procedure.

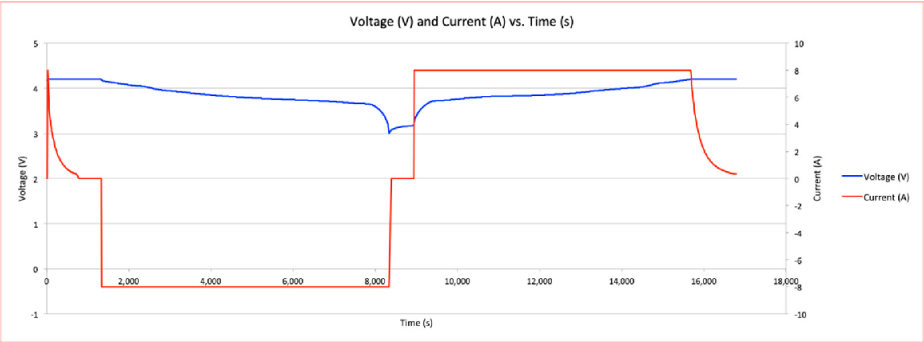

Figure 15. Battery individual cell testing: Voltage and current vs. time.

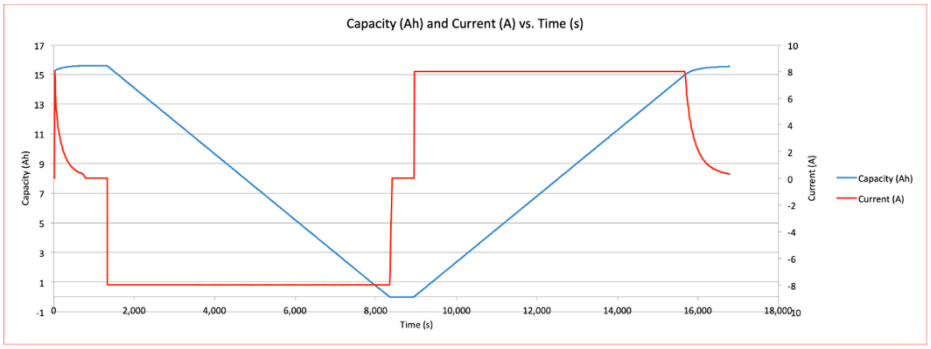

Figure 16. Battery individual cell testing: Capacity and current vs. time.

Flight Load Profile

In order to ensure the behavior of the battery individual cells during the flight, they were tested under a typical flight load profile.

This profile, as can be seen in the Figures 17 and 18, starts with 4 min demanding 4 KW, which corresponds to the launching needs and, after that, the power demand decreases to 1 KW, which is enough to ensure a stable cruise speed at 30 m/s. The experiment shown in the Figures 17 and 18 also includes a 10 min rest period after the discharge under the flight load profile and the subsequent recharging of the battery.

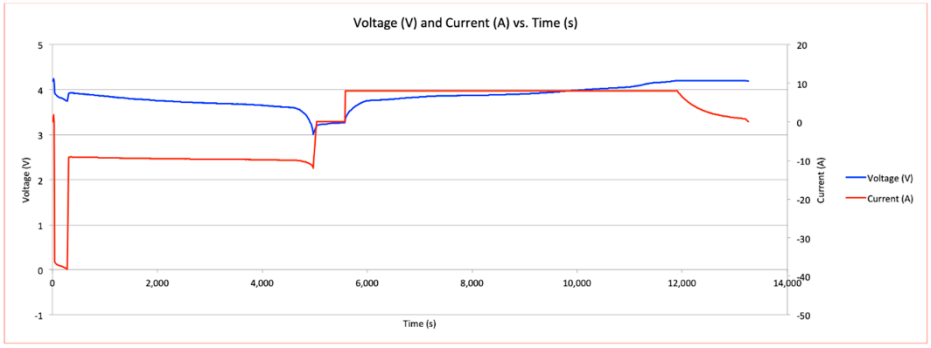

Figure 17. Battery individual cell testing under flight load profile: Voltage and current vs. time.

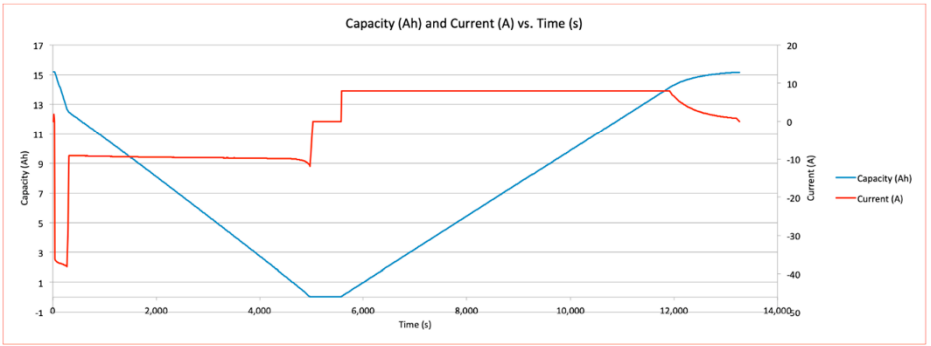

Figure 18. Battery individual cell testing under flight load profile: Capacity and current vs. time.

These power values are referred to the complete battery pack, so, in order to test the battery pack, individual cells were proportionally scaled taking into account the battery pack setup (14S2P).

The power needed in the original ALO, both during launching and cruise, is stablished regarding the total power of the motor (6.8 HP) and the percentage of throttle commanded by the pilot.

During the launching, this percentage of throttle will vary with the wind conditions but it can be considered as standard in most of the duration of the launching. The percentage of throttle in the majority of the launchings is stablished at 70% [85–87]:

$$6.8 \text{ HP} = 5070.76 \text{ W}$$

$$5070.76 \text{ W} \times 70\% = 3549.53 \text{ W}$$

The percentage of throttle needed during cruise in the original ALO will be affected by weather conditions and flight altitude, but it can be considered as standard in the major part of the typical flights. The value of throttle in the majority of cruise situations was established at 15%:

$$6.8 \text{ HP} = 5070.76 \text{ W}$$

$$5070.76 \text{ W} \times 15\% = \mathbf{760.61\ W}$$

Thus, it can be confirmed that the values of 4 and 1 kW, which were used during testing a typical flight load profile, are more demanding than during a normal flight.

3.1.2. Battery Pack Tests

The battery pack was tested under the typical flight load profile to ensure its endurance when in flight. It should be noted that this flight profile is quite demanding. The final result of flight autonomy will be greater than that obtained in this test bench because the cut-off voltage will be lowered to 42 V when real operations will take part.

Figures 19 and 20 correspond to the test performed to the battery pack under flight load profile. The first step of this profile demands 4 KW during 4 min. Figure 19 shows the voltage decrease due to the high current demand. In the second step, with a demanding power of just 1 KW, the voltage increases around 1.5 V due to the change on demanding current. Figure 20 shows the remaining capacity of the battery pack and how the capacity decreases faster in the first step of the simulation when the power demand is higher.

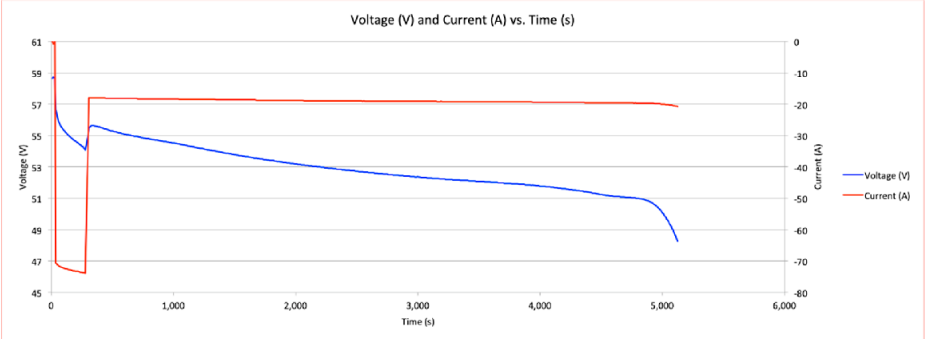

Figure 19. Battery pack test. Battery pack behavior under flight load profile.

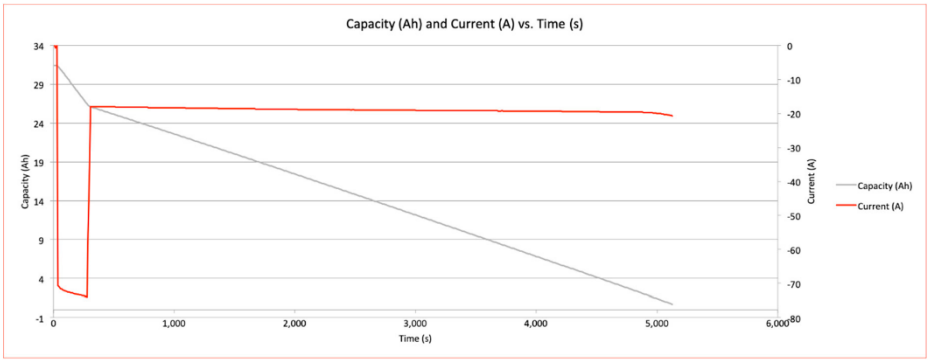

Figure 20. Battery pack test. Battery pack behavior under flight load profile.

As shown in Figure 21, the test starts at t = 0 s with 4.20 V per cell, which corresponds to a battery pack total voltage of 58.80 V (4.20 V × 14 = 58.80 V).

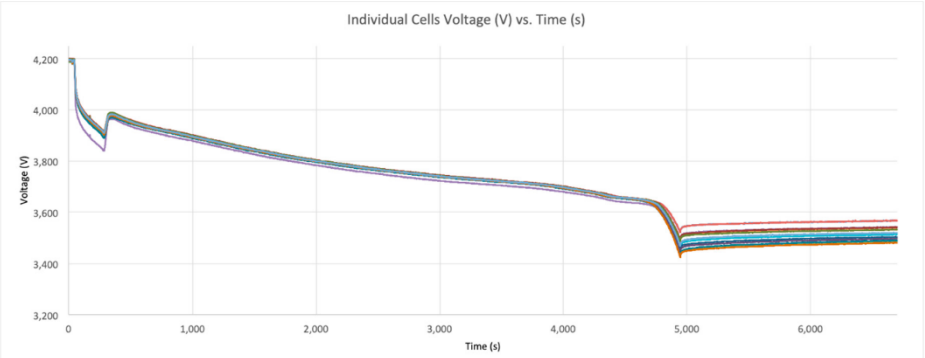

Figure 21. Battery pack test. Individual cells voltage behavior under flight load profile.

The test finishes at t = 4900 s with 3.42 V per cell, which corresponds to a battery pack total voltage of 47.88 V (3.42 V × 14 = 47.88 V).

This test results in an estimated autonomy of around 90 min (4900 s/60 s = 81.6 min).

The battery cells cut-off voltage was stablished in 3.42 V to avoid unnecessary degradation of cells during the different endurance tests.

This cut-off voltage will be lowered to 3.00 V [76] when real operations will take part.

Taking into account this lowered cut-off voltage level, it can be assumed that the total estimated autonomy will overcome the 90 min goal, achieving the total time of 5500 s (5500 s/60 s = 91.66 min).

3.2. Thrust Tests

The main objective of the thrust test consists of checking the dynamometer value and power consumption with different throttle demands that will be used in a typical flight mission, while the ALO is installed in the thrust test bench.

When available power, P_A, and power required, $P_{R\ cruisser}$, are equal to each altitude, h, the maximum and minimum speeds of the system were obtained under these conditions. Figure 22 (from Annex 3) shows available power and required power for each flight altitude.

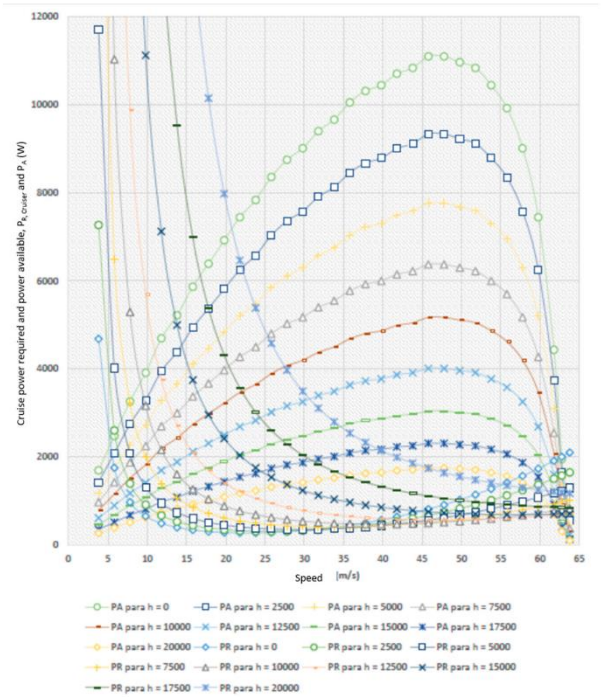

Figure 22. Available power and required power for each flight altitude. Where P_A is power available (W) and h is altitude (m).

Experimental results of the electric ALO thrust test are presented in Figure 23. Thrust and power consumption increase with motor input. The launching could be performed at 60% of engine input, with a power consumption of around 4.5 KW and a thrust of 12 kg. In order to maintain cruise speed when the RPA reaches its objective altitude, a very low thrust is needed and less than 35% of motor input is enough.

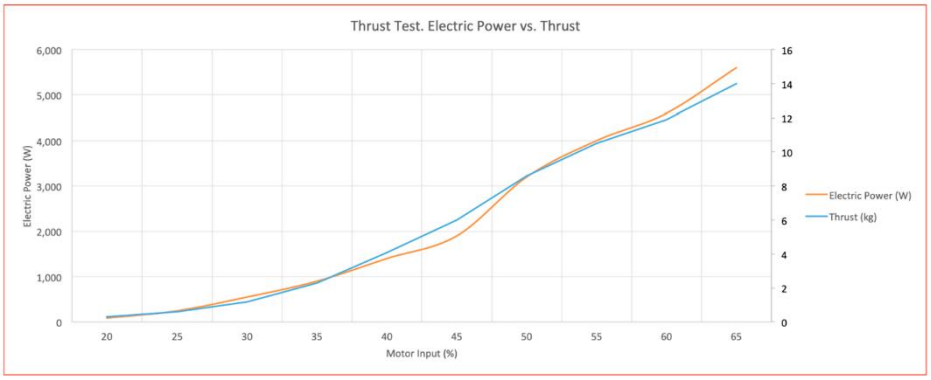

Figure 23. Electric ALO thrust test. Electric power vs. thrust.

Figure 24 shows a thrust comparison between the Electric ALO and ICE configuration. Thrust results confirm that both configurations reach around 12 kg thrust at 60% motor input, which would be enough for the launching needs.

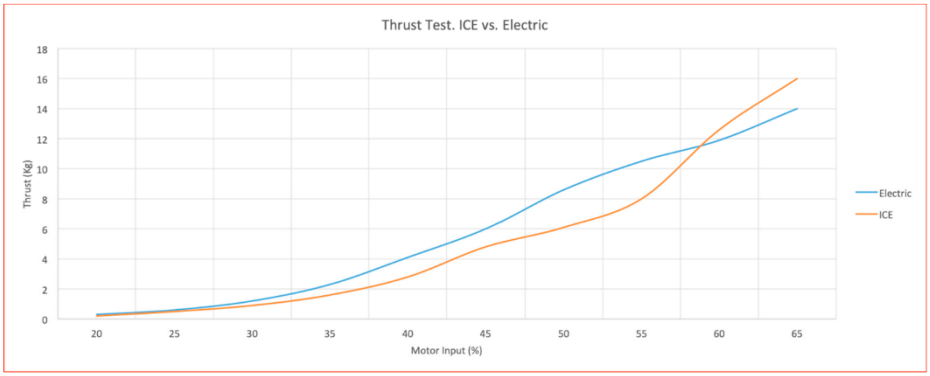

Figure 24. ALO thrust tests: ICE vs. electric configurations.

Since the modifications performed in the original ALO do not affect the weights nor the surfaces, the flight envelope for both configurations are the same. With this static thrust test, it can be assumed that the performance of the modified ALO will be the same when in flight.

3.3. Launching Dummy Tests

In order to test the QuinetiQ© Energy Catapult Launcher with the increased weight of the new electric ALO, a launch test was performed. To make the tests, a dummy was built with the same weight of the new electric ALO, Figure 14.

The experiment performed consists of determining the number of dual elastic bands needed to appropriately launch the RPA. The electric ALO needs to reach a speed of at least 32 m/s to take-off (phase 1 of ascent). In order to check different situations, five launchings were performed with different numbers of dual elastic bands and measuring the speed at the end of the launcher in each case. As shown in Figure 25, minimum take-off speed can be ensured using at least 10 elastic bands.

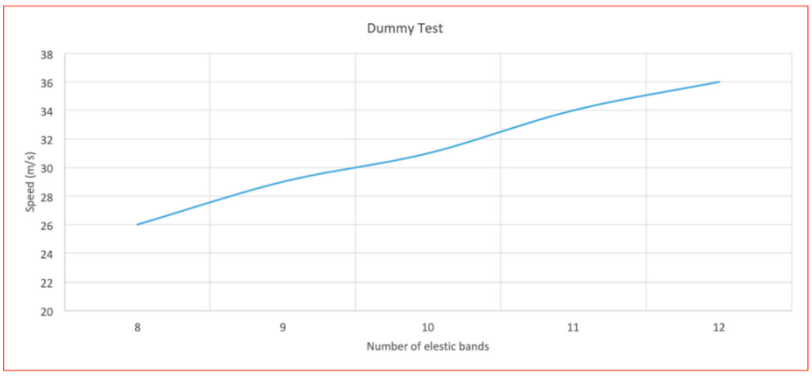

Figure 25. Dummy launching speed test.

In addition, it was found that it is not necessary to count on the old launcher. This QuinetiQ© Energy Catapult Launcher perfectly fulfills that function.

4. Discussion

The tests carried out in the test bench, with the energy storage system (batteries) in the flight regime, indicate that the expected autonomy of this electric unmanned airplane will exceed 90 min of

flight (Figures 19–21). This represents 50% more flight autonomy than in its original configuration with the internal combustion engine fueled with gasoline. It should be noted that the flight autonomy tests, to which the electric RPAS was subjected, were based on a very demanding flight profile, so that the final autonomy achieved will surely be greater than the one described. As can be seen from Table 10, the batteries do not consume all the stored energy, calculated in 6156×10^6 J(3), in fact it is far from this situation, presenting a surplus of energy of $\Delta E = 2{,}64 \times 10^6\ J$ so it could still be increased even more flight autonomy in cruise mode.

$$E_{e,batteries} = 200\frac{Wh}{kg};\ m_{\text{batteries}} = 8.55\ \text{kg};\ E_{\text{t, batteries}} = 6156 \times 10^6\ \text{J} \quad (3)$$

Table 11 reflects the main differences between the two versions of the RPA, the internal combustion engine and the electric, in terms of weight, maximum payload, flight autonomy, emissions and maintenance needs. Figure 26 offers an idea of the comparison of sizes between the new components and the old ones.

Table 11. ICE ALO vs. electric ALO main features.

	ICE ALO	Electric ALO
Fuselage	3.50 kg	3.50 kg
Motor	3.50 kg	1.90 kg
Propeller	0.35 kg	0.40 kg
FCS (flight control system)	0.85 kg	0.31 kg
Telemetry Module	0.70 kg	0.20 kg
Harnesses	0.15 kg	0.35 kg
Fuel Tanks + Fuel	6.35 kg	-
Fuel Supply System	0.27 kg	-
ESC + Mounting	-	2.39 kg
Main Battery	-	8.47 kg
BMS + Battery Case	-	0.95 kg
FCS Auxiliary Battery	1.76 kg	1.37 kg
Weight Without Payload	17.43 kg	19.84 kg
Max. Payload	7.57 kg	5.16 kg
Endurance	60 min	90 min
Emissions	CO_2 + CO + NO_X	Zero
Maintenance Schedule	Every flight	Every 20 flight hours

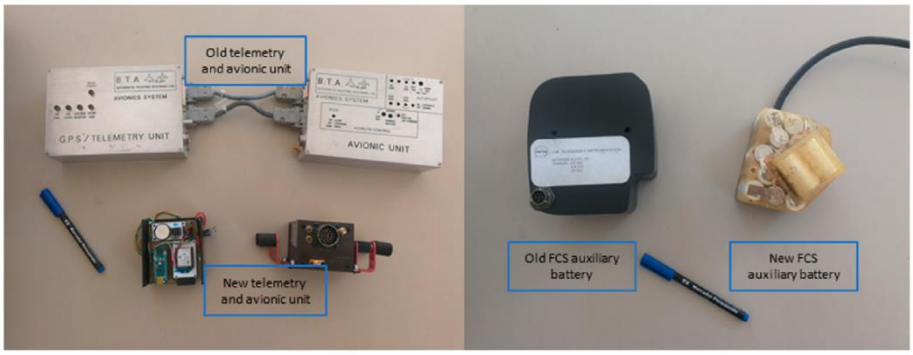

(a) **(b)**

Figure 26. Comparison between: (**a**) old systems used as telemetry and fly control systems and new ones and (**b**) new and old batteries necessary to feed the FCS.

Concerning the electricity to recharge the RPAS, INTA has been producing electricity in a renewable way since the 1990s. This comes from several photovoltaic fields of different technologies as well as from a wind turbine. All these renewable energy sources are integrated in a microgrid that can also store excess energy in different types of batteries and in the form of hydrogen [88]. This is the reason why the electric RPAS is considered a zero-emission device; in this case, generation of electric energy does not involve fuel-consuming techniques.

The behavior of the electric engine during the performed thrust tests has been as expected (Figures 22 and 23).

On the other hand, the performed launching dummy tests indicate that the new ALO unmanned aerial vehicle can be launched with the same systems as other RPAS without the need to modify the launcher ramps, which represents an advantage in logistics within the testing center (Figure 14).

Figure 27 represents the electric RPA ready to fly.

Figure 27. Electric ALO unmanned aerial vehicle ready to fly.

5. Conclusions and Future Works

This paper presents a real and practical case of a transformation of a fixed-wing unmanned aerial system, used as an aerial target and powered by an internal combustion engine, in an electric RPA for use in the cultivation of olive trees and other species that occupy large areas of land. Similarly, and taking advantage of one of the main characteristics of electric airplanes, such as its low-noise level, this electric RPA could be used in protected environments, such as natural parks, for the surveillance and supervision of different animal species.

The main reason for carrying out this transformation is to increase the flight autonomy of the RPA in order to be able to take measurements of the different parameters that affect a large-scale crop. This purpose was achieved by increasing the range by almost 50% compared with the ICE model, and much more if it is compared with the electric multicopters actually used in the project TecnOlivo. The payload was reduced but the increase in flight autonomy compensates this decrease. If compared with other commercial electric fixed-wing UAVs (Table 12), it can be realized that new features of the electric ALO can be compared with them, even improving them in most of the cases.

On the other hand, the present work is an intermediate step to complete an RPA that is moved with hydrogen. Future works on this aerial platform will consist of replacing some of the batteries on board with a hydrogen-based system and fuel cells. In this way it is intended to further increase the autonomy of the UAV [89,90]. The INTA laboratory has vast experience (since 1990) in hydrogen technology and fuel cells and this is not the first RPAS built at INTA based on hydrogen and fuel cells [91]. Thu, in the following months, a new RPA with hydrogen on board will be flying across the sky.

Table 12. Comparison of some commercial fixed-wing UAVs with the electric ALO.

Model	Max. Payload (kg)	MTOW (kg)	Autonomy (min)
Fulmar X	8.0	19	400
FV1-ATyges	2.0	4.2	180
Electric ALO	5.1	25	90
WingtraOne	0.8	4.5	55
Firebird FPV	0.1	1.2	30
DV Wing	0.1	0.94	85
Lancaster 5	1.0	2.4	45
Fulmar X	8.0	19	400

Author Contributions: Conceptualization, F.I.L., Á.F.B. and J.A.B.; Methodology, F.I.L., F.S. and J.M.A.; Software, Á.F.B. and J.A.B; Validation, F.I.L., Á.F.B. and J.A.B.; Formal Analysis, F.I.L., Á.F.B. and J.A.B.; Investigation, F.I.L., Á.F.B. and J.A.B.; Resources, F.I.L., Á.F.B., J.A.B., F.S. and J.M.A.; Data Curation, Á.F.B. and J.A.B.; Writing – Original Draft Preparation, F.I.L.; Writing – Review & Editing, all; Visualization, F.I.L.; Supervision, F.S. and J.M.A.; Project Administration, F.I.L.; Funding Acquisition, F.I.L. All authors have read and agreed to the published version of the manuscript.

Funding: Part of this work was supported by "Tecnologías para el manejo y supervisión del cultivo del olivo (Tecnolivo)", a project of the program Interreg V-A España-Portugal (POCTEP 2014-2020) and was co-funded by FEDER (0115_TECNOLIVO_6_E).

Acknowledgments: The authors would like to thank Manuel Gil for his helpful advice in various technical issues regarding the testing platform.

Conflicts of Interest: The authors declare no conflicts of interest.

List of Acronyms

BMS	Battery management system
CAN	Controller area network
ESC	Electronic speed controller
DSM	Digital surface models
FCS	Flight control system
FLIR	Forward-looking infrared
GCS	Ground control station
HP	Horse power
ICE	Internal combustion engine
IGBT	Insulated gate bipolar transistor
LiPo	lithium-ion polymer
MOSFET	Metal-oxide-semiconductor field-effect transistor
NIR	Near infrared
NGFCS	Navigation guidance and flight control systems
NTC	Negative temperature coefficient
PWM	pulse-width modulation
RGB	Read green blue
RPA	Remotely piloted aircraft
RPAS	Remotely piloted aircraft system
Rpm	Revolutions per minute
SOC	State of charge
UART	Universal asynchronous receiver-transmitter
UAS	Unmanned aerial system
UAV	Unmanned aerial vehicles

References

1. Granshaw, S.I. RPV, UAV, UAS, RPAS . . . or just drone? *Photogramm. Rec.* **2018**, *33*, 160–170. [CrossRef]

2. Chiesa, S.; Fioriti, M.; Fusaro, R. MALE UAV and its systems as basis of future definitions. *Aircr. Eng. Aerosp. Technol.* **2016**, *88*, 771–782. [CrossRef]
3. Valavanis, K.P.; Vachtsevanos, G.J. *Handbook of Unmanned Aerial Vehicles*; Springer Reference: New York, NY, USA, 2015; ISBN 9789048197071.
4. Puri, V.; Nayyar, A.; Raja, L. Agriculture drones: A modern breakthrough in precision agriculture. *J. Stat. Manag. Syst.* **2017**, *20*, 507–518. [CrossRef]
5. Shi, Y.; Thomasson, J.A.; Murray, S.C.; Pugh, N.A.; Rooney, W.L.; Shafian, S.; Rajan, N.; Rouze, G.; Morgan, C.L.S.; Neely, H.L.; et al. Unmanned Aerial Vehicles for High-Throughput Phenotyping and Agronomic Research. *PLoS ONE* **2016**, *11*, e0159781. [CrossRef]
6. Honkavaara, E.; Saari, H.; Kaivosoja, J.; Pölönen, I.; Hakala, T.; Litkey, P.; Mäkynen, J.; Pesonen, L. Processing and Assessment of Spectrometric, Stereoscopic Imagery Collected Using a Lightweight UAV Spectral Camera for Precision Agriculture. *Remote Sens.* **2013**, *5*, 5006–5039. [CrossRef]
7. Candiago, S.; Remondino, F.; De Giglio, M.; Dubbini, M.; Gattelli, M. Evaluating Multispectral Images and Vegetation Indices for Precision Farming Applications from UAV Images. *Remote Sens.* **2015**, *7*, 4026–4047. [CrossRef]
8. Csillik, O.; Cherbini, J.; Johnson, R.; Lyons, A.; Kelly, M. Identification of Citrus Trees from Unmanned Aerial Vehicle Imagery Using Convolutional Neural Networks. *Drones* **2018**, *2*, 39. [CrossRef]
9. Cano, E.; Horton, R.; Liljegren, C.; Bulanon, D. Comparison of Small Unmanned Aerial Vehicles Performance Using Image Processing. *J. Imaging* **2017**, *3*, 4. [CrossRef]
10. Adão, T.; Hruška, J.; Pádua, L.; Bessa, J.; Peres, E.; Morais, R.; Sousa, J. Hyperspectral Imaging: A Review on UAV-Based Sensors, Data Processing and Applications for Agriculture and Forestry. *Remote Sens.* **2017**, *9*, 1110. [CrossRef]
11. Matese, A.; Di Gennaro, S. Practical Applications of a Multisensor UAV Platform Based on Multispectral, Thermal and RGB High Resolution Images in Precision Viticulture. *Agriculture* **2018**, *8*, 116. [CrossRef]
12. de Castro, A.; Jiménez-Brenes, F.; Torres-Sánchez, J.; Peña, J.; Borra-Serrano, I.; López-Granados, F. 3-D Characterization of Vineyards Using a Novel UAV Imagery-Based OBIA Procedure for Precision Viticulture Applications. *Remote Sens.* **2018**, *10*, 584. [CrossRef]
13. Gnädinger, F.; Schmidhalter, U. Digital Counts of Maize Plants by Unmanned Aerial Vehicles (UAVs). *Remote Sens.* **2017**, *9*, 544. [CrossRef]
14. Du, M.; Noguchi, N. Monitoring of Wheat Growth Status and Mapping of Wheat Yield's within-Field Spatial Variations Using Color Images Acquired from UAV-camera System. *Remote Sens.* **2017**, *9*, 289. [CrossRef]
15. Yue, J.; Yang, G.; Li, C.; Li, Z.; Wang, Y.; Feng, H.; Xu, B. Estimation of Winter Wheat Above-Ground Biomass Using Unmanned Aerial Vehicle-Based Snapshot Hyperspectral Sensor and Crop Height Improved Models. *Remote Sens.* **2017**, *9*, 708. [CrossRef]
16. González-Jorge, H.; Martínez-Sánchez, J.; Bueno, M.; Pedor Arias, A. Unmanned Aerial Systems for Civil Applications: A Review. *Drones* **2017**, *1*, 2. [CrossRef]
17. Wan, L.; Li, Y.; Cen, H.; Zhu, J.; Yin, W.; Wu, W.; Zhu, H.; Sun, D.; Zhou, W.; He, Y. Combining UAV-Based Vegetation Indices and Image Classification to Estimate Flower Number in Oilseed Rape. *Remote Sens.* **2018**, *10*, 1484. [CrossRef]
18. Acorsi, M.G.; das Dores Abati Miranda, F.; Martello, M.; Smaniotto, D.A.; Sartor, L.R. Estimating Biomass of Black Oat Using UAV-Based RGB Imaging. *Agronomy* **2019**, *9*, 344. [CrossRef]
19. Vanegas, F.; Bratanov, D.; Powell, K.; Weiss, J.; Gonzalez, F. A Novel Methodology for Improving Plant Pest Surveillance in Vineyards and Crops Using UAV-Based Hyperspectral and Spatial Data. *Sensors* **2018**, *18*, 260. [CrossRef]
20. Wu, D.; Sun, D.W. Advanced applications of hyperspectral imaging technology for food quality and safety analysis and assessment: A review—Part I: Fundamentals. *Innov. Food Sci. Emerg. Technol.* **2013**, *19*, 1–14. [CrossRef]
21. Boreman, G.D. Classification of imaging spectrometers for remote sensing applications. *Opt. Eng.* **2005**, *44*, 013602. [CrossRef]
22. Mogili, U.R.; Deepak, B.B.V.L. Review on Application of Drone Systems in Precision Agriculture. *Procedia Comput. Sci.* **2018**, *133*, 502–509. [CrossRef]

23. Herwitz, S.R.; Johnson, L.F.; Dunagan, S.E.; Higgins, R.G.; Sullivan, D.V.; Zheng, J.; Lobitz, B.M.; Leung, J.G.; Gallmeyer, B.A.; Aoyagi, M.; et al. Imaging from an unmanned aerial vehicle: Agricultural surveillance and decision support. *Comput. Electron. Agric.* **2004**, *44*, 49–61. [CrossRef]
24. Maurya, P. Hardware Implementation of a Flight Control System for an Unmanned Aerial Vehicle. *Comput. Sci. Eng.* **2015**. Available online: http://www.cse.iitk.ac.in/users/moona/students/Y2258.pdf (accessed on 8 January 2020).
25. Herwitz, S.R.; Johnson, L.F.; Arvesen, J.C.; Higgins, R.G.; Leung, J.G.; Dunagan, S.E. Precision agriculture as a commercial application for solar-powered unmanned aerial vehicles. In Proceedings of the 1st UAV Conference, Portsmouth, VA, USA, 20–23 May 2002.
26. Pederi, Y.A.; Cheporniuk, H.S. Unmanned Aerial Vehicles and new technological methods of monitoring and crop protection in precision agriculture. In Proceedings of the 2015 IEEE 3rd International Conference Actual Problems of Unmanned Aerial Vehicles Developments, APUAVD 2015—Proceedings, Kyiv, Ukraine, 13–15 October 2015; pp. 298–301.
27. Huang, Y.; Thomson, S.J.; Hoffmann, W.C.; Lan, Y.; Fritz, B.K. Development and prospect of unmanned aerial vehicle technologies for agricultural production management. *Int. J. Agric. Biol. Eng.* **2013**, *6*, 1–10.
28. Guidetti, R.; Bodria, L.; Best, S.; Giles, D.K.; Billing, R.C. Deployment and Performance of a UAV for Crop Spraying. In *Chemical Engineering Transactions*; A publication of AIDIC (The Italian association of chemical engineering): Milano, Italy, 2015; Volume 44.
29. Xue, X.; Lan, Y.; Sun, Z.; Chang, C.; Hoffmann, W.C. Develop an unmanned aerial vehicle based automatic aerial spraying system. *Comput. Electron. Agric.* **2016**, *128*, 58–66. [CrossRef]
30. Shilin, W.; Jianli, S.; Xiongkui, H.; Le, S.; Xiaonan, W.; Changling, W.; Zhichong, W.; Yun, L. Performances evaluation of four typical unmanned aerial vehicles used for pesticide application in China. *Int. J. Agric. Biol. Eng.* **2017**, *10*, 22–31. [CrossRef]
31. Qin, W.; Xue, X.; Zhang, S.; Gu, W.; Wang, B. Droplet deposition and efficiency of fungicides sprayed with small UAV against wheat powdery mildew. *Int. J. Agric. Biol. Eng.* **2018**, *11*, 27–32. [CrossRef]
32. Spoorthi, S.; Shadaksharappa, B.; Suraj, S.; Manasa, V.K. Freyr drone: Pesticide/fertilizers spraying drone—An agricultural approach. In Proceedings of the 2nd International Conference on Computing and Communications Technologies, Maharashtra, India, 15–16 December 2017; pp. 252–255.
33. Kabra, T.S.; Kardile, A.V.; BMane, D.; Bhosale, P.R.; Belekar, A.M. Design, Development & Optimization of a Quad-Copter for Agricultural Applications. *Int. Res. J. Eng. Technol.* **2017**, *4*.
34. Meivel, S.M.; Professor, A.; Maguteeswaran, R.; Gandhiraj, N.B.; Srinivasan, G. Quadcopter UAV Based Fertilizer and Pesticide Spraying System. *Int. Acad. Res. J. Eng. Sci.* **2016**, *1*, 8–12.
35. Sohail, S.; Nasim, S.; Khan, N.H. Modeling, controlling and stability of UAV Quad Copter. In Proceedings of the ICIEECT 2017—International Conference on Innovations in Electrical Engineering and Computational Technologies 2017, Karachi, Pakistan, 5–7 April 2017.
36. Qasim, M.; Susanto, E.; Wibowo, A.S. PID control for attitude stabilization of an unmanned aerial vehicle quad-copter. In Proceedings of the 2017 5th International Conference on Instrumentation, Control, and Automation, Yogyakarta, Indonesia, 9–11 August 2017; pp. 109–114.
37. Yallappa, D.; Veerangouda, M.; Maski, D.; Palled, V.; Bheemanna, M. Development and evaluation of drone mounted sprayer for pesticide applications to crops. In Proceedings of the GHTC 2017—IEEE Global Humanitarian Technology Conference, San Jose, CA, USA, 19–22 October 2017; pp. 1–7.
38. Sarghini, F.; De Vivo, A. Interference analysis of an heavy lift multirotor drone flow field and transported spraying system. *Chem. Eng. Trans.* **2017**, *58*, 631–636.
39. Berner, B.; Chojnacki, J. Use of Drones in Crop Protection. In Proceedings of the Uniwersytet Przyrodniczy w Lublinie; IX International Scientific Symposium "Farm Machinery and Processes Management in Sustainable Agriculture", Lublin, Poland, 22–24 November 2017; pp. 46–51.
40. Zhang, Y.L.; Lian, Q.; Zhang, W. Design and test of a six-rotor unmanned aerial vehicle (UAV) electrostatic spraying system for crop protection. *Int. J. Agric. Biol. Eng.* **2017**, *10*, 68–76.
41. Sarghini, F.; De Vivo, A. Analysis of preliminary design requirements of a heavy lift multirotor drone for agricultural use. *Chem. Eng. Trans.* **2017**, *58*, 625–630.
42. Bendig, J.; Bolten, A.; Bareth, G. Introducing A Low-Cost Mini-Uav for Thermal- and Multispectral-Imaging. *ISPRS-Int. Arch. Photogramm. Remote Sens. Spat. Inf. Sci.* **2012**, *XXXIX-B1*, 345–349. [CrossRef]

43. Tang, Q.; Zhang, R.R.; Chen, L.P.; Xu, M.; Yi, T.C.; Zhang, B. Droplets movement and deposition of an eight-rotor agricultural UAV in downwash flow field. *Int. J. Agric. Biol. Eng.* **2017**, *10*, 47–56.
44. Shah, S.S.H. Development of UAV Octocopter Based on Pesticides Spraying System. *Univ. Wah J. Sci. Technol.* **2018**, *2*, 13–17.
45. Yemle, S.; Durgude, Y.; Kondhalkar, G.; Pol, K. Design & Analysis of Multi-Frame for Octo & Quad Copter Drones. *Int. Res. J. Eng. Technol.(IRJET)* **2019**, *6*.
46. Flethes, S.G.; Suárez, A.; Carlos, G.; Placer, C. Cálculo y selección de sistema de propulsión para mini UAV de apoyo a pequeñas unidades de Infantería de Marina. Available online: http://calderon.cud.uvigo.es/xmlui/handle/123456789/50 (accessed on 8 January 2020).
47. Iqbal, U.; Irtiza, S.; Shah, A.; Jamil, M.; Gillani, S.O.; Ayaz, Y. Selection Of Unmanned Aerial System (Uas) For Disaster Relief Operations: A Comparison. *Sci. Int.* **2015**, *27*, 3199–3203.
48. Skrzypietz, T. *Unmanned Aircraft Systems for Civilian Missions*; Brandenburgisches Institut für Gesellschaft und Sicherheit (BIGS): Potsdam, Germany, 2012.
49. Jaeger, M.; Adair, D. Conceptual design of a high-endurance hybrid electric unmanned aerial vehicle. *Mater. Today Proc.* **2017**, *4*, 4458–4468. [CrossRef]
50. Glassock, R.R.; Hung, J.Y.; Gonzalez, L.F.; Walker, R.A. Multimodal hybrid powerplant for unmanned aerial systems (UAS) Robotics. In Proceedings of the Twenty-Fourth Bristol International Unmanned Air Vehicle Systems Conference, Bristol, UK, 30 March–1 April 2009.
51. Hassanalian, M.; Radmanesh, M.; Sedaghat, A. Increasing flight endurance of MAVs using multiple quantum well solar cells. *Int. J. Aeronaut. Space Sci.* **2014**, *15*, 212–217. [CrossRef]
52. Swieringa, K.A.; Hanson, C.B.; Richardson, J.R.; White, J.D.; Hasan, Z.; Qian, E.; Girard, A. Autonomous battery swapping system for small-scale helicopters. In Proceedings of the IEEE International Conference on Robotics and Automation, Anchorage, Alaska, 3–8 May 2010; pp. 3335–3340.
53. Achtelik, M.C.; Stumpf, J.; Gurdan, D.; Doth, K.-M. Design of a flexible high performance quadcopter platform breaking the MAV endurance record with laser power beaming. In Proceedings of the 2011 IEEE/RSJ International Conference on Intelligent Robots and Systems, San Francisco, CA, USA, 25–30 September 2011; pp. 5166–5172.
54. Muttin, F. Umbilical deployment modeling for tethered UAV detecting oil pollution from ship. *Appl. Ocean Res.* **2011**, *33*, 332–343. [CrossRef]
55. José Caparrós Mancera, J.; José Vivas Fernández, F.; Manuel Andujar Marquez, J. Optimized Balance of Plant for a medium-size PEM electrolyzer. Design, Modelling and Control. In Proceedings of the EUROSIM 2019 Abstract Volume, 10th EUROSIM Congress, La Rioja, Logroño, Spain, 1–5 July 2019. [CrossRef]
56. Rajendran, P.; Smith, H. Review of Solar and Battery Power System Development for Solar-Powered Electric Unmanned Aerial Vehicles. *Adv. Mater. Res.* **2015**, *1125*, 641–647. [CrossRef]
57. Shiau, J.K.; Ma, D.M.; Yang, P.Y.; Wang, G.F.; Gong, J.H. Design of a solar power management system for an experimental UAV. *IEEE Trans. Aerosp. Electron. Syst.* **2009**, *45*, 1350. [CrossRef]
58. Brelje, B.J.; Martins, J.R.R.A. Electric, hybrid, and turboelectric fixed-wing aircraft: A review of concepts, models, and design approaches. *Prog. Aerosp. Sci.* **2019**, *104*, 1–19. [CrossRef]
59. Donateo, T.; Lucia De Pascalis, C.; Ficarella, A. Synergy Effects in Electric and Hybrid Electric Aircraft. *Aerospace* **2019**, *6*, 32. [CrossRef]
60. Lei, T.; Yang, Z.; Lin, Z.; Zhang, X. State of art on energy management strategy for hybrid-powered unmanned aerial vehicle. *Chin. J. Aeronaut.* **2019**, *32*, 1488–1503. [CrossRef]
61. Boukoberine, M.N.; Zhou, Z.; Benbouzid, M. A critical review on unmanned aerial vehicles power supply and energy management: Solutions, strategies, and prospects. *Appl. Energy* **2019**, *255*, 113823. [CrossRef]
62. Dutczak, J. Liquefied and chemical hydrogen storage in contemporary small drones' fuel cell propulsion systems. In Proceedings of the IOP Conference Series: Materials Science and Engineering, Nanjing, China, 17–19 August 2018; Volume 421.
63. Herrera, G.J.; Dechant, J.A.; Green, E.K. *Technology Trends in Small Unmanned Aircraft Systems (sUAS) and Counter-UAS: A Five-Year Outlook*; Institute for Defense Analyses Alexandria: Alexandria, VA, USA, 2017.
64. Babayomi, O.O.; Makarfi, A.U. Energy Efficiency in Unmanned Aircraft Systems: A Review. In Proceedings of the 2019 IEEE PES/IAS PowerAfrica, Abuja, Nigeria, 20–23 August 2019; pp. 569–574.
65. Gramatikov, P. *Electric Motor-Generators for Unmanned Aerial Vehicles*; Bulgarian Academy of Sciences. Space Research and Technology Institute: Sofia, Bulgaria, 2017; Volume 29.

66. Griffis, C.; Wilson, T.; Schneider, J.; Pierpont, P. *Unmanned Aircraft System Propulsion Systems Technology Survey*; Air Traffic Organization. NextGen & Operations Planning Office of Research and Technology Development: Washington, DC, USA. Available online: https://commons.erau.edu/publication/72.DOT/FAA/AR-09/11 (accessed on 8 January 2020).
67. Tecnolivo–Programa INTERREG V-A España-Portugal (POCTEP 2014–2020). Available online: https://www.tecnolivo.eu/en/ (accessed on 2 January 2020).
68. Isorna, F.; Fernandez Barranco, A.; Bogeat, J.A.; Segura, F.; Andujar, J.M. (PDF) Use of unmanned fuel cell ground vehicles (UGVs) for precision agricul-ture (TecnOlivo Project). In Proceedings of theVII Symposium on Hydrogen, Fuel Cells and Advanced Batteries (HYCELTEC 2019), Barcelona, España, 1–3 July 2019. Available online: https://www.researchgate.net/publication/335060764_Use_of_unmanned_fuel_cell_ground_vehicles_UGVs_for_precision_agricul-_ture_TecnOlivo_Project (accessed on 25 January 2020).
69. Ponce, J.M.; Aquino, A.; Millan, B.; Andujar, J.M. Automatic Counting and Individual Size and Mass Estimation of Olive-Fruits Through Computer Vision Techniques. *IEEE Access* **2019**, *7*, 59451–59465. [CrossRef]
70. Ponce, J.M.; Aquino, A.; Andujar, J.M. Olive-Fruit Variety Classification by Means of Image Processing and Convolutional Neural Networks. *IEEE Access* **2019**, *7*, 147629–147641. [CrossRef]
71. Adamski, M. Analysis of propulsion systems of unmanned aerial vehicles. *J. Mar. Eng. Technol.* **2018**, *16*, 291–297. [CrossRef]
72. Gabriel, D.L.; Meyer, J.; Du Plessis, F. Brushless DC motor characterisation and selection for a fixed wing UAV. In Proceedings of the IEEE AFRICON Conference, Livingstone, Zambia, 13–15 September 2011.
73. Hughes, A.; Drury, B. *Electric Motors and Drives: Fundamentals, Types and Applications*; Newnes: Waltham, MA, USA; ISBN 978-0-08-098332-5.
74. MGM COMPRO, Ing. G. Dvorský. HBC - SERIES V7 Programmable brushless controllers for industry using Operating Manual – firmware version 3.8 or higher. Republic, C. Hsbc - Series V7. 1–54. Available online: www.mgm-compro.com (accessed on 8 January 2020).
75. Farmann, A.; Waag, W.; Marongiu, A.; Sauer, D.U. Critical review of on-board capacity estimation techniques for lithium-ion batteries in electric and hybrid electric vehicles. *J. Power Sources* **2015**, *281*, 114–130. [CrossRef]
76. Yanping, Z.; Zhenguo, Y. *Model No: glpa875170 16000 15c 3.7v*; SHENZHEN GREPOW BATTERY CO., LTD: Shenzhen, China, 2013. Available online: http:www.grepow.com (accessed on 8 January 2020).
77. Traub, L.W. Range and endurance estimates for battery-powered aircraft. *J. Aircr.* **2011**, *48*, 703–707. [CrossRef]
78. Avanzini, G.; Giulietti, F. Maximum range for battery-powered aircraft. *J. Aircr.* **2013**, *50*, 304–307. [CrossRef]
79. Tu, W.; Bai, Z.; Deng, Z.; Zhang, H.; Tang, H. In-situ synthesized Si@C materials for the lithium ion battery: A mini review. *Nanomaterials* **2019**, *9*, 432. [CrossRef] [PubMed]
80. Levchenko, I.; Bazaka, K.; Belmonte, T.; Keidar, M.; Xu, S. Advanced Materials for Next-Generation Spacecraft. *Adv. Mater.* **2018**, *9*, 432. [CrossRef] [PubMed]
81. Mauger, A.; Julien, C.M. Nanoscience supporting the research on the negative electrodes of Li-ion batteries. *Nanomaterials* **2015**, *5*, 2279–2301. [CrossRef] [PubMed]
82. Energus Power Solutions Ltd. Tiny BMS User Manual. 30 July 2018, pp. 1–148. Available online: https://www.energusps.com/ (accessed on 8 January 2020).
83. Arbin. *BT-ML*; Arbin Instrument: College Station, TX, USA, December 2015.
84. Arbin. *Arbin Instruments User's Manual*; Arbin Instrument: College Station, TX, USA, 2013.
85. Chung, P.H.; Ma, D.M.; Shiau, J.K. Design, manufacturing, and flight testing of an experimental flying wing UAV. *Appl. Sci.* **2019**, *9*, 3043. [CrossRef]
86. Zhai, R.; Zhou, Z.; Zhang, W.; Sang, S.; Li, P. Control and navigation system for a fixed-wing unmanned aerial vehicle. *AIP Adv.* **2014**, *4*. [CrossRef]
87. Grant, P.R. *AER1216: Fundamentals of UAVs performance*; (CARRE) Centre for aerial robotics research and education, NSERC, CRSNG: Canada, 2016.
88. Lopez, E.; Monteiro, J.; Carrasco, P.; Saenz, J.; Pinto, N.; Blazquez, G. Development, implementation and evaluation of a wireless sensor network and a web-based platform for the monitoring and management of a microgrid with renewable energy sources. In Proceedings of the SEST 2019—2nd International Conference on Smart Energy Systems and Technologies, Porto, Portugal, 9–11 September 2019.

89. Bradley, T.H.; Moffitt, B.A.; Fuller, T.F.; Mavris, D.N.; Parekh, D.E. Comparison of design methods for fuel-cell-powered unmanned aerial vehicles. *J. Aircr.* **2012**, *46*, 1945–1956. [CrossRef]
90. Bradley, T.H.; Moffitt, B.A.; Thomas, R.W.; Mavris, D.; Parekh, D.E. *Test Results for a Fuel Cell-Powered Demonstration Aircraft*; SAE Technical Papers; SAE International: Warrendale, TX, USA, 2006.
91. Chacón, E.; Martínez, G.; Anchuelo, C.; Cuevas, R.; Chacón, E.; Martínez, G.; Anchuelo, C.; Cuevas, R. Unmanned Aerial Vehicle Driven by Fuel Cell Technology, AVIZOR. In *Proceedings of the 18th World Hydrogen Energy Conference 2010 - WHEC 2010*; Forschungszentrum Jülich GmbH, Zentralbibliothek Verlag: Jülich, Germany, 2010; Volume 78, ISBN 978-3-89336-655-2.

© 2020 by the authors. Licensee MDPI, Basel, Switzerland. This article is an open access article distributed under the terms and conditions of the Creative Commons Attribution (CC BY) license (http://creativecommons.org/licenses/by/4.0/).

4.3. Artículo 3

Hydrogen vs battery-based propulsion systems in unipersonal vehicles. Developing solutions to improve the sustainability of urban mobility

F. Isorna Llerena, E. López González, J.J. Caparrós, F. Segura, J.M. Andújar

Published in:

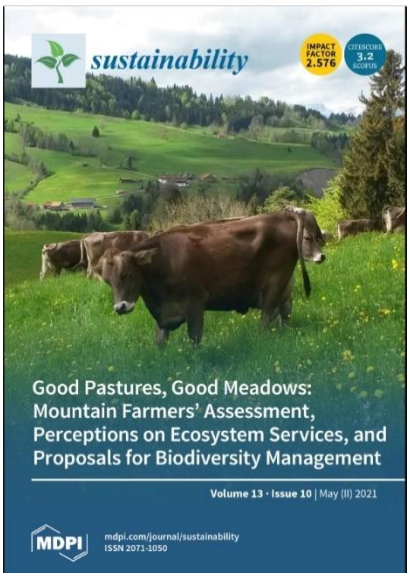

Journal: Sustainability
Editorial: MDPI
Academic Editor: Tomonobu Senjyu
Reference: Sustainability 2021, 13, 5721
Year: 2021
ISSN: 2071-1050
doi.org/10.3390/su13105721

Categoría	Rango revista / Total revista	Cuartil
Environmental Sciences	120 / 265	Q2
Environmental Studies	53/123	Q2
Impact Factor (2019)	2,576	

sustainability

MDPI

Article

Hydrogen vs. Battery-Based Propulsion Systems in Unipersonal Vehicles—Developing Solutions to Improve the Sustainability of Urban Mobility

F. Isorna Llerena [1,*], E. López González [1], J. J. Caparrós Mancera [1], F. Segura Manzano [2] and J. M. Andújar [2]

[1] Instituto Nacional de Técnica Aeroespacial (INTA), Área de Energía. Ctra. Huelva-Matalascañas, km. 34. Mazagón, 21130 Huelva, Spain; lopezge@inta.es (E.L.G.); jcapman@inta.es (J.J.C.M.)
[2] Centro de Investigación en Tecnología, Energía y Sostenibilidad (CITES), Universidad de Huelva, 21007 Huelva, Spain; francisca.segura@diesia.uhu.es (F.S.M.); andujar@diesia.uhu.es (J.M.A.)
* Correspondence: isornaf@inta.es; Tel.: +34-959208847

Abstract: The percentage of the population in urban areas has increased by ten points from 2000 (46%) to 2020 (56%); it is expected to reach up to 70% by 2050. This undoubtedly will encourage society to use alternative transports. On the other hand, the widespread fear of pandemics seems to be here to stay, and it is causing most people to leave public transport to use private cars, and a few have chosen unipersonal electric vehicles. As a consequence, the decision of using private cars negatively affects the air quality, and consequently urban population health. This paper aims to demonstrate a sustainable solution for urban mobility based on a hydrogen powered unipersonal electric vehicle, which, as shown, provides great advantages over the conventional battery powered unipersonal electric vehicle. To show this, the authors have developed both vehicles in comparable versions, using the same platform, and ensuring that the total weight of the unipersonal electric vehicle was the same in both cases. They have been subjected to experimental tests that support the features of the hydrogen-based configuration versus the battery-based one, including higher specific energy, more autonomy, and shorter recharge time.

Keywords: sustainable urban mobility; unipersonal hydrogen-based electric vehicle; unipersonal battery-based electric vehicle; experimental comparison

check for updates

Citation: Isorna Llerena, F.; López González, E.; Caparrós Mancera, J.J.; Segura Manzano, F.; Andújar, J.M. Hydrogen vs. Battery-Based Propulsion Systems in Unipersonal Vehicles—Developing Solutions to Improve the Sustainability of Urban Mobility. *Sustainability* **2021**, *13*, 5721. https://doi.org/10.3390/su13105721

Academic Editor: Tomonobu Senjyu

Received: 29 April 2021
Accepted: 17 May 2021
Published: 20 May 2021

Publisher's Note: MDPI stays neutral with regard to jurisdictional claims in published maps and institutional affiliations.

Copyright: © 2021 by the authors. Licensee MDPI, Basel, Switzerland. This article is an open access article distributed under the terms and conditions of the Creative Commons Attribution (CC BY) license (https://creativecommons.org/licenses/by/4.0/).

1. Introduction

According to the World Data Bank [1], the percentage of urban population has increased by 10 points in the 21st century (in 2000, the urban population was 46%, and in 2020 it reached 56%), and it is expected to reach 70% by 2050. This undoubtedly forces cities to undertake a sustainable transformation of their urban model, and society to use alternative transports. Although public transport plays an important role, a recent analysis has quantified a 60% decrease in public ridership due to the COVID-19 pandemic [2]. Most people have swapped public transport for private cars, and few have chosen the bike. This decision, widely extended across society, negatively affects the air quality and, consequently, urban population health [3].

Therefore, in these times in which people receive daily instruction to avoid social interaction (fear of sharing with another person) while humanity must continue to preserve sustainability and respect for the environment, it is crucial to develop urban transport solutions that guarantee the inevitable 1.5 m physical distance while preserving our planet. In this sense, battery-powered unipersonal vehicles show some challenges not yet resolved. Firstly, the batteries are heavy and have great proportions, in terms of limited specific power [4]. Regarding autonomy, specific energy can also be limiting with respect to interurban mobility. Batteries also have considerable degradation during their lifetime. This implies a lower performance in the electric vehicles over time [5,6]. Additionally, with

the increased use of electric vehicles, a large number of batteries is required to be produced. However, the raw materials, such as lithium, are limited, and recycling will not be enough to continue supplying lithium in a few decades. It would not make sense to repeat the political and economic fights regarding fossil fuels to new materials [7]. Additionally, safety issues must also be taken into account; in recent years, there have been numerous cases of Li-ion battery fires and explosions, resulting in property damage and bodily injuries [8–10]. On the other hand, the design and fabrication of new sustainable electrode materials is taking on greater importance in recent years, so that they may be used as a substitute for traditional raw materials [11,12].

Thus, sustainable alternatives with hydrogen as the energy carrier, obtained from renewable energy [13], are being considered for urban mobility in electric unipersonal vehicles [14–18]. Hydrogen-powered unipersonal electric vehicles offer advantages such as fast charging, long range and low on-board pressure. Pressure tanks are the best option for the hydrogen delivery when low hydrogen demand is needed, and the distances are short between hydrogen production and delivery sites [19].

Comparing the behavior of battery-powered unipersonal electric vehicles versus hydrogen-powered unipersonal electric vehicles, this work presents the advantages in terms of high efficiency, high power density, fast start-up and response to load changes, and long life in favor of the latter. However, there are also disadvantages, such as the current cost of hydrogen technology and the availability of recharging points. As far as technological development is concerned, and in comparison with previous scientific works found in the literature, this paper presents important novelties such as the specific design of the test platform, the use of comparable propulsion systems and real tests in a controllable urban circuit [20–23].

Table 1 shows the main conclusions obtained from the scientific literature. The different technological configurations include the use of batteries, as well as the use of hydrogen through fuel cells (FCs), solar propulsion and various combinations. In comparison to these works, this paper makes a proposal for sustainable urban mobility in which two technologies, battery and the hybridization of battery + hydrogen, are compared, obtaining a scalable model with great autonomy and fast recharge.

Table 1. Comparison of the proposed paper's findings with previous scientific works.

Reference	Powertrain	Nominal Power	Autonomy (km)	Recharge Time	Weight (kg)	On-Road Test	Velocity (m/s)
Authors' proposal	BAT + H2	250	290	1.8 min	33	Yes	3.33
[20]	PV + BAT	800	37	8 h	85	Yes	5.39
[21]	H2	300	800	-	65	No	12.5
[23]	BAT + H2	5000	-	-	475	No	6.91
[24]	PV + BAT	370	31	11 h	-	Yes	7.22
[25]	BAT + H2	6000	200	-	130	No	16.6
[26]	BAT + H2	120	-	-	-	No	-
[27]	H2	250	250	-	-	No	-

2. Materials and Methods

To demonstrate the capabilities of hydrogen hybridization in electric urban transport versus battery-based technology, two unipersonal vehicles were designed: a battery-powered unipersonal electric vehicle and a hydrogen-based unipersonal electric vehicle. The goal was to mount the battery-based and the hydrogen-based powertrains on similar platforms and ensuring the total weight of the unipersonal electric vehicle was the same in both cases. Figure 1 shows the platform built with an iron chassis including all the components of the propulsion system. It should be noted that the hydrogen used in these facilities was green hydrogen, produced from renewable sources [28–30].

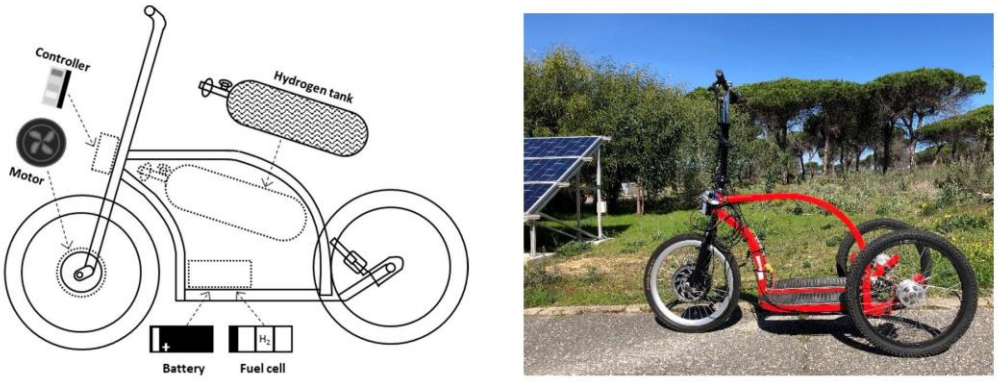

Figure 1. Unipersonal electric vehicle platform: (**a**) conceptual design; (**b**) physical implementation.

The platform integrated an electric motor of 24 V and 250 W by Golden Motor®, model MP3-20F Magic Pie® 3, attached to the front 20-inch wheel. It was sized in a range to meet the typical energy requirements in commercial batteries and fuel cells [31–34], promoting design scalability. The system was regulated through the programmable controller, model Magic® MX25 BAC-281P by Golden Motor®. System specifications are summarized in Table 2.

Table 2. Motor system specifications.

Device	Parameter	Value
Motor	Voltage (V) Power (W) Weight including wheel (kg)	24 250 7.5
Wheel	Size (cm)	50.8
Brushless motor controller	Voltage ranges (V) Max. power (W)	24, 36, 48 1000

2.1. Battery-Powered Unipersonal Electric Vehicle Configuration

The first design was based on the implementation of an electric unipersonal vehicle powered by battery, Figure 2 The motor, managed though its controller C_M, receives the necessary current directly from the battery, and the motor operating voltage matches with battery nominal voltage. In addition to the specific parameters previously described, motor voltage V_{motor}, current I_{motor} and battery current I_{bat} were monitored. Battery technical characteristics are summarized in Table 3.

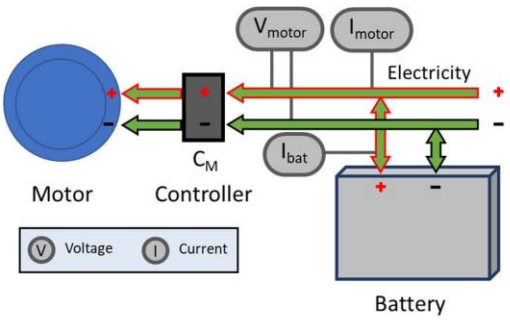

Figure 2. Battery-based propulsion system.

Table 3. Battery technical characteristics.

Parameter	Value
Model	Herewin MG-12000P
Nominal Voltage (V)	24 V
Rated Energy (Wh)	266
Capacity (Ah)	12
Weight (kg)	3.6
Technology	LiPo

2.2. *Hydrogen-Powered Unipersonal Electric Vehicle Configuration*

The hydrogen-based propulsion system bases its energy input on hydrogen technology together with a buffer battery, Figure 3.

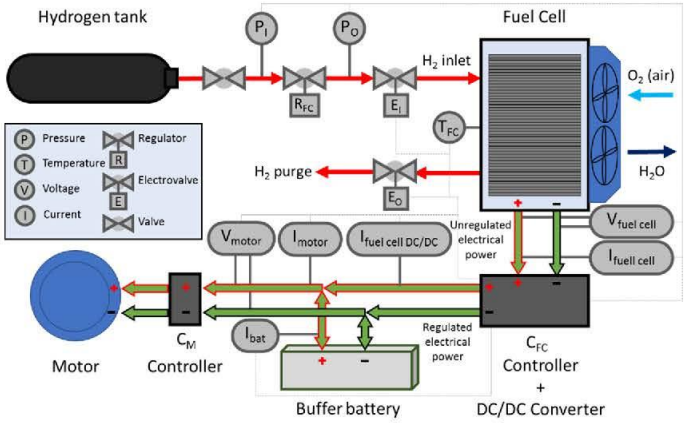

Figure 3. Hybridized hydrogen-based propulsion system.

The hydrogen-powered unipersonal electric vehicle has a hydrogen storage tank able to store up to 7 L, at a maximum pressure of 350 bar. The pressure of the stored hydrogen is reduced through the regulator R_{FC}. This reduction is carried out to adapt the hydrogen to the range of inlet pressure in the fuel cell. The selected fuel cell was the BMPower® 500, with a nominal power of 500 W. Due to commercial availability and cost/nominal power effective ratio, this model was the most suitable according to the requirements of the application (the objective is to compare two platforms with similar weight). To guarantee a safe operation, both inlet pressure, P_I, and output pressure, P_O, obtained at the ends of the regulator were monitored.

To allow hydrogen flow into the fuel cell, the inlet solenoid valve, E_I, is activated. The fuel cell produces electricity and water, from hydrogen and oxygen. A fan was used to blow the air from outside to provide oxygen to the cathode and to cool the fuel cell.

The electricity produced by the fuel cell passes through a DC/DC power converter that, through the controller C_{FC}, regulates the output according to the power demanded by the motor and the buffer battery's state of charge. The integration of the buffer battery aims to provide greater specific power and flexibility to the system in the face of demand peaks from the motor.

The motor controller, C_M, is based on the electromechanical systems of the electric vehicle, which are accelerator and brake. The fuel cell controller, C_{FC}, monitors hydrogen pressures P_I and P_O, fuel cell temperature T_{FC}, fuel cell voltage $V_{fuel\ cell}$, fuel cell current before the converter $I_{fuel\ cell}$ and after the converter $I_{fuel\ cell\ DC/DC}$, buffer battery current I_{bat}, motor voltage V_{motor}, and motor current I_{motor}. Based on these variables, and the operating instructions, the controller acts on the hydrogen inlet, E_I, to supply the hydrogen to the fuel cell, and on the purge solenoid valve, E_O, to periodically purge the hydrogen

not consumed by the fuel cell, ventilation system and air supply, and establishes a power command for the output of the DC/DC converter.

These parameters were monitored through a Wi-Fi connection and recorded during the experimental tests of the system. The BM Power® software tool is intended for monitoring and controlling the operation of the propulsion system, Figure 4. Technical specifications of the hybrid propulsion system are shown in Table 4

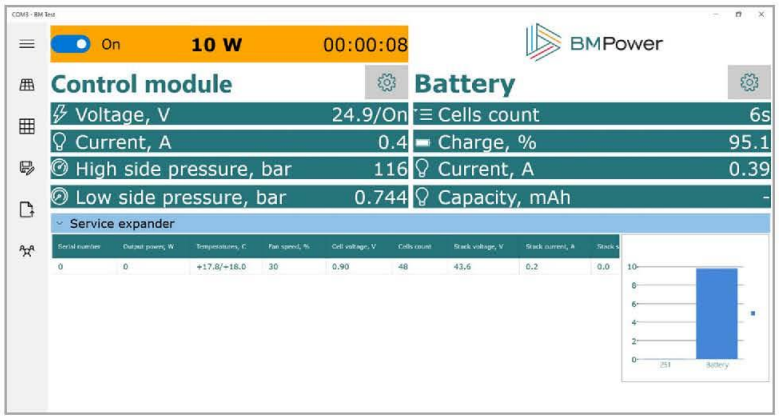

Figure 4. Control system software interface.

Table 4. Hybridized hydrogen-based propulsion system technical specifications.

Device	Parameter	Value
Storage tank	Volume (L)	7
	Weight (kg)	2.3
	Dimensions with regulator (mm)	Ø148 × 600
Fuel Cell	Model	BMPower® 500
	Rated Supply Voltage (V)	25–650
	Nominal Power (W)	500
	Dimensions with controller (mm)	225 × 145 × 124
	Weight including fan, controller and converter (kg)	1.1
	Cells	48
Controller + DC/DC converter	Rated Supply Voltage (V)	10–30
	Topology	Three synchronized lowering converters
Fan	Model	San Ace® 80 9G0824H101
	Voltage (V)	24
	Current (A)	0.42
	Power (W)	10.1
Buffer battery	Rated Supply Voltage (V)	22.2
	Rated Energy (Wh)	73
	Capacity (Ah)	3.3
	Weight (kg)	0.5
	Technology	LiPo
Wiring and piping	Weight (kg)	07

2.3. Physical Implementation—Battery vs. Hydrogen Technology Comparison

Figure 5 shows the physical implementation of the battery-based and the hybridized hydrogen-based unipersonal electrical vehicle. Both were implemented in the same platform, with an arrangement that allowed the pilot to manage and guaranteed an adequate air flow for correct ventilation and air supply.

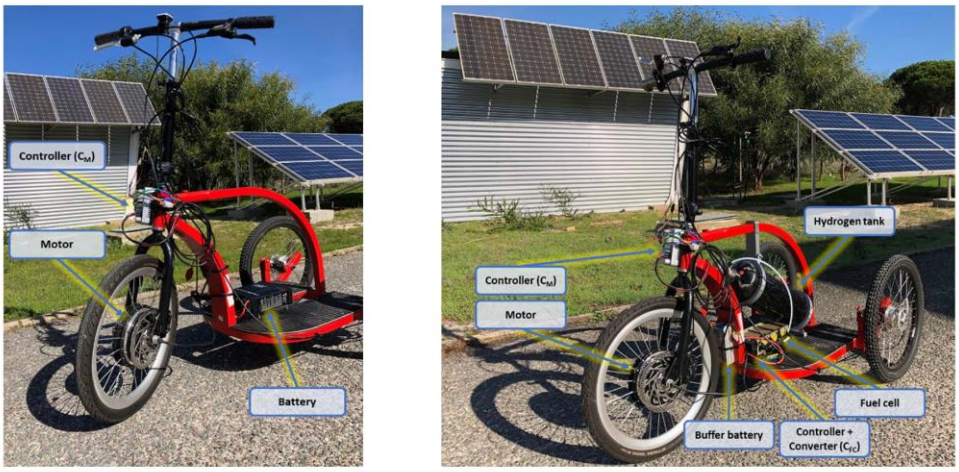

(**a**) (**b**)

Figure 5. System implementation: (**a**) battery-based unipersonal electric vehicle; (**b**) hydrogen-based unipersonal electric vehicle.

The technology comparison was carried out regarding the energy capacity of each design.

The specific energy supplied by the battery-based system is calculated by applying Equation (1):

$$e_{battery} = \frac{E_{battery}}{m_{battery}} \quad (1)$$

where:

$$E_{battery} \text{ (Battery energy)} = 266 \text{ Wh};$$
$$m_{battery} \text{ (Battery mass)} = 3.6 \text{ kg}.$$

Then, the battery specific energy is 74 Wh/kg.

In the hydrogen-based system, to calculate the specific energy it is necessary to know the amount of hydrogen stored in the tank. The hydrogen moles number, n_{H2}, can be obtained from Equation (2):

$$n_{H2} = \frac{p \cdot V}{Z \cdot R \cdot T} \quad (2)$$

where:

$$p \text{ (Pressure)} = 3.5 \times 10^7 \text{ Pa};$$
$$V \text{ (Volume)} = 0.007 \text{ m}^3;$$
$$Z \text{ (Compressibility factor for 350 bar and 298.15 K)} = 1.25205;$$
$$R \text{ (Ideal gas constant)} = 8.314472 \frac{m^3 \cdot Pa}{K \cdot mol};$$
$$T \text{ (Temperature)} = 298.15 \text{ K}.$$

Therefore, the hydrogen tank provides 78.9359 mol of H_2.

To obtain the hydrogen energy, hydrogen properties considered are:

HHV_{H2} (hydrogen higher heating value) = 141.86 MJ/kg.

The hydrogen energy provided is 6221 Wh; and the hydrogen specific energy supplied is obtained by applying Equation (3):

$$e_{H2} = \frac{E_{H2}}{m_{H2}} \quad (3)$$

where:

$$E_{H2} \text{ (Hydrogen energy)} = 6221 \text{ Wh};$$
$$m_{H2} \text{ (Hydrogen system mass)} = 4.2 \text{ kg}.$$

Then, the hydrogen specific energy provided is 1481 Wh/kg.

The hybridized hydrogen-based system also included a buffer battery of 73 Wh and 0.5 kg. Applying the Equation (1), the buffer battery specific energy is 146 Wh/kg, while full hybrid system specific energy is 1339 Wh/kg.

Additionally, to compare the energy–volume relation in both powertrains, it is necessary to know the whole volume of each system. The battery-based powertrain volume is 2139 cm^3. In the hydrogen-based powertrain, the tank volume is 7958 cm^3, fuel cell volume is 3289 cm^3 and buffer battery volume is 243 cm^3. Therefore, the battery-based powertrain energy-volume relation is 124,357 Wh/m^3, while in the hydrogen-based powertrain the relation is 541,426 Wh/m^3.

Quantitative comparison of both platforms is shown in Table 5; improvements were verified both in specific energy and energy–volume relation for the hydrogen-based design. This can be quantified as an increase of 1790% in specific energy and 335% in energy–volume relation.

Table 5. Battery vs. hydrogen technology comparison.

Powertrain System	Energy (Wh)	Specific Energy (Wh/kg)	Energy-Volume (Wh/m^3)	Volume (cm^3)	Autonomy (km) *	Recharge Time (h)	Weight (kg)
Battery-powered	266	74	124,357	2139	15	4	3.6
Hydrogen-powered	6294	1339	541,426	11,490	290	0.03	4.7

*: Obtained from experimental road test, Section 3.4.

3. Results

To obtain the experimental data results, dynamic laboratory and dynamic road tests were carried out over the two configurations: battery-based and hydrogen-based unipersonal electric vehicle, Figure 6.

(**a**) (**b**)

Figure 6. Unipersonal electric vehicle test benches: (**a**) laboratory dynamic test; (**b**) road test.

The dynamic laboratory test consisted of applying acceleration over the motor, and then provoking friction or manual braking. For the dynamic road test, a real driving test was applied over the unipersonal electric vehicle in movement.

3.1. Experimental Test from Battery-Powered Unipersonal Vehicle

To check the battery-powered unipersonal vehicle platform, it was firstly subjected to a dynamic laboratory driving profile, Figure 7. Different acceleration stages were applied, causing friction or manual braking. As it can be observed, the battery current followed the motor current demand, $I_{bat} = -I_{motor}$ (authors considered a positive sign when current

was leaving the device, and negative sign when current was entering the device). State of charge [35] of the battery (SOC) was calculated applying Equation (4):

$$SOC(t) = SOC(t-1) + \frac{I(t)}{Q_n}\Delta t \quad (4)$$

where:

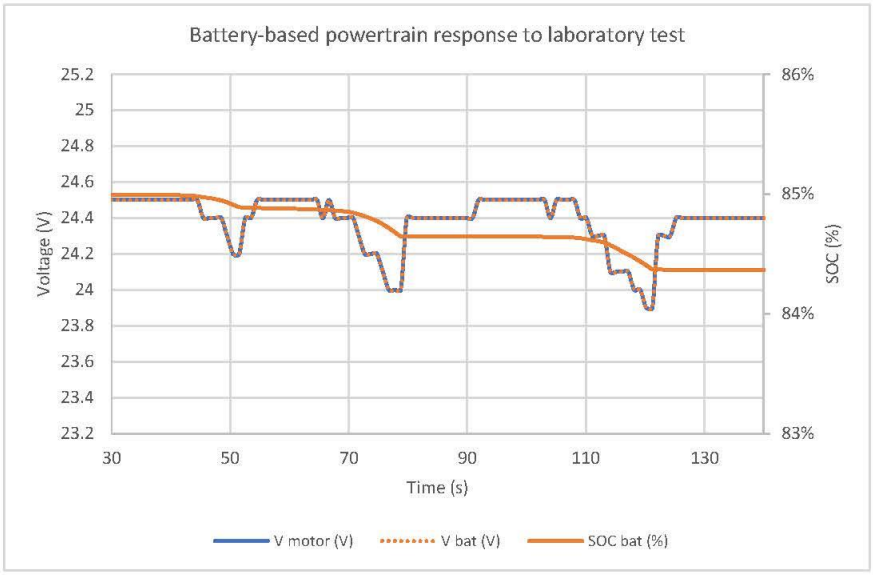

(**a**)

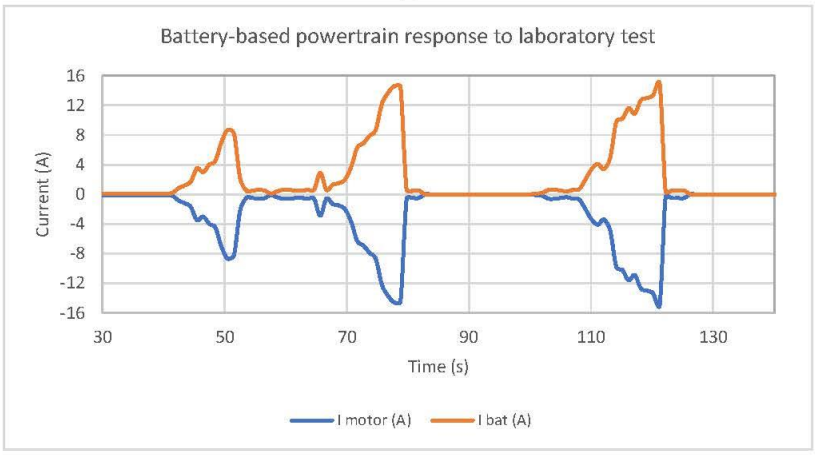

(**b**)

Figure 7. Battery-based unipersonal electric vehicle response to laboratory dynamic test: (**a**) motor and battery voltage and SOC vs. time; (**b**) battery and motor current vs. time. Initial condition: SOC = 85%.

$SOC(t)$ is state of charge in a time t;
$SOC(t-1)$ is the SOC at the previous instant;
$I(t)$ is the battery current (A);
Q_n is nominal capacity of the battery (Ah);
Δt is time differential (s).

The second test consisted of an evaluation of the battery-based unipersonal electric vehicle behavior, when it was put on-road. Battery supplied the motor demand, and as a consequence, the battery SOC decreased with time, Figure 8.

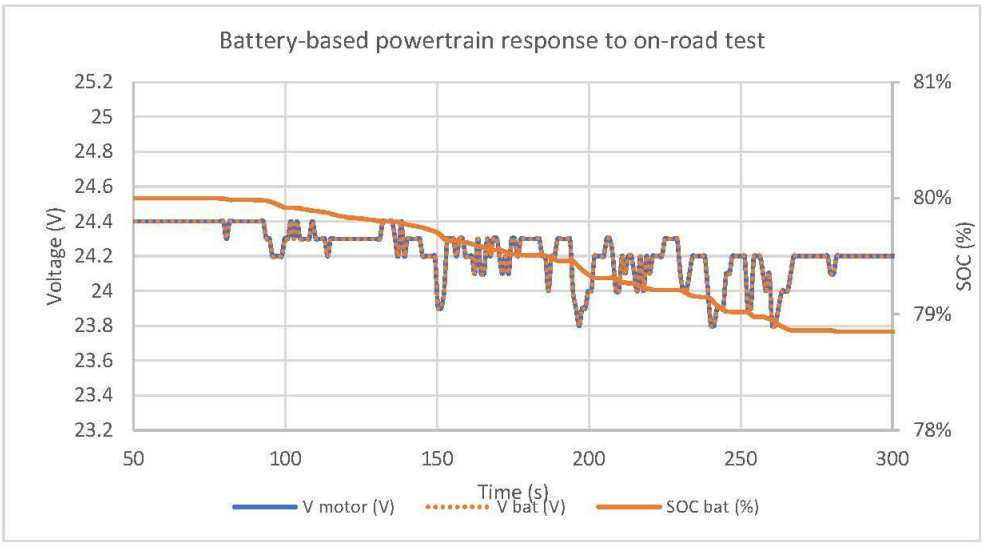

(**a**)

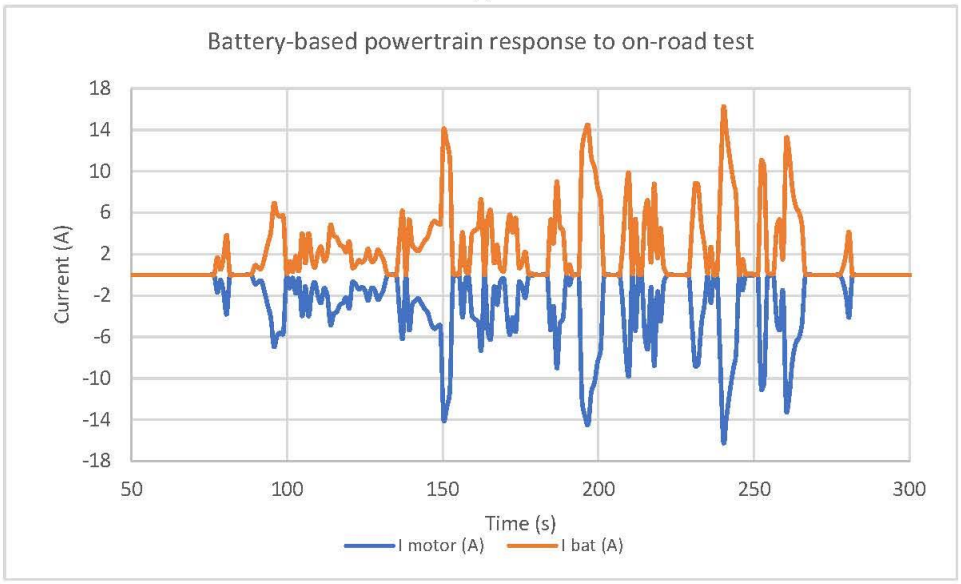

(**b**)

Figure 8. Battery-based unipersonal electric vehicle response to on-road dynamic test: (**a**) motor voltage and battery voltage and SOC vs. time; (**b**) battery and motor current vs. time. Initial condition: SOC = 80%.

3.2. *Experimental Test from Hydrogen-Powered Unipersonal Vehicle*

In this case, the test consisted of evaluating the unipersonal electric vehicle behavior when the powertrain was hybridized with a fuel cell and the battery. As demonstrated

above, in the first test, the hybrid hydrogen-based unipersonal vehicle was subjected to a laboratory dynamic driving profile. This test observed the initial current hybridization between the fuel cell current and the buffer battery current to satisfy the current demanded by the motor. The motor voltage was fixed by the battery (nominal voltage 24 V), and the fuel cell converter acted as step-down stage (fuel cell voltage varied between 42.2 V and 33.2 V, and it reduced to 24 V). Based on the difference between the motor demand and the maximum current supplied by the fuel cell, the controller varied the converter duty-cycle with the aim to put the fuel cell into the appropriate operating point.

When the motor demand was lower than the maximum fuel cell current, the controller adjusted the DC/DC converter to put the fuel cell operating at the point that satisfies the motor demand, and the remaining current was used to recharge the battery ($I_{bat} = -1$ A), Figure 9. Note that the fuel cell provided almost all of the motor current demand. Sudden changes in the demand were reflected in the fuel cell. The battery filtered instabilities and provided current peaks when the demand was higher than the fuel cell nominal current. Through the test, as the battery absorbed current from fuel cell, the battery SOC increased gradually. Hydrogen was consumed, so the pressure in the tank was reduced. Power balance can be at each operating point; for example, at t = 12,000 s, $I_{fuelcell} = 4.2$ A, which converted to I_{fuel} cell DC/DC = 5.1 A. Fuel cell converter output current was consumed by the motor ($I_{motor} = -4.1$ A) and the battery ($I_{bat} = -1$ A).

The last test consisted of an on-road dynamic test to assess the capability of the designed powertrain in meeting the requirements of a real driving profile, Figure 10.

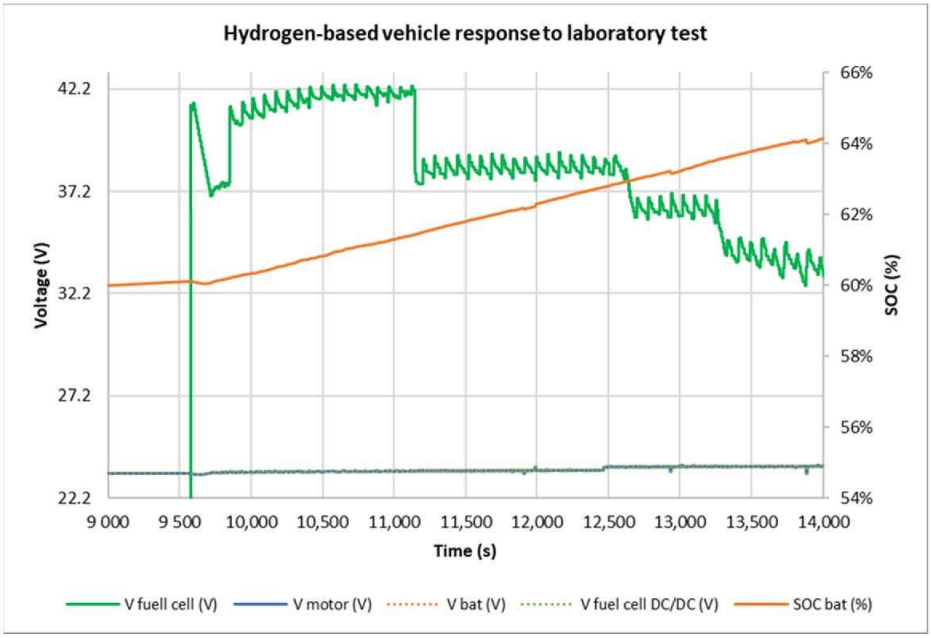

(**a**)

Figure 9. *Cont.*

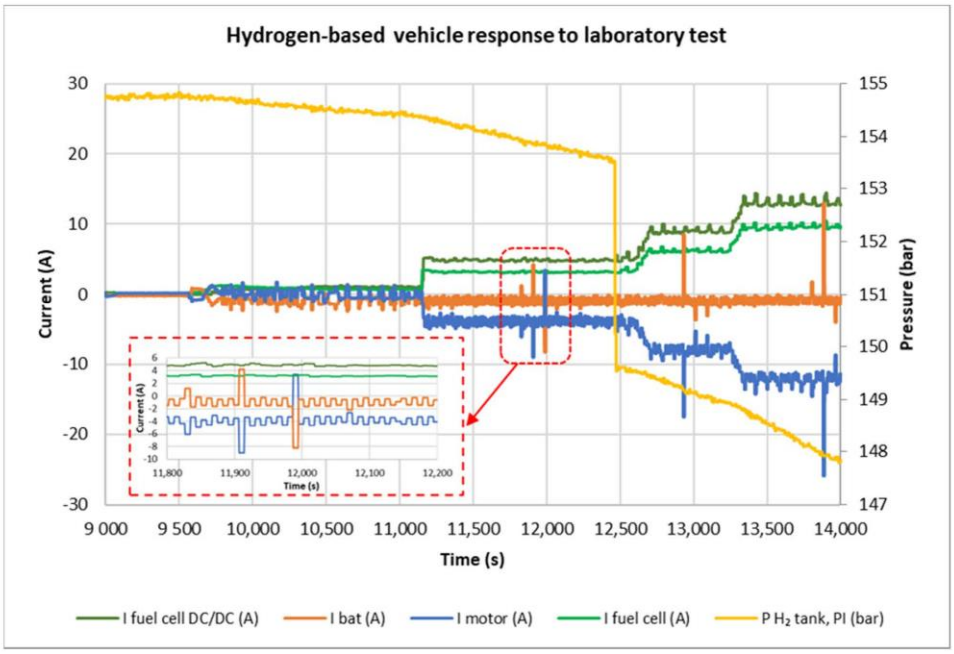

(**b**)

Figure 9. Hydrogen-based unipersonal electric vehicle response to laboratory dynamic test. (**a**) Motor and fuel cell voltages and battery SOC vs. time; (**b**) fuel cell, motor, battery currents and pressure vs. time. Initial condition: SOC = 60%; H2 Pressure = 154.6 bar.

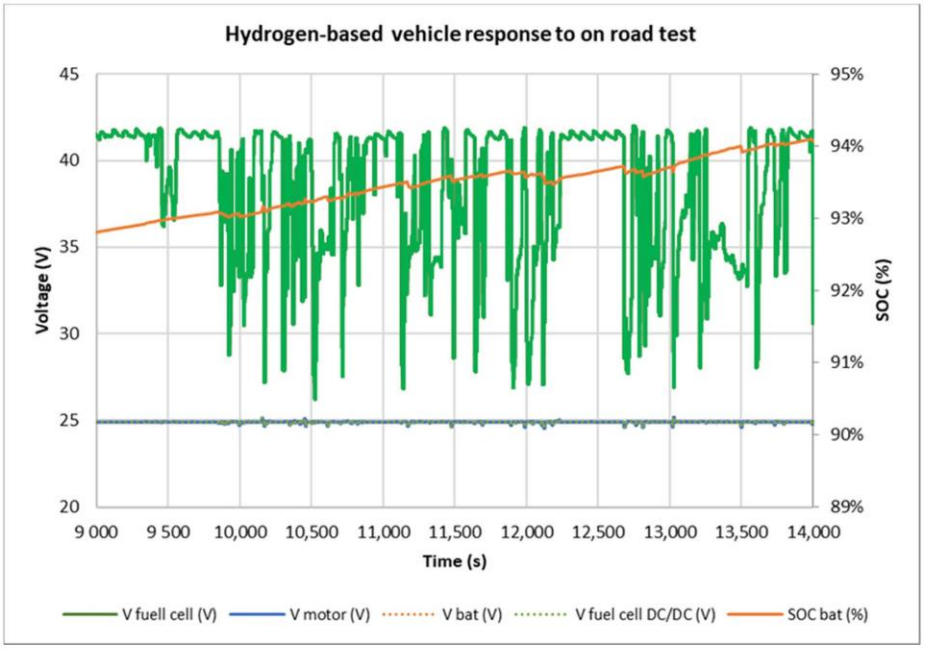

(**a**)

Figure 10. *Cont.*

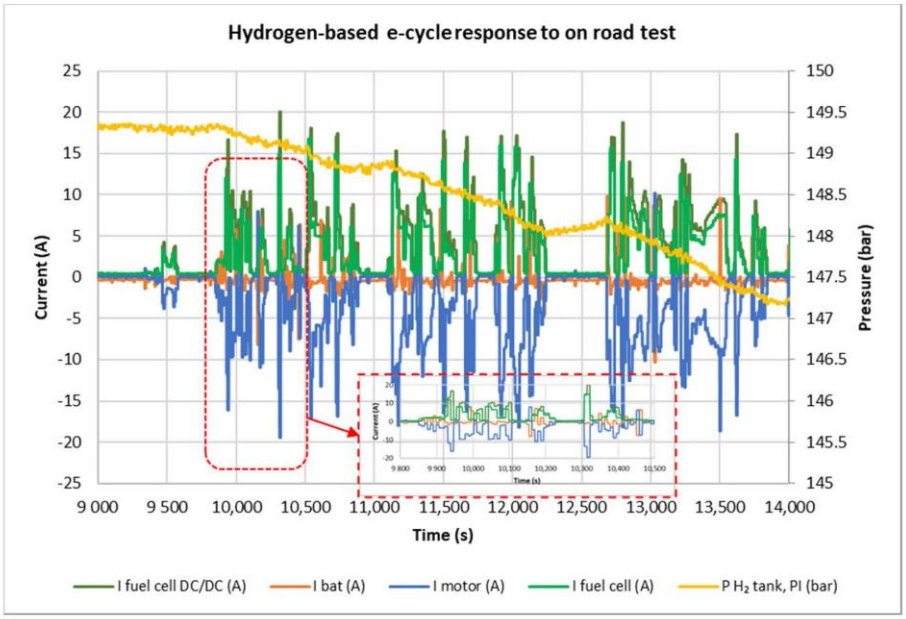

(**b**)

Figure 10. Hydrogen-based unipersonal electric vehicle response to on-road dynamic test: (**a**) fuel cell, motor, battery voltages and SOC vs. time; (**b**) fuel cell, motor, battery currents and pressure vs. time. SOC = 93%; initial pressure = 149.3 bar.

In this test, the hydrogen-based powertrain was subjected to sudden changes in the driving profile. Note that the fuel cell provided almost all the current while the battery filtered instabilities and provided current peaks. Battery SOC started at 93%, as it was continuously charging, meanwhile it did not provide the required current peaks. When motor current peaks needed to be provided by the battery, its SOC decreased instantaneously. Hydrogen pressure in the storage tank reduced and can be measured to later estimate the autonomy of the system. Overall, the fuel cell responded with enough power to meet the motor demand and to charge the battery, validating the hybrid design along the buffer battery.

3.3. Temperature Test

During the on-road tests of the hybridized hydrogen-based unipersonal electric vehicle, it was verified that the temperature remained in an adequate range, with the corresponding increase in the fan speed for cooling during higher peaks of current supplied by the fuel cell. Although the system guarantees good cooling, it is interesting to consider innovative solutions in battery cooling [36] to scale the hybrid propulsion system to higher power developments. The temperature evolution during on-road test according to the current and the fan interaction is verified in Figure 11.

3.4. On-Road Autonomy Test

The on-road autonomy test covered a total of 48 km at an average speed of 12 km/h. The unipersonal electric vehicle was first operated with battery-based powertrain and then with hydrogen-based powertrain, on a bicycle path, from INTA facilities to the town of Mazagón. Taking into account the hydrogen-based system, initially the hydrogen pressure tank achieved 350 bar. At the end of the test, pressure was reduced 68 bar. Using the Redlkich–Kwong equation of state [37], a hydrogen consumption of 26.5 g was obtained, assuming that the tank was at 25 °C during the entire test. This resulted in an energy

consumption of 1044 Wh (HHV). On the other hand, according to Table 5, Section 2.3, the total amount of energy available in hydrogen-based system was 6294 Wh (HHV), and 266 Wh in battery-based system. This means there was a maximum autonomy of 290 km for the hydrogen-based system while just 15 km for the battery-based system.

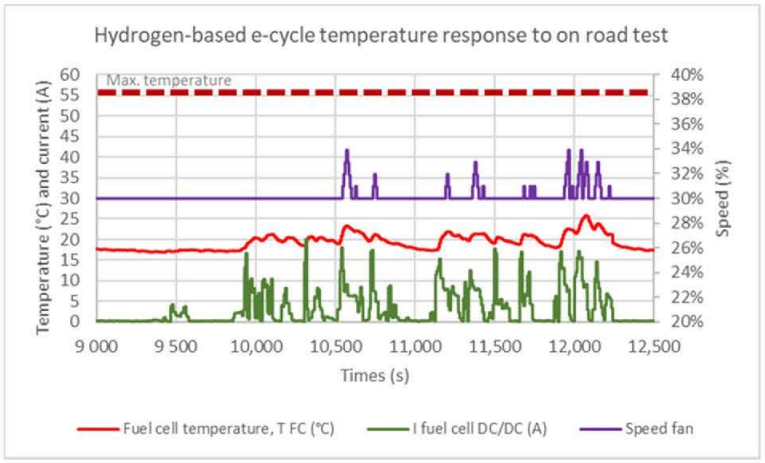

Figure 11. Hydrogen-based hybrid electric vehicle temperature response to on-road dynamic test.

4. Discussion

This section presents an analysis of the main results obtained in the tests. Both battery-based and hydrogen-based unipersonal electric vehicles developed in this work have been exposed to real laboratory and on-road driving test conditions, according to the urban mobility conditions for which they have been developed.

4.1. Battery-Based System Response

The battery system has a direct energy exchange between the motor demand and the battery supply. In this way, as the motor accelerates, it demands more electrical current, supplied directly from the electrical energy stored in the battery. This causes a reduction in the battery SOC and, thus, the battery voltage. The system limits its flexibility to that provided by the characteristics of the battery. Therefore, for a battery-based unipersonal electric vehicle, it must be scaled based on the selected battery since the entire propulsion system—acceleration, autonomy, recharging, etc.—is directly linked to the battery selection.

4.2. Hydrogen-Based System Response

In the hydrogen-based hybrid system, in response to the demand of the motor, there is a stabilized supply from the fuel cell, through its DC/DC converter. In this system, the battery acts as a buffer, providing current and energy, in cases where the fuel cell is not able to supply instantaneous high current demand peaks from the motor. Slow motor demand transients can be supplied by the fuel cell. In short transient demand peaks, the battery supplies the necessary current. Likewise, the battery undergoes instantaneous SOC decreases, which are recovered in the next driving step. Regarding the hydrogen consumption, it also decreases the pressure in the hydrogen tank as it is consumed by the fuel cell for the electricity production. Therefore, the system shows an energy flexibility scalable to the supply capacity of the hydrogen system. The greater the storage tank capacity, the greater the autonomy, the larger the fuel cell and its converter, and the more energy that can be supplied directly. Power flexibility depends not only on the hydrogen system, but also on the buffer battery. Once it has been verified that it provides the current peaks demanded by the motor, it must be scaled based on the corresponding urban mobility application.

5. Conclusions

In this work, a test platform was built to establish a comparison between a unipersonal electric vehicle powered only by batteries, and the same one powered by a hybrid system based on hydrogen and batteries. Both systems had similar weight. In this way, it is possible to compare both technologies, their advantages and disadvantages, in the same platform. The autonomy of the hybrid hydrogen-based system was 290 km, being much greater than that of the battery-based system that reached approximately 15 km. Preliminary conclusions allow us to recognize that energy hybridization provides great specific advantages to urban mobility applications. Indeed, the improvements can be quantified as an increase of 1790% in specific energy and 335% in energy–volume relation. The results show that the unipersonal electric vehicle equipped with a hydrogen-based powertrain provides not only greater autonomy, but also has shorter recharge times.

The capacities obtained in terms of autonomy, recharging time and, above all, environmental advantages regarding the reduction in pollutants, make this a promising and scalable proposal for use in sustainable cities.

Author Contributions: Conceptualization, F.I.L. and F.S.M.; methodology, F.I.L., J.M.A., E.L.G. and F.S.M.; validation, J.J.C.M. and E.L.G.; formal analysis, F.I.L. and F.S.M.; investigation, All; resources, F.I.L. and E.L.G.; data curation, J.J.C.M.; writing—original draft preparation, F.I.L. and J.J.C.M.; writing—review and editing, All; supervision, J.M.A. All authors have read and agreed to the published version of the manuscript.

Funding: This research received no external funding.

Institutional Review Board Statement: Not applicable.

Informed Consent Statement: Not applicable.

Data Availability Statement: Not applicable.

Acknowledgments: The authors would like to thank Manuel Gil for his helpful advice in various technical issues regarding the testing platform.

Conflicts of Interest: The authors declare no conflict of interest.

List of Acronyms

BAT	Battery
DC	Direct current
FC	Fuel cell
HHV	Higher heating value
SOC	State of charge

Notation and Symbols

$C\text{-}rates$	charge/discharge rates
Δt	time differential (s)
$E_{battery}$	Battery energy (Wh)
E_{H2}	Hydrogen energy (Wh)
$e_{battery}$	Battery specific energy (Wh/kg)
e_{H2}	Hydrogen system specific energy (Wh/kg)
$I(t)$	Discharging current (A)
$m_{battery}$	Battery mass (kg)
m_{H2}	Hydrogen system mass (kg)
n_{H2}	number of hydrogen mol (mol)
p	Pressure (Pa)
Q_n	Nominal capacity (Ah)
T	Temperature (K)
V	Volume (m^3)
HHV_{H2}	Hydrogen higher heating value (141.86 MJ/kg)
R	Ideal gas constant (8.314472 $m^3 \cdot Pa/K \cdot mol$)
Z	Hydrogen Compressibility factor at 350 bar and 298.15 K (1.25205)

References

1. Urban Population (% of Total Population) | Data. Available online: https://data.worldbank.org/indicator/SP.URB.TOTL.IN.ZS?end=2019&name_desc=false&start=1960&view=chart (accessed on 28 January 2021).
2. Jenelius, E.; Cebecauer, M. Impacts of COVID-19 on public transport ridership in Sweden: Analysis of ticket validations, sales and passenger counts. *Transp. Res. Interdiscip. Perspect.* **2020**, *8*, 100242. [CrossRef]
3. Thurston, G.D. Outdoor Air Pollution: Sources, Atmospheric Transport, and Human Health Effects. In *International Encyclopedia of Public Health*; Elsevier BV: Amsterdam, The Netherlands, 2017; pp. 367–377.
4. Redman, C. The Impact of Motorcycles on Air Quality and Climate Change: A Study on the Potential of Two-Wheeled Electric Vehicles. Senior Thesis, Claremont McKenna College, Claremont, CA, USA, 2015.
5. Diaz-Cachinero, P.; Munoz-Hernandez, J.I.; Contreras, J. A Linear Model for Operating Microgrids with Renewable Resources, Battery Degradation Costs and Electric Vehicles. In Proceedings of the 2018 15th International Conference on the European Energy Market (EEM), Lodz, Poland, 27–29 June 2018; Volume 2018, pp. 1–5.
6. Wang, S.; Guo, D.; Han, X.; Lu, L.; Sun, K.; Li, W.; Sauer, D.U.; Ouyang, M. Impact of battery degradation models on energy management of a grid-connected DC microgrid. *Energy* **2020**, *207*, 118228. [CrossRef]
7. Qiao, D.; Wang, G.; Gao, T.; Wen, B.; Dai, T. Potential impact of the end-of-life batteries recycling of electric vehicles on lithium demand in China: 2010–2050. *Sci. Total. Environ.* **2021**, *764*, 142835. [CrossRef]
8. Ryan and Phil. Events with Smoke, Fire, Extreme Heat, Or Explosion Involving Lithium Batteries. Available online: https://www.faa.gov/hazmat/resources/lithium_batteries/media/Battery_incident_chart.pdf (accessed on 18 May 2021).
9. Safety Concerns with Li-ion Batteries-Battery University. Available online: https://batteryuniversity.com/learn/article/safety_concerns_with_li_ion (accessed on 18 May 2021).
10. Larsson, F.; Andersson, P.; Blomqvist, P.; Mellander, B.-E. Toxic fluoride gas emissions from lithium-ion battery fires. *Sci. Rep.* **2017**, *7*, 1–13. [CrossRef] [PubMed]
11. Minakshi, M.; Higley, S.; Baur, C.; Mitchell, D.R.G.; Jones, R.; Fichtner, M. Calcined chicken eggshell electrode for battery and supercapacitor applications. *RSC Adv.* **2019**, *9*, 26981–26995. [CrossRef]
12. Minakshi, M.; Mitchell, D.R.G.; Jones, R.; Pramanik, N.C.; Jean-Fulcrand, A.; Garnweitner, G. A Hybrid Electrochemical Energy Storage Device Using Sustainable Electrode Materials. *ChemistrySelect* **2020**, *5*, 1597–1606. [CrossRef]
13. Mancera, J.J.C.; Manzano, F.S.; Andújar, J.M.; Vivas, F.J.; Calderón, A.J. An Optimized Balance of Plant for a Medium-Size PEM Electrolyzer: Design, Control and Physical Implementation. *Electronics* **2020**, *9*, 871. [CrossRef]
14. Chen, H.-S.; Tsai, B.-K.; Hsieh, C.-M. Determinants of Consumers' Purchasing Intentions for the Hydrogen-Electric Motorcycle. *Sustainability* **2017**, *9*, 1447. [CrossRef]
15. Chen, H.-S.; Tsai, B.-K.; Hsieh, C.-M. The Effects of Perceived Barriers on Innovation Resistance of Hydrogen-Electric Motorcycles. *Sustainability* **2018**, *10*, 1933. [CrossRef]
16. Handa, K.; Yamaguchi, S.; Minowa, K.; Mathison, S. Development of New Hydrogen Fueling Method for Fuel Cell Motorcycle. *SAE Int. J. Altern. Powertrains* **2017**, *6*, 219–227. [CrossRef]
17. Weigl, J.D.; Henz, M.; Inayati; Saidi, H. Converted battery-powered electric motorcycle and hydrogen fuel cell-powered electric motorcycle in South East Asia: Development and performance test. In Proceedings of the Joint International Conference on Electric Vehicular Technology and Industrial, Mechanical, Electrical and Chemical Engineering (ICEVT & IMECE), Surakarta, Indonesia, 4–5 November 2015; pp. 1–4.
18. Di Trolio, P.; Di Giorgio, P.; Genovese, M.; Frasci, E.; Minutillo, M. A hybrid power-unit based on a passive fuel cell/battery system for lightweight vehicles. *Appl. Energy* **2020**, *279*, 115734. [CrossRef]
19. Li, M.; Bai, Y.; Zhang, C.; Song, Y.; Jiang, S.; Grouset, D.; Zhang, M. Review on the research of hydrogen storage system fast refueling in fuel cell vehicle. *Int. J. Hydrogen Energy* **2019**, *44*, 10677–10693. [CrossRef]
20. Paudel, A.M.; Kreutzmann, P. Design and performance analysis of a hybrid solar tricycle for a sustainable local commute. *Renew. Sustain. Energy Rev.* **2015**, *41*, 473–482. [CrossRef]
21. Pios hydrogen fuel cell tricycle. *Int. J. Hydrogen Energy* **2005**, *30*, 1035–1036. [CrossRef]
22. Devan, P.; Bibin, C.; Krrishana, A.G.; Ashwin, M.; Kumar, K.B.; Dinesh, K. A comprehensive review on solar tricycles. In Proceedings of the Materials Today: Proceedings; Elsevier BV: Amsterdam, The Netherlands, 2020; Volume 33, pp. 229–231.
23. Piumsomboon, P.; Pruksathorn, K.; Hunsom, M.; Tantavichet, N.; Charutawai, K.; Kittikiatsophon, W.; Nakrumpai, B.; Sripakagorn, A.; Damrongkijkarn, P. Road testing of a three-wheeler driven by a 5 kW PEM fuel cell in the absence and presence of batteries. *Renew. Energy* **2013**, *50*, 365–372. [CrossRef]
24. Masud, M.H.; Akhter, S.; Islam, S.; Parvej, A.M.; Mahmud, S. Design, Construction and Performance Study of a Solar Assisted Tri-cycle. *Period. Polytech. Mech. Eng.* **2017**, *61*, 234. [CrossRef]
25. Lin, B. Conceptual design and modeling of a fuel cell scooter for urban Asia. *J. Power Sources* **2000**, *86*, 202–213. [CrossRef]
26. De León, C.P.; Walsh, F.; Patrissi, C.; Medeiros, M.; Bessette, R.; Reeve, R.; Lakeman, J.; Rose, A.; Browning, D. A direct borohydride–peroxide fuel cell using a Pd/Ir alloy coated microfibrous carbon cathode. *Electrochem. Commun.* **2008**, *10*, 1610–1613. [CrossRef]
27. Masterflex, Veloform link for fuel cell bikes. *Fuel Cells Bull.* **2004**, *2004*, 4. [CrossRef]
28. López, E.; Isorna, F.; Rosa, F. Optimization of a solar hydrogen storage system: Exergetic considerations. *Int. J. Hydrogen Energy* **2007**, *32*, 1537–1541. [CrossRef]

29. González, E.L.; Llerena, F.I.; Pérez, M.S.; Iglesias, F.R.; Macho, J.G. Energy evaluation of a solar hydrogen storage facility: Comparison with other electrical energy storage technologies. *Int. J. Hydrogen Energy* **2015**, *40*, 5518–5525. [CrossRef]
30. López, E.; Isorna, F.; Rosa, F. Optimization of a Solar Hydrogen Storage System: Safety Considerations. In Proceedings of the Conference WHEC16: 16, World Hydrogen Energy Conference, Lyon, France, 13–16 June 2006. INIS-FR-6794.
31. Hellmann, J.V.; Sandel, R.J. Dual/High Voltage Vehicle Electrical Systems. *SAE Tech. Paper Ser.* **1991**. [CrossRef]
32. Corbo, P.; Migliardini, F.; Veneri, O. Performance investigation of 2.4kW PEM fuel cell stack in vehicles. *Int. J. Hydrogen Energy* **2007**, *32*, 4340–4349. [CrossRef]
33. Lu, F.; Zhang, H.; Zhu, C.; Diao, L.; Gong, M.; Zhang, W.; Mi, C.C. A Tightly Coupled Inductive Power Transfer System for Low-Voltage and High-Current Charging of Automatic Guided Vehicles. *IEEE Trans. Ind. Electron.* **2018**, *66*, 6867–6875. [CrossRef]
34. Hamdan, M.M.; Holler, G.; Grolle, K.A.; Macnamara, J.M.; Thakkar, K.A. System and method for detecting alternator condition. Google Patents , Patent US 6,862,504 B2, 1 March 2005.
35. Chang, W.-Y. The State of Charge Estimating Methods for Battery: A Review. *ISRN Appl. Math.* **2013**, *2013*, 1–7. [CrossRef]
36. Divakaran, A.M.; Hamilton, D.; Manjunatha, K.N.; Minakshi, M. Design, Development and Thermal Analysis of Reusable Li-Ion Battery Module for Future Mobile and Stationary Applications. *Energies* **2020**, *13*, 1477. [CrossRef]
37. Tsonopoulos, C.; Heidman, J. From Redlich-Kwong to the present. *Fluid Phase Equilibria* **1985**, *24*, 1–23. [CrossRef]

4.4. Congreso 1

Comparison of the influence of ammonia as a contaminant in high and low temperature proton exchange membrane fuel cell performance

Isorna Llerena, Fernando, López González, Eduardo, De las Heras Jiménez, Ainhoa, Saenz Cuesta, Jaime, Andújar, J.M. and Bolívar Raya, Juan Pedro

Presentado en:

Evento: V Iberian Symposium on Hydrogen, Fuel Cells and Advanced Batteries
Organizador: Universidad de La Laguna
Fecha: 05/07/2015 – 08/07/2015
Lugar: Tenerife, España.

4.5. Congreso 2

Influence of ammonia as contaminant on high temperature proton exchange membrane fuel cell performance

Fernando Isorna Llerena, Eduardo López González, Jaime Luis Sáenz Cuesta, Felipe Rosa Iglesias, Juan Pedro Bolívar Raya

Presentado en:

Evento: European Hydrogen Energy Conference (EHEC 2014)

Organizador: AeH_2, Spanish Hydrogen Association

Fecha: 12/03/2014 – 14/03/2014

Lugar: Sevilla, España

4.6. Congreso 3

Converting a fixed wing ICE RPA into an electric LiPo battery driven RPA for Precision Agricultural Purposes

F. Isorna Llerena, A. Fernández Barranco, J.A. Bogeat, J.M. Andújar, F. Segura

Presentado en:

Evento: VII Symposium on Hydrogen, Fuel Cells and Advanced Batteries, HYCELTEC 2019
Organizador: Universidad de Barcelona
Fecha: 01/07/2019 – 03/07/2019
Lugar: Barcelona, España
ISSN: 0360-3199

4.7. Congreso 4

Fuel cell-battery hybrid powered electric tricycle as a testing platform

F. Isorna Llerena, A. Fernández Barranco, J.A. Bogeat, J. Sáenz Cuesta; J.M. Andújar, F. Segura

Presentado en:

Evento: VII Symposium on Hydrogen, Fuel Cells and Advanced Batteries, HYCELTEC 2019
Organizador: Universidad de Barcelona
Fecha: 01/07/2019 – 03/07/2019
Lugar: Barcelona, España
ISSN: 0360-3199

4.8. Congreso 5

Use of unmanned fuel cell ground vehicles (UGVs) for precision agriculture (TecnOlivo Project)

F. Isorna Llerena, A. Fernández Barranco, J.A. Bogeat, E. López González, J.M. Andújar, F. Segura

Presentado en:

Evento: VII Symposium on Hydrogen, Fuel Cells and Advanced Batteries, HYCELTEC 2019
Organizador: Universidad de Barcelona
Fecha: 01/07/2019 – 03/07/2019
Lugar: Barcelona, España
ISSN: 0360-3199

Capítulo 5

Conclusiones Generales

Capítulo 5. Conclusiones Generales

La investigación experimental que comprende esta Tesis ha permitido obtener varios aspectos destacados y conclusiones importantes que se describen a continuación:

El hidrógeno renovable se posiciona como uno de los principales vectores energéticos en el largo plazo debido a que su producción y consumo es neutral climáticamente y no genera emisiones contaminantes. A diferencia de otros vectores energéticos renovables, el hidrógeno tiene la capacidad de ser almacenado, como gas a presión, hidruros metálicos, como otros compuestos químicos o en estado líquido, lo que permite un mayor grado de gestión.

Del mismo modo, permite desplazar el uso de materias primas industriales o fuentes de energía de origen fósil por materia prima renovable, abriendo una nueva ruta tecnológica para la electrificación del transporte y la movilidad sostenible.

La aplicación del hidrógeno renovable en el sector transporte se materializa en el uso de pilas de combustible. Estas pilas de combustible suelen instalarse en combinación con baterías eléctricas formando sistemas híbridos que pueden además aprovechar las ventajas del frenado regenerativo para recargar las baterías.

La utilización de pilas de combustible combinadas con baterías en vehículos, aporta una notable ventaja competitiva sobre los vehículos eléctricos de baterías eléctricas, permitiendo reducir los tiempos de recarga e incrementar la distancia recorrida por el vehículo antes del repostaje, al tiempo que se reduce el peso del vehículo al disminuir el tamaño de las baterías.

Actualmente, la tecnología de las pilas de combustible se encuentra totalmente desarrollada, aunque aún hay que investigar sobre el efecto de ciertos contaminantes en el rendimiento de las mismas.

En el caso de la aviación se espera que las pilas de combustible constituyan una alternativa como medio de propulsión para aeronaves. En la actualidad, solo se han desarrollado proyectos demostrativos para su uso en vuelos no comerciales. En el sector de pequeñas aeronaves no tripuladas se ha demostrado su aplicabilidad inmediata.

Respecto a las conclusiones obtenidas sobre los trabajos de contaminación del hidrógeno, este trabajo contribuye a los pocos estudios que cubren los efectos del NH_3 en las celdas de combustible de polímero de alta y baja temperatura, mostrando los mecanismos por los cuales el rendimiento de la membrana disminuye después de una etapa de intoxicación.

Como se ha justificado, es común encontrar trabajos enfocados a analizar los potenciales contaminantes del hidrógeno (básicamente CO, CO_2 y H_2S), pero difícilmente se pueden encontrar otros que muestren el efecto del NH_3 sobre las pilas de combustible de polímero de baja

temperatura (LT-PEFC) y hay una falta de trabajos de investigación que cubran el efecto del NH_3 en las pilas de combustible de polímero de alta temperatura (HT-PEFC).

Con respecto a los estudios experimentales (baja y alta temperatura), los resultados muestran claramente que la presencia de trazas de NH_3 en la corriente de alimentación del ánodo envenena el conjunto de electrodos de membrana, lo que provoca una caída del rendimiento de la celda. El envenenamiento depende de la cantidad de NH_3 en la corriente de alimentación del ánodo.

Con respecto a los experimentos llevados a cabo con la plataforma aérea, el trabajo presenta un caso real y práctico de transformación de un sistema aéreo no tripulado de ala fija, utilizado como objetivo aéreo y propulsado por un motor de combustión interna, en un RPAS eléctrico. Asimismo, y aprovechando una de las principales características de los aviones eléctricos, como es su bajo nivel sonoro, este RPAS eléctrico podría ser utilizada en entornos protegidos, como parques naturales, para la vigilancia y supervisión de diferentes especies animales.

El principal motivo para haber llevado a cabo esta transformación ha sido el aumentar la autonomía de vuelo del avión. Este propósito se ha logrado aumentando el rango en casi un 50%.

Los trabajos futuros en esta plataforma aérea consistirán en la sustitución de parte de las baterías a bordo por un sistema a base de hidrógeno y pilas de combustible.

Por último, se ha construido una plataforma de pruebas para establecer una comparación entre un vehículo eléctrico unipersonal alimentado únicamente por baterías, y el mismo alimentado por un sistema híbrido basado en hidrógeno y baterías. Ambos sistemas tenían un peso similar. De esta forma, es posible comparar ambas tecnologías, sus ventajas y desventajas, en una misma plataforma. La autonomía del sistema híbrido a base de hidrógeno fue estimada en 290 km, siendo mucho mayor que la del sistema a batería que alcanzó aproximadamente 15 km. Las conclusiones preliminares permiten reconocer que la hibridación energética aporta grandes ventajas específicas a las aplicaciones de movilidad urbana. De hecho, las mejoras se pueden cuantificar como un aumento del 1.790% en la energía específica y del 335% en la relación energía-volumen. Los resultados muestran que el vehículo eléctrico unipersonal equipado con un sistema de propulsión a base de hidrógeno proporciona no solo una mayor autonomía, sino que también tiene tiempos de recarga más cortos.

Las capacidades obtenidas en términos de autonomía, tiempo de recarga y, sobre todo, ventajas medioambientales en cuanto a la reducción de contaminantes, hacen de esta una propuesta prometedora y escalable para su uso en ciudades sostenibles.

Capítulo 6

Otras contribuciones científicas

Capítulo 6. Otras contribuciones científicas

6.1. Contribución 1

Multi-Objective Fuzzy Logic-Based Energy Management System for Microgrids with Battery and Hydrogen Energy Storage System

Francisco José Vivas, Francisca Segura, José Manuel Andújar, Adriana Palacio, Jaime Luis Sáenz, Fernando Isorna and Eduardo López

Publicado en:

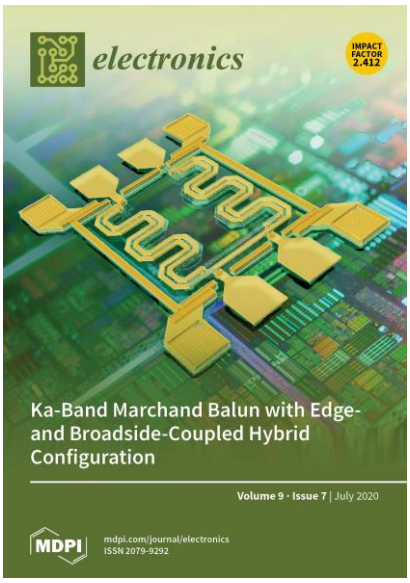

Revista: Electronics
Editorial: MDPI
Editor Jefe: Prof. Dr. Flavio Canavero
Referencia: Electronics 2020, 9, 1074
Año: 2020
ISSN: 2079-9292
DOI 10.3390/electronics9071074

Categoría	Rango revista / Total revista	Cuartil
Engineering, Electrical & Electronic	125 / 266	Q2
Impact Factor (2020)	2,412	
Citations	9	

electronics

MDPI

Article

Multi-Objective Fuzzy Logic-Based Energy Management System for Microgrids with Battery and Hydrogen Energy Storage System

Francisco José Vivas [1,*], Francisca Segura [1], José Manuel Andújar [1], Adriana Palacio [2], Jaime Luis Saenz [2], Fernando Isorna [2] and Eduardo López [2]

[1] Department of Electronic Engineering, Computer Systems and Automatic, University of Huelva, 21007 Huelva, Spain; francisca.segura@diesia.uhu.es (F.S.); andujar@diesia.uhu.es (J.M.A.)
[2] Instituto Nacional de Técnica Aeroespacial, INTA (Spanish Institute Aerospace Technique); Ctra. San Juan del Puerto, Km. 33, 21130 Mazagón, Spain; palacioca@inta.es (A.P.); saenzcjl@inta.es (J.L.S.); isornaf@inta.es (F.I.); lopezge@inta.es (E.L.)
* Correspondence: francisco.vivas@diesia.uhu.es

Received: 19 May 2020; Accepted: 26 June 2020; Published: 30 June 2020

check for updates

Abstract: This paper proposes a fuzzy logic-based energy management system (EMS) for microgrids with a combined battery and hydrogen energy storage system (ESS), which ensures the power balance according to the load demand at the time that it takes into account the improvement of the microgrid performance from a technical and economic point of view. As is known, renewable energy-based microgrids are receiving increasing interest in the research community, since they play a key role in the challenge of designing the next energy transition model. The integration of ESSs allows the absorption of the energy surplus in the microgrid to ensure power supply if the renewable resource is insufficient and the microgrid is isolated. If the microgrid can be connected to the main power grid, the freedom degrees increase and this allows, among other things, diminishment of the ESS size. Planning the operation of renewable sources-based microgrids requires both an efficient dispatching management between the available and the demanded energy and a reliable forecasting tool. The developed EMS is based on a fuzzy logic controller (FLC), which presents different advantages regarding other controllers: It is not necessary to know the model of the plant, and the linguistic rules that make up its inference engine are easily interpretable. These rules can incorporate expert knowledge, which simplifies the microgrid management, generally complex. The developed EMS has been subjected to a stress test that has demonstrated its excellent behavior. For that, a residential-type profile in an actual microgrid has been used. The developed fuzzy logic-based EMS, in addition to responding to the required load demand, can meet both technical (to prolong the devices' lifespan) and economic (seeking the highest profitability and efficiency) established criteria, which can be introduced by the expert depending on the microgrid characteristic and profile demand to accomplish.

Keywords: energy management system; fuzzy logic controller; renewable source-based microgrid; battery and hydrogen energy storage system

1. Introduction

Renewable energy-based microgrids are receiving increasing interest in the research community, since they play a key role in the challenge of designing the next energy transition model [1]. However, the stochastic character exhibited by the most important renewable energy sources (RES), such as photovoltaic (PV) and wind, represents a huge disadvantage for the stability, security, and reliability of microgrids. To solve this problem, the integration of energy storage systems (ESS) is required to

allow the absorption of the energy surplus, and to ensure power supply when the renewable resource is insufficient.

Regarding the ESS technology, the combined use of battery-and-hydrogen ESS is a promising solution, especially if hydrogen is produced in the microgrid itself and exclusively through renewable resources [2]. This hybrid ESS can be used not only to meet the load demand, but it can also be managed with economic interests. Indeed, the ESSs can participate in the electrical market by purchasing the energy from the main power grid during the off-peak hours (cheaper energy), storing it, and selling it later to the main power grid during the peak demand hours (more expensive energy).

On the other hand, in these convulsive times (COVID-19 pandemic), where the world population is obliged to be confined to preserve global health, good development of the productive activity and entertainment (teleworking, e-commerce, social networks, audiovisual contents, e-learning, etc.) inevitably depends, on the last instance, on a reliable electrical supply. Grid disconnections are detrimental to both customers and providers [3–5].

After an unexpected interruption, if a microgrid reacts to the new working conditions in order to restore the normal expectations of the users, it receives the name of *resilient* microgrid [6,7]. The use of combined battery-and-hydrogen ESS in resilient microgrids offers multiple advantages, like [8]: (1) high electric efficiency (> 45%); (2) overall efficiency of 85–93%; (3) low noise (silent operation); (4) reduction of air pollution (low emission); (5) high availability (24/7); (6) dispatchable with the capability to follow the load.

Finding a commitment between the size of the renewable microgrid, its ESS, and the quality and supply required towards the user, is not an easy task. Today, regardless of the environmental benefits, 100% renewable networks are still expensive, due especially to the large size that this type of grid requires, due to the intermittency of renewable resources (it is the case of solar and wind energy). Therefore, several authors agree that in microgrids, an energy management system (EMS) is essential for optimal use of these distributed energy resources in intelligent, secure, reliable, and coordinated ways [9]. The planning of the operation of this type of grid based on renewable energy sources requires both an efficient dispatching for the available and the demanded energy, and a reliable short- and long-term forecasting tool [10,11]. That is, the management of renewable energy-based microgrids brings significant challenges that need to be addressed with advanced control techniques [12].

Having already demonstrated the relevance of EMS in microgrids, Zia et al. [9] classified the EMS solutions into six categories: (1) classical techniques, such as linear and nonlinear programming methods, dynamic programming, and rule-based methods; (2) EMSs based on meta-heuristic approaches, such as those based on genetic and swarm optimization; (3) EMSs based on artificial intelligent methods such as fuzzy logic and neural networks or multi-agent systems; (4) EMSs based on stochastic and robust programming approaches; (5) EMSs based on model predictive control (MPC); (6) hybrid EMSs approaches.

However, EMS developers not only have to decide which technique to use, but also establish management criteria. In this sense, Vivas et al. [13] deduced that energy management strategies in renewable microgrids can be classified according to the three following energy distribution criteria: (1) to ensure the demand, (2) to meet technical decision factors, and (3) to look for the best economic return. Nevertheless, in the three cases, the solutions for the EMS found in the literature are based on simple heuristic strategies based on hysteresis operation modes [14–16], fuzzy logic [17–19], and model-based control algorithms aimed to optimize multi-objective functions [20–22]. Regarding their characteristics, the major inconvenience of the hysteresis operation mode is its inability to allow partial-load operation of the devices [23–25], while the model-based control requires explicit and detailed models that faithfully describe the plant behavior.

Fuzzy logic has demonstrated for decades (end of the 20th century) its innate ability to solve complex modeling and control problems, both from an analytical [26] and heuristic [27] perspective. The well-known Mamdani-type fuzzy inference system [28] that makes it possible to carry out practical controllers based on linguistic (heuristic) rules, without the need to have a precise plant model,

has attracted a lot of interest towards the field of renewable energy systems, since linguistic rules can simplify the control of these complex systems [29]. By this kind of fuzzy control system, the part-load operation of hydrogen-based systems like fuel cells [29,30] and electrolyzers [31] is technically feasible. For all these devices, the efficiency is increased by part-load operation, so it is expected that the microgrid will become more efficient.

Based on the literature review, fuzzy logic can be used not only in the development of the microgrid EMS, but also in the definition of protection strategies and the establishment of decision rules. Based on this, Bukhariet et al. [32] developed two different fuzzy systems to detect, classify, and locate the faults in microgrids, and Oliveira et al. [10] proposed a fuzzy-based methodology approach for microgrids under an islanded operation that aimed to maximize the number of supplied customers during a minimum period of time.

Regarding the scientific works that propose EMS based on fuzzy logic controllers, in [33] the stochastic nature of the solar energy collection was handled by the fuzzy logic system, which provides continuous control conditions, instead of direct digital control, where the boundaries are discontinuous.

On the other hand, Kamel et al. presented recently in [34] a comparative study to validate the results of the classic PI control with the results of a fuzzy control system. The controller must establish the fuel cell current reference on the basis of three input signals: the load power, PV power, and battery SOC. It is a simple controller that consists of eight fuzzy rules, and although the authors confirmed the PI controller is easier for implementation, they recognize future research should be focused on improving the system with regard to cost optimization.

In spite of the simplicity of these solutions, the non-use of optimization parameters based on equipment degradation, operation modes, or operating costs of the microgrid causes an inefficient solution from a technical and economic point of view.

On the other hand, technical criteria were included in the fuzzy logic-based EMS presented by Zhang et al. in [17]. The target was to use solar power to meet the power demand and the surplus to maximize the hydrogen production. This allowed for minimizing the usage of battery and therefore the overall microgrid's efficiency increased, and the battery lifespan was prolonged.

Fuzzy logic-based EMSs that include economic parameters can help to determine an optimal solution from an economic point of view. Thereby, El-Bidairi et al. proposed in [35] a multi-objective optimization technique for stand-alone microgrids which determines the optimal power generation scheduling and selects the optimal capacity of the ESSs with minimal operational cost. In this same line, the objective of the study carried out in [18] was to examine the effects of time-varying electricity prices on the performance of ESS for a grid-tied microgrid utilizing an optimized fuzzy logic controller (FLC). However, these economic solutions, with more global goals, do not determine a favorable operation for the involved devices due to not having enough technical criteria to avoid problems associated with different operating regimes.

Based on the above, the main contribution of this paper is the proposal of a multi-objective fuzzy logic-based EMS with Mandani-type structure and inference, for microgrids with combined battery-and-hydrogen ESS, which ensures the power balance according to the load demand, taking into account the improvement of microgrid performance from technical and economic points of view. The fuzzy logic approach is chosen since linguistic rules are interpretable and they can incorporate the knowledge that an expert has of the microgrid, which can simplify the management and control of it, given its complexity. In fact, the developed FLC combines the microgrid knowledge from experts and collected data to define the fuzzy rule bases. Then, the developed FLC, in addition to responding to the load demand, can meet both technical criteria (to prolong the devices' lifespan) and economic criteria (to reduce the electricity purchased from the main power grid and to improve the trade and profitability of the sale/purchase of energy). Additionally, the developed FLC considers the power balance forecast. In this case, the prediction model used to obtain the solar generation profile is based on the use of a multilayer neural network, and the demand profile model is based on a specific consumption profile proposed for a residential type application. Therefore, knowing the models of renewable production

and consumption profile, the power balance in the following sampling period can be calculated as the difference between both terms.

To highlight the novelty of the research, Table 1 summarizes the main characteristics of the authors' proposal in comparison with revised literature.

Table 1. Comparison of the findings of the proposed paper with previous scientific works.

Reference	Objective	Decision-Making	ESS	Power Balance Forecast	Operating Time
Authors' proposal	Power balance, Conservative use of ESS, Cost	Short- and long-term	Battery and Hydrogen	Yes	3 days (able to be extended)
[33,34]	Power balance	Short-term	Battery and Hydrogen	No	1 day
[17]	Power balance, Conservative use of Battery,	Short-term	Battery and Hydrogen	Yes	1 year
[35]	Power balance, Size ESS, Cost	Long-term	Battery	No	12 days
[18]	Power balance, Size ESS, Cost	Long-term	Battery and Hydrogen	No	7 days

This paper is organized as follows: Section 2 describes all the facilities, devices, and software that have been used to carry out the research. Section 3 develops step by step the fuzzy logic-based EMS, which will be further tested in Section 4. The results are discussed in Section 5, highlighting the principal aspects regarding the EMS functioning. Finally, in Section 6 the principal conclusions of the research are addressed.

2. Materials and Methods

The microgrid used to test the developed EMS is shown in Figure 1, found at the Spanish Institute of Aerospace Technology, (Spanish acronym: INTA), and it is based on the use of renewable generation and hybrid ESS based on batteries and hydrogen.

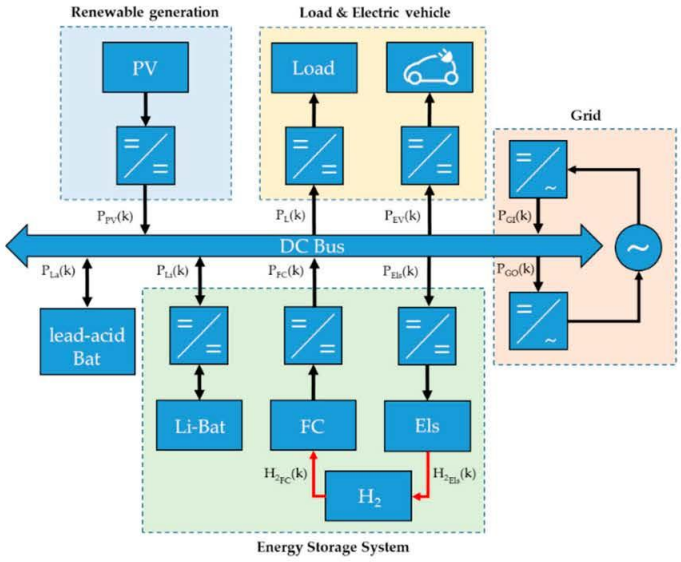

Figure 1. Residential-type microgrid.

The proposed configuration is designed to respond to a residential-type application, in which a bidirectional flow of energy is allowed between the renewable microgrid and the main power grid.

This configuration was chosen because it allows the development of different strategies in the field of the electricity market and, in the last instance, to get an end-consumer perspective.

In the microgrid scheme of Figure 1, renewable generation is given by a 5 kW_p monocrystalline technology PV field, and the use of associated power electronics to supply to the DC bus the maximum available renewable power. To decrease the current in the microgrid, reducing losses due to parasitic resistances and the sections in cables and printed circuit boards, the microgrid has been designed around a high voltage DC bus (360 VDC).

According to the demand, typical profiles for low-medium power residential applications (<10 kWe) were adopted. Additionally, the load profile associated with the recharging process of a medium-capacity electric vehicle was considered.

Regarding ESS, it is made up of two subsystems, a Li-ion battery bank (43.2 kWh) and a hydrogen system. The lead-acid battery bank (36 kWh) has the function to stabilize the DC bus voltage, therefore the lead-acid battery bank is directly connected to the DC and it will not serve as an energy storage system. This implies that lead-acid battery SOC must always be kept high, avoiding the need for a specific control system. This direct connection of the lead-acid battery bank makes it possible to take advantage of three keys issues: (1) If the lead-acid battery bank was not connected to DC bus, the grid controller would be responsible for regulating the DC bus voltage. This involves a more complex control logic because the grid is responsible for the voltage control and the setting of the operating power of the grid according to the EMS setpoint. This requires a perfect synchronism between the rectifier (energy input to the bus) and the inverter (energy output from the bus) and the rest of the elements of the microgrid, and control dynamic fast enough to guarantee the stability of the bus voltage under fast changes in generation/consumption profile. (2) The use of the lead-acid battery bank as a backup system ensures that the DC bus voltage is maintained within a known operating range under any circumstances, while guaranteeing the power balance during the transients associated with the switching on and off of the rest of the equipment, mainly the hydrogen system. In this way, the equipment linked to grid operation, rectifier, and inverter only have the function of imposing the power setpoint established by the EMS, greatly reducing the associated control complexity. Finally, (3) the battery bank can act as a short/medium-term storage system, and therefore a further degree of freedom in energy management definition is available.

With respect to the ESS, the objective of the Li-ion battery bank is to act as a short-medium-term storage system, allowing a considerably lower SOC than the lead-acid battery bank, and taking advantage of its high cycle durability. As a long-term ESS, a hydrogen system is used. In this case, a circular system, which allows the generation of hydrogen by an alkaline electrolyzer (1 Nm^3/h, 5 kWe), its subsequent storage in a pressurized tank (1.044 Nm^3) at the hydrogen outlet pressure of the electrolyzer (30 bar), and the further generation of electrical energy through the use of a polymer electrolyte membrane (PEM) fuel cell (3 kW_p).

A real image of each microgrid component is shown in Figure 2, and their main technical characteristics are collected in Table 2.

As is widely known, a fuzzy logic-based controller has the advantage to manage the microgrid without the need of having a model of the microgrid. Obviously, the microgrid model will be necessary to test and fine-tune the developed EMS (if applicable) by simulation before applying it to the actual microgrid. A model of this type of microgrid (hydrogen systems hybridization with renewable energy systems) has been already developed by the authors in previous works [23]. Therefore, the general model only needs to be adapted to the specific microgrid topology in each case. Figure 3 shows the MATLAB®-Simulink® microgrid configuration and the fuzzy logic-based EMS implemented in MATLAB®-Fuzzy Logic Toolbox™ environment.

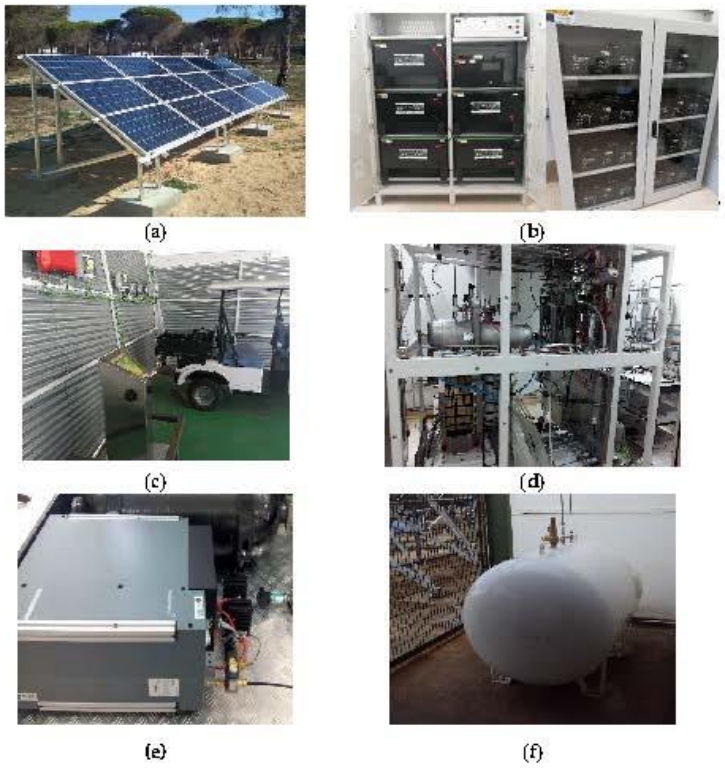

Figure 2. Detail of the microgrid components of Figure 1: (**a**) photovoltaic field; (**b**) Li-ion (left) and lead-acid battery (right); (**c**) Electric vehicle (white car on the background); (**d**) Alkaline electrolyzer; (**e**) polymer electrolyte membrane fuel cell; and (**f**) pressurized hydrogen tank.

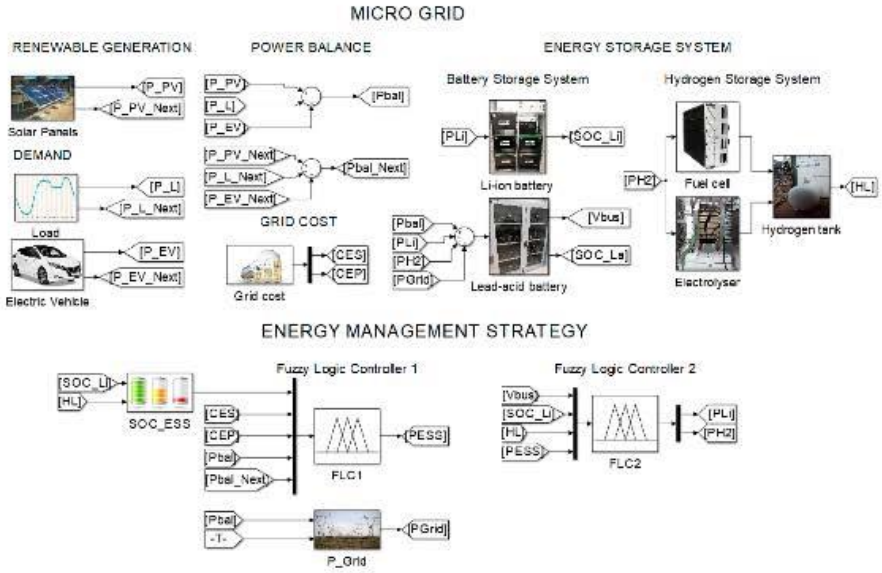

Figure 3. MATLAB®-Simulink® Model of the microgrid of Figure 1 together with its energy management system.

Table 2. Technical characteristics of the subsystems that make up the microgrid.

Component	Manufacturer	Nominal Parameters
Solar PV mono-Si	BP® 60 (BP Solar®, Madrid, Spain)	5 kW_p
Electric Vehicle	Nissan® Leaf (Nissan®, Yokohama, Japan)	30 kWh
Lead-acid battery bank	U-POWER® UP100-12 (POWER®, Sofia, Republic of Bulgaria)	30×12 V, 100 Ah (36 kWh)
Li-ion battery bank	CEGASA® (CEGASA®, Basque Country, Spain)	75×3.2 V, 180 Ah (43.2 kWh)
Alkaline Electrolyzer	ARIEMA® (ARIEMA®, Madrid, Spain)	1 Nm^3/h, 5 kWe
PEM fuel cell	Horizon® H-3000 (Horizon®, Singapore)	3 kW_p
Hydrogen storage tank	Lapesa® LSP1000H (Lapesa®, Zaragoza, Spain)	1.044 Nm^3, 30 bar

3. Energy Management System Design

This section develops the EMS, paying special attention to the FLC. It is assumed that sensors are available to take measurements of the necessary variables, as well as actuators for the control of the power electronics (see Figure 1) that govern the microgrid. None of these elements, parts of the EMS, are the subject of this paper. Next, the FLC design will be explained step by step.

3.1. Power Balance on the DC Bus

Based on Figure 1, the Kirchhoff's Current Law always needs to be accomplished, so the power sum in the DC bus must always be zero. If all the loads are satisfied under any circumstance, this means that the main power grid sometimes will be delivering power to the DC bus (power deficit in the microgrid) and others will be extracting power from the microgrid, which will imply energy transfer from the microgrid to the main power grid. In the microgrid shown in Figure 1, the only power source (in a strict sense) is the PV field. The hydrogen storage system, as part of the ESS, can be a source if the fuel cell is running or a load if the electrolyzer is operating. Regarding the Li-ion battery bank as part of the ESS, it depends on whether the battery bank is recharging or supplying power from/to the DC bus. Then, before adopting a signs convention, the sum of the powers on the DC bus follows Equation (1):

$$P_{PV}(k) + P_{La}(k) + P_L(k) + P_{EV}(k) + P_{ESS}(k) + P_{Grid}(k) = 0, \quad (1)$$

where:

$P_{PV}(k)$: renewable generation (PV panels) at sampling time k (W);
$P_{La}(k)$: lead-acid battery bank power at sampling time k (W);
$P_L(k)$: residential load demand at sampling time k (W);
$P_{EV}(k)$: electric vehicle demand at sampling time k (W);
$P_{ESS}(k)$: energy storage system power at sampling time k (W);
$P_{Grid}(k)$: main power grid power at sampling time k (W).
Being, following Figure 1:

$$P_{ESS}(k) = P_{Li}(k) + P_{H_2}(k), \quad (2)$$

where:

$P_{Li}(k)$: Li-ion battery bank power at sampling time k (W);
$P_{H_2}(k)$: hydrogen system power at sampling time k (W), $P_{H_2}(k) = P_{Els}(k)$ or $P_{H_2}(k) = P_{FC}(k)$, where $P_{Els}(k)$ is the electrolyzer power at sampling time k (W) and $P_{FC}(k)$ is the fuel cell power at sampling time k (W).
Again, following Figure 1:

$$P_{Grid}(k) = P_{GI}(k) \text{ or } P_{Grid}(k) = P_{GO}(k), \quad (3)$$

where:

$P_{GI}(k)$: input power; power supplied from the main power grid at sampling time k (W);
$P_{GO}(k)$: output power; power supplied to the main power grid at sampling time k (W).

The adopted signs criteria are determined by the direction of the energy flow in the DC bus, considering the energy injected to the DC bus as positive, and the energy extracted from the bus as negative. Depending on the microgrid operation state, the signs of the different powers must assure Equation (1), taking into account Equations (2) and (3) regarding whether the subsystems are injecting to the DC bus or extracting power to/from it. Of course, in a dynamic system as the microgrid of Figure 1, the only way to satisfy Equation (1) is by means of the EMS.

3.2. *Fuzzy Logic Controller Structure*

The fuzzy logic-based EMS proposed in this paper is shown in Figure 4. Note that to elaborate the fuzzy rule base, the FLC input variables have been grouped into two sets, named FLC1 and FLC2. The first makes decisions about the exchange with the main power grid, and the second over the ESS use. This will be explained below.

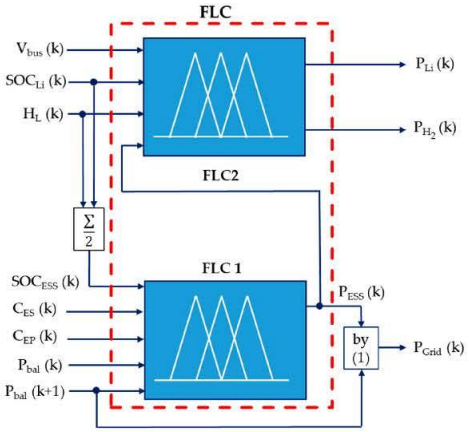

Figure 4. Fuzzy logic-based EMS control structure.

As already said, the only source (in the strict sense) in the microgrid is the PV field, so the power balance must be guaranteed by the ESS and/or the main power grid. Consequently, following the adopted sign criteria, the power balance will be defined by Equation (4), see Figure 1:

$$P_{bal}(k) = P_{PV}(k) - P_L(k) - P_{EV}(k). \tag{4}$$

$P_{bal}(k)$ will be positive when there is energy surplus in the microgrid and negative in case of deficit. In the first case, the surplus energy must be managed by the EMS producing hydrogen and/or recharging batteries and/or selling energy to the main power grid. In the second case, the microgrid power will be balanced taking the power of the batteries, and/or fuel cell and/or the main power grid. So, $P_{bal}(k)$ needs to be an input variable of the FLC. However, the EMS cannot act and verify the results of its action in the same sampling to make the appropriate decisions, so it must have information in advance. Then, for the best EMS functioning, the FLC needs to know the P_{bal} forecasting, so $P_{bal}\ (k+1)$ needs to be the other FLC input variable. Although it is not the subject of this document, there is a large bibliography on renewable generation forecasts and consumption profiles.

As was explained in Section 2, and based on Figure 1, the role of the lead-acid battery bank is to regulate the DC bus voltage. Therefore, it does not have tasks related to power management, except the instantaneous ones in the DC bus. So, the lead-acid battery SOC must be always high in order to assure the proper voltage in the DC bus, $V_{bus}(k)$. According to this, the EMS must have information in each sampling about the V_{bus}, so this voltage must be an input variable of the FLC.

Unlike the previous case, the operating voltage of the Li-ion battery bank is not a fundamental parameter in the operation of the microgrid (see Figure 1 to note that the Li-ion battery bank is not

directly connected to the DC bus). Its role in the microgrid is its ability to store energy to be used by the microgrid when needed. The EMS needs to know its SOC ($SOC_{Li}(k)$)—consequently, this value must be an input variable of the FLC. Furthermore, since the Li-ion battery bank must effectively contribute to the achievement of Equation (1) delivering/absorbing energy to/from the DC bus, the EMS must decide on its power, $P_{Li}(k)$ and its sign, so this is an FLC output variable.

The last element of the ESS is the hydrogen system. Its availability to deliver power to the DC bus through the fuel cell is given by the level of hydrogen in the storing tank, $HL(k)$; therefore, this need to be another input variable. On the other hand, depending on the energy state in the microgrid, surplus or deficit, the EMS must decide, respectively, to have the electrolyzer operating producing hydrogen or the fuel cell delivering energy to the DC bus. So, $P_{H_2}(k)$ and its sign (negative for electrolyzer operating or positive in the case of the fuel cell) will be another FLC output variable.

Additionally, since Li-ion battery bank and hydrogen storage subsystem made up the ESS, and they need to work as a whole, it is interesting that the EMS knows the joint possibilities to deliver power to the DC bus. Thus, a new FLC input variable has been created as the average value of $SOC_{Li}(k)$ and $HL(k)$; its name is $SOC_{ESS}(k)$.

So far, the relationships between the internal elements of the microgrid have been described. The way EMS interacts with the main power grid will be explained below. As Figure 4 shows, the FLC decides the utilization of the main power grid based on the actual $SOC_{ESS}(k)$, $P_{bal}(k)$, and the forecasting power of the ESS, $P_{ESS}(k+1)$, and of the power balance, $P_{bal}(k+1)$, together with the purchase price, $C_{EP}(k)$, and the sale price, $C_{ES}(k)$, of the electricity. Then, for example, in case there is power deficit and the electricity cost from the main power grid is low and SOC_{ESS} is also low, it will be interesting to use the main power grid to balance the microgrid power and to recharge the ESS. However, if the electricity cost is high, it will be interesting to use the main power grid only for power balancing.

The FLC system schematized in Figure 4 shows that it is a complex multivariable control system with nine inputs and three outputs. Taking into account its structure, the fuzzy inference is defined by two fuzzy rule bases (one for FLC1 and other for FLC2); however, to facilitate the inference logic, FLC1 has been built using two fuzzy rule bases, one for energy surplus situations and another for deficit situations.

Integrated into the EMS, the FLC functions as follows (see Figure 4): In the sampling time k, it receives the real (physical) variables ($V_{bus}(k)$, $SOC_{Li}(k)$, $HL(k)$, $P_{ESS}(k)$, $SOC_{ESS}(k)$, $C_{ES}(k)$, $C_{EP}(k)$, $P_{bal}(k)$ and the predicted $P_{bal}(k+1)$). Then, it fuzzifies these variables to convert them in linguistic ones ($V_{bus-fuzz}(k)$, $SOC_{Li-fuzz}(k)$, $HL_{-fuzz}(k)$, $SOC_{ESS-fuzz}(k)$, $C_{ES-fuzz}(k)$, $C_{EP-fuzz}(k)$, $P_{bal-fuzz}(k)$, $P_{bal-fuzz}(k+1)$). From here, FLC can use the linguistic variables to make the fuzzy inference, that is, to evaluate the fuzzy rules of each fuzzy rule base, which delivers the output linguistic variables $P_{Li-fuzz}(k)$, $P_{H_2-fuzz}(k)$, and $P_{ESS-fuzz}(k)$. After that, the FLC makes a defuzzification process to obtain the real output variables of the FLC: $P_{Li}(k)$, $P_{H_2}(k)$, and $P_{ESS}(k)$ (Figure 5). Now, these can be used by the EMS in order to act over the microgrid and control it.

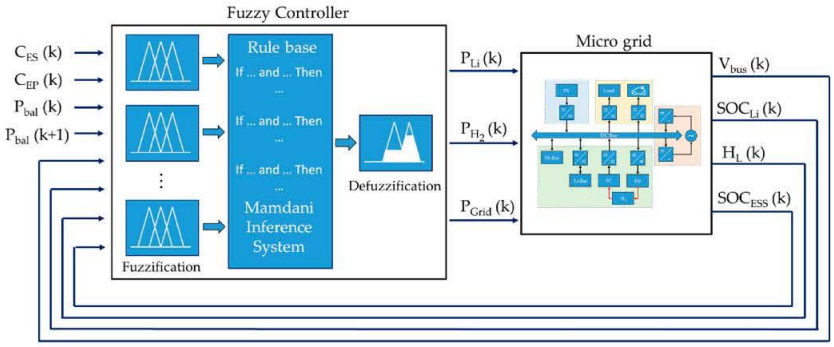

Figure 5. EMS control structure.

3.3. Fuzzy Sets

Based on the knowledge of the microgrid and in its operation way already explained in the previous section, the fuzzy sets of Figure 6 have been defined. Due to its simplicity and the fact that the microgrid does not need overly smooth control, fuzzy sets have been defined using triangular membership functions. The universe of discourse of each variable has been decided according to technical characteristics and the microgrid operation, Equation (5).

$$\begin{gathered} 350\ \mathrm{V} \le V_{bus}(k) \le 440\ \mathrm{V};\ 20\% \le SOC_{Li}(k) \le 100\%;\ 2\ Nm^3 \le HL(k) \le 20\ Nm^3; \\ 15\% \le SOC_{ESS}(k) \le 100\%; -5000\ W \le P_{bal}(k) \le 5000\ W; -5000\ W \le P_{bal}(k+1) \le 5000\ W; \\ -5000\ W \le P_{Li} \le 5000\ W; -5000\ W \le P_{H_2} \le 3000\ W; -5000\ W \le P_{ESS} \le 5000\ W; \\ 0 \le C_{ES} \le 0.08\ €;\ 0 \le C_{EP} \le 0.12\ € \end{gathered} \tag{5}$$

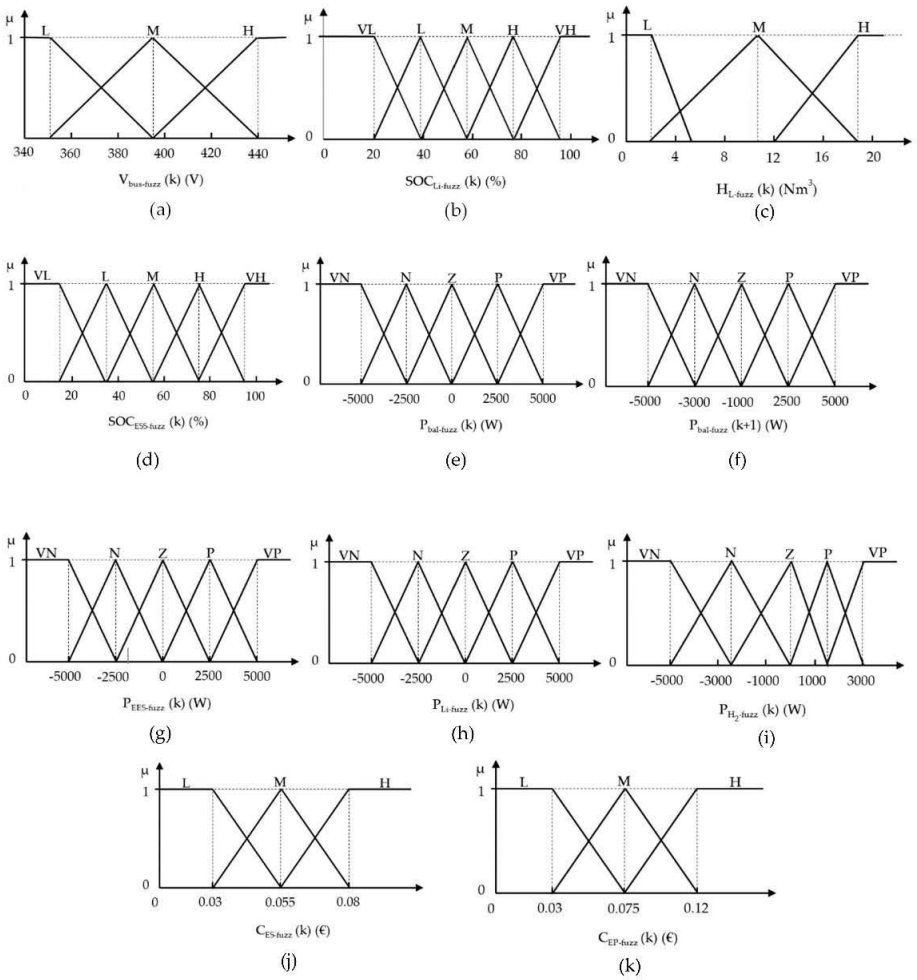

Figure 6. Membership functions of the fuzzy sets for: (**a**) bus voltage, $V_{bus-fuzz}(k)$; (**b**) Lithium battery state of charge, $SOC_{Li-fuzz}(k)$; (**c**) hydrogen level, $HL_{-fuzz}(k)$; (**d**) ESS state of charge, $SOC_{ESS-fuzz}(k)$; (**e**) Power balance, $P_{bal-fuzz}(k)$; (**f**) Power balance prediction, $P_{bal-fuzz}(k+1)$; (**g**) ESS power setpoint, $P_{ESS-fuzz}(k)$; (**h**) Lithium battery power setpoint,$P_{Li-fuzz}(k)$; (**i**) Hydrogen-based system power setpoint, $P_{H_2-fuzz}(k)$; (**j**) Grid selling cost, $C_{ES-fuzz}(k)$; (**k**) Grid purchase cost, $C_{EP-fuzz}(k)$.

Then, for example, limits of the DC bus voltage ($V_{bus}(k)$) have been determined using two fundamental criteria, the connected devices permissible operating range (350–450 VDC), as well as the safe operating voltage for the lead-acid battery bank (330–440 VDC), responsible for maintaining the voltage in range on the DC bus. The upper and lower limits are determined by the most limiting condition. In this case, the lower limit is the connected devices' permissible operating range (350 V). On the other hand, the upper limit will be the maximum recommended battery charging voltage, which is 440 V (2.4 V/cell). See Figure 6a.

The operation limit of the Li-ion battery bank ($SOC_{Li}(k)$) must correspond with its role as short-medium-term ESS. Taking advantage of its cycle durability, its minimum permissible SOC is 20%. This type of battery can operate in this range without suffering damage. See Figure 6b.

On the other hand, the lead-acid battery bank has the pivotal mission of guaranteeing the voltage stability in the DC bus, as well as to act in the very short term, guaranteeing the power balance during the transient switching of the rest of the elements connected to the DC bus. In addition to that, and as it is well known, the allowed SOC in this type of batteries is considerably more restrictive than in the case of Li-ion (never less than 60%). In any case, this is guaranteed by the range allowed for $V_{bus}(k)$.

On the other hand and regarding the second actor of the ESS, the universe of discourse of the hydrogen level ($HL(k)$) is determined by the maximum capacity of the storage tank (20 Nm^3), and the recommended value to ensure a minimum operating pressure (2 Nm^3). See Figure 6c. Then, $SOC_{Li}(k)$ and $HL(k)$ ranges define the $SOC_{ESS}(k)$ range, whose minimum value is the average between 10% and 20%, i.e., 15%. See Figure 6d.

Regarding $P_{bal}(k)$, when all the $P_{PV}(k)$ is available and there is no consumption in the microgrid Equation (4), its value is that corresponding to the PV field, i.e., 5000 W. On the contrary, if there is not $P_{PV}(k)$ available and the consumption is the maximum, its value is −5000 W. See Figure 6e for $P_{bal}(k)$ and Figure 6f, obviously the same for $P_{bal}(k+1)$. Similarly, when the ESS is being charged from the microgrid or it is supplying to the microgrid, its power range ($P_{ESS}(k)$) can vary from −5000 W to 5000 W, respectively (Figure 6g). The first case represents the maximum load power of the ESS from the microgrid; the second indicates that all the microgrid loads are supplied by the ESS. In the ESS, the power will be shared between the Li-ion battery bank and the hydrogen system, so this leads to the given range of the universes of discourse in Equation (5) for P_{Li}, P_{H_2}, and P_{ESS}. Remember that the fuel cell maximum power is 3000 W. See Figure 6h,i.

Finally, the universes of discourse of $C_{ES}(k)$ and $C_{EP}(k)$ shown in Figure 6j,k have been defined, taking into account the Spanish market at the time of writing the paper.

3.4. Fuzzy Rules Base

On the basis of the above considerations respect to the microgrid functioning and considering the memberships functions described in Figure 6, three fuzzy rule bases have been defined (two for FLC1, depending on if the situation is purchasing or selling electricity to the main power grid, and one for FLC2). Each fuzzy rule base, as usual, is composed of rules of the form IF-THEN, as follows:

$$\text{IF } V_{bus-fuzz}(k) \text{ is } L \text{ and } P_{ESS-fuzz}(k) \text{ is } VP \text{ and } SOC_{Li-fuzz}(k) \text{ is } VL \text{ THEN} \begin{cases} P_{Li-fuzz}(k) \text{ is } P \\ P_{H_2-fuzz}(k) \text{ is } Z \end{cases}$$

FLC2 includes 59 rules and FCL1 contains 98 rules (36 rules in case of energy surplus and 62 in case of energy deficit). Regarding the high number of rules, the usual format (detail rule by rule from each fuzzy rule base) may not be the easiest and most illustrative way to do this. Therefore, to illustrate in a glance the inference of the three fuzzy rule bases, Figures 7–9 illustrate the respective flow charts.

In the case of energy excess, Figure 7 ($P_{bal}(\mathrm{k}) > 0$), the use of the microgrid's own resources is prioritized over the use of the main power grid, as long as the energy stored is close to its maximum level ($SOC_{ESS-fuzz}(k) = \mathrm{VH}$). In the event that the ESS is not capable of absorbing more energy ($SOC_{ESS-fuzz}(k) = \mathrm{VH}$), exclusive use of the main power grid is made to accomplish Equation (1).

In the event that the energy stored reaches a medium or high value, it is possible to sell the energy excess to the main power grid with the aim that while the energy reserves in the ESS are guaranteed, the EMS looks for economic profits. Energy sales to the main power grid will be determined by the energy excess, sale price, stored energy, and the power balance forecast in the next sampling period. Finally, if the ESS is not capable of absorbing more energy, exclusive use of the main power grid is made to accomplish Equation (1).

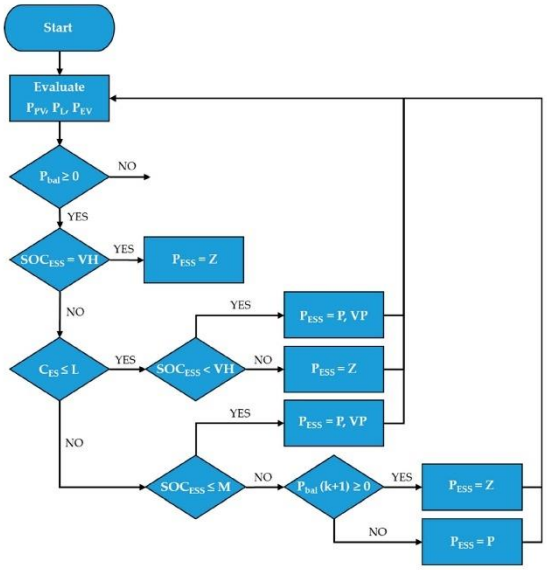

Figure 7. FLC1 flowchart diagram in the sampling k when there is an energy surplus situation (VL: Very Low, L: Low, M: Medium, Z: Zero; P: Positive, VP: Very Positive, VH: Very High; according to membership functions defined in Figure 5). It is understood that the sets used are fuzzy.

By contrast, during energy deficit situations, Figure 8 ($P_{bal}(k) < 0$), the use of the microgrid's resources is prioritized over the use of the main power grid, as long as the energy stored is not close to its minimum level ($SOC_{ESS-fuzz}(k) = \text{VL}$). If this is the case, to guarantee the power balance the EMS makes use of the main power grid.

On the other hand, if the stored energy in ESS is at an intermediate level, joint use of the ESS and main power grid can be made to satisfy demand if the cost of purchasing energy is low, allowing a more conservative use of the microgrid's resources. As in the previous case, energy purchases from the main power grid will be determined by the energy deficit, purchase price from the main power grid, stored energy, and prediction of generation and consumption in the next sampling period.

With respect to the FLC2, the designed flow chart to build its fuzzy rule base is shown in Figure 9. Its function is to calculate the power setpoint of each device that integrates the ESS: the Li-ion battery bank and hydrogen system. The control premise is determined by the role of each system, the level of stored energy, and operating restrictions.

With respect to the Li-ion battery bank, its high performance and the high number of operating cycles mean the battery bank does not require special control actions for its operation. Its storage capacity will be maximized by making use of its high depth of discharge (DOD), resulting in a more conservative use of the hydrogen system.

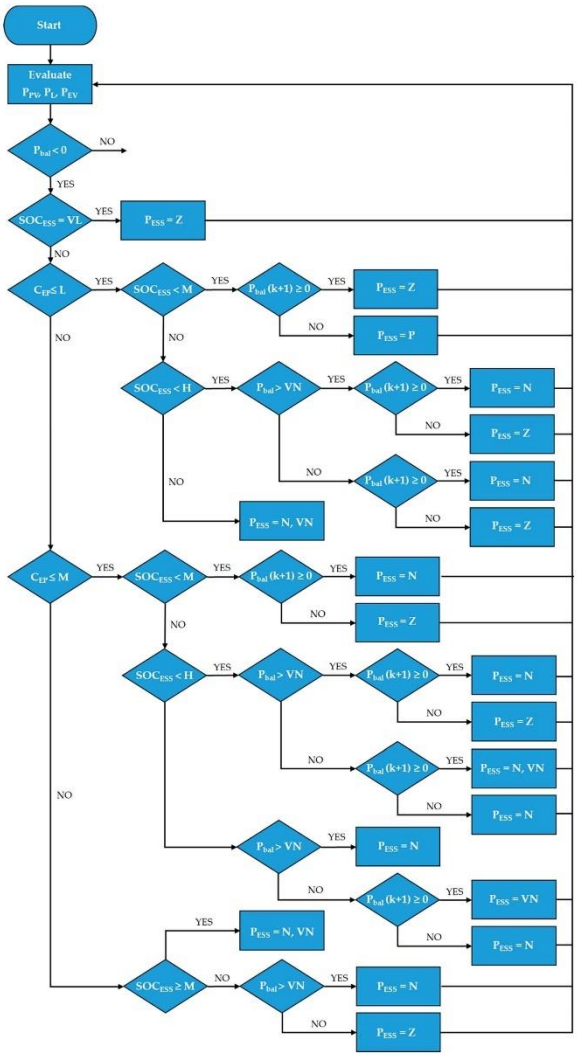

Figure 8. FLC1 flowchart diagram in the sampling k when there is an energy deficit situation (VL: Very Low, VN: Very Negative, L: Low, N: Negative; Z: Zero; M: Medium, H: High; P: Positive, VP: Very Positive, VH: Very High; according to membership functions defined in Figure 5). It is understood that the sets used are fuzzy.

Considering the direct connection of the lead-acid battery bank to DC high voltage bus (Figure 1), it is necessary to implement a maximum voltage charging protocol, which guarantees the safe and efficient use of the battery bank. It is also necessary to limit the minimum discharging voltage, ensuring the DC bus voltage. Based on the described functionality and with the objective of prolonging the lead-acid battery bank lifespan, a strict V_{bus} control has been defined.

Considering the hydrogen system, due to its role as a long-term storage system, its reduced lifespan, and high cost, it is necessary to guarantee a conservative use. To get it, the developed FLC2 will work on two lines of action. The first one is to prioritize the use of the Li-ion battery bank, and the second is to reduce the operating stress of electrolyzer and fuel cell. For this purpose, it is necessary to

carry out the correct definition of the membership functions of the FLC2 in order to guarantee smooth changes in the power set-points.

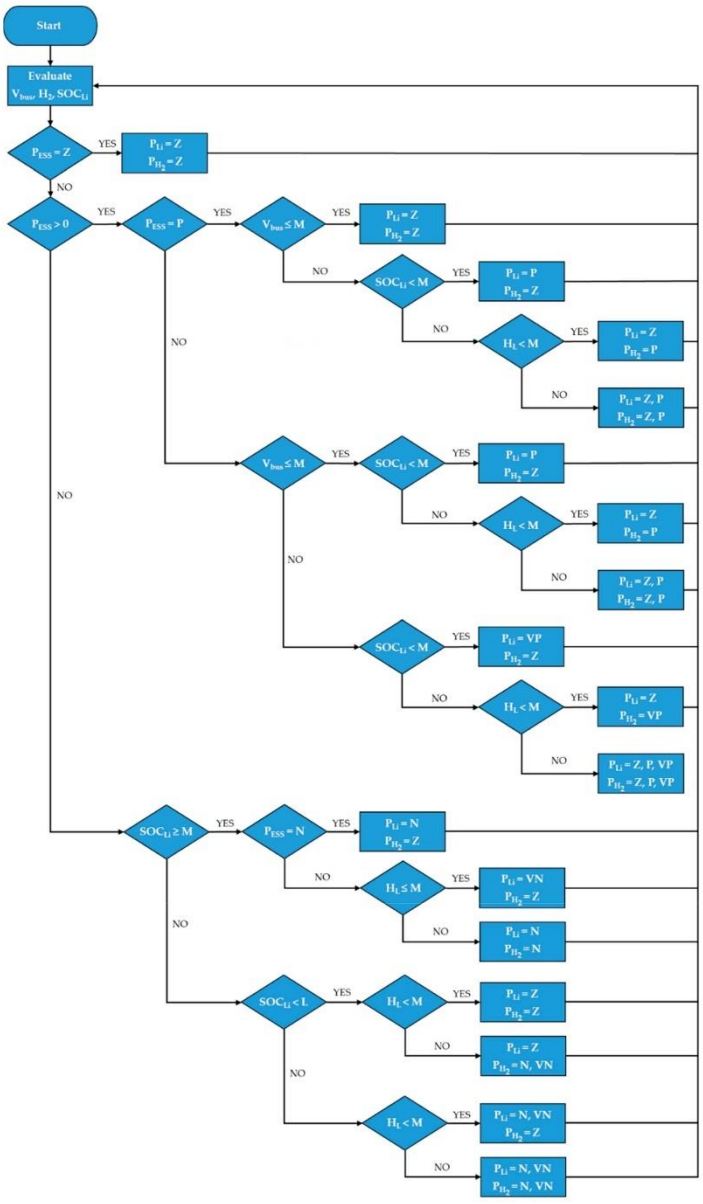

Figure 9. FLC2 flowchart diagram in the sampling k (VL: Very Low, VN: Very Negative, L: Low, N: Negative; Z: Zero; M: Medium, H: High; P: Positive, VP: Very Positive, VH: Very High; according to membership functions defined in Figure 5). It is understood that the sets used are fuzzy.

Based on the above criteria, in case of energy excess, the ESS can take energy from the DC bus to be charged ($P_{ESS} < 0$). Then, the lead-acid battery bank will be ready to be recharge until a medium DC bus voltage is reached ($V_{bus-fuzz}(k) \leq$ M; $V_{bus}(k) \leq 390$ V). Once this voltage is reached, the Li-ion battery bank and hydrogen subsystem will be used to absorb the energy surplus, implementing a

maximum charging voltage protocol. The priority in the recharge energy coming from the DC bus will be determined by the role of each element in the ESS, prioritizing the use of the Li-ion battery over the hydrogen system if its SOC is low ($SOC_{Li-fuzz}(k) \leq$ M).

On the other hand, in case the ESS should supply energy to the microgrid ($P_{ESS} > 0$), energy deficit situation, the use of the Li-ion battery bank will be prioritized in the first instance ($P_{Li-fuzz}(k) =$ P and $P_{H_2-fuzz}(k) =$ Z) if its SOC is above 60% ($SOC_{Li-fuzz}(k) \geq$ M). In this case, the hydrogen level shall be assessed ($HL_{-fuzz}(k) \leq$ M), a prominent use of this resource shall be made while maintaining a medium-high level as long as possible.

Finally, in all the situations where both storage systems have energy available, $\left(Low < SOC_{Li-fuzz}(k) < \text{Medium}\right)$ and $\left(Low < HL_{-fuzz}(k) < \text{Medium}\right)$, energy distribution between Li-ion batteries and the hydrogen system will be chosen, depending on the power balance and their stored energy capability.

3.5. *Defuzzification*

After the inference process, the fuzzy sets $P_{Li-fuzz}(k)$, $P_{H_2-fuzz}(k)$ and $P_{ESS-fuzz}(k)$ need to be converted to real variables (crisp values). For that, a defuzzification process needs to be implemented to lead to $P_{Li}(k)$, $P_{H_2}(k)$, and $P_{ESS}(k)$. In this case, the centroid method has been used.

4. Results

In order to validate the proposed fuzzy-based EMS, two simulation tests in MATLAB® environment of the microgrid defined in Section 2 were developed, in accordance with the configuration shown in Figure 1. To carry out the test, the MATLAB®-Simulink® microgrid model of Figure 3 was used.

In the simulation test, a residential-type daily profile of renewable generation, grid utilization cost, and typical residential consumption was created. The generation profile corresponded to a 5 kW_p photovoltaic field, for typical radiation and ambient temperature in Huelva (southwest of Spain).

The cost of purchasing energy from the main power grid corresponded to a typical night rate profile in Spain, Figure 10. On the other hand, the sale of energy to the grid (considering the Spanish situation) was carried out by a decrease in the bi-monthly electricity invoice, with a fixed rate value agreed with the electricity company of −0.06 €/kWh.

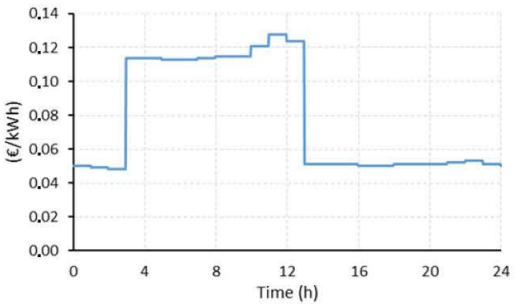

Figure 10. Energy cost profile.

In the test, a sampling time of 1 min was used. The microgrid was tested in its whole configuration, i.e., as showed in Figure 1. In order to check the correct operation of the proposed controller, solar generation profile was considered without and with fluctuations (Figures 11 and 12, respectively).

The usual residential profile, where residents are outside during most of the daylight hours, is characterized by consumption valleys during the day (when it takes place the maximum production of photovoltaic) and consumption peaks just after the noon (if residents go home for lunch) and especially at night (involving the ESS use); hence the interest of the night rate (see Pload in Figures 11 and 12). As a residential type microgrid, the electric vehicle contributes to the demand profile (see PEV

in Figures 11 and 12). It reflects a daily use of the vehicle corresponding to 40% of its energy capacity, and the recharge energy consumption will be carried out coinciding with the night rate.

Finally, to evaluate the economic performance of the proposed strategy against traditional control techniques, the reference study case presented in [24] was chosen. This reference proposes a hysteresis SOC-based EMS. This EMS determines the power setpoint of the energy storage system and grid, taking into account only the battery SOC and hydrogen level. The main grid will be used to guarantee the power balance in extreme conditions. The parameters that defined the EMS strategy are shown in Table 3.

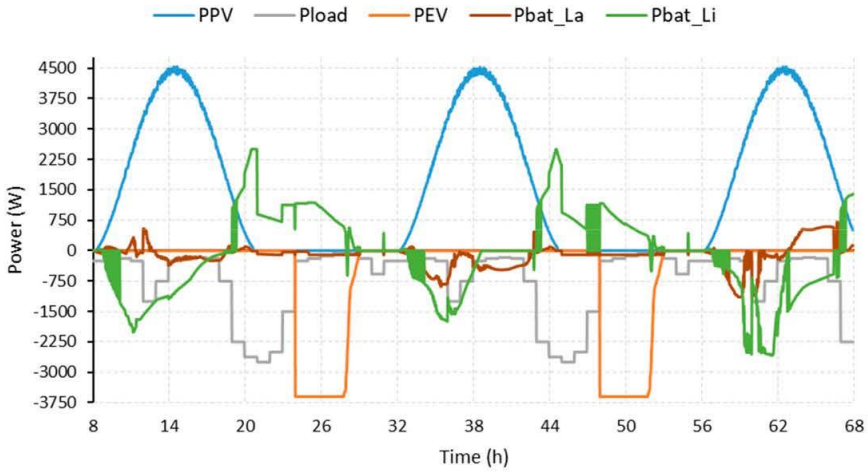

(**a**)

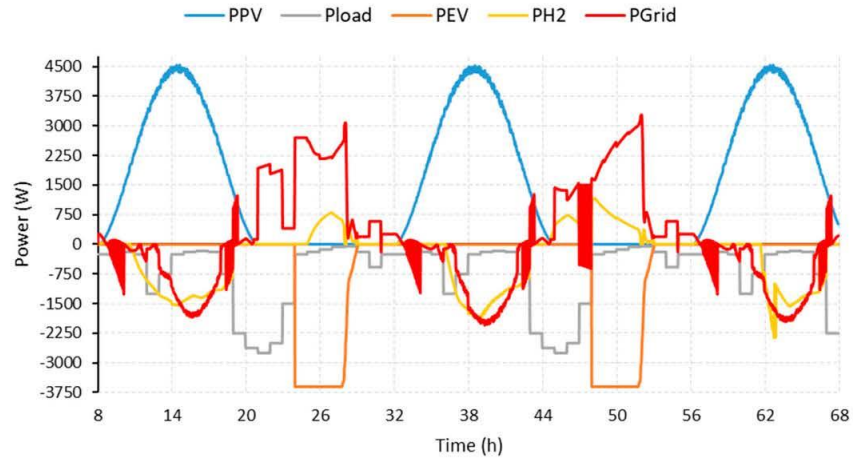

(**b**)

Figure 11. Microgrid power variables: (**a**) renewable (photovoltaic) power (PPV), residential consumption (Pload), electric vehicle consumption (PEV), lead-acid battery power (Pbat_La), and Li-ion battery power (Pbat_Li) for stable solar profile; (**b**) renewable (photovoltaic) power (PPV), residential consumption (Pload), electric vehicle consumption (PEV), hydrogen system power (PH2), and main power grid (PGrid) for stable solar profile.

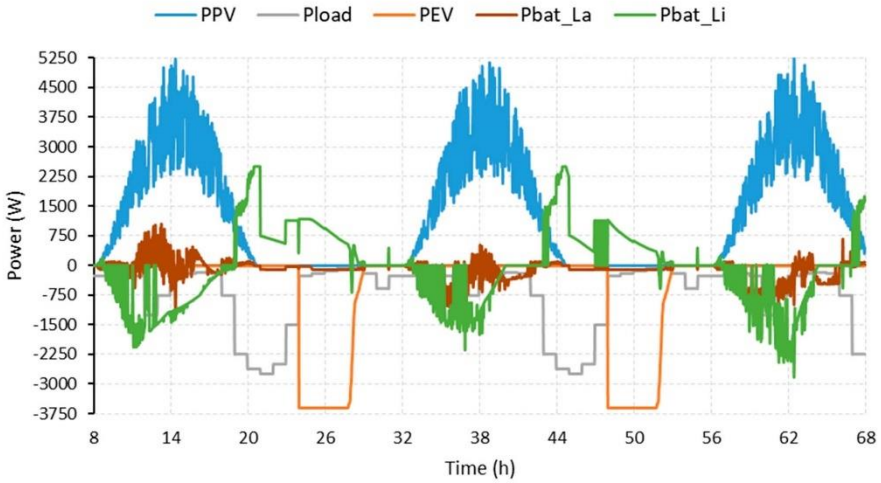

(**a**)

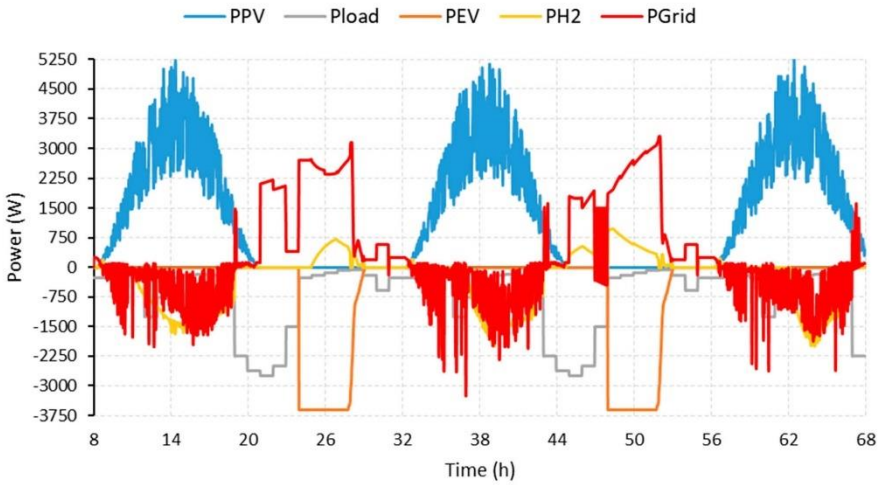

(**b**)

Figure 12. Microgrid power variables: (**a**) renewable (photovoltaic) power (PPV), residential consumption (Pload), electric vehicle consumption (PEV), lead-acid battery power (Pbat_La), and Li-ion battery power (Pbat_Li) for fluctuating solar profile; (**b**) renewable (photovoltaic) power (PPV), residential consumption (Pload), electric vehicle consumption (PEV), hydrogen system power (PH2), and main power grid (PGrid) for fluctuating solar profile.

Table 3. Parameters used in the reference study case (hysteresis-based EMS parameters).

EMS Parameter	Value
Minimum SOC threshold	50%
Maximum SOC threshold	90%
Hysteresis bandwidth	10%
Maximum Hydrogen level	20 Nm^3
Minimum Hydrogen level	2 Nm^3

The results from the test carried out are shown in Figures 11 and 12. Similarly, the DC bus voltage profile and the energy stored (SOC_{La}, SOC_{Li}, and HL) are shown in Figures 13 and 14 respectively. Figure 15 allows the comparison of the hourly grid cost obtained from the proposed fuzzy-based EMS with respect to the traditional case connected exclusively to the main power grid and the reference study case based on hysteresis EMS (€ > 0 means residential facility purchases energy to the main power grid, € < 0 means that the microgrid of the residential facility sells energy to the main power grid).

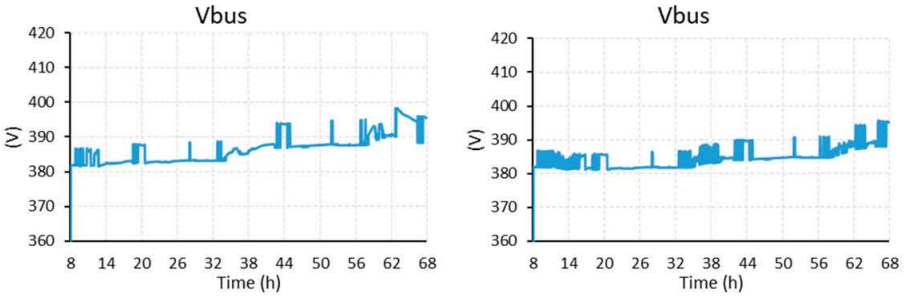

Figure 13. DC bus voltage for (**a**) stable solar profile and (**b**) fluctuating solar profile.

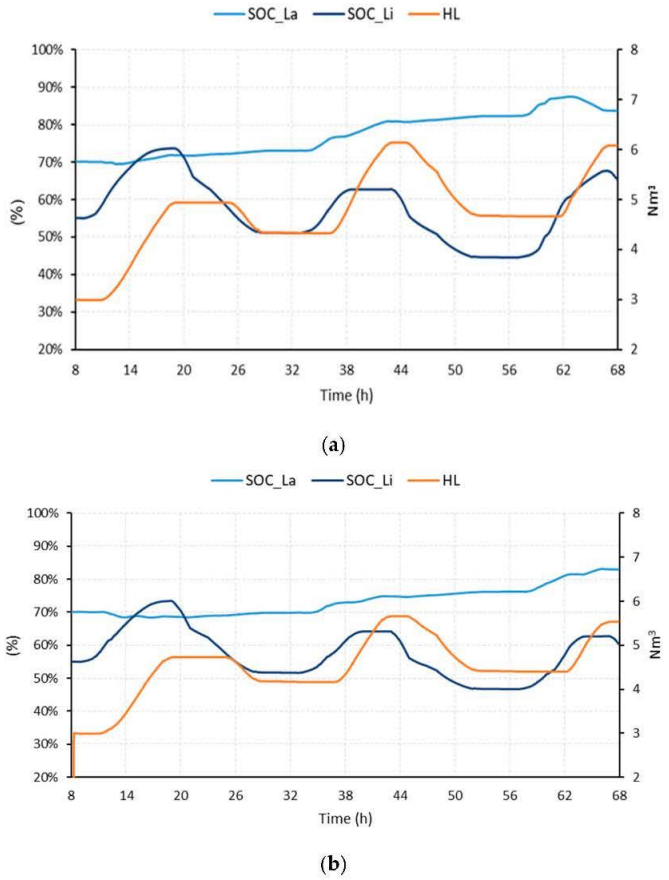

Figure 14. Lead-acid battery SOC (SOC_La), Li-ion battery SOC (SOC_Li), and hydrogen level (HL) for (**a**) stable solar profile and (**b**) fluctuating solar profile.

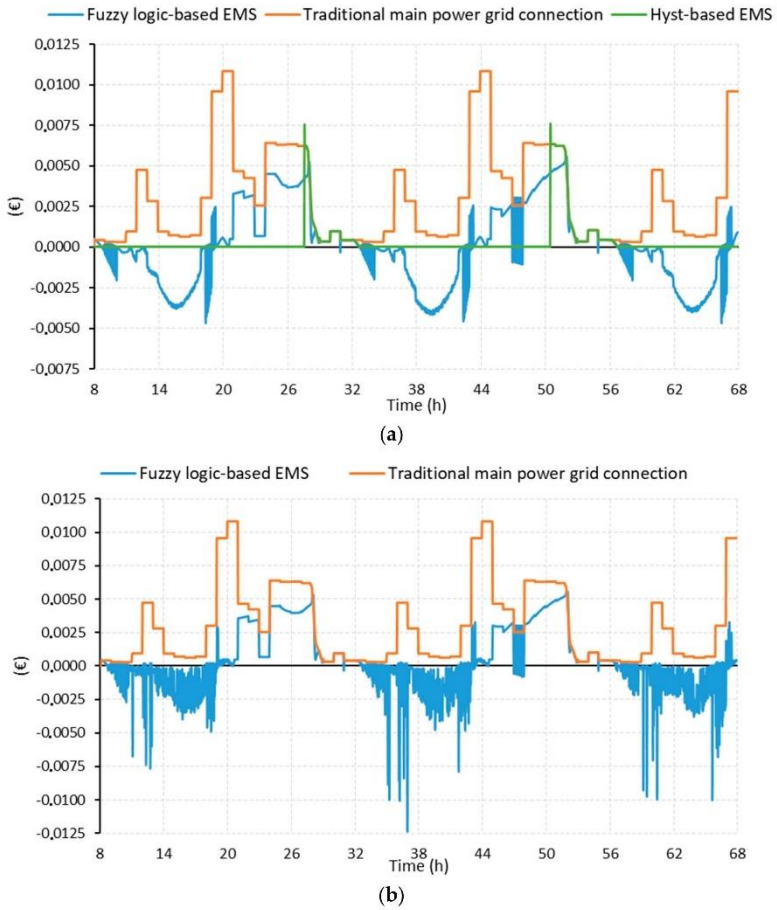

Figure 15. Grid cost for proposed fuzzy logic-based EMS versus traditional main power grid connection and hysteresis-based EMS for (**a**) stable solar profile and (**b**) fluctuating solar profile.

5. Discussion

According to the generation and consumption profile, Figures 11 and 12, the microgrid started daylight hours in an energy surplus situation that remained virtually during the period 8 h $\leq t \leq$ 19 h. This was used by the EMS to recharge the Li-ion battery bank (Figures 11a and 12a). As there was still energy surplus, the EMS ordered to start the hydrogen production (Figures 11b, 12b and 14). Despite the electrolyzer operation, there was still energy excess, which was sold to the main power grid (Figures 11b and 12b).

According to the EMS performance, the decision criteria of the fuzzy logic-based controller are not only meet with the load demand but also guarantee the best performance according to technical and economic parameters. Then, with the aim to enlarge the electrolyzer lifespan, it was tried that the electrolyzer had an operation regime that was as stable as possible, to the detriment of more variable use of the Lithium battery bank and grid.

Along the first considered period (8 h $\leq t \leq$ 19 h) it was easy to demonstrate that the behavior of the lead-acid battery bank was as expected. Indeed, its contribution to the DC bus power was very little and only dedicated to balancing the bus (Figures 11a and 12a). On the other hand, the DC bus voltage was really under control, with fluctuations below 10 Volts, i.e., less than 4% (see Figure 13). Additionally, the bus voltage kept on increasing until the end of the simulation time. The reason is

that the control strategy made it possible to derive part of the surplus energy directly to the lead-acid battery bank if the voltage value was below the design voltage established at 390–400 VDC, see FLC2 flowchart in Figure 9. Moreover, this voltage guaranteed the proper SOC of the lead-acid battery bank, always over limits values (see Figure 14).

From 19 h $< t \leq$ 32 h, an energy deficit situation appeared; the load demand increased and energy was required for the residential load and to charge the electric vehicle, while the supply from the PV panels went on decreasing until it was null. In this period, the load demand was guaranteed by the Li-ion battery bank (Figures 11a and 12a) and the main power grid support (Figures 11b and 12b). In energy deficit periods, the EMS criterium is to promote a joint use of the ESS and the main power grid, which is recommendable when the cost of purchasing energy is low. This allows a more conservative use of the microgrid's resources. The fuel cell operation was delayed until 24 h $< t \leq$ 29 h (Figures 11b and 12b), i.e., until the moment when the SOC of the Li-ion battery bank began to drop considerably (Figure 14). The power setpoint of each device that makes up the ESS was defined by FLC2 (Figure 9), and it was established that the hydrogen subsystem provides energy ($P_{H_2-fuzz}(k)$ = Positive) when Low $\leq$ $SOC_{Li-fuzz}(k)$ < Medium (40% $\leq$ $SOC_{Li}(k)$ < 60%) and Low $\leq$ $HL_{-fuzz}(k)$ < Medium (2 $Nm^3 \leq HL(k) <$ 10 Nm^3). This situation generated, obviously, the consequent decreasing of the stored hydrogen level (Figure 14). In the last part of the one-day period, 29 h $< t \leq$ 32 h, the residential load was supplied exclusively by the main power grid (Figures 11b and 12b). This is the case (see Figure 8) when $C_{EP-fuzz}(k) \leq$ Medium ($C_{EP}(k) \leq 0.075$ €) and $SOC_{ESS-fuzz}(k)$ < Medium ($SOC_{Li}(k) = 50\%$ and $HL(k) = 4\ Nm^3$), so $P_{ESS-fuzz}(k)$ = Zero (Figures 11 and 12). During this interval, the lead-acid battery bank harnessed the energy availability to slightly increase its state of charge (Figure 14). This increasing was, sensibly, more accused at the beginning of the new period because $P_{bal}(k)$ was positive, renewable (photovoltaic) power was available (see Figures 11 and 12).

The behavior described above was repeated during the following two days. It is possible to see from Figure 14 the little delay between the charging/discharging of the Li-ion battery bank and the hydrogen tank. The EMS prioritizes the use of the battery bank versus the hydrogen tank, with the aim to make more conservative use of the hydrogen-based devices and avoid them having a higher degradation rate. On the other hand, Figure 13 shows that the use of the lead-acid battery bank was reduced and was limited to guaranteeing the power balance during the switching transient of the rest of the systems, and to keep the voltage of the DC bus inside the allowed range (380 V $\leq V_{bus}(k) \leq$ 400 V). Really, the behavior is excellent because of the allowed margin, Equation (5): 350 V $\leq V_{bus}(k) \leq$ 440 V.

Finally, taking into account the main power grid utilization cost (Figure 15), the developed EMS allows a higher economic performance of the residential-type microgrid. It takes advantage of selling energy excess and promoting energy consumption in the most favorable situations according to the energy cost rate. Then, during the three-day test, the electricity invoice and grid utilization ascended up to €5.33 and 73 kWh in the case of the main power grid connection, while in the case of microgrid with hysteresis-based strategy, the cost associated with the use of the grid and grid utilization decreased to €0.5772, 11.17 kWh, and €0.8063, 15.76 kWh for low renewable fluctuations and variable generation profile, respectively. For the proposed fuzzy logic-based EMS, the electricity invoice and grid utilization descended to €0.15, 7.6 kWh, and €0.6, 18.07 kWh for low renewable fluctuations and variable generation profile, respectively. This means a cost saving of 97.2% and 88.74% for the full grid utilization, and 74.0% and 25.59% for the hysteresis-based EMS for favorable and variable generation profile, respectively. In light of the results, it can be seen how the proposed fuzzy logic-based strategy increases the economic performance of the system with respect to the other cases studied, considering the use of the grid and the purchase/sale price as an additional decision factor.

6. Conclusions

This paper has presented a fuzzy logic-based EMS for microgrids with hybrid ESS based on a batteries and hydrogen system, which ensures the power balance according to the load demand,

while taking into account the improvement of microgrid performance from a technical and economic point of view.

The fuzzy logic approach was chosen because: (1) linguistic rules are interpretable and they can simplify the management and control of complex microgrids, (2) it can incorporate expert knowledge that takes advantage of the accumulated knowledge about the microgrid, and (3) it does not need to dispose of the microgrid model to carry out the controller design.

The developed fuzzy logic-based EMS uses the knowledge from experts, which is incorporated into fuzzy rules bases. This allows the inclusion of both technical and economic criteria into the inference process, which ensures the power balance of the microgrid at all times, pursuing, in addition, its best performance and efficiency, ensuring the best lifespan of its elements and the most advantageous economic exchange with the main power grid.

On the other hand, with the objective to test the microgrid performance in a stress situation, the developed EMS has been subjected to a residential-type profile consumption for 72 hours (three days) and stable and fluctuating solar generation profiles. The residential profile is characterized by consumption valleys during the sunny hours, while consumption peaks take place at night, out of sunlight hours, compromising the use of battery and hydrogen storage system.

The results show that the fuzzy logic-based EMS guarantees the residential-type demand, while it keeps a conservative use of those systems that suffer higher degradation. Regarding economic criteria, the developed fuzzy logic-based EMS allows savings of up to €630/year in the electricity invoice.

Author Contributions: Conceptualization, F.S., A.P. and F.J.V.; methodology, A.P., F.S. and F.J.V.; software, A.P. and F.J.V.; experimental data acquisition and model validation, A.P. and J.L.S.; writing, F.J.V. and F.S.; supervision, F.S., J.M.A., F.I. and E.L.; All authors have read and agreed to the published version of the manuscript.

Funding: This research was funded by "Configuration and management of micro-grid based on renewable energy and hydrogen technology (H2SMART- μGRID)" Spanish Government, grant Ref: DPI2017-85540-R.

Conflicts of Interest: The authors declare no conflict of interest.

List of Acronyms

DOD	Depth of discharge
EMS	Energy management system
ESS	Energy storage system
FLC	Fuzzy logic controller
INTA	(Spanish acronym) Instituto Nacional de Técnica Aeroespacial (Spanish Institute of Aerospace Technology)
PEM	Polymer electrolyte membrane
SOC	State of charge

Notation and Symbols

$HL(k)$	Hydrogen storage level (Nm^3)
$P_{bal}(k)$	Power balance (W)
$P_{Els}(k)$	Electrolyser operating power (W)
$P_{ESS}(k)$	Energy storage system power (W)
$P_{EV}(k)$	Electric vehicle charging power (W)
$P_{FC}(k)$	Fuel cell operating power (W)
$P_{Grid}(k)$	Main power grid operating power (W)
$P_{GI}(k)$	Purchased power from the main power grid (W)
$P_{GO}(k)$	Sold power to the main power grid (W)
$P_{H_2}(k)$	Hydrogen system operating power (W)
$P_L(k)$	Residential load power (W)
$P_{La}(k)$	Lead-acid battery bank power (W)
$P_{Li}(k)$	Li-ion battery bank power (W)
$P_{PV}(k)$	Renewable (solar) power (W)
$SOC_{La}(k)$	State of charge of lead-acid battery bank (Ah)
$V_{bus}(k)$	DC bus voltage (V)

References

1. Abid, S.; Alghamdi, T.A.; Haseeb, A.; Wadud, Z.; Ahmed, A.; Javaid, N. An Economical Energy Management Strategy for Viable Microgrid Modes. *Electronics* **2019**, *8*, 1442. [CrossRef]
2. Lin, R.H.; Zhao, Y.Y.; Wu, B.D. Toward a hydrogen society: Hydrogen and smart grid integration. *Int. J. Hydrog. Energy* **2020**. [CrossRef]
3. Adibi, M.M.; Martins, N. Impact of power system blackouts. In Proceedings of the IEEE Power and Energy Society General Meeting, Denver, CO, USA, 26–30 July 2015; pp. 1–15. [CrossRef]
4. Morrissey, K.; Plater, A.; Dean, M. The cost of electric power outages in the residential sector: A willingness to pay approach. *Appl. Energy* **2018**, *212*, 141–150. [CrossRef]
5. Shuai, M.; Chengzhi, W.; Shiwen, Y.; Hao, G.; Jufang, Y.; Hui, H. Review on Economic Loss Assessment of Power Outages. *Procedia Comput. Sci.* **2018**, *130*, 1158–1163. [CrossRef]
6. Brunaccini, G.; Sergi, F.; Aloisio, D.; Randazzo, N.; Ferraro, M.; Antonucci, V. Fuel cells hybrid systems for resilient microgrids. *Int. J. Hydrog. Energy* **2019**, *44*, 21162–21173. [CrossRef]
7. Sayed, K.; Abo-Khalil, A.G.; Alghamdi, A.S. Optimum Resilient Operation and Control DC Microgrid Based Electric Vehicles Charging Station Powered by Renewable Energy Sources. *Energies* **2019**, *12*, 4240. [CrossRef]
8. Kantamneni, A.; Brown, L.E.; Parker, G.; Weaver, W.W. Survey of multi-agent systems for microgrid control. *Eng. Appl. Artif. Intell.* **2015**, *45*, 192–203. [CrossRef]
9. Zia, M.F.; Elbouchikhi, E.; Benbouzid, M. Microgrids energy management systems: A critical review on methods, solutions, and prospects. *Appl. Energy* **2018**, *222*, 1033–1055. [CrossRef]
10. Oliveira, D.Q.; Zambroni de Souza, A.C.; Santos, M.V.; Almeida, A.B.; Lopes, B.I.L.; Saavedra, O.R. A fuzzy-based approach for microgrids islanded operation. *Electr. Power Syst. Res.* **2017**, *149*, 178–180. [CrossRef]
11. Monforti Ferrario, A.; Vivas, F.J.; Segura Manzano, F.; Andújar, J.M.; Bocci, E.; Martirano, L. Hydrogen vs. Battery in the Long-term Operation. A Comparative Between Energy Management Strategies for Hybrid Renewable Microgrids. *Electronics* **2020**, *9*, 698. [CrossRef]
12. Nespoli, A.; Mussetta, M.; Ogliari, E.; Leva, S.; Fernández-Ramírez, L.; García-Triviño, P. Robust 24 hours ahead forecast in a microgrid: A real case study. *Electronics* **2019**, *8*, 1434. [CrossRef]
13. Vivas, F.J.; De las Heras, A.; Segura, F.; Andújar, J.M. A review of energy management strategies for renewable hybrid energy systems with hydrogen backup. *Renew. Sustain. Energy Rev.* **2018**, *82*, 126–155. [CrossRef]
14. Torreglosa, J.P.; García, P.; Fernández, L.M.; Jurado, F. Energy dispatching based on predictive controller of an off-grid wind turbine/photovoltaic/hydrogen/battery hybrid system. *Renew. Energy* **2015**, *74*, 326–336. [CrossRef]
15. Tesfahunegn, S.G.; Ulleberg, Ø.; Vie, P.J.S.; Undeland, T.M. Optimal shifting of Photovoltaic and load fluctuations from fuel cell and electrolyzer to lead acid battery in a Photovoltaic/hydrogen standalone power system for improved performance and life time. *J. Power Sources* **2011**, *196*, 10401–10414. [CrossRef]
16. Ipsakis, D.; Voutetakis, S.; Seferlis, P.; Stergiopoulos, F.; Papadopoulou, S.; Elmasides, C. The effect of the hysteresis band on power management strategies in a stand-alone power system. *Energy* **2008**, *33*, 1537–1550. [CrossRef]
17. Zhang, F.; Thanapalan, K.; Procter, A.; Carr, S.; Maddy, J.; Premier, G. Power management control for off-grid solar hydrogen production and utilisation system. *Int. J. Hydrog. Energy* **2013**, *38*, 4334–4341. [CrossRef]
18. Athari, M.H.; Ardehali, M.M. Operational performance of energy storage as function of electricity prices for on-grid hybrid renewable energy system by optimized fuzzy logic controller. *Renew. Energy* **2016**, *85*, 890–902. [CrossRef]
19. García, P.; Torreglosa, J.P.; Fernández, L.M.; Jurado, F. Optimal energy management system for stand-alone wind turbine/photovoltaic/ hydrogen/battery hybrid system with supervisory control based on fuzzy logic. *Int. J. Hydrog. Energy* **2013**, *38*, 14146–14158. [CrossRef]
20. Bordons, C.; García-Torres, F.; Valverde, L. Gestión Óptima de la Energía en Microrredes con Generación Renovable. *RIAI Rev. Iberoam. Autom. Inform. Ind.* **2015**, *12*, 117–132. [CrossRef]
21. Talebian, M.E.; Plant, P.; Sobhani, S.; Borzooi, A. New Hybrid System of Fuel Cell Power Plant and Wind Turbine for Household Consumption. In Proceedings of the 3rd International Conference on Electric Power and Energy Conversion Systems, Istanbul, Turkey, 2–4 October 2013.

22. Wang, X.; Tong, C.; Palazoglu, A.; El-Farra, N.H. Energy Management for the Chlor-Alkali Process with Hybrid Renewable Energy Generation using Receding Horizon Optimization. In Proceedings of the 53rd IEEE Conference on Decision and Control, Los Angles, CA, USA, 15–17 December 2014.
23. Zhou, K.; Ferreira, J.A.; de Haan, S.W.H. Optimal energy management strategy and system sizing method for stand-alone photovoltaic-hydrogen systems. *Int. J. Hydrog. Energy* **2008**, *33*, 477–489. [CrossRef]
24. Vivas, F.J.; De las Heras, A.; Segura, F.; Andújar, J.M. H2RES2 simulator. A new solution for hydrogen hybridization with renewable energy sources-based systems. *Int. J. Hydrog. Energy* **2017**, *42*, 13510–13531. [CrossRef]
25. Segura, F.; Andújar, J.M. Power management based on sliding control applied to fuel cell systems: A further step towards the hybrid control concept. *Appl. Energy* **2012**, *99*, 213–225. [CrossRef]
26. Andújar, J.M.; Bravo, J.M.; Peregrín, A. Stability analysis and synthesis of multivariable fuzzy systems using interval arithmetic. *Fuzzy Sets Syst.* **2004**, *148*, 337–353. [CrossRef]
27. Mamdani, E.H.; Assilian, S. An experiment in linguistic synthesis with a fuzzy logic controller. *Int. J. Man. Mach. Stud.* **1975**, *7*, 1–13. [CrossRef]
28. Bilodeau, A.; Agbossou, K. Control analysis of renewable energy system with hydrogen storage for residential applications. *J. Power Sources* **2006**, *162*, 757–764. [CrossRef]
29. Harrag, A.; Messalti, S. How fuzzy logic can improve PEM fuel cell MPPT performances? *Int. J. Hydrog. Energy* **2018**, *43*, 537–550. [CrossRef]
30. Casteleiro-Roca, J.-L.; Barragán, A.J.; Manzano, F.S.; Calvo-Rolle, J.L.; Andújar, J.M. Fuel Cell Hybrid Model for Predicting Hydrogen Inflow through Energy Demand. *Electronics* **2019**, *8*, 1325. [CrossRef]
31. Ngamroo, I. Application of electrolyzer to alleviate power fluctuation in a stand alone microgrid based on an optimal fuzzy PID control. *Int. J. Electr. Power Energy Syst.* **2012**, *43*, 969–976. [CrossRef]
32. Bukhari, S.B.A.; Haider, R.; Saeed Uz Zaman, M.; Oh, Y.S.; Cho, G.J.; Kim, C.H. An interval type-2 fuzzy logic based strategy for microgrid protection. *Int. J. Electr. Power Energy Syst.* **2018**, *98*, 209–218. [CrossRef]
33. Stewart, E.M.; Lutz, A.E.; Schoenung, S.; Chiesa, M.; Keller, J.O.; Fletcher, J.; Ault, G.; McDonald, J.; Cruden, A. Modeling, analysis and control system development for the Italian hydrogen house. *Int. J. Hydrog. Energy* **2009**, *34*, 1638–1646. [CrossRef]
34. Kamel, A.; Rezk, H.; Shehata, N.; Thomas, J. Energy Management of a DC Microgrid Composed of Photovoltaic/Fuel Cell/Battery/Supercapacitor Systems. *Batteries* **2019**, *5*, 63. [CrossRef]
35. El-Bidairi, K.S.; Duc Nguyen, H.; Jayasinghe, S.D.G.; Mahmoud, T.S.; Penesis, I. A hybrid energy management and battery size optimization for standalone microgrids: A case study for Flinders Island, Australia. *Energy Convers. Manag.* **2018**, *175*, 192–212. [CrossRef]

© 2020 by the authors. Licensee MDPI, Basel, Switzerland. This article is an open access article distributed under the terms and conditions of the Creative Commons Attribution (CC BY) license (http://creativecommons.org/licenses/by/4.0/).

6.2. Contribución 2

Experimental evaluation of a passive fuel cell/battery hybrid power system for an unmanned ground vehicle

E. López; J. Sáenz; F. José Vivas; F. Isorna; M. A. Ridao; C. Bordons; E. Hernández; A. Efes

Publicado en:

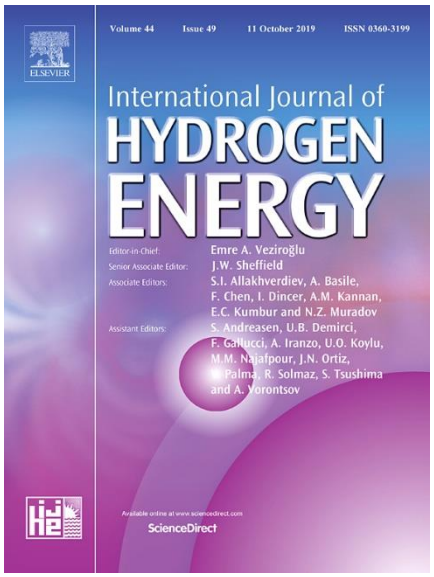

Revista: International Journal of Hydrogen Energy
Editorial: ELSEVIER
Editor Jefe: T. Nejat Veziroglu
Referencia: Vol. 44, Issue 25, pp. 12772-12782
Año: 2018
ISSN: 0360-3199
DOI 10.1016/j.ijhydene.2018.10.107

Categoría	Rango revista / Total revista	Cuartil
Energy & Fuels	31 / 103	Q2
Electrochemistry	48 / 148	Q2
Chemistry	8 / 26	Q2
Impact Factor (2018)	4.084	
Citations	16	

6.3. Contribución 3

Comprehensive diagnosis methodology for faults detection and identification, and performance improvement of Air-Cooled Polymer Electrolyte Fuel Cells

J.M. Andújar, F. Segura, F. Isorna, A.J. Calderón

Publicado en:

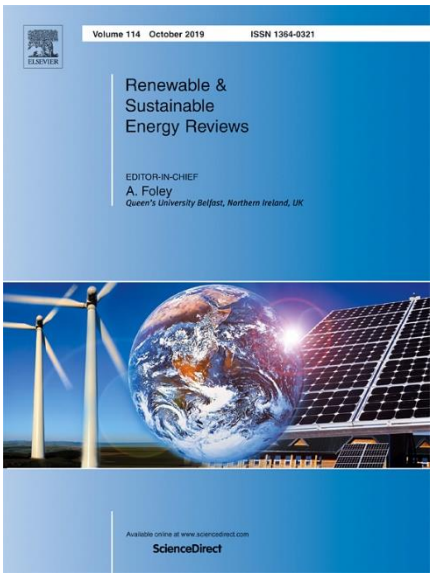

Revista: Renewable and Sustainable Energy Reviews
Editorial: ELSEVIER
Editor Jefe: Aoife M. Foley
Referencia: Vol. 88, May 2018, Pages 193-207
Año: 2018
ISSN: 1364-0321
DOI 10.1016/j.rser.2018.02.038

Categoría	Rango revista / Total revista	Cuartil
Energy & Fuels	7 / 103	Q1
Green & sustainability science & technology	1 / 35	Q1
Impact Factor (2018)	10,556	
Citations	10	

6.4. Contribución 4

Proyecto IUFCV: Incremento de la autonomía en vehículos no tripulados mediante el uso de sistemas híbridos de potencia con pila de combustible

Eduardo López, Fernando Isorna, Miguel Ángel Ridao, Carlos Bordons, Alberto Elfes, Emili Hernández

Publicado en:

Revista: Boletín de Observación Tecnológica en Defensa

Editorial: Sistema de Observación y Prospectiva Tecnológica (SOPT)

Editor: Ministerio de Defensa. Secretaría General Técnica

Referencia: Boletín de Observación Tecnológica en Defensa n.º 53. Primer trimestre 2017

Año: 2017

ISSN: 2444-4839; NIPO: 083-15-183-4

6.5. Contribución 5

Optimization of a PEM fuel cell operating conditions: Obtaining the maximum performance polarization curve

J. Antonio Salva; Alfredo Iranzo; Felipe Rosa; Elvira Tapia; Eduardo Lopez; Fernando Isorna

Publicado en:

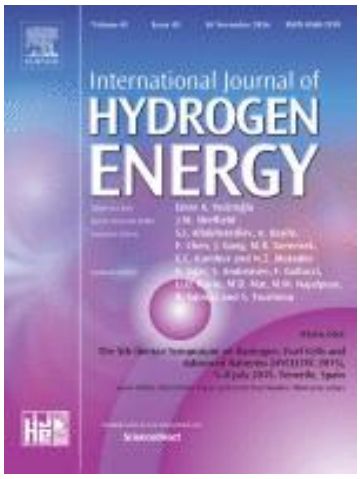

Revista: International Journal of Hydrogen Energy
Editorial: ELSEVIER
Editado por: Elena Pastor Tejera, Juan Carlos Ruíz Morales, María Jesús Lázaro
Referencia: Volume 41, Issue 43, 16 November 2016, Pages 19713-19723
Year: 2016
ISSN 3603199
http://dx.doi.org/10.1016/j.ijhydene.2016.03.136

Categoría	Rango revista / Total revista	Cuartil
Energy Engineering and Power Technology	28/92	Q1
Impact Factor (2016)	3,582	
Citations	37	

ARTICLE IN PRESS

INTERNATIONAL JOURNAL OF HYDROGEN ENERGY XXX (2016) 1 – 11

Available online at www.sciencedirect.com

ScienceDirect

journal homepage: www.elsevier.com/locate/he

Optimization of a PEM fuel cell operating conditions: Obtaining the maximum performance polarization curve

J. Antonio Salva [a,*], Alfredo Iranzo [a], Felipe Rosa [b], Elvira Tapia [a], Eduardo Lopez [c], Fernando Isorna [c]

[a] AICIA, Andalusian Association for Research and Industrial Cooperation, School of Engineering, University of Seville, Camino de los Descubrimientos s/n, 41092 Sevilla, Spain

[b] Thermal Engineering Group, Energy Engineering Department, School of Engineering, University of Seville, Camino de los Descubrimientos s/n, 41092 Sevilla, Spain

[c] INTA, National Institute of Aerospace Technology, Ctra. San Juan del Puerto-Matalascañas, km 33, 21130, Mazagón, Huelva, Spain

ARTICLE INFO

Article history:
Received 10 November 2015
Received in revised form
3 February 2016
Accepted 21 March 2016
Available online xxx

Keywords:
Single PEM fuel cell
Analytical validated model
Optimization
Operating conditions
Polarization curve

ABSTRACT

This work presents the operating conditions optimization of a 50 cm^2 PEM fuel cell using a one dimensional analytical model previously validated against experimental data for a comprehensive set of different operating conditions of cell temperature, pressure, reactants relative humidity and cathode stoichiometry. The analytical model is used to predict the operating conditions that provide the maximum (and the minimum) power output of the given PEM fuel cell for every value of current intensity. Thus, a maximum performance polarization curve is developed where the operating conditions are not fixed for every current intensity, but modified in order to provide the maximum possible power output for every value of current intensity. The obtained operating conditions have been tested in the real cell showing a good agreement between experimental and modeling results where the maximum error is below 2% for the case of maximum power and 3% for the case of minimum power. The comparison shows that the power output using the operating conditions for the curve of maximum power is about 100% higher than using the curve of minimum power.

Copyright © 2016, Hydrogen Energy Publications, LLC. Published by Elsevier Ltd. All rights reserved.

Introduction

PEM fuel cells are considered to play a fundamental role in the future energy sector due to its high power density, low operating temperatures, low local emissions, simplification of stack design, fast start-up and shutdown [1]. However, it is necessary to overcome some technological barriers such as reduced the costs, weight and volume in order to achieve the PEM fuel cell technology to be competitive versus other traditional power systems like the internal combustion engine [2–4]. In this way, mathematical models and simulations are

* Corresponding author. Tel.: +34 954482254; fax: +34 954487247.
E-mail address: jsalva@etsi.us.es (J.A. Salva).

http://dx.doi.org/10.1016/j.ijhydene.2016.03.136

0360-3199/Copyright © 2016, Hydrogen Energy Publications, LLC. Published by Elsevier Ltd. All rights reserved.

Please cite this article in press as: Salva JA, et al., Optimization of a PEM fuel cell operating conditions: Obtaining the maximum performance polarization curve, International Journal of Hydrogen Energy (2016), http://dx.doi.org/10.1016/j.ijhydene.2016.03.136

needed to improve the fuel cell design and for optimizing the operating conditions in order to increase the performance and the power output of the fuel cell.

PEM fuel cell operating conditions play a very important role in the performance of the device [6,7]. In this way, it is advisable to know the operating conditions that provide the maximum possible power depending on the selected working point of current intensity. Depending on the current intensity, the operating conditions to reach the maximum power are different, and for that reason it is advisable to have a knowledge of the complete operation map of the PEM fuel cell.

Some works have been developed in order to find the operating conditions for which the maximum power is obtained [8,9]. However, these works do not model the physics of the PEM fuel cell and use empirical expressions to model the polarization curve. Because of this, this kind of models can not predict correctly the performance of the PEM and the models do not provide the knowledge about what is happening inside the PEM fuel cell in order to detect weak points in the design.

In a previous work, an analytical one dimensional model was developed to model the main phenomena that occur during the operation of the fuel cell such as electrochemistry, mass transport (liquid and gas) and heat transfer [11]. Furthermore, the analytical model was thoroughly validated experimentally with both the cell voltage and the water content inside the PEM fuel cell. The validation of the model with two parameters simultaneously ensures the accuracy of the results. The model was validated for different operating conditions of temperature, pressure, relative humidity in anode and cathode, and cathode stoichiometry.

In this work, the validated analytical model has been used to obtain the operating conditions that provide the maximum power output for every value of current intensity, in order to increase the performance of the PEM fuel cell. The objective of obtaining better performances (or electrical power) can be applied for every PEM fuel cell system. In the case of stationary applications where in principle the fuel cell will be working in a specific operating point during a long time, it is interesting to select the best operating condition in order to increase the performance of the PEM fuel cell. In the case of mobile applications, the control system could select the most favorable operating conditions in order to increase performance within the operating and control range of the system. Thus, a maximum performance polarization curve has been obtained, where the operating conditions are not fixed, but change for every value of current intensity instead of the traditional way for operating with constant operating conditions In addition, the operating conditions that provide the minimum power have been also obtained in order to compare with the previous one. Finally, the operating conditions obtained with the validated analytical model have been tested in the real cell in order to check the accuracy of the numerical results, obtaining a very good agreement between numerical and experimental results.

Description of the single PEM fuel cell

The fuel cell used was a 50 cm^2 active area cell from Electro-Chem Inc., with five-channel serpentine flow fields. The Monopolar Plates (MP) layout is cross-flow, with horizontal channels in the anode and vertical channels in the cathode. The material used for the monopolar plate was Graphite. A set of Gas Diffusion Layers (GDL) from SGL Group (Sigracet 10BC) were used. The GDL contains 5% of PTFE and a Micro Porous Layer (MPL) for enhanced performance of the GDL-catalyst layer interface. A Catalyst Coated Membrane from Baltic Fuel Cells was used, with catalyst loading at anode and cathode electrodes 0.3 mg Pt/cm2 and 0.6 mg Pt/cm2 respectively. The membrane material is Nafion-117. Two images of the single PEM fuel cell are shown in Fig. 1.

Modeling of the single PEM fuel cell

The single PEM fuel cell was modeled including the main phenomena such as electrochemistry, heat transfer and mass transport of water (liquid and gas), oxygen and hydrogen within the cell. The model presents the following assumptions:

- Steady state.
- Mixture gas properties are modeled as ideal gas.
- Two phases of water has been modeled according to liquid–gas equilibrium.
- Hydrogen, oxygen and water vapor mass transfer within the GDL, MPL and CL (Catalyst Layer) have been modeled using the Fick diffusion equation.
- Liquid water transport has been modeled according to capillary pressure.
- Water transport through the Nafion membrane is considered to be a combination of diffusion and electro-osmotic drag.
- Electrical and thermal conductivity of the BP, GDL, MPL and CL are considered to be constant within all the range of the operating temperature (50–75 °C).
- Radiation heat transfer is neglected. Only heat conduction and convection have been modeled.
- Reactants and products temperature are assumed to be at the same temperature as the component they flow through (BP, GDL, MPL, CL, Membrane).

The model was implemented in the commercial software EES Version 9.705-3D (Engineering Equation Solver). EES is a general equation-solving program that can numerically solve systems of coupled non-linear algebraic and differential equation [12]. Next, the most important phenomena such as electrochemistry, heat transfer and species transport are briefly explained. The complete definition of the analytical model was defined in a previous work [11].

Single PEM fuel cell performance

The single fuel cell voltage (V_{cell}) can be expressed as in Eq (1) [6,7].

$$V_{cell} = V_{oc} - \eta_{a,a} - |\eta_{a,c}| - \eta_r - \eta_{m,a} - |\eta_{a,c}| \quad (1)$$

where V_{oc} is the open-circuit potential of the cell (V), $\eta_{a,a}$ and $\eta_{a,c}$ are the activation overpotentials in anode and cathode (V),

Please cite this article in press as: Salva JA, et al., Optimization of a PEM fuel cell operating conditions: Obtaining the maximum performance polarization curve, International Journal of Hydrogen Energy (2016), http://dx.doi.org/10.1016/j.ijhydene.2016.03.136

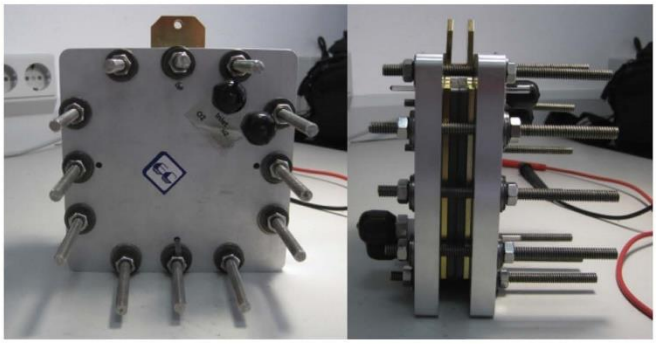

Fig. 1 – Images of the single PEM fuel used during the experimental part.

η_r is the ohmic overpotential (V) and $\eta_{m,a}$ and $\eta_{m,c}$ are the concentration overpotentials in anode and cathode (V).

The activation overpotentials in anode and cathode have been modeled according to Tafel kinetics where the cathode reference exchange current density has been used as fitting parameter of the analytical model [13]. The expressions for the activation overpotentials and the reference exchange current density are shown in Eq (2) and Eq (3) respectively. Where the index "i" represents the anode or cathode side, R is the constant of the ideal gases (J/mol.K), F is the Faraday constant (A.s/mol), T is the operating temperature (K), α_i is the charge transfer coefficient in anode or cathode, i is the current density (A/m^2), $i_{o,i}$ is the exchange current density in anode or cathode, $i_{ref,i}$ is the reference exchange current density in anode or cathode (A/m^2), $C_{i,GDL-CL}$ is the hydrogen (anode side) or oxygen (cathode side) concentration in the GDL-CL interface (mol/m^3), C_{ref} is the reference concentration (mol/m^3) in anode or cathode side, $E_{a,i}$. is the activation energy in anode or cathode side (J/mol) and γi is the reaction order for the elementary charge transfer step.

$$\eta_{a,i} = \frac{RT}{\alpha_i F}\ln\left(\frac{i}{i_{0,i}}\right) \tag{2}$$

$$i_{o,i} = i_{ref,i}\left(\frac{C_{i,GDL-CL}}{C_{ref}}\right)^{\gamma i}\exp\left(-\frac{E_{a,i}}{RT}\right) \tag{3}$$

The ohm's law has been used to model the ohmic overpotential [6,7] as it is shown in Eq (4). The electrical conductivity of the membrane has been modeled according to Springer [14] (Eq (5)) where t and σ represent the thickness (m) and the electrical conductivity (1/Ωm) of the monopolar plate (MP), GDLs, MPLs, CLs and MEA, λ is the water content inside the membrane and T is the operating temperature (K). Finally, $R_{contact}$ represents the contact resistance between the GDL and the monopolar plate (Ωm^2). $R_{contact}$ has been estimated experimentally according to a well-defined technique [7].

$$\eta_r = i\left(2\frac{t_{MP}}{\sigma_{MP}} + 2\frac{t_{GDL}}{\sigma_{GDL}} + 2\frac{t_{MPL}}{\sigma_{MPL}} + 2\frac{t_{CL}}{\sigma_{CL}} + \frac{t_{Mem}}{\sigma_{Mem}} + 2R_{contact}\right) \tag{4}$$

$$\sigma_{Mem} - \exp\left(1268\left(\frac{1}{303} - \frac{1}{T}\right)\right)(0.005193\lambda - 0.00326) \tag{5}$$

The concentration overpotentials in anode and cathode have modeled according to M. Mench [6]. The expression for the concentration overpotentials are shown in Eq (6) where the index "i" represents the anode or cathode side, R is the constant of the ideal gases (J/mol.K), T is the operating temperature (K), n_i are the equivalent electrons per mole of reactant (2 for anode side and 4 for cathode side), i is the current density (A/m^2) and $i_{lim,i}$ is the limiting current density in anode or cathode side (A/m^2).

$$\eta_{m,i} = -\frac{RT}{n_i F}\ln\left(1 - \frac{i}{i_{lim,\,i}}\right) \tag{6}$$

The development of all the terms described in Eq (1) is fully detailed in a previous work [11].

Species transport

The transport of gases (hydrogen, oxygen and water vapor) within the GDL, MPL and CL have been modeled according to Fick diffusion model.

Liquid water transport has been modeled according to Darcy's law as it is shown in Eq (7), where the index "i" is referring to the different layers of the PEM fuel cell (GDL, CL and MPL), $u_{l,i}$ is the liquid water velocity inside the medium "i" (m/s), $k_{l,i}$ is the liquid permeability of the porous media (m^2), μ is the liquid water dynamic viscosity (kg/s.m) and $P_{c,i}$ is the capillary pressure (Pa).

$$u_{l,i} = \frac{-k_{l,i}}{\mu_l}\nabla P_{c,i} \tag{7}$$

The capillary pressure has been modeled using the Leverett approach [6] according to Eq (8) and Eq (9).

$$P_c = \gamma\cos\theta\left(\frac{\varepsilon_i}{k_i}\right)^{0.5} J(s) \tag{8}$$

Please cite this article in press as: Salva JA, et al., Optimization of a PEM fuel cell operating conditions: Obtaining the maximum performance polarization curve, International Journal of Hydrogen Energy (2016), http://dx.doi.org/10.1016/j.ijhydene.2016.03.136

$$J(s)=\begin{cases}1.417(1-s_i)-2.12(1-s_i)^2+1.263(1-s_i)^3 \text{ if } \theta<90^\circ \text{ (Hydrophilic)}\\ 1.417s_i-2.12s_i^2+1.263s_i^3 \text{ if } \theta>90^\circ \text{ (Hydrophobic)}\end{cases} \quad (9)$$

where θ is the contact angle (deg) and γ represents the surface tension (N/m).

The diffusion coefficient for each species has been correlated considering the effect of the liquid water accumulation inside the porous medium according to Zamel et al. [10] as it is shown in Eq (10), where the index "i" is referring to the different layers (GDL, MPL and CL) and the index "j" is referring to the gas used in anode (air) or cathode (hydrogen), ε_i is the porosity of the layer and s_i is the liquid saturation inside the layer.

$$D^i_{eff,j}=\left[1-\left(2.76\varepsilon_i\cosh(3\varepsilon_i-1.92)3\left(\frac{1-\varepsilon_i}{3-\varepsilon_i}\right)\right)\right]D_j(1-s_i)^2 \quad (10)$$

In the case of the membrane, a combined effect of diffusion and electro-osmotic drag has been considered. The entire species transport model is fully detailed in a previous work [11].

Heat transfer

In order to obtain the temperature in each layer of the fuel cell, the energy balance in each layer has been solved [11]. The developed heat transfer model solves both heat conduction (one dimensional in the through-plane direction) and heat convection on the outer walls of the cell. Radiation heat transfer has been neglected due to its minor contribution. The heat generated in the cathode catalyst layer has been calculated according to Eq (11) [6,7].

$$Q_{generated}=I\,(V_{oc}-V_{cell}) \quad (11)$$

where I is the current (A), V_{oc} is the open-circuit potential of the cell (V) and V_{cell} is the fuel cell voltage (V).

Experimental validation of the single PEM fuel cell model

A total of six different tests were carried out in order to characterize the fuel cell behavior [11]. The first four tests were carried out in order to obtain the value of cell voltage and water content within the PEM fuel cell for a specific value of current density using neutron radiographs. The other two tests were carried out to obtain the full cell polarization curve.

The operating conditions for each test used for validation are shown in Table 1.

The validation results of the cell voltage and the water content within the PEM fuel cell from Test 1 to Test 3 are shown in Fig. 2. It is observed that the model results accurately predict both water content and cell voltage, showing an error less than 4%.

The model validation against Test 5 and the Test 6 are shown in Fig. 3. The full polarization curve obtained with the model accurately fits the experimental results, where the maximum error is always less than 3% for both tests.

The presented results show that the one dimensional analytical model predicts with accuracy the cell voltage and the water content within the single PEM fuel cell. Furthermore, the model has been validated for different operating conditions. The complete experimental validation of the analytical model is fully detailed in a previous work [11].

Once the analytical model has been validated with experimental results, the model can be used for different purposes such as evaluate the effect of the main operating parameters in the performance of the PEM fuel cell or to provide a complete map of operation of the PEM fuel cell. In this work, the model has been used to optimize the operating conditions in order to provide the maximum possible power out of the given PEM fuel cell.

Optimization of the single PEM fuel cell operating conditions

The validated analytical model has been used in order to maximize the power output of the single PEM fuel cell by selecting the best operating conditions for every value of current intensity. In this way, a parametric table was obtained by modifying the main operating conditions such as the stoichiometry in cathode and anode, relative humidity in anode and cathode, and the operating temperature. The operating pressure was kept constant with a value of 1 bar. The values used for every variable are shown in Table 2.

The goal of the operating conditions optimization is not focused on finding a set of parameters for all the range of current intensity. In this work, the optimization is carried out for every value of current intensity. This results in a novel and maximum performance polarization curve, which is defined with variable operating conditions, and depending on the current intensity instead of the traditional way.

To obtain the polarization curve which provides the maximum and minimum power for every value of current intensity, it was required to solve a parametric table with all the possible combinations of the variables described in Table 2 for every value of current intensity. A total of 9038 cases have been solved from 0 to 29 A, so that a comprehensive map of the single PEM fuel cell operation was obtained. The time to solve every case was less than 1 s so it is evident the low computational time required for the analytical model. In total, 2.1 h were needed to solve the whole parametric table.

The results of the operating conditions that offer the maximum power output and the values of the cell voltage for those conditions are shown in Table 3 for every value of current intensity. It is observed that the polarization curve

Table 1 – Testing Operating conditions.

	T (°C)	P (bar)	$RH_{a/c}$ (%)	I (A)	λ_a	λ_c
Test 1	60	2	35	10	1.5	3.5
Test 2	60	2	60	10	1.5	3.5
Test 3	60	2	90	10	1.5	3.5
Test 4	60	2	90	10	1.5	5
Test 5	50	1	100	–	1.5	2
Test 6	60	1	100	–	1.5	3.5

Please cite this article in press as: Salva JA, et al., Optimization of a PEM fuel cell operating conditions: Obtaining the maximum performance polarization curve, International Journal of Hydrogen Energy (2016), http://dx.doi.org/10.1016/j.ijhydene.2016.03.136

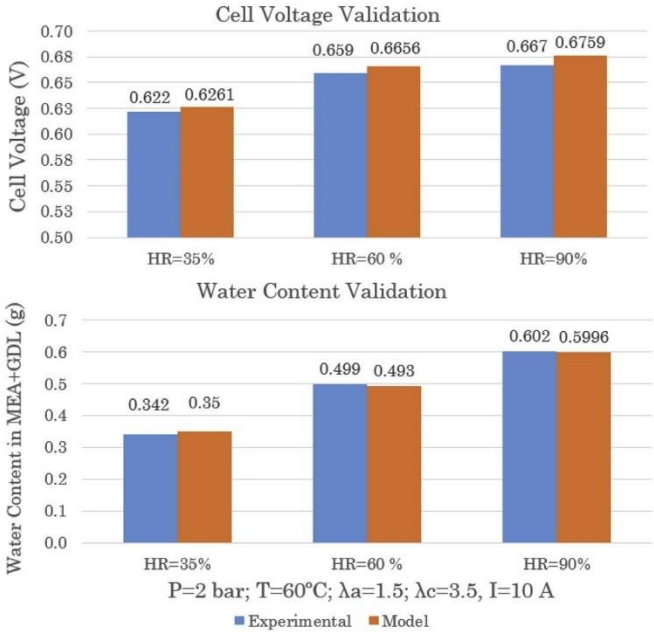

Fig. 2 – Validation results of the cell voltage and the water content (MEA + GDLs) from Test 1 to Test 3.

obtained is formed by the combination of eight traditional set of different polarization curves.

For low values of current intensity, the analytical model predicts that the optimum operating conditions are high values of temperature, relative humidity and anode stoichiometry. On the other hand, it is advisable to operate with low value of cathode stoichiometry. For this set of operating conditions, the activation losses are minimum. This result is according to the literature because high temperature and cathode stoichiometry decrease the activation losses [15–18].

For medium values of current intensity, the analytical model recommends to reduce the temperature from 75 °C to 60 or 50 °C. For this values of temperature, different combinations of relative humidity and cathode stoichiometry are proposed to achieve the maximum power output of the single PEM fuel cell. For the anode stoichiometry, the maximum value is required. With these combinations of operating conditions, the ohmic losses are minimum as the membrane is well hydrated [6], [18].

Finally, for high values of current intensity, it is necessary to increase the cathode stoichiometry to the maximum possible value and reduce the relative humidity step by step. For the anode stoichiometry, maximum value is required too. These operating conditions allow to avoid the concentration zone of the polarization curve and increase the single PEM fuel cell performance for high current intensity [5].

The polarization curves for the eight different set of operating conditions are shown in Fig. 4. Furthermore, the polarization curve formed with the combination of the highest values of cell voltage for every value of current intensity is also shown in Fig. 4. It is observed the difference of performance between every polarization curve. For example, Set 1 has good performance in the range of low current intensity. However, for medium/high values of current intensity the performance is one of the worst. On the other hand, Set 8 has poor performance for low and medium current intensity. However, for a current of 29 A, Set 8 offers the best performance.

This result clearly shows the importance of selecting the operating conditions according to the working point of current intensity in order to increase the power output provided for a particular PEM fuel cell.

The results of the operating conditions that offer the minimum power and the values of the cell voltage for those conditions are shown in Table 4 for every value of current intensity. In this case, the polarization curve with worst performance is formed by the combinations of three different polarization curve.

For low current, high cathode stoichiometry and low temperature, relative humidity and anode stoichiometry is the combination of operating conditions that provide the lowest supplied power. For that combination, the activation losses are the highest [15–18].

Please cite this article in press as: Salva JA, et al., Optimization of a PEM fuel cell operating conditions: Obtaining the maximum performance polarization curve, International Journal of Hydrogen Energy (2016), http://dx.doi.org/10.1016/j.ijhydene.2016.03.136

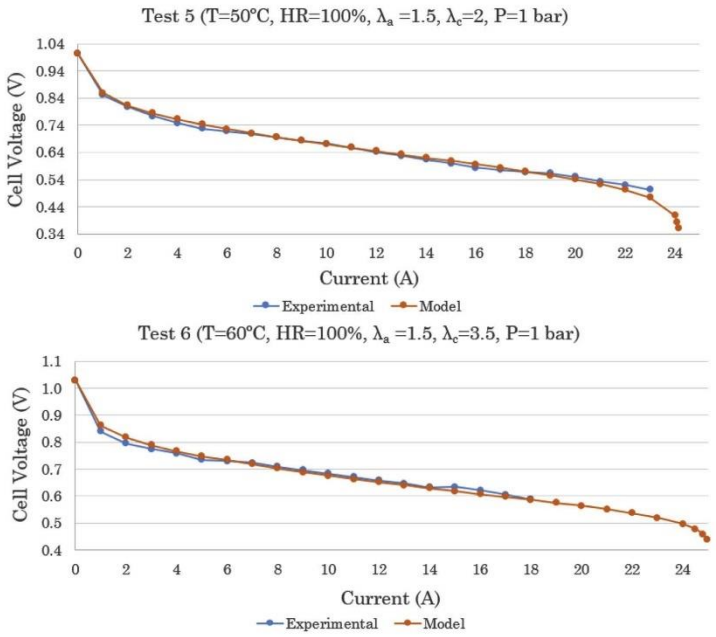

Fig. 3 – Validation results of the polarization curve for Test 5 and Test 6.

For medium current, the only operating condition that it is necessary to change is the operating temperature. According to the analytical model, it is necessary to increase the temperature from 50 to 60 °C. This change is done in order to increase the ohmic losses. With these operating conditions, vapor water formation favored the drying of the membrane [6,7,18].

Finally, for a value of 13.4 A, it is the first value of current intensity where it is possible to reach an oxygen concentration with a value of zero on the catalyst layer. This value of current intensity is known as limiting current [6,7]. The value of cell voltage in that condition is zero because the oxygen molecule can not reach the catalyst layer and the cathode reaction does not occur. According to the analytical model, the first value of limiting current occurs at 13.4 A operating with high value of the temperature and relative humidity and a low value of cathode stoichiometry.

The polarization curves for the three different sets of operating conditions are shown in Fig. 5. In addition, the polarization curve formed with the lowest values of cell voltage for every value of current intensity is also shown in Fig. 5. It is observed that Set 3 has good performance compare with Set 1 and Set 2. However, Set 3 reaches the limiting current for 13.4 A while for Set 1 and Set 2 the limiting current is reached for values of current intensity higher than 30 A.

Table 2 – Used values to developed the parametric table.

Variable	Used values
λ_c	2, 3, 4 and 5
λ_a	1.5, 3, 4 and 5
$RH_{c/a}$ (%)	40, 50, 60, 70, 80, 90 and 100
Temperature (°C)	50, 60, 70 and 75

The operating conditions obtained from the validated analytical model for the cases of maximum and minimum power output were tested in the facilities of INTA in order to verify the accuracy of the numerical results.

The numerical and experimental results of the polarization curve and the power curve for the cases of the maximum and the minimum power output are shown in Fig. 6. It is observed that both numerical and experimental results present a very good agreement. The maximum error for the case of the curve of maximum power output is 1.63% for 7 A and for the case of minimum power output is 2.92% for 13 A. This results confirm the accuracy of the validated analytical model predicting the performance of the single PEM fuel cell for different operating conditions.

The results of power output show that operating with the conditions of maximum performance it is possible to reach a value close to 12 W. In contrast, the maximum power obtained with the conditions of minimum performance is around 6 W. This result shows that the difference (in the point of maximum power) between the curve of maximum and

Please cite this article in press as: Salva JA, et al., Optimization of a PEM fuel cell operating conditions: Obtaining the maximum performance polarization curve, International Journal of Hydrogen Energy (2016), http://dx.doi.org/10.1016/j.ijhydene.2016.03.136

Table 3 – Operating conditions and cell voltage results for the case of maximum power.

Current (A)	λ_a	λ_c	$RH_{c/a}$ (%)	T (°C)	Cell voltage (V)
0	5	5	100	75	1.02
1	5	5	100	75	0.8906
2	5	5	100	75	0.8315
3	5	2	100	75	0.7916
4	5	2	100	75	0.7606
5	5	2	100	60	0.738
6	5	2	100	60	0.7214
7	5	2	100	60	0.7065
8	5	2	100	60	0.6927
9	5	2	100	60	0.68
10	5	2	100	60	0.669
11	5	2	100	60	0.6565
12	5	2	100	60	0.6443
13	5	2	100	60	0.6322
14	5	2	100	60	0.62
15	5	2	100	60	0.6076
16	5	2	90	60	0.5974
17	5	2	90	60	0.5846
18	5	2	90	60	0.5712
19	5	3	100	60	0.5573
20	5	5	100	50	0.5456
21	5	5	90	50	0.5355
22	5	5	90	50	0.5243
23	5	5	90	50	0.5125
24	5	5	90	50	0.5001
25	5	5	90	50	0.479
26	5	5	90	50	0.464
27	5	5	90	50	0.4462
28	5	5	90	50	0.422
29	5	5	70	50	0.391

Table 4 – Operating conditions and cell voltage results for the case of minimum performance.

Current (A)	λ_a	λ_c	$RH_{c/a}$ (%)	T (°C)	Cell voltage (V)
0	1.5	5	40	50	0.99
1	1.5	5	40	50	0.8162
2	1.5	5	40	50	0.7574
3	1.5	5	40	50	0.7151
4	1.5	5	40	50	0.68
5	1.5	5	40	50	0.6489
6	1.5	5	40	50	0.6206
7	1.5	5	40	50	0.5942
8	1.5	5	40	50	0.5694
9	1.5	5	40	50	0.5565
10	1.5	5	40	60	0.5333
11	1.5	5	40	60	0.5113
12	1.5	5	40	60	0.4904
13	1.5	5	40	60	0.4705
13.4	1.5	2	100	75	0

minimum power output is about 100%. Therefore, it is clearly demonstrated the importance of selecting the operating conditions depending on the value of the current intensity.

To understand the big difference in the PEM fuel cell performance between the polarization curve of maximum and minimum power output, the validated analytical model has been used in order to estimate the different overpotentials (activation, ohmic and concentration) of the single PEM fuel cell. The three overpotentials are shown in Fig. 7 where the difference in the ohmic overpotential is the most significant. It is important to note that the value of 13.4 A, in the minimum performance curve, is the limiting current density so the operating conditions are totally different from 13 A. This causes the sudden drop in the ohmic overpotential and the sudden rise in the concentration overpotential. For the case of the activation overpotential, it is observed that just for low values of intensity the differences are appreciable.

According to Eq (4), the unique parameter that affect the ohmic overpotential between the scenario of the maximum and minimum power output is the electrical conductivity of the membrane. The rest of the parameters are not considered to vary with the temperature in the range from 50 to 75 °C [11].

It is well known that the membrane electrical conductivity depends strongly on the water content in the membrane [6,7] as it was shown in Eq (5) according to Springer [14].

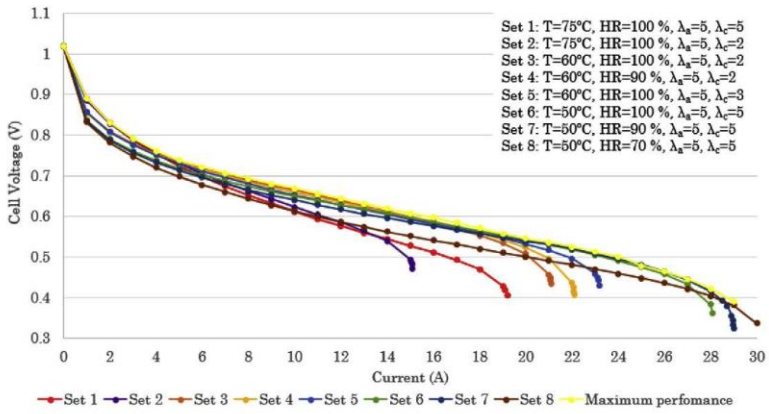

Fig. 4 – Polarization curves for the eight different combinations of operating conditions and for the maximum performance.

Please cite this article in press as: Salva JA, et al., Optimization of a PEM fuel cell operating conditions: Obtaining the maximum performance polarization curve, International Journal of Hydrogen Energy (2016), http://dx.doi.org/10.1016/j.ijhydene.2016.03.136

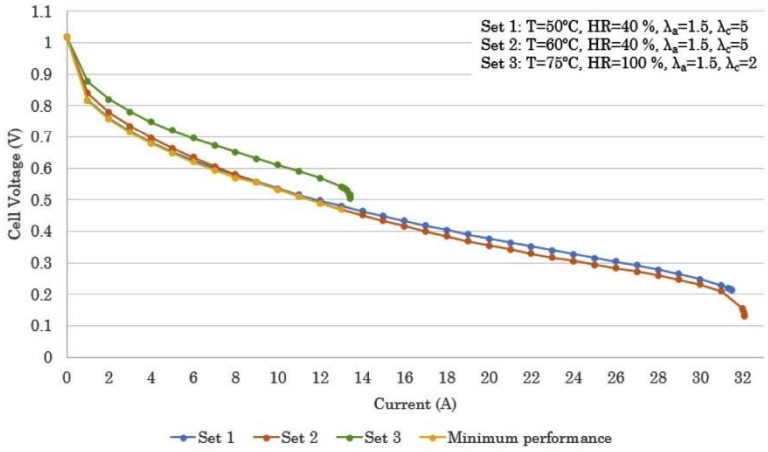

Fig. 5 – Polarization curves for the three different combinations of operating conditions and for the minimum performance.

The water content for the case of maximum and minimum power output is shown in Fig. 8. It is clearly observed that the case of maximum performance has more water in the membrane so the membrane is better hydrated. In addition, it is shown that the value of water content for the case of maximum performance is 14 which means that the membrane is fully hydrated [6,7].

In this way, the model has been able to predict the maximum and minimum power output of the given PEM fuel cell with accuracy (error always less than 3% compared with the experimental results). In addition, the model has been used in order to explain the big difference in the PEM fuel cell performance between the polarization curve of maximum and minimum power output.

Potential use of the validated analytical model

A maximum performance polarization curve has been defined where the operating conditions are variable depending on the value of the current intensity instead of the traditional way with constant operating conditions. Once the single PEM fuel cell is modeled and characterized, the validated analytical model can be used to design the

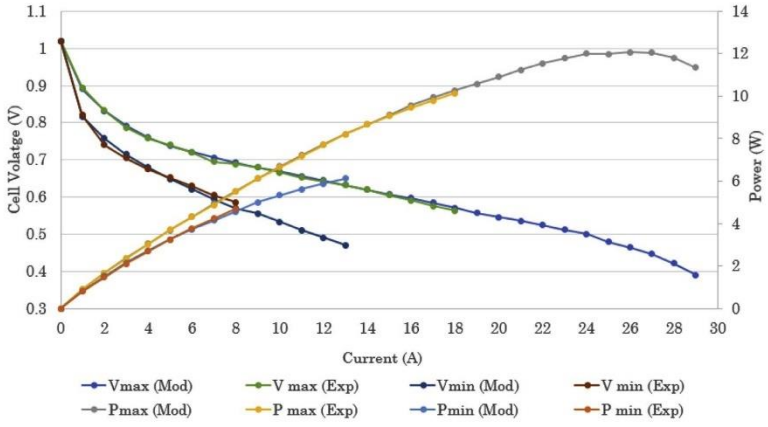

Fig. 6 – Numerical and experimental results of the polarization curve and the power curve for the cases of the maximum and the minimum power.

Please cite this article in press as: Salva JA, et al., Optimization of a PEM fuel cell operating conditions: Obtaining the maximum performance polarization curve, International Journal of Hydrogen Energy (2016), http://dx.doi.org/10.1016/j.ijhydene.2016.03.136

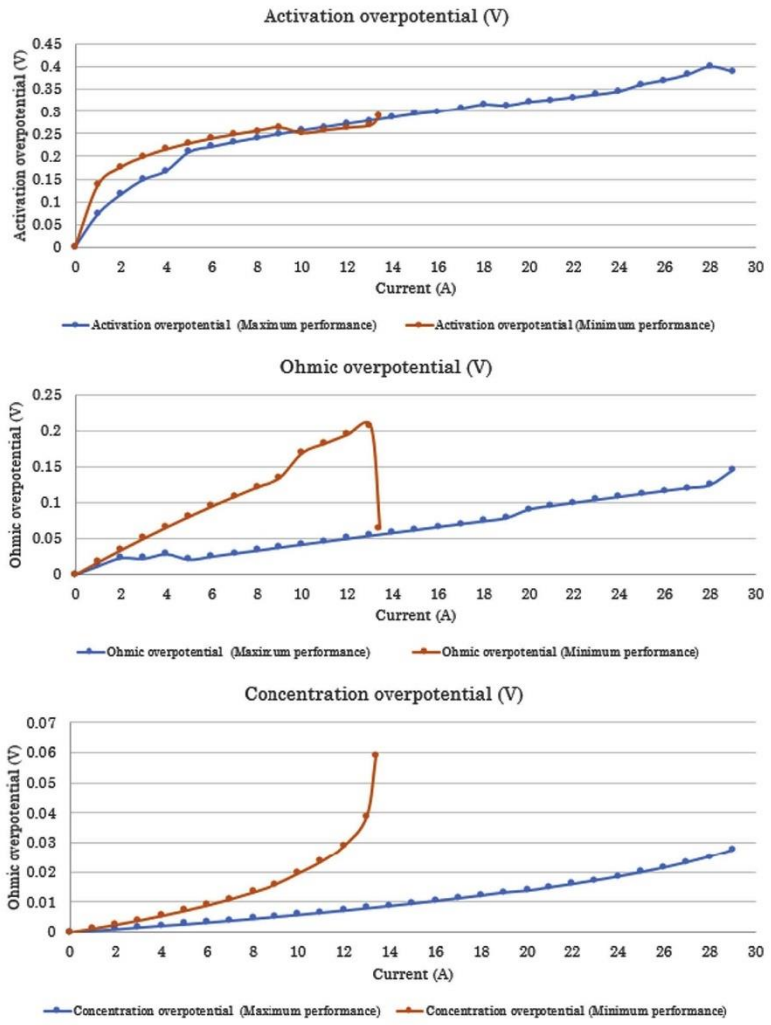

Fig. 7 – Activation, ohmic and concentration overpotential for the cases of maximum and minim power.

optimize size of a stack. Although the analytical model has been used for a particular PEM fuel cell, this can be potentially applied to any PEM fuel cell provided the model parameters are characterized. If not available, a set of experimental tests would be required in order to characterize the model parameters.

Because the results of the analytical model are the maximum power output and the way to obtain this performance giving the operating conditions, it is possible to use the analytical model to design the size of the stack to provide a specific power. According to the results of the analyzed PEM fuel cell, operating with the curve of maximum power output instead of operating with the curve of minimum power output can save around half of the material required (half of bipolar plates, GDLs and Membranes).

This reduction of materials is not only translated into cost saving but also in reductions in weight and volume. The reduction of this three aspects are fundamental to do the fuel

Please cite this article in press as: Salva JA, et al., Optimization of a PEM fuel cell operating conditions: Obtaining the maximum performance polarization curve, International Journal of Hydrogen Energy (2016), http://dx.doi.org/10.1016/j.ijhydene.2016.03.136

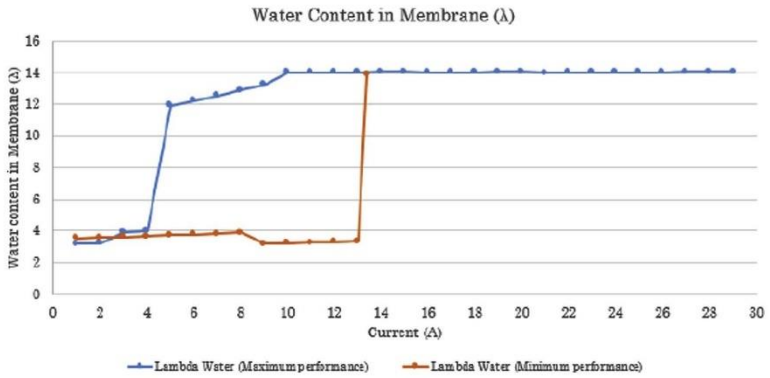

Fig. 8 – Polarization curves for the three different combinations of operating conditions and for the minimum performance.

cell technology competitive versus traditional power systems like internal combustion engine [19–23].

Conclusions

A one dimensional analytical model has been used in order to optimize the operating conditions of a PEM fuel cell. In this way, a maximum performance polarization curve has been defined where the operating conditions are variable depending on the value of current instead of the traditional way with constant operating conditions for all the range of operation. The results show that it is possible to use the analytical model to optimize the performance of the single PEM fuel cell. For this particular case, operating with the conditions of maximum performance, it is possible to increase the power by almost 100% more than operating with the conditions of minimum performance (12 W versus 6 W). In addition, the model has been used in order to explain the big difference in the PEM fuel cell performance between the polarization curve of maximum and minimum power output.

The operating conditions obtained with the validated analytical model have been tested in the facilities of INTA using the real PEM fuel cell. The results present a very good agreement between the experimental and the model results where the maximum error is less than 3% for the cell voltage.

The analytical validated model can be used to design the size of a stack to provide a specific power output saving costs, weight and volume. The reduction of this three aspects are fundamental to make the fuel cell technology competitive versus traditional power systems.

REFERENCES

[1] Mehta V, Smith CJ. Review and analysis of PEM fuel cell design and manufacturing. J Power Sources 2003;114:32e53.
[2] Murphy OJ, Cisar A, Clarke E. Low-cost light weight high power density PEM fuel cell stack. Electrochim Acta 1998;43(24):3829–40.
[3] Jayakumar K, Pandiyan S, Rajalakshmi N, Dhathathreyan KS. Cost-benefit analysis of commercial bipolar plates for PEMFC's. J Power Sources 2006;161(1):454–9.
[4] Li X, Sabir I. Review of bipolar plates in PEM fuel cells: flow-field designs. Int J Hydrogen Energy 2005;30(4):359–71.
[5] Wang CY. Fundamental models for fuel cell engineering. Chem Rev 2004;104:4727–65.
[6] Mench Matthew M. Fuel cell engines. 1st ed. United States: John Wiley & Sons, Inc; 2008.
[7] Barbir Frano. PEM fuel cells: theory and practice. ELSEVIER; 2005.
[8] Kanani H, Shams M, Hasheminasab M, Bozorgnezhad A. Model development and optimization of operating conditions to maximize PEMFC performance by response surface methodology. Energy Convers Manag 2015;93:9–22.
[9] Wishart J, Dong Z, Secanell M. Optimization of a PEM fuel cell system based on empirical data and a generalized electrochemical semi-empirical model. J Power Sources 2006;161(2):1041–55.
[10] Chan C, Zamel N, Li X, Shen J. Experimental measurement of effective diffusion coefficient of gas diffusion layer/microporous layer in PEM fuel cells. Electrochim Acta 2012;65(0):13–21.
[11] Antonio Salva J, Iranzo A, Rosa F, Tapia E. Validation of cell voltage and water content in a PEM fuel cell model using neutron imaging for different operating conditions. Energy 2016;101:100–12.
[12] http://www.fchart.com/ees/.
[13] Iranzo A, Muñoz M, Rosa F, Pino J. Numerical model for the performance prediction of a PEM fuel cell. Model results and experimental validation. Int J Hydrogen Energy 2010;35:11533–50.
[14] Springer TE, Zawodzinski TA, Gottesfeld S. Polymer electrolyte fuel cell model. J Electrochem Soc 1991;138:2331–42.
[15] Kabza DA. Fuel cell formulary. 2015.
[16] Noorkami M, Robinson JB, Meyer Q, Obeisun OA, Fraga ES, Reisch T, et al. Effect of temperature uncertainty on polymer electrolyte fuel cell performance. Int J Hydrogen Energy 2014;39(3):1439–48.
[17] Song C, Tang Y, Zhang JL, Zhang J, Wang H, Shen J, et al. PEM fuel cell reaction kinetics in the temperature range of 23-120 °C. Electrochim Acta 2007;52(7):2552–61.

Please cite this article in press as: Salva JA, et al., Optimization of a PEM fuel cell operating conditions: Obtaining the maximum performance polarization curve, International Journal of Hydrogen Energy (2016), http://dx.doi.org/10.1016/j.ijhydene.2016.03.136

[18] J.W., J.Z., Zhang Jianlu, Zhang Huamin. PEM fuel cell testing and diagnosis. 2013.
[19] Wong KH, Loo KH, Lai YM, Tan SC, Tse CK. A theoretical study of inlet relative humidity control in PEM fuel cell. Int J Hydrogen Energy 2011;36(18):11871–85.
[20] Jayakumar K, Pandiyan S, Rajalakshmi N, Dhathathreyan KS. Cost-benefit analysis of commercial bipolar plates for PEMFCS. J Power Sources 2006;161:454–9.
[21] Murphy OJ, Cisar A, Clarke E. Low-cost light weight high power density PEM fuel cell stack. Electrochimica Acta 1998;43(24):3829–40.
[22] Makkus RC, Janssen AHH, de Bruijn FA, Mallant RK. Stainless steel for cost-competitive bipolar plates in PEMFCS. Fuel Cells Bull 2000;3(17):5–9.
[23] Baron I, Kirchain R, Roth R. Technical cost analysis for PEM fuel cells. J Power Sources 2002;109:71–5.

Please cite this article in press as: Salva JA, et al., Optimization of a PEM fuel cell operating conditions: Obtaining the maximum performance polarization curve, International Journal of Hydrogen Energy (2016), http://dx.doi.org/10.1016/j.ijhydene.2016.03.136

6.6. Contribución 6

Effect of carbon dioxide on the contamination of low temperature and high temperature PEM (polymer electrolyte membrane) fuel cells. Influence of temperature, relative humidity and analysis of regeneration processes

Manuel Antonio Díaz, Alfredo Iranzo, Felipe Rosa, Fernando Isorna, Eduardo López, Juan Pedro Bolivar

Publicado en:

Journal: Energy
Editorial: Elsevier
Editor jefe: Professor Henrik Lund
Reference: Energy 90 (2015) 299e309
Year: 2015
ISSN: 0360-5442
doi.org/10.1016/j.energy.2015.06.097

Available online at www.sciencedirect.com
ScienceDirect

Categoría	Rango revista / Total revista	Cuartil
Energy & Fuels	15/88	Q1
Impact Factor (2015)	4,292	
Citations	23	

6.7. Contribución 7

Energy evaluation of a solar hydrogen storage facility: Comparison with other electrical energy storage technologies

Eduardo López González, Fernando Isorna Llerena, Manuel Silva Pérez, Felipe Rosa Iglesias, José Guerra Macho

Publicado en:

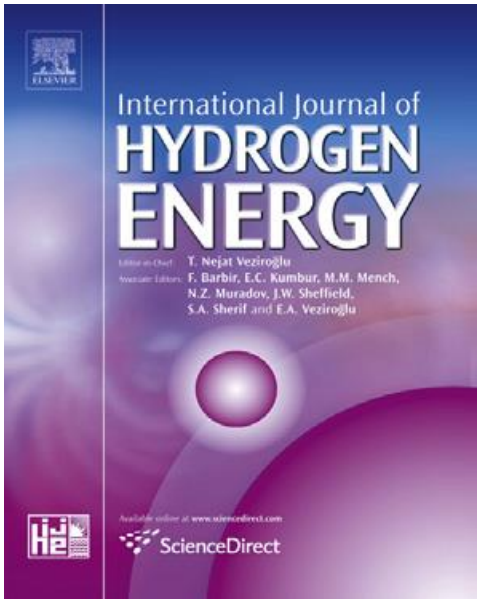

Revista: International Journal of Hydrogen Energy
Editorial: ELSEVIER
Editor Jefe: T. Nejat Veziroglu
Referencia: Vol 40, Issue 15, 27/04/15, Pp 5518-5525
Año: 2015
ISSN: 0360-3199
http://dx.doi.org/10.1016/j.ijhydene.2015.01.181

Categoría	Rango revista / Total revista	Cuartil
Energy & Fuels	28/88	Q2
Chemistry	8 / 27	Q2
Impact Factor (2015)	3,205	
Citations	64	

6.8. Contribución 8

Development, integration and evaluation of hybrid fuel cell power systems for unmanned ground vehicles

E. López González, J. Sáenz Cuesta, F. Isorna Llerena, M.A. Ridao, C. Bordons, E. Hernandez, J. Brett

Presentado in:

Evento: VII Symposium on Hydrogen, Fuel Cells and Advanced Batteries, HYCELTEC 2019

Organizador: Universidad de Barcelona

Fecha: 01/07/2019 – 03/07/2019

Lugar: Barcelona, España

ISSN: 0360-3199

6.9. Contribución 9

Energy Management System for a Microgrid with hydrogen storage and two batteries using Model Predictive Control

Miguel A. Ridao, P. Fernández, C. Bordons, E. López, F. Isorna

Presentado en:

Evento: VII Symposium on Hydrogen, Fuel Cells and Advanced Batteries, HYCELTEC 2019

Organizador: Universidad de Barcelona

Fecha: 01/07/2019 – 03/07/2019

Lugar: Barcelona, España

ISSN: 0360-3199

6.10. Contribución 10

EVALUACIÓN DE UN VEHÍCULO TERRESTRE NO TRIPULADO (UGV) CON PILA DE COMBUSTIBLE

Eduardo López González, Jaime Sáenz Cuesta, Fernando Isorna Llerena, M.A. Ridao, E. Hernández

Presentado en:

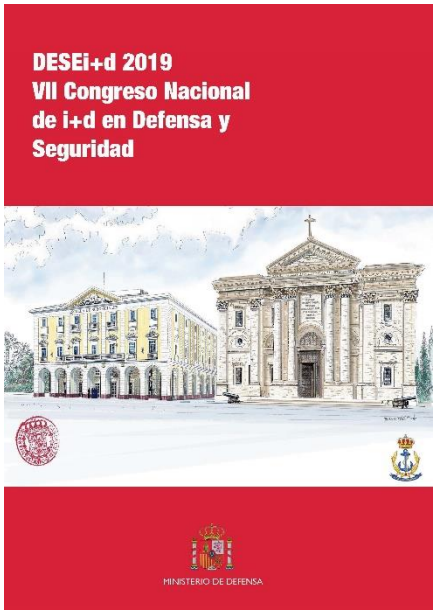

Evento: VII Congreso Nacional de i+d en Defensa y Seguridad DESEi+d 2019
Fecha: 19-21 noviembre 2019
Lugar: San Fernando, Cádiz (España)
NIPO: 083-19-215-9

DESEID-2019-96

EVALUACIÓN DE UN VEHÍCULO TERRESTRE NO TRIPULADO (UGV) CON PILA DE COMBUSTIBLE

Eduardo López González, Jaime Sáenz Cuesta, Fernando Isorna Llerena, M.A. Ridao, E. Hernández

Los vehículos no tripulados ofrecen múltiples posibilidades en aplicaciones industriales, científicas y de defensa, permitiendo recopilar datos de alta calidad en tiempo real con un menor coste que otros métodos tradicionales, a la vez que facilita el acceso y la operación en entornos hostiles a operadores humanos. El almacenamiento de energía a bordo es uno de los factores más relevantes a tener en cuenta en el diseño, desarrollo y operación de estas plataformas, debido a su impacto en las prestaciones y autonomía de operación, en términos de duración de las misiones. En el marco del proyecto «Improving efficiency and operational range in low-power unmanned vehicles through the use of hybrid fuel-cell power systems (IUFCV)», el Laboratorio de Sistemas de Energía del INTA en El Arenosillo (Huelva) ha desarrollado en colaboración con otros socios un sistema de potencia híbrido, basado en baterías de ion litio y una pila de combustible PEM de cátodo abierto alimentada con hidrógeno a presión, que ha sido ensayado y caracterizado en bancos de ensayo, y posteriormente integrado en un vehículo terrestre no tripulado. En este trabajo se presentan los resultados obtenidos en la evaluación experimental del vehículo en diferentes condiciones y perfiles de uso en operaciones reales, simulando posibles misiones, en aplicaciones de vigilancia y detección con cámaras, GNSS y lídar. Se ofrecen datos comparativos de la autonomía del vehículo en su configuración original, solo con baterías, y con el sistema híbrido; las nuevas especificaciones del vehículo con este sistema híbrido (peso, carga útil permitida, etc.), así como las modificaciones realizadas en la plataforma en este proceso de integración.

6.11. Contribución 11

Green hydrogen production methods. A review of solar-driven water splitting techniques

Fernando Isorna Llerena, F. Segura Manzano y José M. Andújar Márquez

Presentado en:

Evento: European Hydrogen Energy Conference 2018 (EHEC 2018)
Organizador: Spanish Hydrogen Association
Fechas: 14 a 16 marzo 2018
Lugar: Málaga, España.

6.12. Contribución 12

Evaluation of fuel cell/battery passive hybrid power systems for unmanned vehicles

E. López; J. Sáenz; F. José Vivas; F. Isorna; M. A. Ridao; C. Bordons; E. Hernández; A. Efes

Presentado en:

Evento: European Hydrogen Energy Conference
Organizador: Spanish Hydrogen Association
Fechas: 14 a 16 marzo 2018
Lugar: Málaga, España.

6.13. Contribución 13

Diseño y desarrollo de una microrred para la gestión y el almacenamiento de energía eléctrica de origen renovable

Isorna Llerena, Fernando, López González, Eduardo y Sáenz Cuesta, Jaime Luis

Presentado en:

Evento: VI Congreso Nacional de i+d en Defensa (DESi+d 2018)
Organizador: Spanish hydrogen Association
Fecha: 20-22 Noviembre 2018
Lugar: Valladolid, España.

6.14. Contribución 14

Increasing energy efficiency and autonomy in unmanned vehicles using hybrid fuel cell power systems

Eduardo López, Fernando Isorna Miguel A. Ridao, Carlos Bordons, A. Elfes, Emili Hernández

Presentado en:

Evento: VI Symposium on Hydrogen, Fuel Cells and Advanced Batteries, HYCELTEC 2017

Fecha: 19-23 Junio 2017

Lugar: Oporto, Portugal.

ISBN 978-972-752-233-0

6.15. Contribución 15

Cómo incrementar la duración de las misiones en vehículos submarinos no tripulados (y otras plataformas robóticas) Proyecto IUFCV

Eduardo López, Fernando Isorna Miguel A. Ridao, Carlos Bordons, A. Elfes, Emili Hernández

Presentado en:

Evento: 15ª Feria de las Ciencias

Organiador: Sociedad Andaluza para la Divulgación de la Ciencia y Fundación Descubre

Director: Josechu Ferreras Tomé

Fecha: 11/05/2017 – 13/05/2017

Lugar: Sevilla, España.

6.16. Contribución 16

Incremento de la eficiencia energética y autonomía en vehículos no tripulados mediante el uso de sistemas de energía híbridos con pila de combustible

López González, Eduardo, Isorna Llerena, Fernando, Ridao Carlini, Miguel Ángel, Bordons Alba, Carlos, Elfes, Alberto, Hernández, Emili

Presentado in:

Evento: IV Congreso Nacional de I+D en Defensa y Seguridad, 2016
Organizador: Centro Universitario de la Defensa de San Javier
Fecha: 16/11/2016 – 18/11/2016
ISBN: 978-84-946021-3-9
Lugar: San Javier, Murcia, España.

6.17. Contribución 17

Analysis of high-pressure hydrogen and natural gas cylinders explosions through TNT equivalent method

E. López. R. Rengel, G. W. Mair, F. Isorna

Presentado en:

Evento: V Iberian Symposium on Hydrogen, Fuel Cells and Advanced Batteries

Organizador: Universidad de La Laguna

ISBN: 978-84-606-8621-7

Fecha: 05/07/2015 – 08/07/2015

Lugar: Tenerife, España.

6.18. Contribución 18

Aplicación en vehículos no tripulados de sistemas híbridos de potencia basados en pilas de combustible

López González, Eduardo, Isorna Llerena, Fernando, Argumosa Martínez, Mª Pilar, Maellas Benito, Jesús, Ridao Carlini, Miguel Ángel, Bordons Alba, Carlos

Presentado en:

Evento: II Congreso Nacional de I+D en Defensa y Seguridad, 2014
Organizador: Centro Universitario de la Defensa Zaragoza
ISBN: 978-84-940583-2-5
Fecha: 06/11/2014 – 07/11/2014
Lugar: Zaragoza, España.

6.19. Contribución 19

Energy evaluation of a solar hydrogen storage facility

Eduardo López González, Fernando Isorna Llerena, Manuel Silva Pérez, Felipe Rosa Iglesias

Presentado en:

Evento: European Hydrogen Energy Conference 2014
Organizador: Spanish Hydrogen Association (AEH2)
Fecha: 12/03/2014 – 14/03/2014

Lugar: Sevilla, España.

Lista de Tablas

Lista de Tablas

Tabla 1: Especificaciones del banco de ensayos de pilas de combustible 37

Tabla 2: Características técnicas de la pila de combustible 40

Tabla 3: Características técnicas de las baterías..... 48

Tabla 4: Características técnicas de la batería buffer 50

Tabla 5: Características principales de la aeronave original 50

Tabla 6: Principales diferencias de las dos plataformas aéreas..... 51

Tabla 7: Características del sistema 52

Lista de Figuras

Lista de Figuras

Figura 1: Banco de ensayos de pilas de combustible 37

Figura 2: Membrane Electrode Assembly de alta temperatura 38

Figura 3: Membrane Electrode Assembly de baja temperatura 38

Figura 4: Placas bipolares para ensayos 39

Figura 5: Imágenes de placas bipolares de grafito y una MEA 39

Figura 6: Pila de combustible utilizada BMPowwer© 500 40

Figura 7: Pila de combustible instalada en la plataforma 40

Figura 8: Software de control de la pila de combustible 41

Figura 9: Módulos de alto voltaje 43

Figura 10: Módulos de bajo voltaje 44

Figura 11: Cámara climática 46

Figura 12: Conjunto de cámara climática y bancos de ensayos de baterías 46

Figura 13: Habitáculo de las baterías con los 3 bloques debidamente soldados 48

Figura 14: Baterías conectadas dentro del habitáculo 48

Figura 15: Imágenes de las baterías usadas en el sistema de propulsión de la plataforma 49

Figura 16: Batería buffer 49

Figura 17: Imagen de la plataforma aérea eléctrica 51

Figura 18: Plataforma de vehículo eléctrico unipersonal: (a) diseño conceptual; (b) implementación física. 52

Lista de Acrónimos

ICE	Internal combustión engine
INTA	Instituto Nacional de Técnica Aeroespacial
PEFC	Polymer electrolyte fuel cell
RPA	Remotely piloted aircraft
RPAS	Remotely piloted aircraft system
UAV	Unmanned aerial vehicles